Graphene Modulators for Silicon Photonic Optical Links

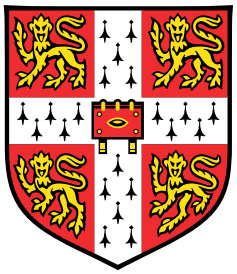

Hannah Fei-Yen Watson

Department of Engineering
University of Cambridge

This dissertation is submitted for the degree of
Doctor of Philosophy

Wolfson College

September 2020

Declaration

I hereby declare that except where specific reference is made to the work of others, the contents of this dissertation are original and have not been submitted in whole or in part for consideration for any other degree or qualification in this, or any other university. This dissertation is my own work and contains nothing which is the outcome of work done in collaboration with others, except as specified in the text and Acknowledgements. This dissertation contains fewer than 65,000 words including appendices, footnotes, tables and equations and has fewer than 150 figures.

Hannah Fei-Yen Watson
September 2020

Abstract

Graphene Modulators for Silicon Photonic Optical Links

Hannah Fei-Yen Watson

The backbone of today's society is the transfer of information. Next-generation data network infrastructures need to support Tb/s data rates. Existing optical fibre communication networks cannot support Tb/s data transmission without consuming an unsustainable amount of power. Optical transceivers send and receive information encoded in light, relying on electro-optic modulators to convert the electrical data signal into the optical domain, and photodetectors to convert the optical signal back into the electrical domain. Power consumption can be reduced by using efficient and compact modulators and photodetectors to integrate the optics closer to the electronics and thus minimise the losses of electrical interconnect at high frequencies. Si photonics technology offers a cost-effective solution for fabricating integrated photonic circuits by combining electronic and photonic components in the same circuit by using existing CMOS technology. This thesis focuses on the development of a scalable graphene-based platform for integrated photonics, and specifically on the electro-optic modulator. I have focused on a double single-layer graphene modulator design in three different configurations that can be used for different types of optical links. This includes a graphene-based electro-absorption modulator, ring resonator modulator, and Mach-Zehnder modulator. The double-layer structure enables the absorption and phase of an optical carrier signal to be electrostatically controlled without the need for doped waveguides. This is the most efficient graphene-based phase modulator to-date with an extracted $V_\pi L \sim 0.12$ V·cm, which is ~ 2 times better than the lowest reported graphene phase modulator. As well as showing very efficient phase modulation, the graphene phase modulator is capable of being operated in the transparency regime where graphene becomes transparent to absorption via interband transitions. Operating in the transparency regime means that the graphene phase modulator is capable of pure phase modulation which is a desirable property for complex modulation formats. Benefiting from efficient phase modulation, the graphene ring resonator modulator has demonstrated an $\mathrm{FOM_{EA}} \sim 4.48$, ~ 2 times better than the highest currently reported for graphene-based modulators. These results represent a step towards the

development of a future graphene-based platform for efficient and compact modulators and photodetectors needed for next-generation optical links.

I would like to dedicate this thesis to Shahab Akhavan and Jakob Münch for sharing the journey, and my 2016 self who decided to start it.

Acknowledgements

I would like to thank Prof. Andrea C. Ferrari and Nokia Bell Labs for accepting me as their PhD student, it has been a privilege. Special thanks goes to Dr Alfonso Ruocco who's experience, knowledge, and humour was greatly appreciated.

I would like to thank the following people for their specific contributions towards this thesis. Dr Alfonso Ruocco who helped with the simulations in chapter 5, designed the passive photonic circuits used in chapter 8 and 10, and helped with the experimental characterisation in chapter 7, 8, 9, and 10. Thanks to Jakob Münch for his continued support and advice, and for the design of the photodector used in chapter 10. Thanks to Dr Osman Balci and Dr Sachin Shinde for growing the CVD graphene that I used for the graphene modulators on Si in chapter 7, 8, 9, and 10, and for the on-going advice to improve the transfer process. Shahab Akhavan, Thomas Albrow-Owen, Dr Alisson Cadore, Dr Alan Colli, Dr Domenico De Fazio, Dr Phillipa Hooper, Ernestine Hui, Dr Jon Griffiths, Dr. Antonio Lombardo, Dr Gyeong C. Park, Dr Lorenzo Pedrazzetti, David Purdie, and Dr Victor Serdio for their advice and training on microfabrication techniques and equipment described in chapter 6. Dr Anna Ott and Dr Eugene Alexeev for their training and advice on Raman. Dr Simone Schuler and Dr Junjia Wang for their help in integrated photonics. Last, but not least, thank you to all the facilities and administrative staff at the Cambridge Graphene Centre, Electrical Engineering, and Physics.

I would like to acknowledge my sources of funding: the Engineering and Physical Sciences Research Council (EPSRC) and Nokia Bell Labs.

Publications and conference presentations

Publications

- **H. F. Y. Watson**, A. Ruocco, J. E. Muench, O. Balci, S. M. Shinde, M. Pantouvaki, D. Van Thourhout, R. Sordan, A. Tomadin, M. Romagnoli, and A. C. Ferrari, *Graphene phase modulators operating in the transparency regime*, Submitted (2020).

- J. E. Muench, A. Ruocco, M. A Giambra, V. Miseikis, D. Zhang, J. Wang, **H. F. Y. Watson**, G. C Park, S. Akhavan, V. Sorianello, M. Midrio, A. Tomadin, C. Coletti, M. Romagnoli, A. C Ferrari and I. Goykhman, *Waveguide-Integrated, Plasmonic Enhanced Graphene Photodetectors*, Nano Letters 19, 7632-7644, (2019).

Conference Presentations

- **H. F. Y. Watson**, A. Ruocco, J. E. Muench, and A. C. Ferrari, *Graphene based integrated photonics for optical interconnect*, Arm Research Summit, Online (2020).

- **H. F. Y. Watson**, A. Ruocco, J. Wang, J. E. Muench, V. Sorianello, M. Bruna, I. Goykhman, M. Romagnoli, and A. C. Ferrari, *Waveguide-Integrated Double-Layer Graphene Modulators on SiN for On-chip Optical Interconnects*, Graphene Week Conference, Helsinki (2019).

- J. E. Muench, A. Ruocco, V. Miseikis, M. A. Giambra, D. Zhang, J. Wang, **H. F. Y. Watson**, G. C. Park, S. Akhavan, V. Sorianello, M. Midrio, C. Coletti, M. Romagnoli, A. C. Ferrari, and I. Goykhman, *Waveguide-Integrated, Plasmonic Enhanced Graphene Photodetectors*, Graphene 2019 Conference, Rome (2019).

- **H. F. Y. Watson**, J. Wang, J. E. Muench, D. Zhang, V. Sorianello, M. Bruna, M. Romagnoli, A. C. Ferrari, and I. Goykhman, *Double-layer Graphene-SiN Modulators for*

On-chip Integrated Optical Interconnects, Graphene Week Conference, San Sebastian (2018).

- J. E. Muench, D. Zhang, J. Wang, **H. F. Y. Watson**, V. Sorianello, S. Akhavan, A. Ruocco, G. Park, M. Romagnoli, A. C. Ferrari and I. Goykhman, *Plasmonic Enhanced Waveguide Integrated Graphene Photodetector for Telecom Wavelengths*, Graphene Week Conference, San Sebastian (2018).

- **H. F. Y. Watson**, J. Wang, J. E. Muench, D. Zhang, V. Sorianello, M. Bruna, M. Romagnoli, A. C. Ferrari, and I. Goykhman, *Waveguide Integrated Double Layer Graphene SiN Modulators for On-chip Optical Interconnects*, 2D Materials Conference, Cranage (2018).

- J. E. Muench, D. Zhang, **H. F. Y. Watson**, J. Wang, S. Akhavan, A. Ruocco, V. Sorianello, M. Romagnoli, A. C. Ferrari and I. Goykhman, *Plasmonic Enhanced Waveguide Integrated Graphene p-n Junction Photodetectors for Telecom Wavelengths*, 2D Materials Conference, Cranage (2018).

- **H. F. Y. Watson**, J. Wang, J. E. Muench, D. Zhang, V. Sorianello, M. Bruna, M. Romagnoli, A. C. Ferrari, and I. Goykhman, *Waveguide Integrated Double Layer Graphene-SiN Modulators For On-chip Optical Interconnects*, Graphene 2018 Conference, Dresden (2018).

- J. E. Muench, D. Zhang, J. Wang, **H. F. Y. Watson**, S. Akhavan, A. Ruocco, V. Sorianello, M. Romagnoli, A. C. Ferrari and I. Goykhman, *Plasmonic Enhanced Waveguide Integrated Graphene p-n Junction Photodetectors for Telecom Wavelengths*, Graphene 2018 Conference, Dresden (2018).

- **H. F. Y. Watson**, J. E. Muench, J. Wang, D. Zhang, A. C. Ferrari, and I. Goykhman, *Waveguide Integrated Double Layer Graphene-Si Modulators for On-chip Optical Interconnect*, 2D Materials Conference, Wyboston (2017).

- J. E. Muench, **H. F. Y. Watson**, D. Zhang, J. Wang, A. C. Ferrari, and I. Goykhman, *Plasmonic enhanced waveguide integrated graphene p-n junction photodetectors for telecom wavelengths*, 2D Materials Conference, Wyboston (2017).

Table of contents

List of acronyms and symbols

Acronyms

ASIC	Application-specific integrated circuit
ASK	Amplitude shift keying
BEOL	Back-end-of-line
BW	Bandwidth
c-Si	Crystalline silicon
CMOS	Complementary metal-oxide-semiconductor
CPU	Central processing unit
CVD	Chemical vapour deposition
DC	Direct current
DPSK	Differential phase shift keying
DSLG	Double single-layer graphene
DUT	Device under test
EAM	Electro-absorption Modulator
EO	Electro-optic
ER	Extinction ratio
FDE	Finite-difference eignenmode solver
FMF	Few-mode fibre

FSR	Free spectral range
FWHM	Full width at half maximum
GPD	Graphene photodetector
h-BN	Hexagonal boron nitride
HCF	Hollow-core fibre
ICP	Inductively coupled plasma
IL	Insertion Loss
LN	Lithium niobate
LNOI	Lithium niobate-on-insulator
LO	Local oscillator
LPE	Liquid phase exfoliation
MCF	Multicore fibre
MDM	Mode-division multiplexing
MGM	Metal-graphene-metal
MMF	Multi-mode fibre
MMI	Multi-mode interference coupler
MOS	Metal-oxide-semiconductor
MZI	Mach-Zehnder interferometer
MZM	Mach-Zehnder modulator
NEP	Noise equivalent power
NRZ	Non-return-to-zero
OFDM	Orthogonal-frequency division multiplexing
OOK	On-off keying
PAM	Pulse-amplitude modulation

PCB	Printed circuit board
PD	Photodetector
PDM	Polarisation-division multiplexing
PECVD	Plasma-enhanced chemical vapour deposition
Poly-Si	Polysilicon
PSK	Phase shift keying
PV	Photovoltaic
Q-factor	Quality factor
QAM	Quadrature amplitude modulation
RF	Radio frequency
RIE	Reactive-ion etching
RR	Ring resonator
RRM	Ring resonator modulator
RZ	Return-to-zero
SLG	Single-layer graphene
SLG1	Single-layer graphene closest to the waveguide
SLG2	Single-layer graphene farthest from the waveguide
SNR	Signal-to-noise ratio
SOI	Si-on-insulator
SPP	Surface plasmon polaritons
TE	Transverse electric
TLM	Transfer length method
TM	Transverse magnetic
WDM	Wavelength-division multiplexing

WG Waveguide

Symbols

a Single-pass ring resonator transmission coefficient

α Power attenuation coefficient

α_{ring} Power attenuation coefficient of the ring

$\Delta\alpha_{\text{MZM}}$ Difference in absorption between two arms of an MZM

$\Delta\alpha_{\text{MZM,Dirac}}$ Difference in absorption between two arms of an MZM at the Dirac point

$\alpha_{\text{scattering}}$ Propagation loss due to scattering

A Amplitude of electric field

B Number of bits

B_{s} Symbol rate

β Propagation constant

c Speed of light in a medium

c_0 Speed of light in vacuum

$c(t)$ Optical carrier signal

C Circuit capacitance

C_{Q} Quantum capacitance

C_{eq} Equivalent capacitance

C_{ox} Oxide capacitance

C_{th} Heat capacity

D^* Specific detectivity

d Dielectric thickness

e Elementary charge

E Electric field

E_g	Band gap energy
E_F	Fermi level
E_L	Laser excitation energy
ε_r	Relative permittivity
ε_0	Permittivity of free-space
f	Frequency
$f_{3\,dB}$	3 dB cut-off frequency
FOM_{EA}	Figure of merit for electro-absorption modulators
FOM_{ER}	Figure of merit for electro-refractive modulators
γ	Intraband scattering rate
Γ	Confinement factor
$\hbar$	Reduced Planck's constant
I	Intensity
I_{ph}	Photocurrent
I_d	Dark current
$I(\omega)$	Frequency dependent current through the DSLG modulator
j	Imaginary unit
k_B	Boltzmann constant
k_{ext}	Extinction coefficient
$\mathbf{k}$	Wavevector
k	Wavenumber
κ	Coupler cross-coupling coefficient
L_{min}	Minimum DSLG modulator length
L_C	Length of contacted graphene sections

L_{ring}	Length of ring in a ring resonator
L_{mod}	Active device length of modulator
L_{c}	Coupling length
λ	Wavelength
λ_{op}	Operational wavelength
λ_{res}	Resonant wavelength
Λ	Grating period
M	Number of symbols
$m(t)$	Data stream
μ	Charge carrier mobility
μ_{FE}	Charge carrier mobility as measured by the field-effect
μ_{H}	Charge carrier mobility as measured by the Hall effect
μ_{C}	Chemical potential
n	Refractive index
Δn	Refractive index contrast
n_{g}	Group index
n_{eff}	Effective refractive index
$n_{\text{eff,ring}}$	Effective refractive index of
N	Charge carrier concentration
N_{D}	Charge carrier concentration resulting from defects
η_{int}	Internal quantum efficiency
η_{ext}	External quantum efficiency
ω	Angular frequency
P	Power

P_{abs}	Absorbed power
P_{in}	Input power
P_{out}	Output power
P_{min}	Minimum power
P_{max}	Maximum power
P_t	Transmitted power
Φ_C	Coupler transfer matrix
ϕ	Phase
$\Delta\phi$	Phase shift
$\Delta\phi_{MZM}$	Difference in phase between two arms of an MZM
$\Delta\phi_\pi$	π-phase shift
$\Delta\phi_{1V}$	Phase shift in 1 V
R	Circuit resistance
R_{th}	Thermal resistance
R_C	Contact resistance
R_S	Sheet resistance
R_{2P}	2-point resistance
R_I	Current responsivity
R_V	Voltage responsivity
R_H	Hall coefficient
R_{gated}	Resistance of gated graphene sections
$R_{ungated}$	Resistance of ungated graphene sections
ρ	Sheet resistivity
S	Seebeck coefficient

$s(t)$	Modulated optical carrier signal
$\sigma(\omega)$	Optical conductivity
σ_0	Universal optical conductivity
σ_{min}	Minimum electrical conductivity
$\sigma_{\text{d.c.}}$	Electrical sheet conductivity
t	Coupler transmission coefficient
T_{e}	Electronic temperature
T	Transmission
T_{b}	Bit interval
T_{s}	Symbol interval
τ	Intraband scattering Rate
τ_{res}	Response time
τ_{cav}	Cavity photon lifetime
θ_1	Angle of incidence
θ_2	Angle of refraction
V	Voltage
$V_\pi L$	Phase modulation efficiency
V_{ph}	Photovoltage
V_{pp}	Peak-to-peak voltage
V_{PTE}	Photothermoelectric voltage
v_{d}	Drift velocity
v_{F}	Fermi velocity
V_{D}	Drive voltage
V_{G}	Gate voltage

V_{M}	Voltage drop across graphene modulator
V_{Dirac}	Dirac point voltage
W_{gated}	Width of gated graphene sections
W_{ungated}	Width of ungated graphene sections
$Z_{\mathrm{T}}(\omega)$	Total circuit impedance
$Z_{\mathrm{C}}(\omega)$	Impedance of the overlapping SLG section of the DSLG modulator
$Z_{\mathrm{M}}(\omega)$	Impedance of DSLG modulator

Chapter 1

Introduction

1.1 Motivation

The global internet traffic was expected to triple between 2019-2024 with the advent of 5G and the internet of everything [1]. This remarkable growth is fuelled by increased connectivity from the 'Internet of Things' where machine-to-machine connections are expected to make up more than half of the global connected devices and connections by 2022 [1]. Lockdowns in response to COVID-19 have shifted the distribution of data traffic across the network, with an additional $\sim$ 20 - 100% rise, due to home working and increased use of home entertainment services [2]. This vast amount of data relies on high-density data network infrastructures, with 2018 Ethernet standards of 400 Gb/s [3] to be extended $>$ 1 Tb/s by 2025 [4]. Optical fibre technology has kept up with growing data communication rates, shown in figure 1.1, increasing the capacity of a single fibre from a few Gb/s in the 1990's, to hundreds of Tb/s in modern-day systems [5]. These massive data rates put a heavy strain on the existing optical networks, and when it comes down to it, the limiting factor is power. So to make future long-distance networks sustainable, low-power optical transceivers are needed.

To go $>$ 1 Tb/s it is preferable to increase data rates in a single channel [6, 7], rather than increasing the number of channels. By minimising the number of channels, the power consumption and system complexity is reduced, because less electrical drivers and active optical components are needed [6, 7]. The latest development to increase the capacity of existing long-haul optical fibre networks is the introduction of multi-level modulation schemes. Multi-level modulation schemes increase the density of transmitted information, known as spectral efficiency (SE), in comparison to binary modulation schemes. 2018 Ethernet standards for networks that transmit $>$ 100 Gb/s use 4-level pulse-amplitude modulation (PAM) [3] that uses 4 amplitude levels of the transmitted optical signal, to

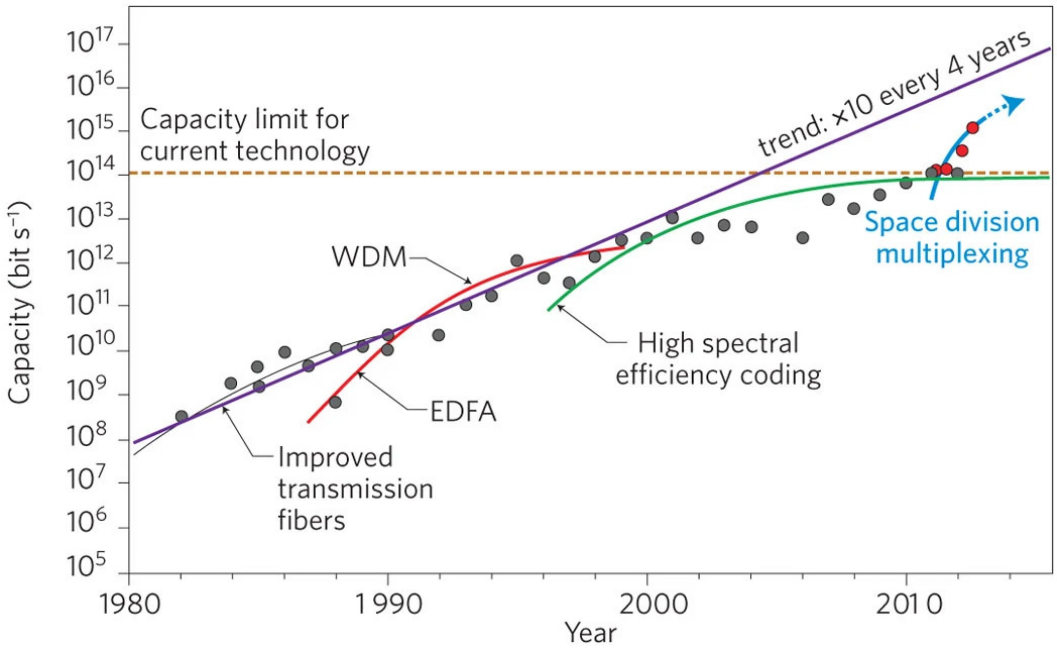

Fig. 1.1 Increasing laboratory demonstrations of transmission capacity in optical fibres, adapted from Ref. [5].

represent 4 symbols that correspond to 2 bits of information [6]. Other multi-level modulation schemes, such as quadrature amplitude modulation (QAM) [8], encode information in both phase and amplitude of the transmitted optical signal [8]. Transmission systems that only encode information in the amplitude of the optical signal are known as direct detection systems [8], and those that use both the phase and amplitude are known as coherent [8]. Coherent systems have an increased noise tolerance in comparison to direct detection ones, because the signal degradation from fibre dispersion can be compensated by the phase of the received signal [8]. Existing optical transceivers that transmit and receive information in the optical domain need to increase the spectral efficiency to cope with the rising data rates.

Processing these staggering amounts of data will become challenging for existing short-reach interconnect networks, that are still based on Cu wires, because the transmission losses become unmanageable at high-frequencies [9]. The interconnect losses are frequency (f) dependent ($\propto \sqrt{f}$ [10]) due to increased resistance caused by the skin effect [10] as more of the current flows at the surface as f increases. The bandwidth (BW) of a single channel that uses binary modulation formats is limited by the BW of the electrical interfaces used to drive the active optical components [6, 7]. The current standard of electrical interfaces to support 400 Gb/s Ethernet is 50 Gb/s [3]. Therefore, for electrical interfaces driving Tb/s data rates, the power consumption of interconnects becomes the limiting factor [9–11] and the adoption

of optical interconnect for shorter length scales becomes more attractive.

Si photonics technology enables a platform for monolithic integration of photonic and electronic components using Si as the optical material [12, 13]. It provides a low-cost method of realising compact and low-power optical transceivers by re-using the already mature Si processing technology [13]. Whilst photodetectors (PD) and modulators based on doped Si have already been demonstrated [13], the band gap of Si severely reduces the efficiency of these devices [13]. Instead, other materials are typically integrated onto the Si photonics platform such as Ge, III-V semiconductors (InP or GaAs) or electro-optic (EO) crystals like $LiNbO_3$ (LN) [13]. Indeed, these materials successfully improve the efficiency of PDs and modulators on the Si photonic platform, but they come at the cost of increased fabrication complexity and cost associated with integrating the materials on Si-on-insulator (SOI) wafers [14, 15]. The unique properties of 2d materials has led to a fast pace and large quantity of graphene research in recent years in a wide range of fields [16]. This has mainly focused on fundamental studies and demonstrating prototype devices, promising to see graphene transition from research into industrial applications in the near future. One of the most encouraging application areas is opto-electronics which benefits from graphene's impressive electrical and optical properties making it intrinsically capable of high-speed, low-power, and broadband operation [16, 17].

This project will focus on developing a graphene-based opto-electronic platform for integrated Si photonic optical links for long-haul and short-reach applications. Integrating graphene into the Si photonic technology platform provides a route to monolithically integrated opto-electronic circuits that benefit from the decades of investment and growth enjoyed by the mature Si industry. This is of industrial significance as today's data networks will struggle to support the ever increasing data rates with the rise of the Internet of Things and 5G without new technologies that can deliver low-power optical transceivers. I will investigate waveguide-integrated (WG) graphene-based modulators on passive photonic platforms. This includes detailed modelling and simulation of the optical and electrical performance of the devices, discussing the important design parameters, trade-offs, and optimisations required for different performance targets. I will design three different configurations of graphene-based modulators that have different operating conditions, and are suited for different applications. These include electro-absorption modulators (EAM) for direct detection systems, compact ring resonator modulators (RRM) for short-reach applications, and Mach-Zehnder modulators (MZM) for coherent systems. These will use different underlying passive photonic components that will be described in chapter 3. I will fabricate

the different modulators using scalable techniques that are suitable for waferscale processing in the back-end-of-line processing in a complementary metal-oxide-semiconductor (CMOS) fab after fabrication of the integrated circuits. I will then evaluate the static and dynamic performance of the individual devices and feedback the results into the device designs. I will then look to system-level integration of the individual devices into a graphene-based IQ transmitter and balanced coherent IQ receiver.

1.2 Structure of Thesis

The thesis is organised as follows,

Chapter 2 gives an introduction and overview of the field of graphene with the focus on the optical and electrical properties that makes graphene suitable for opto-electronic applications. I will discuss different production techniques and their suitability for integrated photonics, and finish with the methods I used to characterise graphene.

Chapter 3 introduces the different components of optical links and Si photonic technology. I will first describe the passive photonic components, explain their operating principles, design parameters, and key metrics. I will then move onto the active components of an optical link, specifically focusing on the EO modulator and PD. This will include the different operating mechanisms, performance metrics, and a review of the existing state-of-the-art technologies used for integrated transmitters and receivers on the Si photonic platform. I will also describe the different modulation formats used to transmit information and explain the principles behind coherent detection. Lastly, I will discuss the history and development of optical networks, focusing on the examples of long-haul and short-haul communications.

Chapter 4 focuses on graphene-based integrated PDs and modulators. I will start with the motivation behind using graphene for opto-electronics, and then move onto describing the underlying operating mechanisms for photodetection and modulation, and review the state-of-the-art WG-integrated device configurations. Finally, I will compare the performance of graphene-based integrated PDs and modulators to existing technologies based on Si photonics and discuss the challenges that remain for a graphene-based opto-electronic platform.

Chapter 5 presents the optical and electrical modelling and simulations that I used to design the double single-layer graphene (DSLG) stack used as the active component of

integrated modulators. I will explain the models that I used to determine the proposed performance of the device and define the performance targets. I used optical modelling to determine the static response of the device, and electrical modelling to determine the dynamic response. I will then discuss the design parameters that I investigated in terms of device cross-section and different photonic platforms. I will then compare the performance of the DSLG modulators to existing technologies and summarise the design considerations chosen to optimise the operational BW.

Chapter 6 describes the scalable techniques that I used to fabricate the DSLG integrated PDs and modulators. This will include the method used for transfer and shaping of polycrystalline single-layer graphene (SLG) grown by chemical vapour deposition (CVD). I will describe the method used to deposit the gate dielectric including characterisation of the deposited dielectric. I will explain how I contacted graphene and characterised the contact resistance of the resulting edge contacts with transfer-length measurements (TLM). I will also describe the experimental setups that I used to characterise the static EO response and the dynamic EO BW of the integrated DSLG modulators.

Chapter 7 presents the results of DSLG EAMs for direct detection systems using Si and SiN optical platforms. I designed the DSLG stack for both Si and SiN platforms and fabricated the DSLG EAMs using passive Si photonic circuits that were designed and fabricated by IMEC, and passive SiN photonic circuits that were designed by CNIT and fabricated by Infotec. I transferred and patterned polycrystalline CVD SLG that was grown by Dr Osman Balci and Dr Sachin Sinde at the University of Cambridge for the Si samples, and supplied by Graphenea for the SiN samples. I measured the EO response and BW of the DSLG EAMs on both Si and SiN platforms and extracted the EO response of graphene.

Chapter 8 reports the results of DSLG RRMs on the Si photonic platform that can be used for short-haul communications that require compact devices. I designed the DSLG stack and fabricated the DSLG RRMs using passive Si photonic circuits designed by Dr Alfonso Ruocco at the University of Cambridge and fabricated by IMEC. I transferred and patterned polycrystalline CVD SLG that was grown by Dr Osman Balci and Dr Sachin Sinde at the University of Cambridge. I measured the EO response and BW of the DSLG RRMs and extracted the EO response of graphene.

Chapter 9 presents the results of the DSLG MZMs on the Si photonic platform and preliminary results of a DSLG IQ modulator that would have applications in coherent trans-

mission systems. I designed the DSLG stack and fabricated the DSLG MZMs using passive Si photonic circuits that were designed and fabricated by IMEC. I transferred and patterned polycrystalline CVD SLG that was grown by Dr Osman Balci and Dr Sachin Sinde at the University of Cambridge. I measured the EO response and BW of the DSLG MZMs and extracted the EO response of graphene.

Chapter 10 summarises the main results of the thesis with a perspective on future work for the further development of graphene-based optical links.

Novel contributions that I have made during this PhD project,

- Demonstrated the highest figure-of-merit for a graphene amplitude modulator, given as the ratio of the extinction ratio and insertion loss, that showed $FOM_{EA} \sim 4.48$, a factor of 2 better than the highest reported to-date.
- Extracted the best modulation efficiency for a graphene phase modulator, given by the product of the voltage required to reach a π-phase shift and the modulator length, that showed $V_\pi L \sim 0.12$ V·cm, a factor of 2 better than the lowest reported to-date.
- Achieved the first demonstration of pure phase modulation with a graphene phase modulator by operating in the transparency regime where optical losses are minimised and do not significantly change with voltage.

Chapter 2

Graphene

2.1 Introduction

Graphene is a single sheet of carbon atoms arranged in a honeycomb structure where its 2d nature leads to many properties that are interesting for optical interconnects. Its structure is defined by the molecular bonds between carbon atoms which are formed by carbon's 4 valence electrons. These occupy 3 in-plane sp^2-orbitals, created by the hybridisation of 1 s-orbital and 2 p-orbitals, and one p-orbital that is perpendicular to the plane [18]. Each carbon atom is covalently bonded to 3 other carbon atoms by the strong σ-bonds from overlapping sp^2-orbitals. These bonds are very strong and are the reason for graphene's lattice strength. Its conductivity, on the other hand, comes from the covalent π-bonds formed above and below the lattice by the overlapping of un-hybridised p-orbitals. The electrons within the π-bonds are delocalised and become free to move throughout the crystal where they behave as a 2d electron gas [18].

Graphene's lattice can be described by sublattices A and B, shown in yellow and blue in figure 2.1a, where each atom is surrounded by 3 atoms from the other sublattice. The associated Brillouin zone, shown in 2.1b, contains one atom from each sublattice at points K and K'. The dispersion relation $E^{\pm}(k_x,k_y)$, that describes the behaviour of graphene's free carriers, can be calculated using the tight-binding Hamiltonian and the nearest-neighbour approximation [17]:

$$E^{\pm}(k_x,k_y) = \pm\gamma_0\sqrt{1+4\cos\frac{\sqrt{3}k_x a}{2}\cos\frac{k_y a}{2}+4\cos^2\frac{k_y a}{2}} \tag{2.1}$$

where $a = \sqrt{3}a_{cc}$, a_{cc} = 1.42 is the length of the carbon-carbon bond, γ_0 is the hopping energy for nearest-neighbour π-orbitals (between 2.9 - 3.1 eV), and (k_x,k_y) are within the first

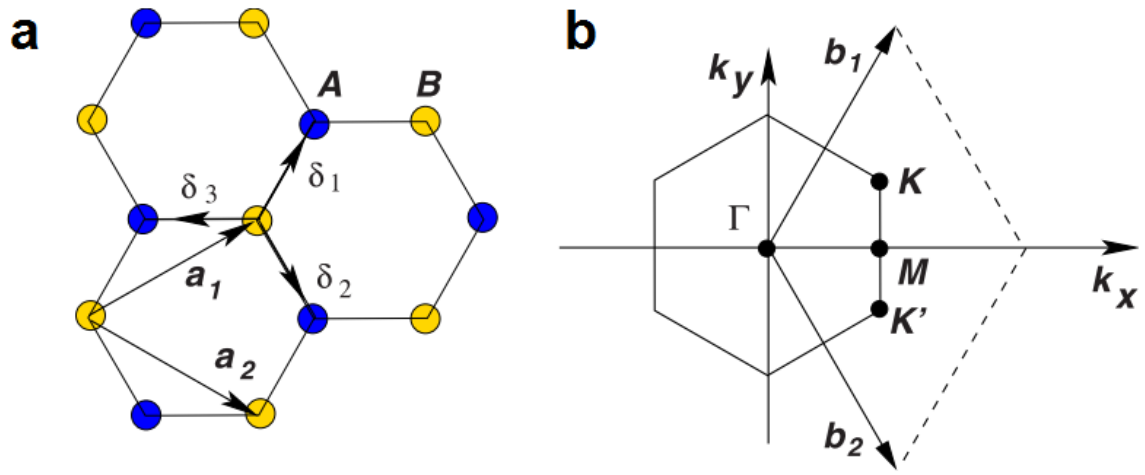

Fig. 2.1 (a) Honeycomb lattice structure made of sub-lattices A and B, with lattice vectors a_1 and a_2, and nearest-neighbour vectors $\delta_1, \delta_2, \delta_3$, (b) Corresponding Brillouin zone where Dirac points are located at K and K', adapted from Ref. [19].

Brillouin zone. The tight binding Hamiltonian can be used because the electronic structure is defined by the π-energy bands because of the large energy gap between σ-energy bands at the edge of the Brillouin zone.

As there is only one valence electron per atom in the un-hybridised π-orbital then the negative energy branch, or valence band, is occupied, and the positive energy branch, or conduction band, is unoccupied. The point at which the valence and conduction bands touch are called Dirac points and are located at points **K** and **K'** in momentum space. Therefore by considering the dispersion-relation at these points this leads to a linear dispersion-relation [17]:

$$E^{\pm}(\mathbf{k}) = \pm\hbar v_F |\mathbf{k}| \tag{2.2}$$

where **k** is the distance in momentum space from the Dirac point and $v_{\mathrm{F}} \sim 9.5 \times 10^5 \mathrm{ms}^{-1}$ [20] is the Fermi velocity. This expression is a solution to the effective Hamiltonian given as [17]:

$$\mathbf{H} = \pm\hbar v_F (\sigma\mathbf{k}) \tag{2.3}$$

where σ is the pseudo-spin Pauli matrices representing the extra degree of freedom from the two sublattices. This means that carriers in graphene are described by the relativistic Dirac equation rather than non-relativistic Schrödinger equation, mimicking massless carriers with an effective speed of light v_{F} rather than an effective mass. These quasiparticles are

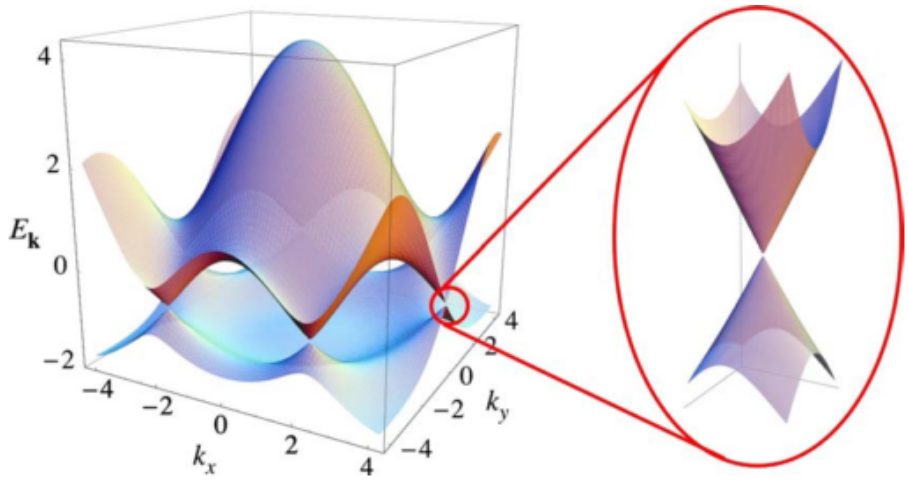

Fig. 2.2 Electronic dispersion relation for graphene showing the conical band structure at one of the Dirac points, adapted from Ref. [19].

called Dirac Fermions [16]. The resulting electronic structure is illustrated in figure 2.2 where the zoomed in region shows the linear dispersion-relation at the Dirac points [19].

2.2 Electrical Properties

Near the Dirac point it was expected that low carrier densities and a vanishing density of states would correspond to zero conductivity, instead a minimum conductivity $\sigma_{\text{min}} \sim 4e^2/h$ was observed [21]. Where e^2/h is the conductivity quantum and the factor of 4 accounts for each carrier type and the double degeneracy in the Brillouin zone [21]. This behaviour is characteristic of 2d Dirac fermions and was found to be independent of mobility [21]. It is attributed to the inhomogeneous distribution of electron and hole puddles from substrate-induced disorder resulting in inhomogeneity of the Fermi level throughout the material [22].

The electronic quality of graphene is usually characterised by the mobility, μ, of it's free carriers, which describes the motion of free carriers in an electric field [23]. The electrical response is limited by intrinsic scattering from electron-electron or electron-phonon interactions, and extrinsic scattering with defects [18]. This is an important parameter that represents the quality of graphene and determines the operational speed of graphene-based opto-electronic devices.

Typical μ for crystalline single layer graphene flakes suspended on Si/SiO_2 substrates is $\sim$ 10,000 cm^2/Vs for carrier concentrations $\sim 10^{12}$ cm^{-2} at room temperature [24], however this is limited by substrate effects such as surface states, charged impurity scattering at the

graphene-substrate interface, and inhomogeneities from surface roughness or wrinkles in the deposited graphene [25]. By using hexagonal boron nitride (h-BN), which is atomically flat, as the dielectric instead of SiO_2 it has been shown to enhance μ to $\sim$ 25,000 cm^2/Vs [25]. This can then be taken even further by completely encapsulating graphene within h-BN to reach $\mu >$ 100,000 cm^2/Vs [26–28], which has the added benefit of protecting graphene from degradation from the environment. To completely reduce the substrate effects in graphene it is possible to remove the substrate all together and have suspended graphene. μ of $\sim$ 200,000 cm^2/Vs for carrier concentrations $\sim 10^{11}$ cm^{-2} have been obtained [29] but these devices are largely impractical for real applications so methods for improving the graphene-substrate interface are preferred.

A useful effect in graphene is that it exhibits a strong ambipolar field effect allowing the electrical properties to be tuned by applying a voltage [24]. The applied voltage will induce a change in carrier concentrations that will shift the Fermi level, where positive voltages induce excess electrons (n-doping) and negative voltages induce excess holes (p-doping) [24]. The peak in resistivity corresponds to the Fermi level coinciding with the Dirac point where the density of states drops significantly [24]. As the Fermi level passes through the Dirac point the change in sign of the Hall coefficient represents the change between the nature of the carriers [24]. The resistivity will then drop as more carriers are induced. For undoped graphene the Dirac point will be at $V_G = 0$, however for doped graphene the Dirac point will shift different voltages. For n-doped graphene the Dirac point will occur at negative voltages, and for p-doped graphene the Dirac point will occur at positive voltages [24].

2.3 Optical Properties

Despite graphene only being one atom thick it has been shown to absorb 2.3% of normally incident white light which scales with the number of layers [30]. 2d Dirac fermions have been predicted to have a universal optical conductance $G_0 = e^2/4\hbar$ that is frequency independent and defined by the fine structure constant $\alpha = e^2/\hbar c$ that represents the coupling between photons and relativistic electrons [30]. Using Fresnel equations in the thin film limit this leads to a transmittance of [30]:

$$T = (1 + 0.5\pi\alpha)^{-2} \approx 1 - \pi\alpha \approx 97.7\% \tag{2.4}$$

This has been confirmed by experimental results, shown in figure 2.4, that show that graphene's reflectance is $< 0.1\%$ and it has an absorbance of $\pi\alpha$ over a broad range of wavelengths [30].

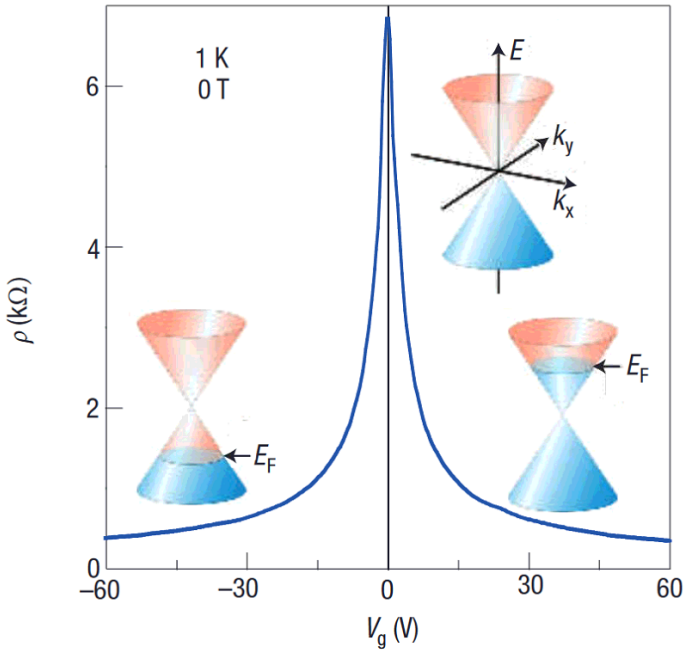

Fig. 2.3 Ambipolar field-effect in graphene where induced carriers from an applied voltage shifts the Fermi level to change the resistivity and type of carrier, adapted from Ref. [16].

Due to the linear dispersion relation, undoped graphene is capable of wavelength independent absorption in the infrared range [30]. Absorption in undoped graphene is dominated by interband transitions, figure 2.5a, when an absorbed photon excites an electron from the valence to the conduction band. As the incoming photon has minimal momentum, this transition between the initial and final state must be vertical. Intraband transitions, figure 2.5b occur within the same energy band and require a change in momentum that can be facilitated by an interaction with an impurity or phonon [23]. Pauli blocking occurs when an incoming photon does not have the required energy for an interband transition and graphene becomes transparent to interband absorption. Interband transitions are blocked when the energy of an incoming photon is greater than twice the Fermi level $(\hbar\omega < 2E_F)$ [31]. Therefore, by controlling the doping of graphene with an applied voltage it is possible to tune the transition to the Pauli blocking regime to different incoming photon energies [32]. Figure 2.5c shows a plot of the optical conductivity of doped graphene for different photon energies, which is represented by the wavenumber ω [32]. Each curve corresponds to a different voltage applied to graphene, and therefore doping. For high energy photons (> 6000 cm^{-1}) the conductivity is flat, which is the same as the undoped case, because photons are being absorbed. However, after a certain point the optical conductivity begins to drop because the photons do not have sufficient energy to excite an electron to the conduction band. We see that the transition to

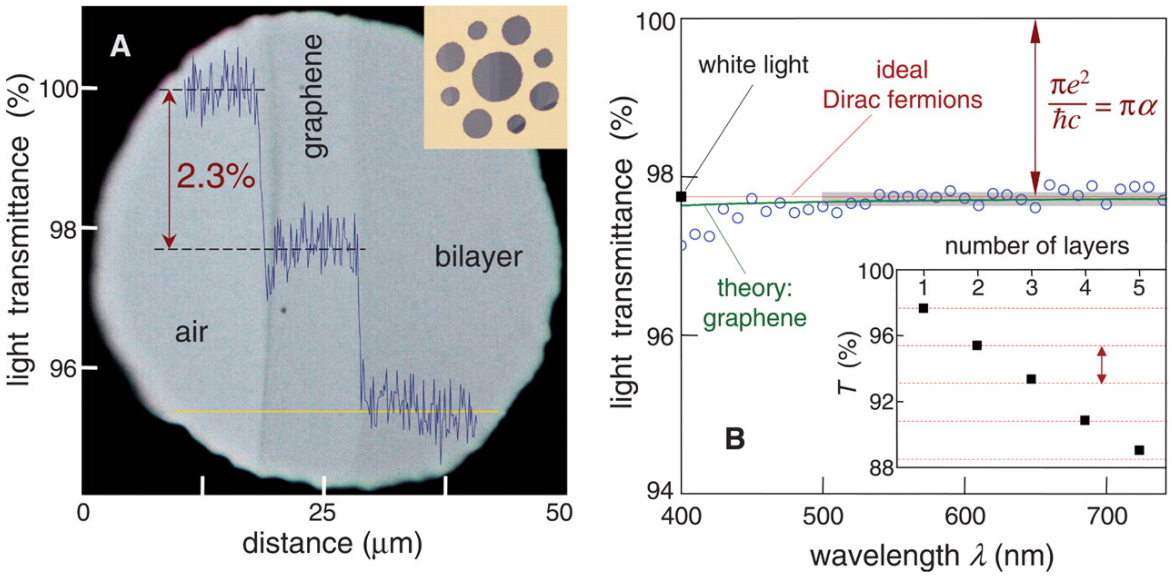

Fig. 2.4 Transmittance of graphene showing dependence on number of layers, adapted from Ref. [30].

Pauli blocking can be moved to different photon energies by changing the doping of graphene by applying a voltage.

2.4 Production Techniques

The choice of production method depends on the desired application [33]. Each different method produces graphene of varying quality and properties which allow a wide range of possible applications. However, the production method is critical to the commercialisation of any of these applications. Figure 2.6 shows different techniques and their applications in terms of the resulting graphene quality and production cost.

2.4.1 Mechanical exfoliation

Mechanical exfoliation, shown in the top right of figure 2.6, involves using sticky tape to overcome the Van der Waals bonds between layers of graphene within graphite and allow them to be peeled off by hand [21]. This leads to crystals up to mm in size which are dependent on the single-crystal size in the graphite crystal [34]. This produces the highest quality crystalline graphene with mobilities $\sim$ 180,000 cm^2/Vs at room temperature [27]. Different exfoliated crystals can be transferred by mechanical transfer to build heterostructures that can be used to encapsulate graphene to improve its electrical properties [25], or design completely new functionalities [35]. The high quality flakes make this an ideal method

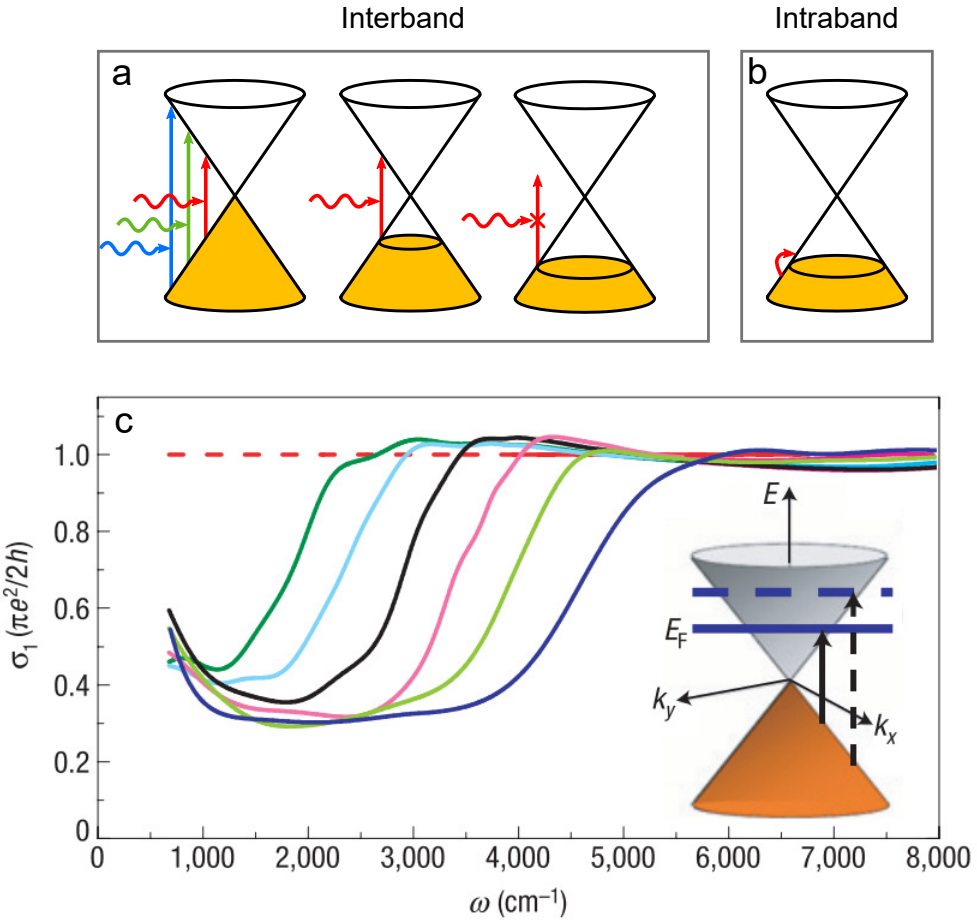

Fig. 2.5 (a) Interband transitions showing wavelength independent absorption for undoped graphene, and Pauli blocking when interband transitions are blocked for doped graphene, (b) intraband transitions in graphene, (c) experimental results showing the real component of the optical conductivity $\sigma(\omega)$ in units of universal optical conductance with relation to wavenumber ω, where the onset of Pauli blocking can be tuned by shifting the Fermi level, adapted from Ref. [32].

for research applications studying the fundamental properties of graphene and other 2d materials. However, the low-throughput and limited flake size make this method not suitable for large-scale industrial applications.

2.4.2 Liquid phase exfoliation

Liquid phase exfoliation (LPE), shown in the bottom left corner of figure 2.6, is a technique for producing graphene flakes by dispersing graphite in organic solvents and then exfoliating graphene with shear forces generated by ultrasonic waves [36, 37]. The applied pressure from the ultrasonic waves create cavities within the solvent that lead to the creation of

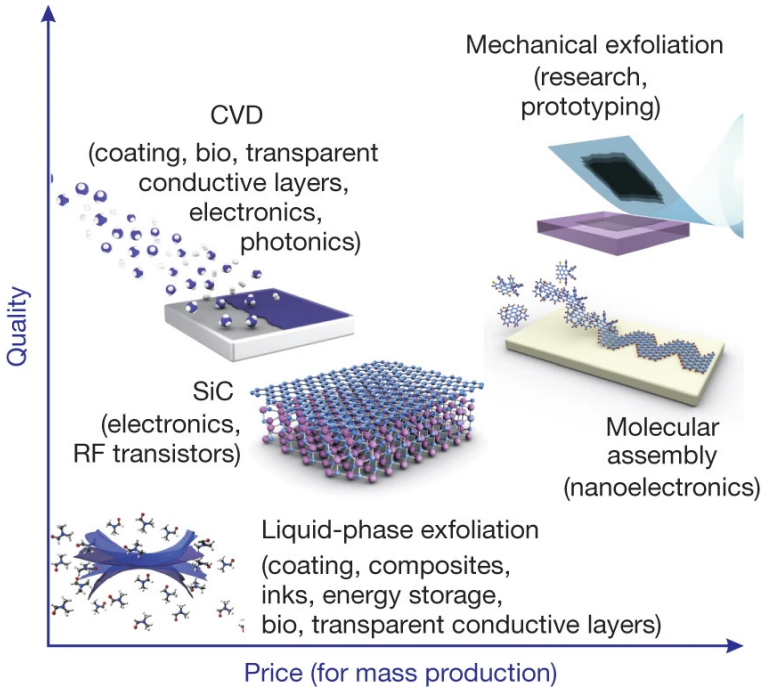

Fig. 2.6 Different production techniques of graphene in relation to the quality of the resulting graphene and the corresponding production cost, adapted from Ref. [33]

microbubbles. These microbubbles grow until they become unstable, where upon collapse they create a mechanical force that is large enough to overcome the Van der Waals forces between the layers of graphene and cause exfoliation. Shear forces can be increased by putting the solvent under pressure or by using a less viscous solvent that will respond to the ultrasonic waves more to increase cavitation. Thicker flakes can be separated by centrifugation, and the resulting dispersion can be stabilised by adding a surfactant that uses coulomb repulsion between flakes to prevent aggregation [37]. Due to the exfoliation and filtration processes involved, flake sizes are typically limited to $< 1\ \mu m^2$ [37]. The conductivity of graphene inks is a result of carrier hopping between the distributed network of flakes and is limited by the concentration of flakes and so typically has mobilities of $\sim$ 90 cm^2/Vs [38]. Graphene-dispersions can be deposited onto flexible and rigid substrates by different techniques, including drop casting and printing, allowing the realisation of graphene-based printed electronics [37]. It is a cost-effective, high-throughput method that is capable of high-volume production of graphene dispersions, however at the cost of a reduced structural quality and size of produced flakes.

2.4.3 Chemical vapour deposition

Chemical Vapour Deposition (CVD), shown in the top left corner of figure 2.6, is a bottom-up approach for producing a film of material by a chemical reaction between gas precursors and the surface of a substrate [39, 40]. Graphene growth uses hydrocarbon gas precursors and has been shown to grow on different metals including Ni, Co, Ru, Ir, and Cu, where Ni and Cu are favoured due to cost and compatibility with the semiconductor industry [39, 40]. In the case of growth on Cu, the growth mechanism was shown to be a surface-adsorption process requiring contact with Cu to facilitate the decomposition of hydrocarbon precursors [39, 40]. The graphene nucleation sites then grow into larger domains that join up to form polycrystalline films [39, 40]. Therefore the process becomes self-limiting as the surface becomes covered in graphene, resulting in large areas of monolayer graphene [39, 40]. This is in stark contrast to the growth mechanism on Ni which form graphene films of varying thickness from surface segregation of carbon followed by further precipitation [39, 40]. The difference in growth processes for Ni and Cu is due to their different carbon solubilites [39, 40]. For Ni, that has a high C solubility, more C can be absorbed into the substrate which leads to greater precipitation during cooling down and non-uniform film thickness [39, 40]. Whereas Cu would absorb far less C so that the main source of C for graphene growth would come from the surface decomposition with the substrate rather than precipitation [39, 40]. CVD is a technique for producing good quality crystalline graphene films that have the potential for large-area production able to produce films 30 in $\times$ 30 in films in a roll-to-roll process [41]. It was found that domain boundaries had an detrimental effect on the electrical quality of the produced graphene [42]. By limiting the density of graphene nucleation sites they would increase the domain sizes in the final film to hundreds of micrometers square [42]. Carrier mobility can be further increased by removing the grain boundaries all together and using single-crystals of graphene instead of a polycrystalline film. By reducing the nucleation density and locally feeding carbon precursors at specific locations single-crystals have been shown to grow up to $\sim$ 3.8 cm [43]. It has also been shown that single-crystals can be grown at predefined locations by using patterned nucleation sites [44]. Entire films, up to 5 $\times$ 50 cm^2 [45], of single-crystal graphene have also been demonstrated by using single-crystal Cu foil. In this case, the graphene single-crystals that grow at multiple nucleation sites are aligned such that they join up to form a single-crystal film.

Using graphene with the highest carrier mobility and largest domain sizes is critical to maximise the performance of graphene-based modulators and photodetectors. It is clear that there are many approaches for integrated CVD graphene onto Si photonic circuits. When using polycrystalline films or single-crystals an important parameter to consider is how the length of the modulator or photodetector compares to the domain size. Domain sizes larger

than the active device lengths are needed to maximise the performance of graphene-based modulators and photodetectors. This could either be through a wafer-scale film of single-crystal graphene or deterministic growth of graphene single-crystal at predefined locations. Growing single-crystals at defined locations is desirable for graphene-based Si photonic links because graphene can be confined to the active region of the active devices and so reduce contamination across the rest of the wafer. However, if graphene can be easily removed from the rest of the wafer, transfer of a wafer-scale film would be preferable because it does not require alignment during transfer which would reduce through-put. Wafer-scale films with large domain sizes are also needed to maximise the yield of graphene-based modulators and photodetectors. This becomes critical when multiple devices are combined together in systems where system functionality depends on consistent device performance across all devices.

2.5 Characterisation Techniques

2.5.1 Optical microscopy

Optical microscopy is a fast and non-destructive way of characterising 2d materials due to the high contrast when placed onto SiO_2 substrates [21, 24]. When light impinges onto the graphene-SiO_2-Si stack the reflected light will be a superposition of fields from multiple reflections at the air-graphene, graphene-SiO_2, and SiO_2-Si interfaces. In a simplified case, the dominant reflected fields will be from the air-graphene (E_G) and SiO_2-Si (E_{Si}) interfaces and therefore the total reflected intensity I_T can be written as [46]:

$$I_T \sim |E_G + E_{\mathrm{Si}}|^2 = |E_G|^2 + |E_{\mathrm{Si}}|^2 + 2|E_G||E_{\mathrm{Si}}|\cos\phi \tag{2.5}$$

Where ϕ is the total phase difference between reflected E_G and E_{Si} fields [46]:

$$\phi = \theta_G - (\theta_{\mathrm{Si}} + 2\pi n_{\mathrm{SiO2}} 2 d_{\mathrm{SiO2}}/\lambda_0) \tag{2.6}$$

This includes phase shifts from the reflections at the air-graphene and SiO_2-Si interfaces, θ_G and θ_{Si}, and the optical path length within SiO_2 in terms of the refractive index n_{SiO2}, thickness d_{SiO2}, and wavelength in free-space λ_0.

The image contrast δ is defined as the difference between the intensity of reflected light from graphene and Si I_{Si}, normalised by the reflected light from Si. Assuming that $|E_G|^2 \simeq 0$ then δ results from interference with the strong reflection from Si [46]:

$$\delta = \frac{(I_{\mathrm{Si}} - I_T)}{I_{\mathrm{Si}}} \simeq -2|E_G||E_{\mathrm{Si}}|\cos\phi \tag{2.7}$$

Rewriting this equation in terms of reflectance of graphene, R_{G}, and Si, R_{Si} [46]:

$$\delta = -2\sqrt{\frac{R_{\mathrm{G}}}{R_{\mathrm{Si}}}}\cos\phi \tag{2.8}$$

Equation 2.8 shows that δ is highly dependent on the optical path within the dielectric, so that δ can be tuned by choosing a the thickness and refractive index of the dielectric. Figure 2.7b shows the calculated δ for different SiO_2 thickness and different excitation wavelengths. It can be seen that for visible light the optimum SiO_2 thickness is $\sim$ 300 nm or $\sim$ 100 nm [46, 47]. This is really useful and quick way to work with layered materials that has been attributed to the reason why there has been so much focus on layered materials [16].

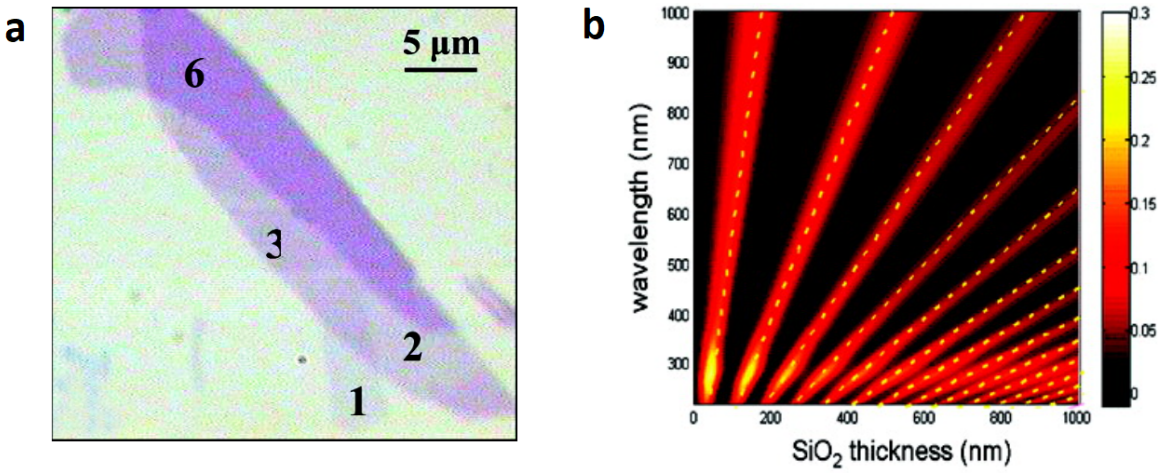

Fig. 2.7 (a) Optical microscopy image of a graphene flake showing different number of layers [46]. (b) Calculated values of SLG contrast on top of SiO_2 of varying thickness and for different excitation wavelengths [46]. The dotted yellow line represents the minimum reflectivity of Si substrate which coincides with the maximum contrast, adapted from Ref. [46].

2.5.2 Raman Spectroscopy

Raman spectroscopy is a non-destructive technique that probes the structure and electronic properties of a material by inelastic scattering of photons by phonons [48] that recombine radiatively to produce scattered light [49]. Light impinging on a medium will induce a time dependent dipole moment and a change in the electric charge distribution that is proportional to the frequency of the incoming photon ω_L. The majority of scattered light undergoes elastic

scattering, also known as Rayleigh scattering, where the frequency of the scattered light (ω_{SC}) is the same as the incident light (ω_L) [49]. A smaller fraction of the scattered light undergoes inelastic scattering, or Raman scattering [48]. This can either reduce ω_{SC} by the emission of a phonon with a frequency ω_q, known as the Stokes process, or increase ω_{SC} by the absorption of a phonon with a frequency ω_q, known as the anti-Stokes process. The shift in energy is expressed in units of cm^{-1} and only the Stokes process is considered because it is more probable and results in a larger intensity [49]. A scattering process is defined as resonant if a real electronic state is accessed, or non-resonant if a virtual state is accessed [49]. This makes Raman spectroscopy a good characterisation technique for graphene because all transitions are resonant for a linear band structure [49]. Due to the conservation of momentum, only phonons near the centre of the Brillouin zone with $q \cong 0$ contribute to Raman scattering [49]. This is known as the fundamental Raman selection rule [49]. For 2 phonon processes this can be satisfied by $\Delta q \cong 0$ [49]:

$$\begin{aligned} \omega_L &= \omega_{SC} \pm \omega_q \\ \mathbf{K}_L &= \mathbf{K}_{SC} \pm \mathbf{q} \end{aligned} \tag{2.9}$$

Where ω_L is the frequency of the incoming photon, ω_{SC} is the frequency of the scattered photon, ω_q is the frequency of the emitted phonon, $\mathbf{K}_L$ is the wavevector of the incoming photon, $\mathbf{K}_{\mathrm{SC}}$ is the wavevector of the scattered photon, and $\mathbf{q}$ is the wavevector of the phonon. Figure 2.8a shows Raman spectra for single layer graphene with increasing amounts of defects. The main Raman peaks associated with graphene are the G ($\sim 1580\ \mathrm{cm}^{-1}$ [52]) and the 2D ($\sim 2680\ \mathrm{cm}^{-1}$ [52]) peaks. The G peak corresponds to the in-plane E_{2g} vibrational mode [53], shown in figure 2.8b, and phonons at the centre of the Brillouin zone [49]. This peak is always present because it is the only peak that obeys the Raman fundamental selection rule where the emitted phonon has $q \sim 0$ [49]. The D peak ($\sim 1350\ \mathrm{cm}^{-1}$ [52]), shown in figure 2.8c, is only activated by defects and corresponds to the breathing mode of the rings of graphene [49]. In this double resonant process, involving phonons from the edge of the Brillouin zone, the emitted phonon momentum is non zero and instead energy and momentum are conserved by scattering from defects [49]. The 2D peak, shown in figure 2.8d, is triply resonant process that is able to conserve momentum because it involves two phonons [49]. Therefore, the 2D peak does not need to be activated by the presence of defects and is always present [49]. The D and 2D peaks result from intervalley scattering and the D' and 2D' peaks result from intravalley scattering [49]. The number of layers can be directly determined from the shape, width, and position of the 2D peak, where it appears sharp and narrow (Lorentzian) for SLG and then widens and shifts up as the number of layers increases

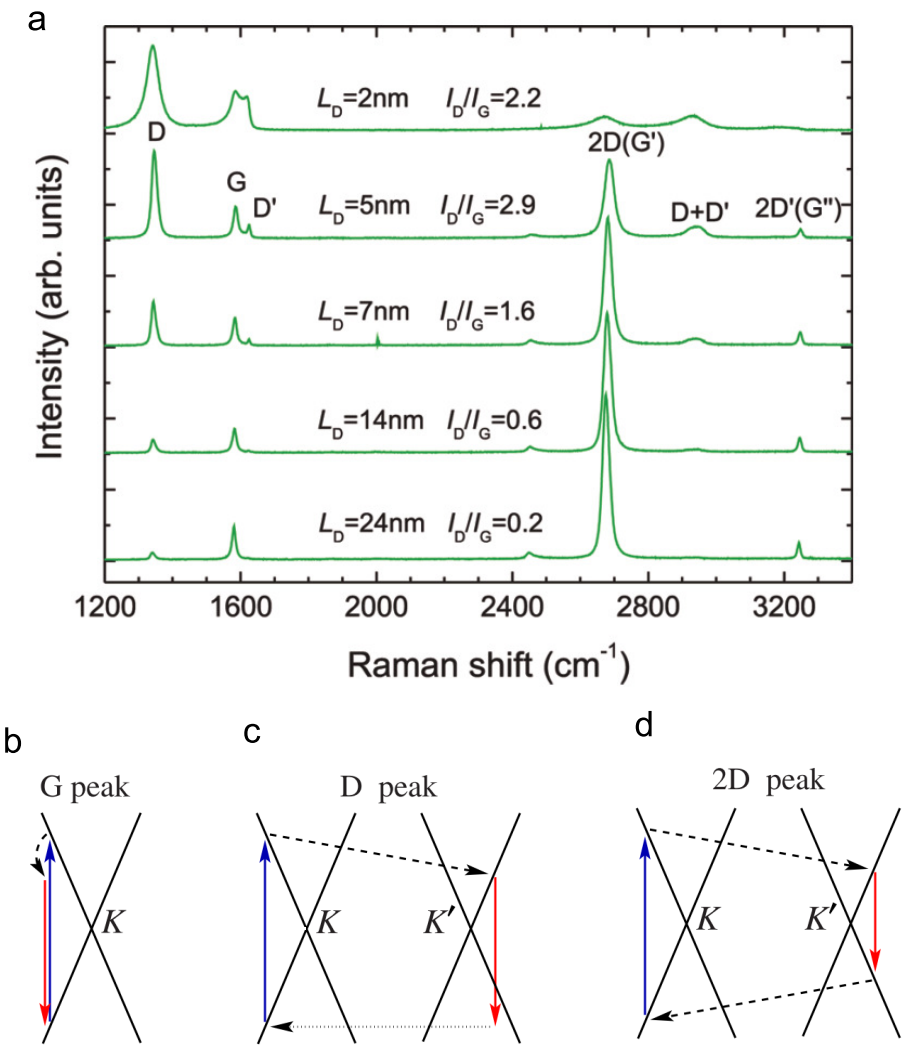

Fig. 2.8 (a) Raman spectrum of SLG with an increasing amount of defects, adapted from Ref. [50], (b) Raman scattering processes for the G peak, adapted from Ref. [51], (c) Raman scattering process for D peak, adapted from Ref. [51], (d) Raman scattering process for 2D peak, adapted from Ref. [51]. Initial photon absorption is depicted by the blue arrow, phonon emission by a dashed line, defect scattering by the dotted line, and scattered photon emission by the red arrow.

[52]. The extra components of the 2D peak are due to electronic band splitting as the number of layers increases [52]. Doping can be determined by the position and width of the G peak due to shifting of the Kohn anomaly with the changing Fermi surface, showing the same shift for electrons and holes [31]. The type of doping can be determined from the position of the 2D peak which shifts down for electrons and up for holes [54]. By comparing the ratio of intensities of the 2D and G peak (I(2D)/I(G)) the doping density can be estimated [54]. The level of structural defects can be determined by the intensity of the D peak [50, 53, 55].

2.5.3 Electrical

The electrical properties of graphene can be determined by 2-point-probe and 4-point-probe measurements as shown in figure 2.9a and 2.9b. The resistance in the 2-point-probe configuration, R_{2P}, is given by Ohm's law as,

$$R_{2P} = 2R_W + R_G + 2R_C \tag{2.10}$$

Where R_G is the graphene resistance, R_C is the contact resistance associated with ohmic contacts, and R_W is the wire resistance which can usually be ignored as $R_W \ll R_G, R_C$. Therefore in order to measure R_G, then the R_C must be excluded. This can be achieved with a 4-point-probe measurement where 2 probes are used to apply a current across the device, and 2 separate probes are used to separate the path of the current supply and measure the potential drop across the device [56]. R_G is then simply just V/I.

Sheet resistance

For 2d materials the typical expression for resistance used by bulk materials is not applicable [24]. Instead, sheet resistance, R_S, is used which is proportional to the resistance of the material, R_G, graphene in this case, and the 2d dimensions of the channel given in terms of the width W and length L [17]:

$$R_S = \frac{\rho}{t} = R_G \frac{W}{L} [\Omega/\square] \tag{2.11}$$

where ρ is the sheet resistivity, which is related to the electrical sheet conductivity, $\sigma_{d.c.}$ by [23],

$$\sigma_{d.c.} = \frac{1}{\rho} \tag{2.12}$$

Contact resistance

R_C can be calculated from the measured R_{2P}, and 4-point-probe resistance, R_G, with equation 2.10 such that,

$$R_C = \frac{R_T - R_G}{2} \tag{2.13}$$

R_C is typically normalised by the width of the channel, and is given in units of $\Omega \cdot \mu$m. Another method to extract both R_S and R_C is the transfer length method [56], shown in figure 2.9c. This involves measuring the 2-point-probe resistance for different channel lengths

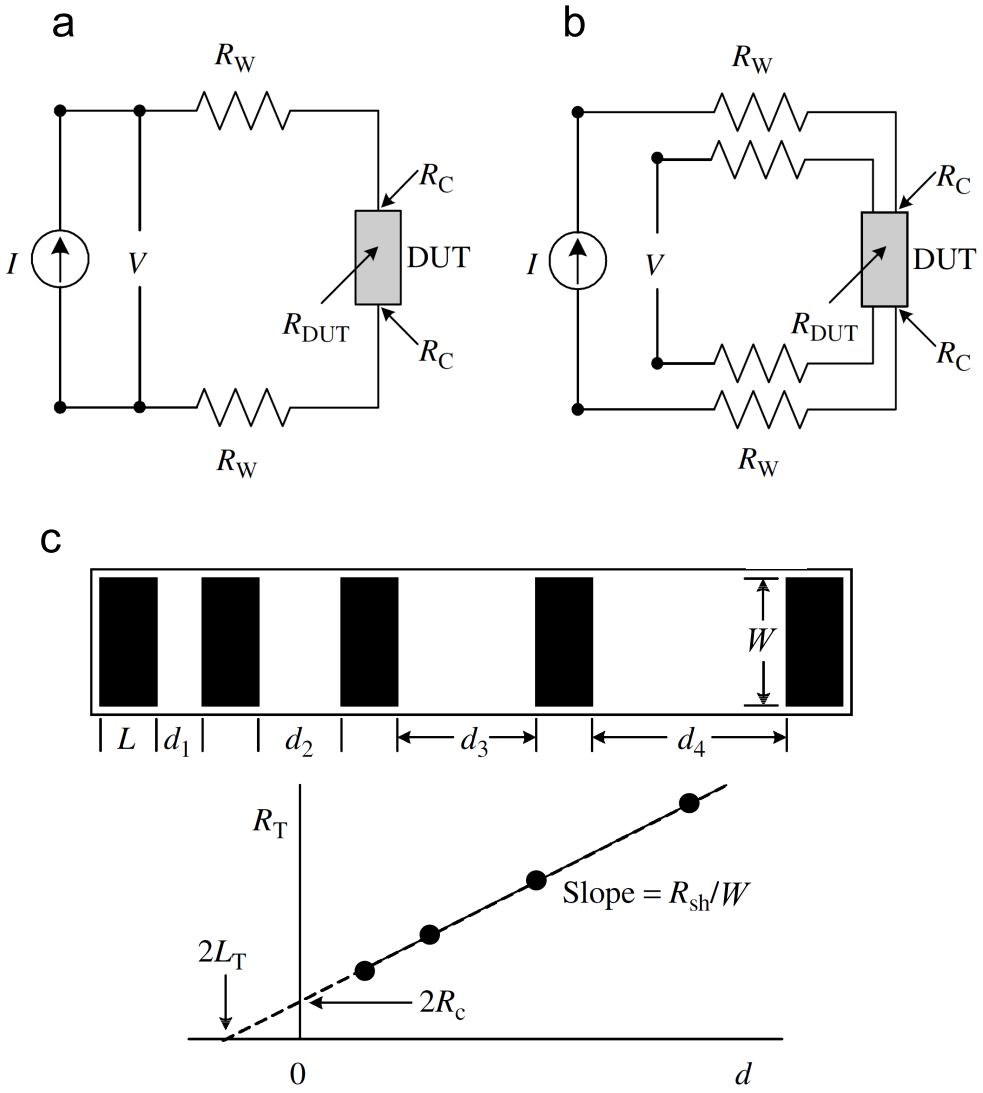

Fig. 2.9 Electrical characterisation measurements for (a) 2-point-probe configuration, and (b) 4-point-probe configuration, (c) transfer length method, adapted from Ref. [56].

whilst keeping the channel width constant. Therefore, when R_T is plotted against length the gradient is proportional to R_S/W and the intercept corresponds to $2R_C$.

$$R_T = \frac{R_S}{W}L + 2R_C \tag{2.14}$$

R_C is a significant problem for graphene, ranging from 100's - 10,000's $\Omega \cdot \mu$m, that arises from charge transfer from 3d materials to 2d materials which have very different density of states and work functions [59]. The efficiency of charge transfer depends on the transmission probabilities of carrier injection into graphene and the following transport along the graphene channel [59]. It has been observed that the majority of charge transfer from

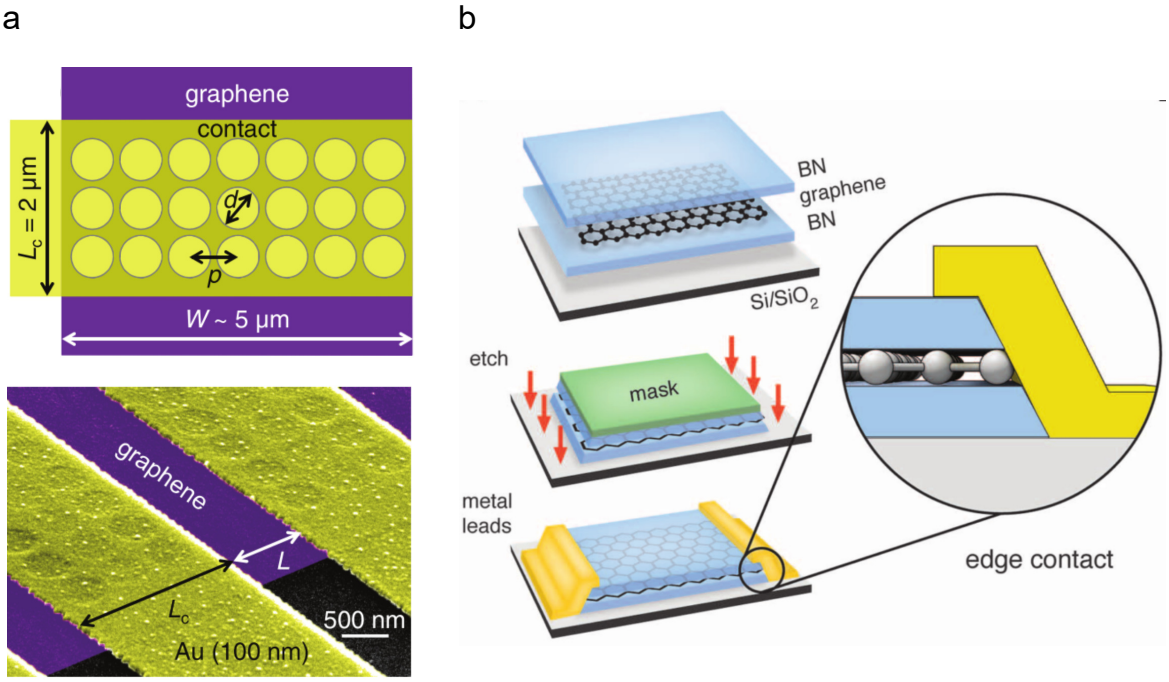

Fig. 2.10 Reducing contact resistance in graphene-based devices by increasing the amount of edge contact by (a) shaping graphene beneath the contacts, adapted from Ref. [57], (b) using 1d contacts, adapted from Ref. [58].

the metal to the graphene occurs at the edge of graphene [60]. Thus, R_C can be reduced by increasing the ratio of edge contact to surface-contact at the metal-graphene interface [60]. Lithography-defined cuts in graphene, figure 2.10a, increase the amount of edge contacts and have been shown to reduce R_C to $\sim 100\ \Omega \cdot \mu$m [57, 61]. This can be taken further by eliminating the remaining surface contact area by removing graphene from beneath the contacts [58, 62]. This has the added benefit of removing contaminants that might remain on graphene's surface which have been shown to increase R_C [62]. Figure 2.10b shows a 1d contact that uses a 45° etch-profile before metallisation to only contact the edge of graphene bringing R_C down to $\sim 100\ \Omega \cdot \mu$m [58].

Carrier Transport

A Hall bar device is used for measuring μ by using either field-effect or Hall measurements, where an induced change in carrier concentration from an applied gate voltage results in a change in sheet resistivity, ρ, of the graphene channel [24]. Figure 2.11A shows how ρ changes with applied voltage, where ρ peaks at the Dirac point, V_{Dirac}, because of the vanishing density of states, and decreases with increasing voltage [24]. For intrinsic graphene, where the V_{Dirac} coincides with $V_G = 0$, this curve would be centred at 0 V [24]. However,

any residual doping will shift V_{Dirac} to positive voltages for p-doping, and negative voltages for n-doping [24]. $\sigma_{\text{d.c}}$ can then be related to μ, and carrier concentration, N, by [23],

$$\sigma_{\text{d.c.}} = Ne\mu \tag{2.15}$$

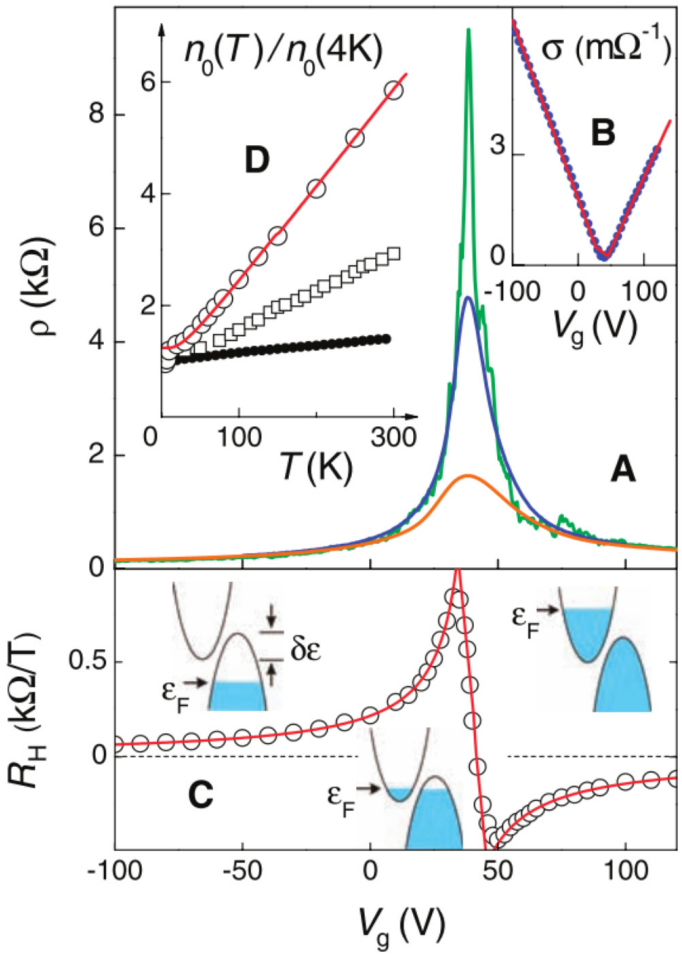

Fig. 2.11 Field-effect and Hall measurements used to determine the mobility of graphene, adapted from Ref. [24].

For 2d materials, the sheet resistance R_S is equivalent to ρ [24]. ρ can be calculated by measuring R_G from a 4-point-probe measurement and then calculating R_S with equation 2.11. ρ can then be converted into $\sigma_{\text{d.c}}$ by equation 2.12. The induced N from the applied gate voltage, V_G, with respect to V_{Dirac}, is determined by the gate capacitance C_{ox} [24]:

$$N = \frac{C_{\text{ox}}}{e}(V_G - V_{\text{Dirac}}) \tag{2.16}$$

Where C_{ox} is given by the relative permittivity of the oxide, ε_r, permittivity of free-space, ε_0, and the dielectric thickness, d_{ox} [10],

$$C_{\mathrm{ox}} = \frac{\varepsilon_r \varepsilon_0}{d_{\mathrm{ox}}} \tag{2.17}$$

The residual doping, defined as the doping at $V_{\mathrm{G}} = 0$, can be calculated from the measured V_{Dirac}. N is calculated at $V_{\mathrm{G}} = 0$ by equation 2.16, and can then be related to E_F by,

$$E_{\mathrm{F}} = \hbar v_{\mathrm{F}} \sqrt{N\pi} \tag{2.18}$$

From equation 2.15 and 2.16 the field-effect mobility, μ_{FE}, can then be calculated by the measured $\frac{d\sigma_{\mathrm{d.c}}}{dV_{\mathrm{G}}}$ [24]:

$$\mu_{\mathrm{FE}} = \frac{1}{C_{\mathrm{ox}}} \frac{d\sigma_{\mathrm{d.c}}}{dV_{\mathrm{G}}} \tag{2.19}$$

Alternatively, by applying a magnetic field perpendicular to the device the induced surface charge density can be measured directly via the Hall coefficient R_{H} and then used to calculate the Hall mobility (μ_H) [24]:

$$\mu_H = \frac{R_{\mathrm{H}}}{\rho} \tag{2.20}$$

Figure 2.11 shows the experimental results used to determine μ of mechanically exfoliated graphene devices with μ varying between 3000 - 10,000 cm^2/Vs. Both field-effect and Hall measurements were used which resulted in the same values of μ. These results also show the minimum conductivity and ambipolar behaviour of the carriers by the changing sign of R_{H} [24].

2.6 Conclusions

This chapter has given an introduction to graphene and described the different properties that make it suitable for the active material in Si photonic optical links. Specifically, the unique combination of broadband and tunable absorption with a high μ at room temperature is not offered by any other material. I have described different production techniques of graphene that each yield graphene with different properties that are suitable for a variety of applications. For the integration of graphene in CMOS compatible processing, CVD has shown to produce graphene films with a suitable combination of electrical properties and low-cost production over large areas. I have summarised different methods to characterise graphene to give information on its structural quality and electrical properties, which are critical parameters for using graphene in optical links. Specifically, the presence and structural

quality of graphene films can be determined by Raman spectroscopy, and TLM and transport measurements can be used to assess the μ and R_C of the grown films.

Chapter 3

Si Photonic Optical Links

3.1 Introduction

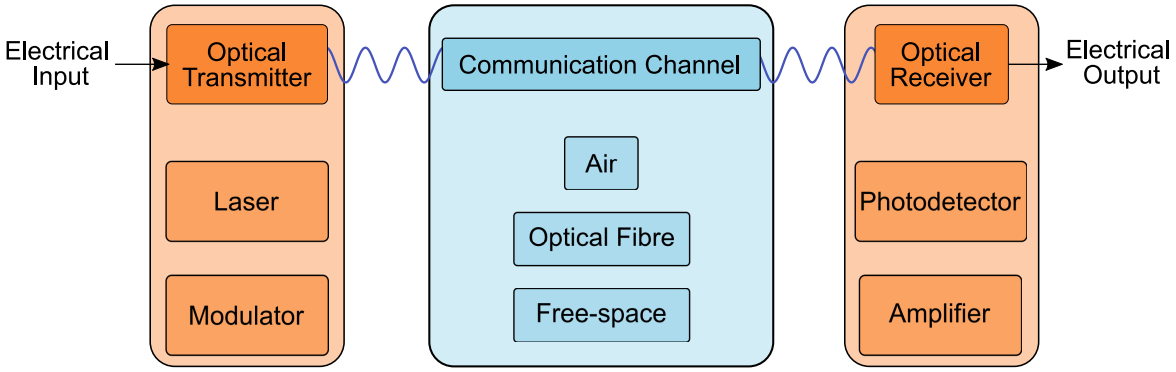

Fig. 3.1 Generic optical communication link focusing on the opto-electronic components. An electrical signal is supplied by an electronic driving circuit and converted into the optical domain by an optical transmitter and launched down a communication channel before being converted back into the electrical domain by an optical receiver, adapted from Ref. [63].

A generic optical communication link is pictured in figure 3.1. This is a generic optical link that consists of an initial data stream in the electrical domain, which is typically driven by CMOS circuitry. This is passed to an optical transmitter which converts the electrical signal into an optical signal with a light source, usually a laser, and a modulator. The modulated optical signal is then transmitted over a communication channel, which can be many different media depending on the environment. For example, for a wireless transmission this would be air, for transmission across a telecommunications network this would likely be across an optical fibre, or in the case of satellites this would be through free space. Once the signal has arrived at the destination it is converted back into an electrical signal by an optical receiver using a PD and some sort of amplifier. Si photonic technology offers a low-cost platform for

integrated opto-electronic circuits by using Si WGs to guide light on-chip [12], promising low-power and high-bandwidth data communication with integrated optical links. The band gap of Si = 1.11 eV at room temperature [23] makes it a very good material for guiding light in the typical wavelength range used by communications ($\lambda \sim$ 1.3 - 1.6 μm [64]) because it has low optical losses.

In this chapter I will describe the operating principles of different passive photonic components that are used in integrated optical transceivers. I will then move onto the active components that are used in the transmitter and receivers. Starting with transmitters, I will describe the operating principles behind Si-based WG-integrated modulators and discuss the parameters used to describe the device performance. I will then review the existing implementations and describe the different modulation schemes that can be used to drive the transmitters. Moving onto receivers, I will discuss the operating principle and the performance parameters for PDs, and review different types of integrated PDs on the Si platform and hybrid platforms of III-V semiconductors and Ge. I will then introduce system level implementations and operating principles of receivers based on coherent detection. Finally, I will put the transmitters and receivers into the context of optical networks and give an overview of existing optical links used in long-haul optical fibre networks and short-haul optical links that are used within data centres.

3.2 Passive Components

3.2.1 Waveguides

Mechanism for Guided Light

When light travels within a medium the medium is described by a complex refractive index [65]. The real component is the refractive index, n, and the imaginary component is the extinction coefficient, k [65]. n represents the reduction of propagation speed within the medium and is defined by $c = c_0/n$, where c is the speed of light in the medium and c_0 is the speed of light in vacuum [65]. The wavevector, $\mathbf{k}$, describes the direction of propagation and its magnitude is given by the wavenumber k [65]. k, is defined as the number of waves per unit distance ($k = 2\pi/\lambda$), and is related to n by $k = nk_0$, where k_0 is the wavenumber in free space [65].

Dielectric WGs guide light around an integrated photonic circuit by using total internal reflection to confine light between materials with different n [65]. Guided light undergoes total internal reflection at the boundary of a material with a lower n, whereas unguided light

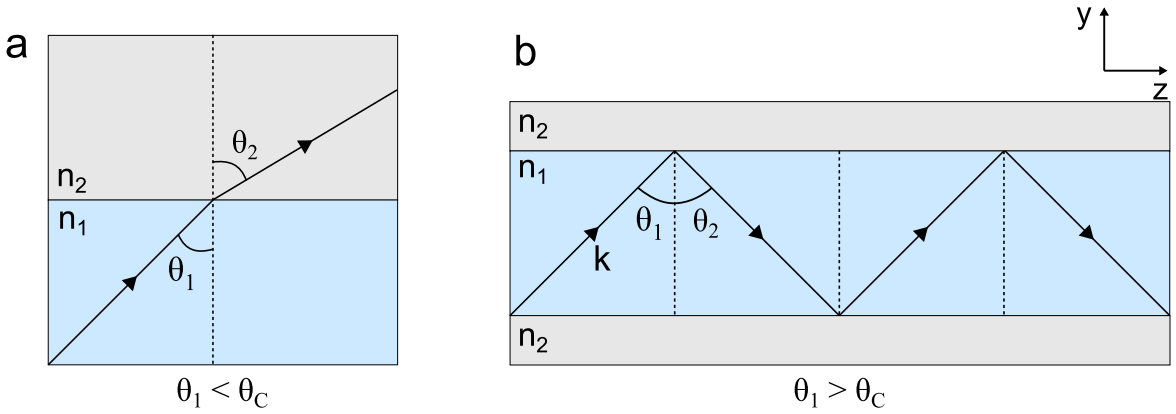

Fig. 3.2 Illustration of Snell's law of refraction for different angles of incidence at the boundary of the core, n_1, and the cladding, n_2, where $n_1 > n_2$. (a) When $\theta_1 < \theta_c$ the light is transmitted into the cladding. (b) When $\theta_1 > \theta_c$ the transmitted light undergoes total internal reflection and results in light being confined within the core.

would be lost due to scattering or radiation [65]. The material which the confined light propagates in is called the core, and the external materials are called cladding. Snell's law of refraction, equation 3.1, relates the angle of the incident, θ_1, and transmitted light, θ_2, at the interface of the core, n_1, and the cladding, n_2 [65]:

$$n_1 \sin\theta_1 = n_2 \sin\theta_2 \tag{3.1}$$

Figure 3.2 shows an example where light with wavevector k is propagating in material n_1 and is incident on material n_2 where $n_1 > n_2$. Below a critical angle, θ_c, the light will be transmitted into the cladding, Fig.3.2a, and above θ_c the light will be reflected back into the core, figure 3.2b. When $\theta_1 > \theta_c$ this is known as total internal reflection, and the light is confined within the core [65]. θ_c corresponds to the case when the angle of the transmitted light is 90^o and Snell's law reduces to [65],

$$\sin\theta_c = \frac{n_2}{n_1} \tag{3.2}$$

By solving Maxwell's equations that relate the electric and magnetic fields of the confined light, it is shown that the guided light propagates in an integer number of modes, each with an associated wavevector, **k**, field distribution, and mode number [65]. Figure 3.2b shows light that is confined within the y-plane and propagating along the z-axis. The confined light will have **k** components $(0, k_y, k_z)$ where $k_y = n_1 k_0 \cos\theta_1$ and $k_z = n_1 k_0 \sin\theta_1$. k_z is known as the propagation constant, β, which describes the change of phase along the direction of

propagation [65]. To include the effect of confinement we define an effective refractive index $n_{\text{eff}} = n_1 \sin\theta_1$ such that $n_2 \leq n_{\text{eff}} \leq n_1$ and [12],

$$\beta = k_0 n_{\text{eff}} \tag{3.3}$$

Rewriting k_0 in terms of λ_0, the phase, ϕ, after propagation length L is given by,

$$\phi = \frac{2\pi}{\lambda_0} n_{\text{eff}} L \tag{3.4}$$

Therefore instead of considering the light bouncing back and forth at the boundaries along the WG, it can be thought of as travelling straight down the WG with an effective refractive index, n_{eff}. These modes can be categorised by the polarisation, either transverse-electric (TE) or transverse-magnetic (TM), and by mode number. The number of modes that are supported by a WG will depend on the WG structure as this will effect the angle of reflection [12]. The field distribution in the cladding is the evanescent field that decays exponentially, which penetrates deeper into the cladding for higher order modes [65]. The proportion of the electric field energy density that is propagating within the WG core compared to its surroundings is given by the confinement factor Γ [12]:

$$\Gamma = \frac{\iint_C |\mathbf{E}(x,y)|^2 \text{dxdy}}{\iint_\infty |\mathbf{E}(x,y)|^2 \text{dxdy}} \tag{3.5}$$

This is dependent on the mode number, the dimensions of the WG, and the refractive index contrast between the core and the cladding, Δn = n_2 - n_1, where n_1 is the refractive index of the core and n_2 is the refractive index of the cladding [12]. Γ will increase when more light is confined within the core and less light is in the evanescent field, which will occur for an increased Δn, a larger core, and lower order modes.

Propagation losses in WGs are attributed to either radiation, absorption, or scattering processes [12]. Radiation occurs in WG bends when evanescent waves are lost to radiative modes [66], known as bending losses. Fig 3.3 shows a mode field profile propagating along a bent WG that is characterised by its bend radius [66]. The outside edge of the evanescent field needs to travel faster to keep up with the wavefronts of the mode in the core [66]. Beyond a critical radius, the required speed of the evanescent field exceeds the speed of light in the medium (c_0/n) and is therefore lost by radiation into the cladding [66]. Smaller bending radii are beneficial for densely integrated photonic circuits, but also result in increased bending losses.

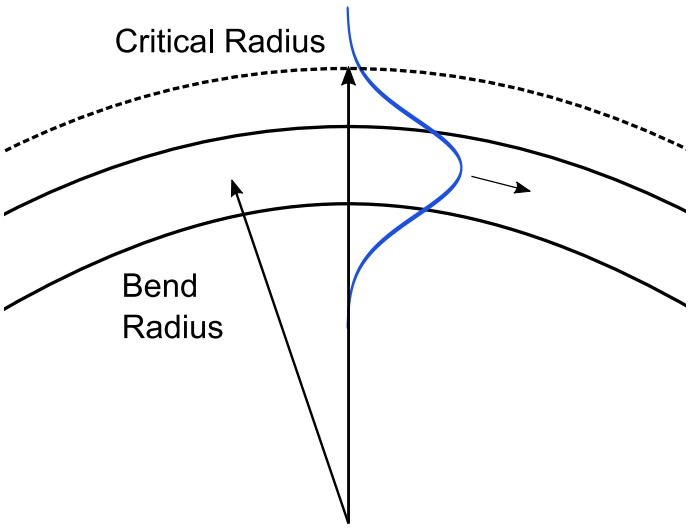

Fig. 3.3 Schematic showing a modal field profile propagating along a WG bend, where the critical radius is shown by the dashed line

Absorption along the direction of propagation is modelled by the imaginary component of the complex refractive index, known as the extinction coefficient, k. k is related to the absorption experienced during propagation by the power attenuation coefficient, α, by [65],

$$\alpha = \frac{4\pi}{\lambda_0} k \tag{3.6}$$

This includes an additional factor of 2 to convert from electric field to intensity [65]. α is then related to the change in intensity, I, along the direction of propagation by [12],

$$\frac{I}{I_0} = e^{-\alpha L} \tag{3.7}$$

Scattering can occur from imperfections in the dielectric material or imperfections resulting from the fabrication process [12]. The dominant scattering source is from sidewall roughness produced by etching processes for shaping the WGs [67]. The top and bottom WG surfaces do not contribute greatly to scattering as they have atomically smooth surfaces produced by deposition processes or mechanical polishing [67]. The propagation losses due to scattering, $\alpha_{\text{scattering}}$, are given by the following equation which relates the roughness σ, Δn, and the overlap between the mode and the core-cladding boundary $\frac{E_S^2}{\int E^2 dx}$ [66]:

$$\alpha_{\text{scattering}} = \frac{\sigma^2 k_0^2 n_{\text{core}}}{n_{\text{eff}}} \cdot \frac{E_S^2}{\int E^2 \text{dx}} \cdot \Delta n^2 \tag{3.8}$$

where E_S is the field intensity at the core-cladding boundary, and E is the field intensity at a position along the cross section of the WG. From this equation it is clear to see that

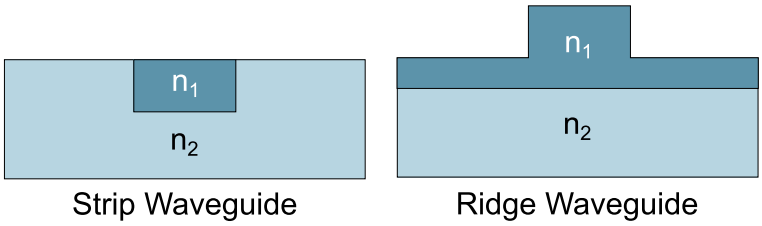

Fig. 3.4 Cross-section of common WG structures.

designs with increased modal overlap with the core-cladding interface, Δn, and roughness will have higher propagation losses.

Design parameters

The choice of material used as the core and cladding have a large effect on the confinement of the optical mode. A high Δn results in strongly confined modes within the core, whereas a lower Δn can be used for evanescent modes that interact with the surrounding materials. Si-on-insulator (SOI) technology was first proposed as a convenient platform for optical WGs in 1988 by Kurdi and Hall [68] where the buried SiO_2 layer acts as the lower cladding to separate the top Si guiding layer from the substrate. It is enables submicron WG dimensions due to the high Δn between Si ($n_{Si} \sim 3.47$ at 1.55μm [69]) and SiO_2 ($n_{SiO2} \sim 1.44$ at 1.55μm [70]). In the telecom operating range of 1.3 - 1.55 μm, absorption in Si is negligible because the band gap of Si 1.1 eV makes it transparent [12]. A high Δn is beneficial to reduce radiative losses, that originate in WG bends, by minimising the extent of the evanescent field in the cladding. This enables bending radii to be reduced which allows more densely integrated photonic circuits [66]. Typically bending radii are in the order of micrometers for SOI WGs [71], but have been shown to go as low as 1 μm [72]. The chosen bending radii will be a trade-off between the additional bending losses and the desired circuit density. However, higher Δn leads to increased scattering loss at the core-cladding boundary which scales proportionally to Δn^2. Scattering loss can be minimised by designing the WG such that less of the mode overlaps with the core-cladding boundary [73]. This can either be by reducing the WG dimensions such that the majority of the mode is propagating in the cladding, or by increasing the dimensions so that the majority of the mode resides within the core. By leveraging the mature CMOS processing technology, side-wall roughness can be minimised and propagation losses for SOI WGs can go below 2.6 dB/m [73]. It is desirable to reduce propagation losses as these result in unnecessary power consumption and signal degradation over long distances. In order to reduce propagation losses, other CMOS compatible materials can be used for the core with a smaller Δn and therefore lower scattering losses. SiN, with $n_{SiN} \sim 2.46$ at $\sim$1.55 μm [74] has $\Delta n \sim$0.55, which is large enough for light to be guided,

but smaller than using Si cores. A lower Δn means that propagation losses can go as low as 0.7 dB/m [75], but at the cost of increased bending radii which are in the millimetre range [75, 76].

The field distribution of the optical mode is determined by the dimensions of the WG. This allows control on the number of supported modes and which parts of the design that the mode is interacting with. Figure 3.4 shows common structures of channel WGs that confine light in 2 dimensions, which are called strip WGs and ridge or rib WGs [77]. Light is confined within the core material, with a refractive index n_1, that is higher than the cladding material, with a refractive index n_2 [12]. Depending on the choice of dimensions, these WGs can support a single-mode or many modes. Multi-mode WGs are useful for long-distance optical communication as the amount of data that can be transmitted in a single optical fibre is increased [63]. However, for integrated photonic circuits single-mode WGs that only support the fundamental mode are favoured because it eliminates intermodal dispersion which degrades the transmitted signal [77].

3.2.2 Couplers

Optical coupling is important in photonic circuits when injecting or extracting light either between WGs or from an optical fibre. Coupling to and from optical fibres is particularly challenging due to the large difference in size between WGs and optical fibre cores. Typically single-mode fibres have core diameters of $< 10\ \mu$m and multi-mode fibres have core diameters $\sim 50\ \mu$m [78]. The large size of optical fibre cores, shown in figure 3.5, is a problem for compact photonic platforms, such as SOI, with high Δn and submicron WG dimensions.

Mechanism for coupled light

We have seen that confinement within WGs causes light to travel in modes, each with a unique transverse field distribution and β [65]. To couple light between WGs or optical fibres the modal field distribution and β of the incoming light and the desired mode within a WG or optical fibre should match [65]. The amount of power transferred between the source and the WG or optical fibre depends on how closely the modal field distributions and β match [65]. Coupling efficiency, η, describes the amount of incident power that is transmitted into a confined optical mode [79]:

$$\eta = \frac{P_{\text{out}}}{P_{\text{in}}} \tag{3.9}$$

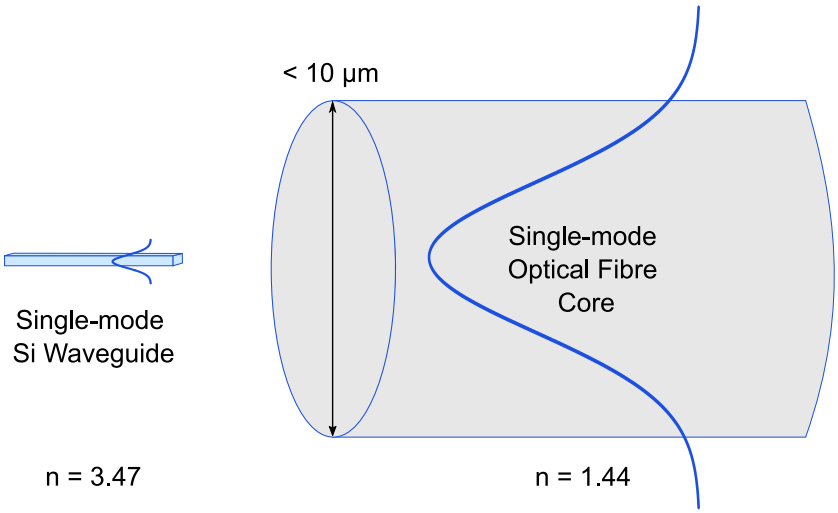

Fig. 3.5 Coupling problem for single mode Si WGs due to the large difference in size compared to a standard optical fibres, adapted from Ref. [77]

This can be related to coupling loss (CL) which is expressed in dB and given by the following formula [80]:

$$\mathrm{CL} = -10\log_{10}(\eta) \tag{3.10}$$

The two main origins of coupling loss are modal mismatch, which is related to the size difference between optical fibres and WGs, and impedance mismatching, which is related differences in n [12]. Figure 3.5 shows the different sizes of modal field profiles for the single-mode Si WG and the single-mode optical fibre. In this case, η is limited by the overlap of the input and output mode profiles, as well as reflections caused by different values of n for the input and output structures.

Coupling techniques

Butt coupling is perhaps the simplest coupling method that transfers power from one WG by abutting it to another [12]. When coupling between structures of different sizes, tapers can be used to overcome a mismatch in modal profile field distribution, and thus reduce coupling loss [77]. Tapers made from high n materials from the dimensions of the WG to the dimensions of the optical fibre have been suggested for improving coupling efficiency, however these usually require long device lengths and suffer from large back reflections at the fibre facet [80]. Instead, by using an inverse taper from the WG dimensions to a small tip the mode profile of the WG slowly expands as it becomes less confined and more evanescent, leading to increased coupling efficiency from greater overlap between the modal profiles of the WG and fibre [80–82]. Figure 3.6 shows how the mode profile of the WG changes due

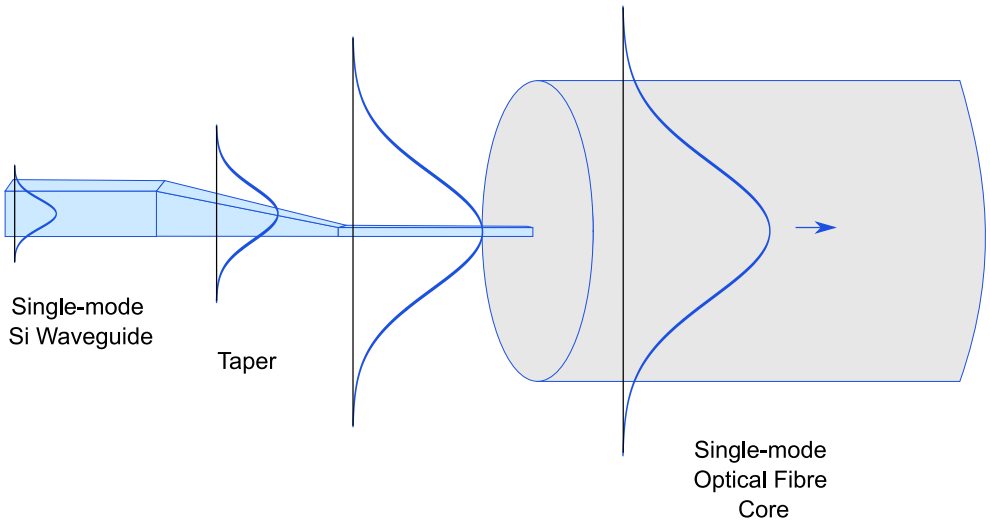

Fig. 3.6 Schematic showing the increasing size of the modal field profile in a Si WG due to an inverse taper for greater overlap with the field profile of the receiving optical fibre, adapted from Ref. [77]

to the inverse taper [77]. A nanotaper, based on the same principles as the inverted taper, that was 40 μm long and 120 nm wide has shown an order of magnitude improvement in coupling efficiency to 0.5 dB for the TE mode [80].

Evanescent coupling can be used for WGs which are close enough so that their evanescent fields overlap [12]. Figure 3.7 shows two WGs of material n_1 that are embedded within material n_20. An initial wave is propagating in the top WG where its evanescent field overlaps with the mode field profile in the bottom WG. Thus, after a certain propagation distance the initial wave has been coupled into the bottom WG and continues to propagate in the same direction. Using coupled-mode theory it is possible to calculate a coupling length L_c over which all of the power is transferred [65].

Grating couplers are used to couple light in or extract light at an angle [12]. A grating coupler consists of a grating placed on top, or etched into a WG that is particularly useful for coupling light into a photonic circuit at any point on a wafer and not just at the edges [12]. For a mode to be excited in the WG the phase-match condition must be met which requires the tangential component of the wavevector of the incoming light, $k_{\text{in,z}}$, must match the propagation constant of the WG mode, β [12]. For phase match to occur [12]:

$$\beta = k_0 n_2 \sin\theta_1 \tag{3.11}$$

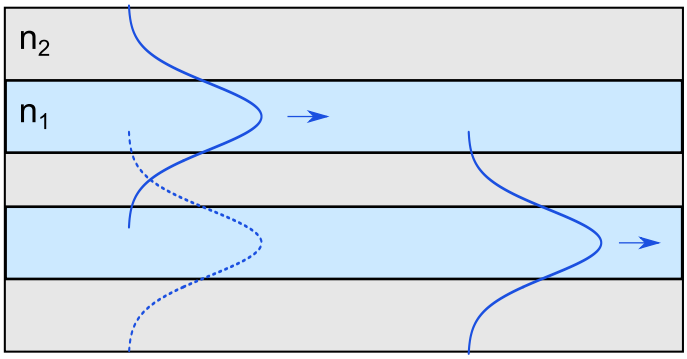

Fig. 3.7 Schematic showing evanescent coupling between WGs that are in close enough proximity that their evanescent modal field profiles overlap.

Where $k_{\mathrm{in,z}}$ is given in terms of the refractive index of the cladding n_2, and the angle of incidence θ_1. As $\beta = n_{\mathrm{eff}} k_0$, and $n_{\mathrm{eff}} > n_2$ for a confined mode, then coupling will never be possible because $\sin\theta_1$ can never be greater than 1 [12]. By introducing a periodic grating into the WG structure, Figure 3.8a, the diffracted light will be periodic and consist of different diffractive modes, m, whose wavenumbers in the direction of propagation, $k_{\mathrm{m,z}}$, are given by [12]:

$$k_{\mathrm{m,z}} = k_{\mathrm{in,z}} + \frac{2\pi m}{\Lambda} \tag{3.12}$$

where Λ is the grating period and m is = ± 1, ± 2, ± 3, etc. Only the positive values of m result in a phase match between the diffracted light, $k_{\mathrm{m,z}}$, and β, where typically only the m = 1 case is used. By rewriting equation 3.12 in terms of refractive indices and substituting $k_0 = 2\pi/\lambda$ it can be shown that the design of the grating, Λ, and choice of incident angle θ_1 enable a specific mode to be excited at a chosen wavelength [12]:

$$\Lambda = \frac{\lambda}{n_{\mathrm{eff}} - n_2 \sin\theta_1} \tag{3.13}$$

Figure 3.8b shows how a grating coupler can be used to couple light from a single-mode optical fibre into a integrated photonic circuit [83]. Here, an adiabatic taper is used to slowly convert the large field distribution of the optical fibre into a smaller size to more closely match the field distribution of the WG.

Design parameters

The coupling efficiency between photonic components can be optimised by designing couplers that maximise the overlap between input and output modal field profiles and minimising reflections due to a refractive index contrast. This will be crucial for integrated opto-electronic

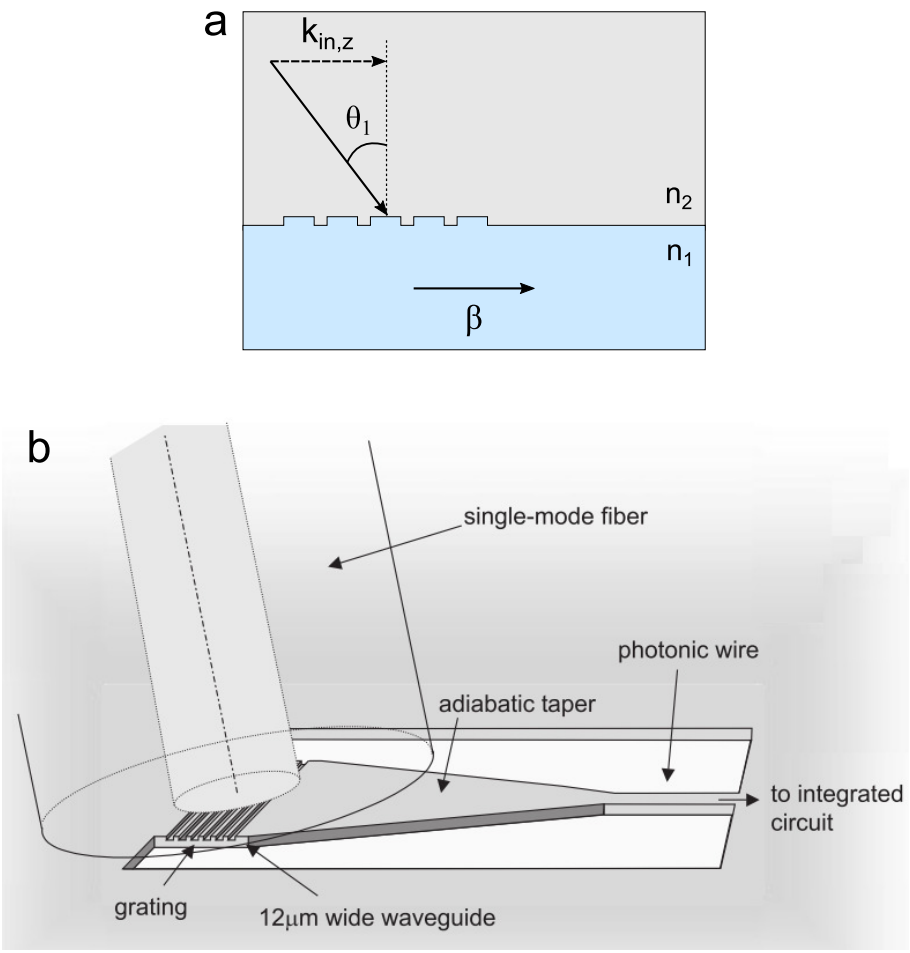

Fig. 3.8 (a) Schematic showing light incident to a grating, (b) Grating coupler design coupling a single mode optical fibre into a Si WG, adapted from Ref. [83]

circuits that require single-mode WGs and the combination of many different components. As well as coupling efficiency, fabrication processes will be a concern as strict alignment tolerances will be undesirable for integration with existing CMOS processing. The choice of coupling technique will be a trade-off between efficiency and fabrication complexity. On-chip coupling between WGs can be achieved with evanescent coupling and in-plane or vertical tapers, whereas fibre-to-chip coupling relies on edge-coupling and grating couplers. Grating couplers offer a practical solution to couple light at arbitrary points on a integrated photonic circuit, and are able to achieve < 1 dB coupling losses [84]. The grating properties, such as periodicity, etch depth, or etch width, can be optimised to manipulate the operating wavelength and shape of the output beam profile [85]. Reflections can be reduced by optimising the optical fibre incident angle or using anti-reflective coatings can also be used to prevent power loss to the substrate [83].

3.2.3 Ring Resonators

Operating Principle

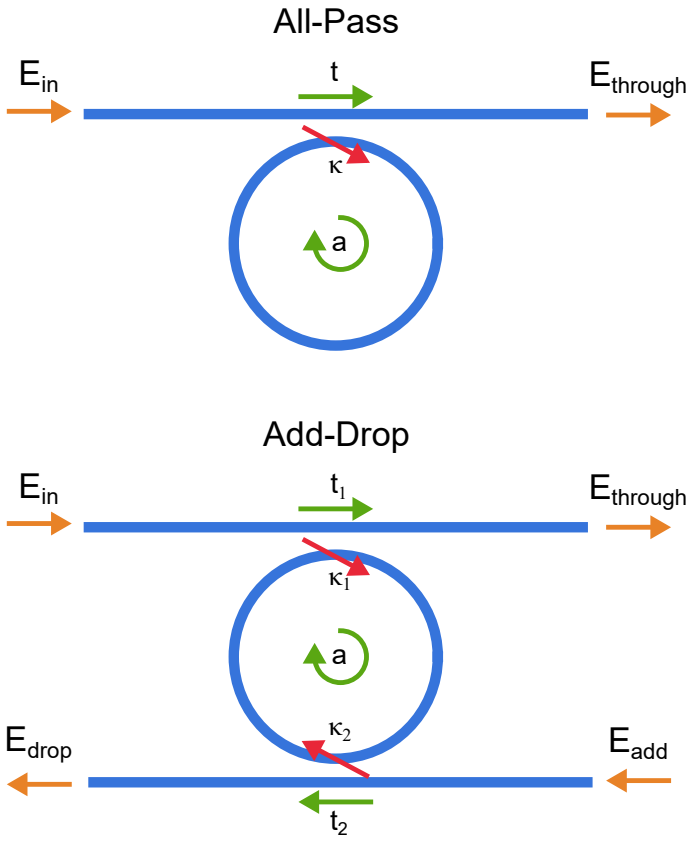

Fig. 3.9 Ring resonator configurations showing input and output electric fields, E_{in} and E_{out} and the respective transmission and cross-coupling coefficients for each directional coupler t and κ. The single-pass transmission coefficient within the ring is given by a.

A ring resonator (RR) is a passive structure consisting of a WG looped back onto itself, that can be accessed by another WG, known as a bus WG, that is close enough that the evanescent field profile overlaps with the ring WG [12]. Ring resonators come in two configurations that are shown in figure 3.9. A structure with one bus WG is called an all-pass ring resonator, whilst a structure with two bus WGs is called an add-drop ring resonator [71]. The bus WG forms a directional coupler with the ring WG. When incoming light travelling along the bus WG comes into proximity with the ring, part of the electric field continues to be transmitted along the bus WG, and part is coupled into the ring [65]. This splitting ratio is determined by transmission and cross-coupling coefficients of the directional coupler t and κ [71]. t is defined as the ratio of the electric field transmitted to the through or drop port and the electric field from the input or add port [65], whilst κ is defined as the ratio of the

electric field transmitted into the ring and the the electric field from the input or add port [65]. Assuming lossless coupling, and to preserve energy conservation, t and κ are related by [65],

$$\sqrt{t^2 + \kappa^2} = 1 \tag{3.14}$$

t and κ can be converted into power splitting ratios rather than electric field splitting ratios by squaring them [65]. For example, a coupler with 50:50 splitting of transmitted power, the transmission coefficient for the electric field will be $t = \sqrt{0.5}$.

A ring resonator is a complex feedback system where light is simultaneously and continuously coupled in and out of the ring by the directional coupler [71]. Light that is coupled into the ring will propagate within the ring until it is either lost or coupled back out to the bus WG [71]. The proportion of light that is lost during propagation in the ring is given by the single-pass transmission coefficient a, which takes into account all sources of loss such as absorption or scattering [71]. After each round trip, the light within the ring will interfere with the incoming light at the directional coupler [71]. Depending on the phase after one round trip a standing wave can be formed, leading to light being stored inside the ring [71]. The phase of the light in the ring is related to the optical cavity length, L, the wavelength, and effective refractive index of the material by equation 3.4. Due to constructive interference, the maximum energy stored in the ring occurs when ϕ matches an integral number of 2π [71]. This is the resonance condition for the ring, which occurs at wavelengths when the optical length of the ring fits an integral number of wavelengths [71]. At resonant wavelengths, λ_{res}, the transmission drops to a minimum because the light that is coupled out of the ring has experienced the cumulative round trip losses whilst being stored in the ring [71]. On the other hand, the maximum transmission occurs when the phase after one trip matches an integral number of π [71]. In this situation the energy stored in the ring is at a minimum because of destructive interference [71]. Therefore, as the wavelength is swept, transmission will decrease as ϕ increases from πm to $2\pi m$ and more light is stored within the ring.

The transmitted power will depend on a combination of t, κ, and a, as well as ϕ after one round-trip of the ring. Transmitted power to the through port, P_{t}, and drop port, P_{d} is given by [71],

$$P_{\text{t}} = \frac{t_2^2 a^2 - 2t_1 t_2 a \cos\phi + t_1^2}{1 - 2t_1 t_2 a \cos\phi + (t_1 t_2 a)^2} \tag{3.15}$$

$$P_{\text{d}} = \frac{(1-t_1)^2(1-t_2)^2 a}{1 - 2t_1 t_2 a \cos\phi + (t_1 t_2 a)^2} \tag{3.16}$$

From equation 3.15 the minimum transmitted power at resonance, P_{res}, occurs when $\cos 2\pi m = 1$ [71],

$$P_{\text{res,t}} = \frac{(t_2 a - t_1)^2}{(1 - t_1 t_2 a)^2} \tag{3.17}$$

$$P_{\text{res,d}} = \frac{(1 - t_1^2)(1 - t_2^2)a}{(1 + t_1 t_2 a)^2} \tag{3.18}$$

And the maximum transmitted power, P_{max}, occurs when $\cos \pi m = -1$ [71],

$$P_{\text{max,t}} = \frac{(t_2 a + t_1)^2}{(1 + t_1 t_2 a)^2} \tag{3.19}$$

$$P_{\text{max,d}} = \frac{(1 - t_1^2)(1 - t_2^2)a}{(1 - t_1 t_2 a)^2} \tag{3.20}$$

Under certain conditions all of the incoming light is transferred into the ring and the transmission at resonance goes to zero [71]. This is known as critical coupling and occurs at two conditions for an add-drop configuration [71]. For a lossless ring when $a = 1$, this occurs when $t_1 = t_2$ [71]. In this case, all of the light will be transmitted to the drop port before it can be coupled back into the through port. This is shown in figure 3.10a where P_{t} goes from 1 to 0 and P_{d} goes from 0 to 1. However, for a lossy ring where $a < 1$, P_{t} will only go to 0 if it balances the combination of losses in the ring and transmission to the drop port. This is satisfied when $t_1 = a t_2$ [71], as shown in figure 3.10b. Here P_{t} goes from 1 to 0, but P_{d} does not go to 1 because light is lost in the ring before it can be coupled out. The effect of the increased losses compared to 3.10a can be seen by the reduction in maximum transmission.

Figure 3.10 shows some important metrics for characterising the transmission of a RR. The extinction ratio (ER) is defined by the ratio of the maximum and minimum transmitted power, and is given by the following formulas for the through and drop port [71],

$$\text{ER}_{\text{t}} = \frac{P_{\text{max,t}}}{P_{\text{res,t}}}, \tag{3.21}$$

$$\text{ER}_{\text{d}} = \frac{P_{\text{max,d}}}{P_{\text{res,d}}}. \tag{3.22}$$

The distance between resonances is given by the free spectral range (FSR) which corresponds to a phase shift of 2π [71],

$$\text{FSR} = \frac{\lambda_{\text{res}}^2}{n_g L} \tag{3.23}$$

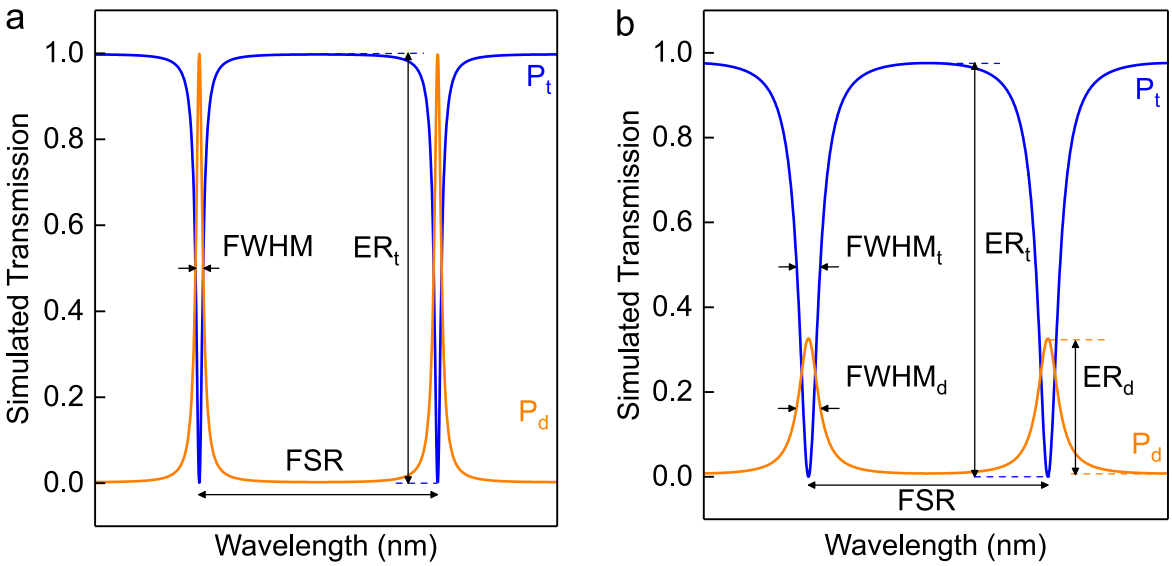

Fig. 3.10 Simulated transmission of an add-drop ring resonator showing transmission to the through port, P_t, and drop port, P_d, at critical coupling. (a) Critical coupling for a lossless ring where $a = 1$ and $t_1 = t_2 = 0.95$. (b) Critical coupling for a lossy ring where $a = 0.9$, $t_2 = 0.95$, and $t_1 = at_2$.

where n_g is the group index which depends on the dimensions of the ring WG and the wavelength dispersion of the WG material [71]. n_g is used rather than n_{eff} because we are interested in transmission over a large wavelength range. n_g is related to n_{eff} by [86]:

$$n_g = n_{eff} - \lambda_0 \frac{dn_{eff}}{d\lambda} \tag{3.24}$$

where λ_0 is the wavelength in free space. The shape of the resonant peak is described by the full-width at half-maximum (FWHM) which is related to the material and geometry of the ring as well as the transmission coefficients of the directional couplers and the ring [71].

$$\text{FWHM} = \frac{(1 - t_1 t_2 a)\lambda_{res}^2}{\pi n_g L \sqrt{t_1 t_2 a}} \tag{3.25}$$

Resonances are typically characterised by the quality factor (Q-factor) which indicates the sharpness of the resonance [71]. It is related to the FWHM by [71]:

$$\text{Q-factor} = \frac{\lambda_{res}}{\text{FWHM}} \tag{3.26}$$

The Q-factor represents the time it takes for the energy stored in the ring to drop to $1/e$, which can also be considered as the photon-lifetime inside the ring [71]. Sharper peaks with smaller FWHM have higher Q-factors, which tend to infinity at critical coupling as the light never comes back out of the ring. Rings with high Q-factor resonances will therefore be

limited in terms of their operational bandwidth (BW) as the increased photon-lifetime limits the speed that power can be injected and depleted from the ring [71]. The Q-factor can be related to the cavity photon lifetime, τ_{cav}, by [87]:

$$\tau_{\text{cav}} = \frac{\lambda_{\text{res}}}{2\pi c} Q \tag{3.27}$$

The maximum optical BW, $f_{\text{3dB}}^{\text{opt}}$, supported by the resonator is then given by [88],

$$f_{\text{3dB}}^{\text{opt}} = \frac{1}{4\pi\tau_{\text{cav}}} \tag{3.28}$$

where larger τ_{cav} leads to lower $f_{\text{3dB}}^{\text{opt}}$. Therefore, the EO BW, $f_{\text{3dB}}^{\text{el-opt}}$, is given by [89],

$$\left(\frac{1}{f_{\text{3dB}}^{\text{el-opt}}}\right)^2 = \left(\frac{1}{f_{\text{3dB}}^{\text{el}}}\right)^2 + \left(\frac{1}{f_{\text{3dB}}^{\text{opt}}}\right)^2 \tag{3.29}$$

3.2.4 Mach-Zehnder Interferometers

Operating Principle

A Mach-Zehnder interferometer (MZI) is a passive WG structure that splits an incoming optical signal into two arms which are later recombined [12]. They typically have one or two input and output ports, and commonly use directional couplers or multi-mode interference (MMI) couplers to split and recombine the propagating signal [77]. Depending on the phase difference between the two arms, $\Delta\phi$, the propagating waves will interfere when recombined. If the propagating waves are in phase, transmission will not depend on λ, however if they are no longer in phase, an interference pattern will appear at the output [12]. An MZI is fully described by the coupler and the change in absorption and phase due to propagation along each of the arms [12]. A 2×2 MZI is illustrated in figure 3.11 with two input and output ports designated as channel 1 and channel 2. The coupler is characterised by transmission and cross-coupling coefficients, t and κ, that define the splitting ratio of the electric field to the through and cross port. The through port is defined when transmission is along the same channel as the input signal, and the cross port is defined when the output crosses to the other channel. A 2×2 coupler can be described by the 2×2 transfer matrix Φ_{C},

$$\Phi_{\text{C}} = \begin{pmatrix} t & -j\kappa \\ -j\kappa & t \end{pmatrix} \tag{3.30}$$

The complete behaviour of an MZI with two input and output ports can be modelled in terms of input and output electric fields by [77],

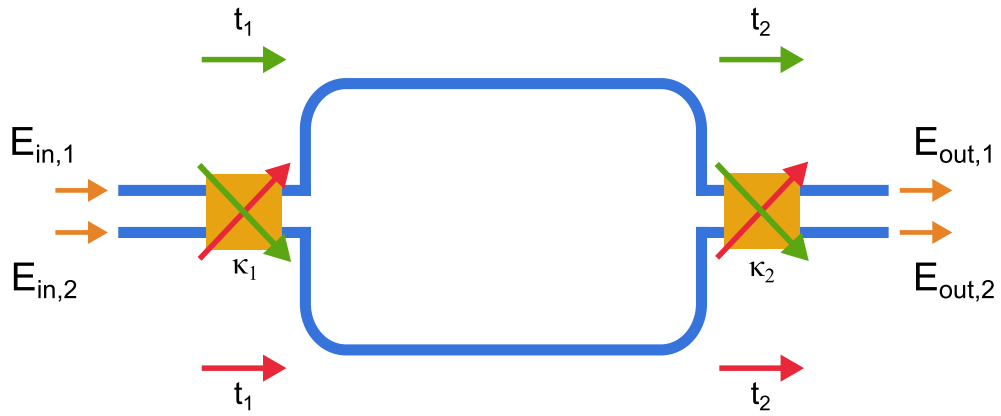

Fig. 3.11 Schematic of an Mach-Zehnder interferometer (MZI) with 2 input and output ports and couplers represented in orange. Input and output electric fields are shown, along with the transmission and cross-coupling coefficients of the couplers, t and κ. Green arrows show the through and drop port transmission for port 1 and red arrows show the same for port 2.

$$\begin{pmatrix} E_1^{\text{out}} \\ E_2^{\text{out}} \end{pmatrix} = \Phi_{\text{C},1} \begin{pmatrix} A_0 e^{-\frac{1}{2}\alpha_1 L_1} \sin(\omega t - \phi_1) & 0 \\ 0 & A_0 e^{-\frac{1}{2}\alpha_2 L_2} \sin(\omega t - \phi_2) \end{pmatrix} \Phi_{\text{C},2} \begin{pmatrix} E_1^{\text{in}} \\ E_2^{\text{in}} \end{pmatrix} \tag{3.31}$$

Equation 3.31 is a product of Φ_{C} and the change in amplitude and phase resulting from propagation along each arm [77]. Both the absorption and phase can be modelled in terms of the complex effective refractive index and propagation length of each arm L [65]. The change in amplitude of the electric field due to absorption is represented by $A_0 e^{-\frac{1}{2}\alpha L}$ and is related to the power attenuation coefficient, α. The phase of the electric field, ϕ, is represented by $\sin(\omega t - \phi_1)$ and is related to the propagation constant β.

Using equation 3.31, and trigonometric identities $\sin^2\theta = \frac{1}{2}(1 - \cos 2\theta)$ and $\sin A \sin B = \frac{1}{2}[\cos(A - B) - \cos(A + B)]$ the transmission from input 1 to output 1, T_{11}, is given by:

$$\left(\frac{E_{\text{out},1}}{E_{\text{in},1}}\right)^2 = \frac{A_0^2}{2}\left(t_1^2 t_2^2 e^{-\alpha_1 L_1} + \kappa_1^2 \kappa_2^2 e^{-\alpha_2 L_2} + 2t_1 t_2 \kappa_1 \kappa_2 e^{\left(-\frac{1}{2}\alpha_1 L_1 - \frac{1}{2}\alpha_2 L_2\right)} \cos(\phi_2 - \phi_1)\right) \tag{3.32}$$

Whilst the transmission from input 1 to output 2, T_{12} is given by:

$$\left(\frac{E_{\text{out},2}}{E_{\text{in},1}}\right)^2 = \frac{A_0^2}{2}\left(t_1^2 \kappa_2^2 e^{-\alpha_1 L_1} + \kappa_1^2 t_2^2 e^{-\alpha_2 L_2} + 2t_1 \kappa_2 \kappa_1 t_2 e^{\left(-\frac{1}{2}\alpha_1 L_1 - \frac{1}{2}\alpha_2 L_2\right)} \cos(\phi_2 - \phi_1)\right) \tag{3.33}$$

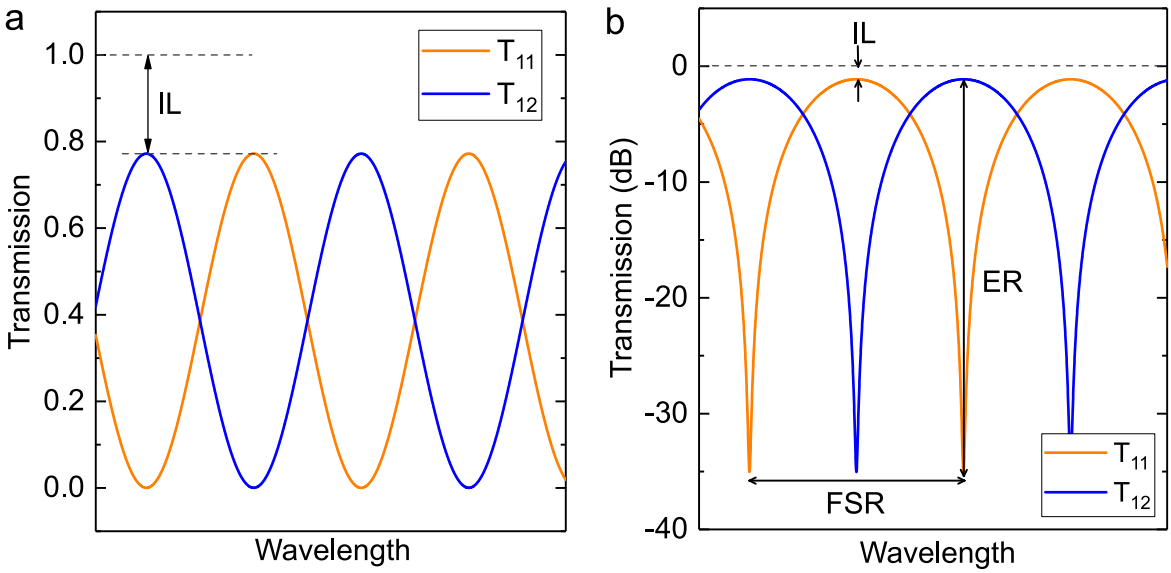

Fig. 3.12 Simulated transmission (a) on a linear scale, and (b) on a logarithmic scale for a 2×2 Mach-Zehnder interferometer (MZI) using equation 3.32 and 3.33. Key device parameters are shown, including insertion loss (IL), extinction ratio (ER), and free-spectral range (FSR).

The simulated transmission T_{11} and T_{12} using equation 3.32 and 3.33 has been normalised to a maximum intensity of 1 and are plotted in figure 3.12. The simulation was performed at λ = 1.55 μm and considered a MZI that was made of 450 nm × 220 nm Si WGs (α = 10 dB/cm), with L_1 = 950 μm and ΔL = 350 μm. The simulation assumes perfect splitting by each coupler such that $t_1 = t_2 = \sqrt{0.5}$ and $\kappa_1 = \kappa_2 = \sqrt{0.5}$. To calculate ϕ as a function of λ, n_{eff} needed to be defined as a function of λ. $n_{\text{eff}}(\lambda)$ was calculated using a finite-difference eigenmode (FDE) simulation in Lumerical's MODE simulator to determine n_{eff} and $\frac{dn_{\text{eff}}}{d\lambda}$. The wavelength-dependent transmission depends on the phase difference between the two arms, $\Delta\phi = \beta_1 L_1 - \beta_2 L_2$. In this case, the simulation assumes that the WGs are the same for each arm ($\beta_1 = \beta_2$), but that the arms have different propagation lengths ($\Delta L > 0$). This is known as an unbalanced MZI, and results in an interference pattern at the output [77]. If instead the arms of the MZI were the same length ($\Delta L = 0$), then the transmission would not vary with wavelength and would correspond to the maximum transmission seen in the unbalanced MZI. The FSR is given by [86]:

$$\text{FSR} = \frac{\lambda_{\text{res}}^2}{n_g \Delta L} \tag{3.34}$$

Therefore, by comparing T_{11} and T_{12} we observe that there is a π-phase difference between the outputs from each channel as a result of the j in the cross-coupling component of the couplers [86]. The extinction ratio (ER) is expressed in dB and defined as the ratio

of the maximum and minimum transmission through the MZI [77]. By examination of equation 3.32 and 3.33 we see that the maximum transmission occurs when $\Delta\phi = 0$ and the minimum transmission occurs when $\Delta\phi = \pi$. Finally, the insertion loss (IL) is given in dB and is defined as the reduction in transmission due to the introduction of the MZI in the transmission line [12]. The IL is given by the maximum transmission. For the ideal case when IL = 0 dB then the maximum transmission would be 0 dB, however any introduced optical losses will appear as a vertical downward shift of the transmission spectrum. Here, additional propagation losses have been added to the simulation to illustrate this effect.

3.3 Transmitters

3.3.1 Modulation Mechanisms in Si

Electro-Optic Effects

Changing the optical properties of a material under a steady or slowly varying electric field is called the electro-optic effect [65]. When this results in a change of the effective refractive index it is called electro-refraction [12]. Even though Δn is typically small ($\sim 10^{-4}$), this can lead to significant changes in phase for light propagating over distances much greater than its wavelength [65]. Depending on the type of medium, Δn can either vary linearly with the applied electric field, which is called the Pockels effect, or quadratically, which is called the Kerr effect [65]. This means that the Pockels effect is highly polarisation dependent as the sign of Δn depends on the direction of the electric field [12]. Therefore for centrosymmetric materials Δn must be invariant to the direction of electric field, which makes the Pockels effect zero leaving only the Kerr effect [65].

It is also possible to change a materials optical properties by changing the power attentuation coefficient ($\Delta\alpha$) of the material which is known as electro-absorption [12]. This affects the extinction coefficient and so also results in Δn through the Kramers-Kronig relations [90]. In bulk semiconductors this is done by the Franz-Keldysh effect where an electric field leads to electron tunnelling that extends the absorption edge to lower energies [65]. This shifts the transition from efficient direct band gap transitions to inefficient indirect transitions to longer wavelengths [91].

Plasma dispersion effect

Soref and Bennett studied the change in refractive index in crystalline Si with applied electric field and found that the Kerr and Franz-Keldysh effects were very weak at telecommunication wavelengths (1.3 - 1.55 μm) [90]. This combined with the lack of Pockels effect due to Si's crystalline structure, mean that other mechanisms need to be used for optical modulation in Si [12].

Instead, the plasma dispersion effect employs changes in free carrier concentrations to modulate the refractive index through absorption by free carriers [12]. This is described by the Drude-Lorenz equations below that relate the change in refractive index Δn and absorption $\Delta\alpha$ to carrier concentrations [12]:

$$\Delta\alpha = \frac{e^3\lambda_0^2}{4\pi^2c^3\varepsilon_0 n}\left(\frac{N_e}{\mu_e(m_{ce}^*)^2}+\frac{N_h}{\mu_h(m_{ch}^*)^2}\right) \tag{3.35}$$

$$\Delta n = \frac{-e^2\lambda_0^2}{8\pi^2c^2\varepsilon_0 n}\left(\frac{N_e}{m_{ce}^*}+\frac{N_h}{m_{ch}^*}\right) \tag{3.36}$$

Soref and Bennett used a Kramer-Kronig analysis to calculate the change of refractive index due to changes in carrier concentrations with experimental absorption and impurity-doping spectra of crystalline Si from the literature. From this they were able to relate the changes in refractive index and absorption coefficient in terms of electron and hole concentrations. These are given below for a wavelength of 1.55μm [90]:

$$\Delta n = \Delta n_e + \Delta n_h = -[8.8\times10^{-22}\times\Delta n_e + 8.5\times10^{-18}\times(\Delta n_h)^{0.8}] \tag{3.37}$$

$$\Delta\alpha = \Delta\alpha_e + \Delta\alpha_h = 8.5\times10^{-22}\times\Delta\alpha_e + 6.0\times10^{-18}\times\Delta\alpha_h \tag{3.38}$$

Thermo-optic effect

The thermo-optic effect [92, 93] generates a change in the optical properties of Si via an electrically induced temperature change. The thermo-optic coefficient for Si is given by [92],

$$\frac{dn}{dT} = 1.86\times10^{-4}/K \tag{3.39}$$

Typically, the induced temperature increase is facilitated by passing an electrical current through a resistive component that is in proximity to the WG. The generated heat will be directly proportional to the device geometry and resistivity. The resistivity could be engineered, for example, by using a metallic channel and choosing metals with a certain

resistivity or by using doped Si with an appropriate doping profile. The resulting device geometry and resistivity will depend on the thermal constraints of the system in terms of how much thermal power that can be delivered and how efficiently it can be dissipated. Thermo-optic Si modulators have been shown that demonstrate a π-phase shift with tens of mW of applied power [93]. However, whilst thermo-optic modulators are simple devices that can achieve a large phase shift, they suffer from low bandwidths. This is due to the thermal time constant of Si which is in the order of μs [93], which limits the operating speeds to the kHz range, unsuitable for high-speed data transmission.

3.3.2 Performance Metrics

Electro-Optic bandwidth

The modulation BW, or speed, relates to the signal speed of the data that is carried by the modulator [94]. This is an important metric for communications applications that have data transmission rates in the GHz range [94]. It is typically defined by the frequency at which the transmitted power drops by 3 dB, $f_{3\text{dB}}$ [94]. A high BW is required in order to maximise the data rates that a single channel can support [94]. For devices that are limited by the RC time constant this can be calculated by the following formula [95]:

$$f_{3\text{dB}} = \frac{1}{2\pi RC} \tag{3.40}$$

Extinction ratio

The ratio of intensities of the modulated optical signal when the transmission is maximised and minimised defines the ER [94]. This is reported in dB and given by the following equation [94]:

$$\text{ER} = 10\log\frac{I_{\text{max}}}{I_{\text{min}}} \tag{3.41}$$

Large ERs will minimise the error rate when reading the transmitted data stream as bit '0' and bit '1' can be easily distinguished [8]. When using multi-level modulation schemes the available ER will need to be large enough to contain the required number of amplitude levels, with adequate spacing to reduce the error rate [8].

Phase modulation efficiency

The efficiency of phase modulation is given as the product of the required voltage swing, V_π, and device length, L, to achieve a π phase shift [96]. $V_\pi L$ is typically given in V·cm where the most efficient phase modulators have the lowest $V_\pi L$. $V_\pi L$ determines the required device

length for the desired operating V, V_{bias}. Typically, we consider a driving $V < 1$ V so that the modulator can be directly driven by CMOS circuitry [97]. A low $V_\pi L$ reduces device area and therefore power consumption. $V_\pi L$ can be reduced by using an active material with a large induced Δn_{eff} or increasing the interaction between the active material and the optical mode.

Power consumption

For a modulator operating at GHz frequencies it is essential to reduce the power required per bit, and in the case for optical interconnect this needs to be less than ~ 10 fJ/bit in order to beat predicted future electrical interconnects [98]. For these high data rates the dominant source of power is the dynamic transient switching that can be reduced by a device with a low dynamic driving voltage [91]. Currently the lowest reported energy consumption per bit, E_{bit}, for a Ge-on-Si electro-absorption modulator is 50 fJ/bit [91]. By considering the energy stored in the electric field of a capacitor, E_{bit} is related to the device capacitance and driving voltage by [95]:

$$E_{\text{bit}} = \frac{CV_{\text{pp}}^2}{4} \tag{3.42}$$

Insertion loss

The insertion loss (IL) is defined as the additional optical loss resulting from inserting the device in the transmission line [12]. IL is reported in dB and given by [96],

$$\text{IL} = \alpha L \tag{3.43}$$

where α is the power attenuation coefficient, or optical losses per unit length, and L is the active device length [94]. IL should be reduced in order to reduce power consumption.

Crosstalk

Crosstalk occurs when power is unintentionally transferred between transmission channels [63]. This could be due to close proximity of channels where the electromagnetic fields overlap, or from imperfect components that leak power. This unwanted power transfer degrades the extinction ratio of the transmitted signal and results in a power penalty for the system. The power penalty is typically given in dB and is associated with the additional power required at the receiver to compensate for the crosstalk [63]. Therefore, to reduce the power consumption of the system it is desirable to minimise crosstalk for multi-channel

transmission systems. It is also important to consider the crosstalk that occurs due to the other components that are used in a transmitter. This includes the electrical driving circuits and any thermal crosstalk as a result of thermo-optic components used for IQ modulation or compensation.

Figure of Merit

Electro-refractive modulators can be compared by the loss-efficiency figure of merit, FOM_{ER}, expressed in VdB and given by [99]:

$$\text{FOM}_{\text{ER}} = V_\pi L \cdot \alpha \tag{3.44}$$

An efficient phase modulator, with a low $V_\pi L$, will have low optical losses and result in a low FOM_{ER}.

The efficiency of electro-absorption modulators can be compared with the ratio of ER and IL [100]:

$$\text{FOM}_{\text{EA}} = \frac{\text{ER}}{\text{IL}} \tag{3.45}$$

A larger value of FOM_{EA} represents a more efficient electro-absorption modulator that is capable of large ER but with low losses [100, 101].

3.3.3 Integrated Device Configurations

Electro-absorption

Modulators that use a change in optical losses of a material to transmit information are called electro-absorption modulators (EAM). The absorption coefficient of Si can be modulated by the Franz-Keldysh effect, however at 1.55 μm thas been shown to be weak [90], so has been combined with Ge [91, 102] that shows a stronger electro-absorption effect [103]. Modulators based on the Franz-Keldysh effect are attractive for photonic applications as they are intrinsically fast, on picosecond time scales [104], allowing for modulation speeds exceeding 100 GHz [91]. The first WG-integrated GeSi EAM on the SOI platform is shown in figure 3.13 [91], where they used epitaxially grown Ge-on-Si in a vertical p-i-n heterojunction operated under a reverse bias. The electro-optic response, shown in figure 3.13b shows how the applied V modulates the transmission by pushing the direct band edge to longer wavelengths [91]. The ER and IL, defined as the transmission with V = 0, are shown in figure 3.13c [91]. It can be seen that the IL increases for shorter wavelengths where absorption in Ge by direct transitions is dominant. At $\sim$ 1550 nm, the device has ER $\sim$ 8

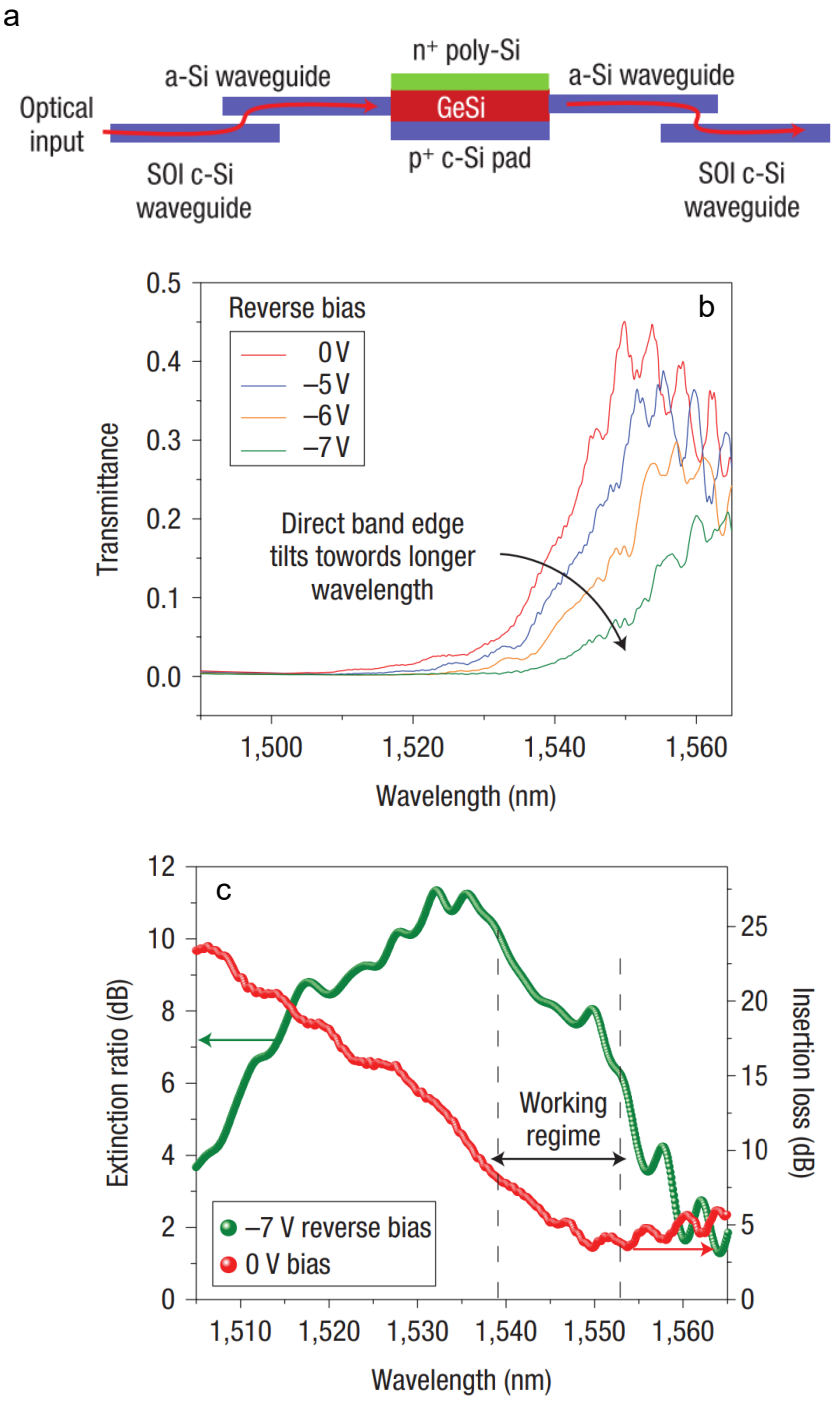

Fig. 3.13 (a) Device schematic of the first experimentally demonstrated WG-integrated GeSi EAM butt-coupled to Si WGs, (b) measured transmission spectra across different wavelengths at different reverse biases, (c) measured ER and IL as a function of wavelength, adapted from Ref. [91]

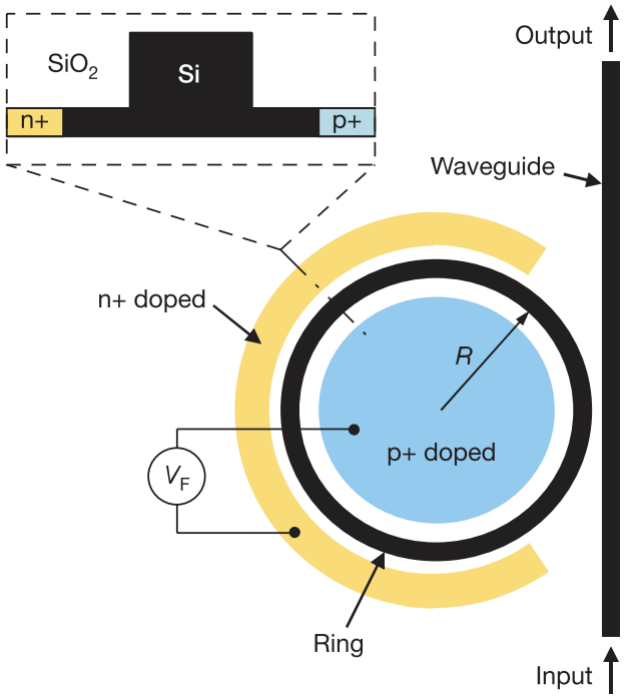

Fig. 3.14 Schematic of Si carrier injection modulator integrated on to a ring resonator, adapted from Ref. [87]

dB and IL $\sim$ 5 dB, leading to an $\text{FOM}_{\text{EA}} \sim 1.6$. They achieved a modulation bandwidth of 1.2 GHz with an active device area of 30 μm^2, but also demonstrated ultra-low energy consumption with only 50 fJ/bit due to a low dynamic driving voltage and low capacitance.

Electro-refractive

Modulators that induce a change in the refractive index of a material are called electro-refractive modulators (ERM), or phase modulators. ERMs work by changing the refractive index of a material to change the phase of a propagating mode according to equation 3.4. The transmitted signal will depend on the passive photonic component that is used. Typically an interferometric device, such as a RR or MZI, is used to translate Δn_{eff} into amplitude modulation of the transmitted signal. Early Si modulators based on the plasma dispersion effect used carrier injection to electrically manipulate carrier concentrations. These used a WG-integrated forward-biased p-i-n diode to injects carriers into the path of the optical mode propagating in the intrinsic region [94]. Confining the optical mode to the intrinsic region limits the losses incurred by absorption of the injected carriers [105]. High ER could be achieved because it involved the injection of majority carriers and a large overlap between the optical mode and the injected carrier profile [87, 106]. However, it suffered from BW limited

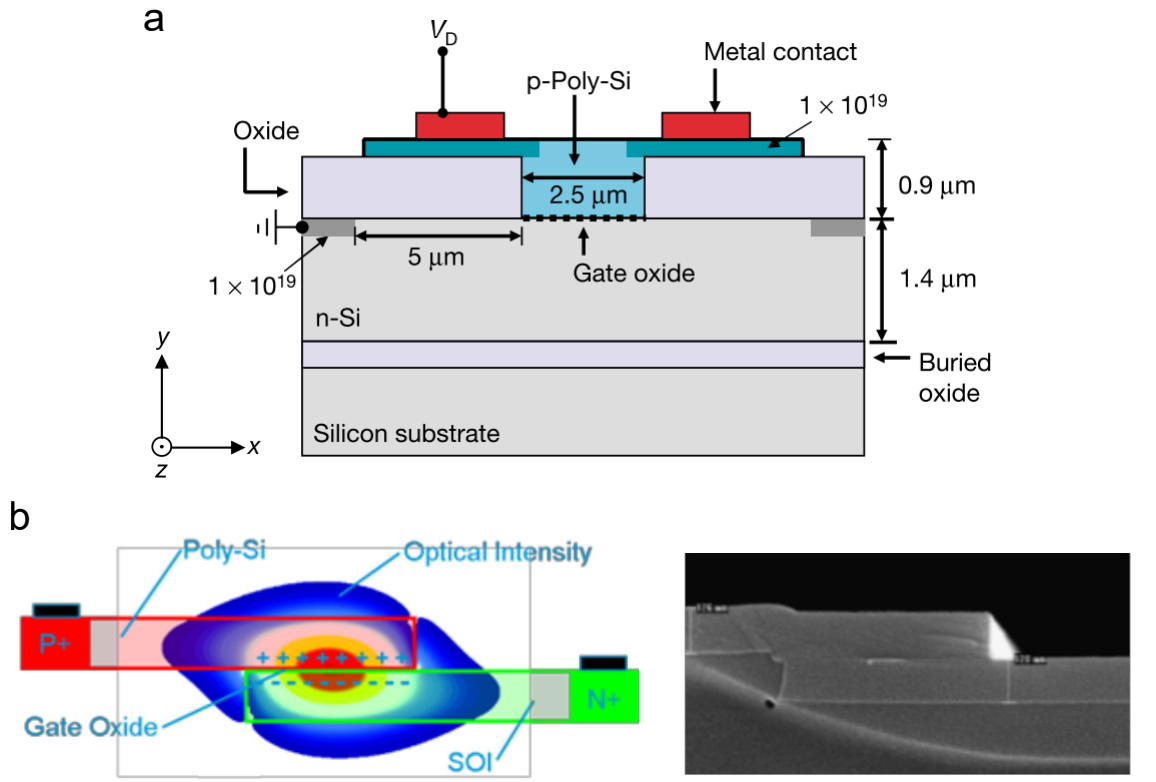

Fig. 3.15 (a) Device schematic of the first Si accumulation phase modulator, adapted from Ref. [107], (b) Device schematic and SEM image of a SISCAP phase modulator, adapted from Ref. [109].

to $<$ 1 GHz because it relied on the slower diffusion transport process and the minority carrier lifetime during carrier generation and recombination [107, 108]. Figure 3.14 shows the device schematic of a carrier injection device where an embedded p-i-n junction was used to modulate the transmission by changing n_{eff} of the RR in order shift λ_{res} [87]. This was the first device integrated on a RR that allowed for a significant reduction in device dimensions compared to MZI structures, with a device length of $\sim$ 14 μm compared to length in the order of mm's [105, 106, 108].

Modulator designs based on carrier accumulation, shown in figure 3.15, used a thin oxide barrier in the intrinsic region of a p-i-n diode to form a capacitor structure where charges can be accumulated in the path of the optical mode [107]. They demonstrated a significant performance improvement because the device was no longer limited by carrier diffusion, reaching data transmission rates of 1 Gb/s with a bandwidth $>$ 1 GHz and $V_\pi L \sim 8$ V·cm [107]. This concept was taken further with the Si-insulator-Si capacitor design, figure 3.15b, where an overlapping poly-Si layer that is separated from the SOI layer by a gate oxide forms a WG [109]. This boosted the modulation efficiency by increasing the overlap between the

accumulated carriers and the optical mode to $V_\pi L < 0.2$ V·cm [109]. They were able to demonstrate 28 Gb/s data transmission, but this was at the cost of increased optical losses ($\sim$ 65 dB/cm, $\text{FOM}_{\text{ER}} \sim 13$) due to the required doping to reduce the contact resistance of the Poly-Si layer [109].

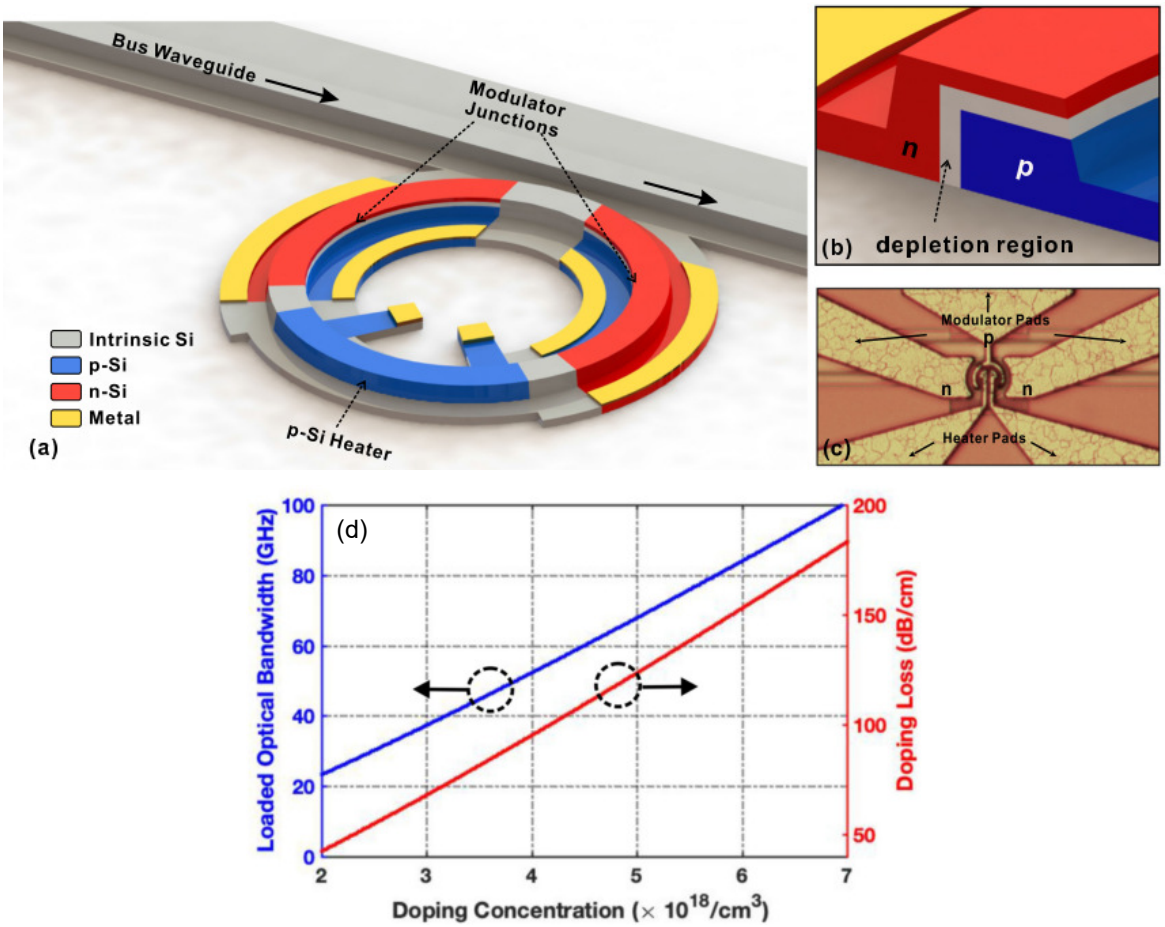

Fig. 3.16 (a) Schematic of a Si RRM using carrier depletion, (b) close-up of depletion region, (c) fabricated device with a RR with a radius of 10 μm, (d) calculated bandwidth and optical loss as a function of doping concentration, adapted from Ref. [110].

Carrier depletion uses a reverse-biased p-n junction to control carrier concentrations by the width of the depletion region [110–114]. As with carrier accumulation, this approach enables higher BWs because it relies on the faster drift process [94]. In this lateral design, figure 3.16, a rib WG was formed from an asymmetrical p-n junction [112]. A larger p-doped region was used to maximise the overlap with the optical mode because holes produced a greater Δn_{eff}, and to minimise the high losses caused by electrons in the n-doped region [90]. The Si depletion RRM shown in figure 3.16 has improved phase modulation efficiency by overlapping the n and p doped region, showing $V_\pi L \sim 0.52$ [110]. The device in figure 3.16

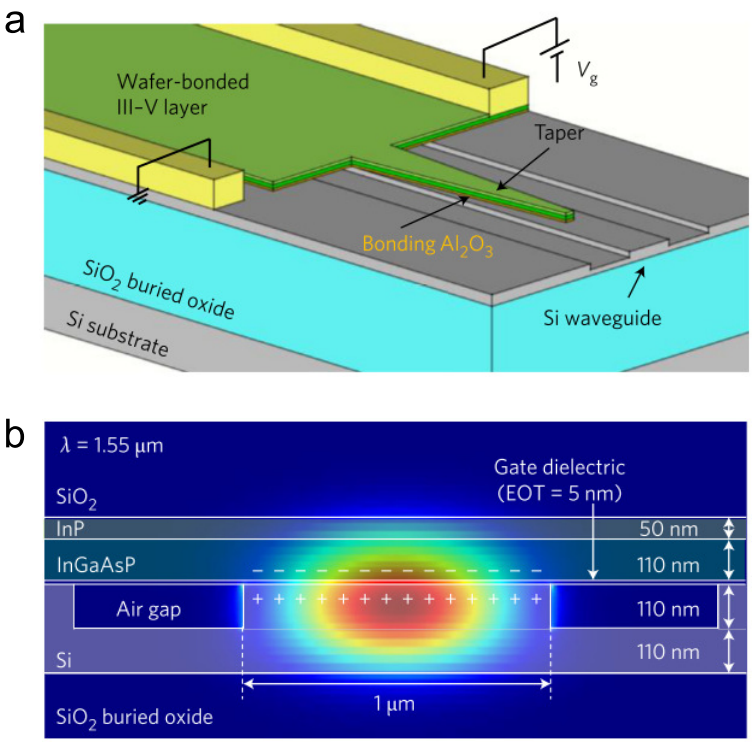

Fig. 3.17 (a) Device schematic of a III-V/Si hybrid MOS MZM, (b) mode field profile when operated in accumulation mode, adapted from Ref. [115]

supports data transmission rates up to 128 Gb/s (64 Gbaud PAM-4) [110]. The electrical BW was shown to be $>$ 100 GHz, but is limited by the BW supported by the RR ($\sim$ 50 GHz) [110]. Increasing the doping concentration can decrease $V_\pi L$ and increase the BW supported by the RR, but this is at the cost of increased IL [110]. Figure 3.16d shows the relationship between the calculated EO BW and associated optical losses as a function of doping concentration. In this case, the device has optical losses of $\sim$ 90 dB/cm, which leads to an $\text{FOM}_{\text{ER}} \sim$ 50 VdB. Si phase modulators will always be a trade-off between low $V_\pi L$ and high optical losses from the dopants of doped Si WGs [90]. Techniques, such as substrate removal, have reduced optical losses to $\sim$ 22 dB/cm [113], but at the cost of an increased $V_\pi L$ of $\sim$ 1.4 V·cm [113]. However, even with an increase in $V_\pi L$, this still results in a better $\text{FOM}_{\text{ER}} \sim$ 30.8 VdB. This shows that because $V_\pi L$ is already low, that the greatest reduction in FOM_{ER} can be achieved by focusing on reducing optical losses of Si WGs.

Hybrid approaches that incorporate III-V compounds [115–118] with doped Si WGs reduce $V_\pi L$ by utilising other effects, such as the band-filling effect, band gap shrinkage, and free-carrier absorption [119]. Figure 3.17 shows a III-V/Si metal-oxide-semiconductor (MOS) MZM that operates in accumulation mode [115]. The device demonstrated $V_\pi L \sim$

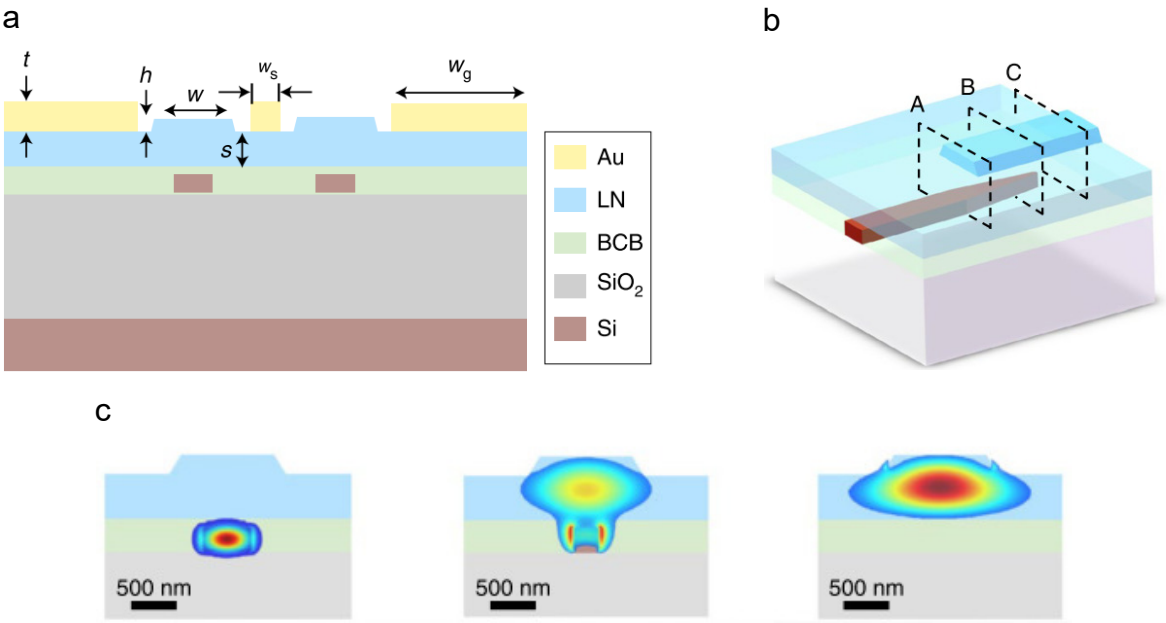

Fig. 3.18 Schematic of (a) a LN modulator cross-section, (b) coupling region between Si and LN WGs, (c) mode profiles at different positions in the coupling region, adapted from Ref. [120].

0.047 V·cm with IL $\sim$ 1 dB [115]. However, the bandwidth of the device is limited to $\sim$ 100 MHz because of the high contact resistance to the Si electrode in the MOS configuration [115]. More moderate values of $V_\pi L$ = 0.24 - 0.3 V·cm [116, 118] are obtained for III-V/Si MZMs operating in depletion mode with bandwidths up to $\sim$ 27 GHz [116]. III-V based MZMs are more efficient than Si based MZMs, enabling a lower $V_\pi L$, but at the cost of more complex fabrication with expensive III-V processing [14].

$LiNbO_3$ (LN) is the traditional material that uses the Pockel's effect for phase modulation [65]. Integrated phase modulators have been demonstrated on the thin-film LN-on-insulator (LNOI) platform [121, 122] which uses LN WGs with a refractive index contrast $\sim$ 0.67 [121] and propagation losses $\sim$ 3 dB/cm [121]. Thin-film LN modulators can also be integrated onto SOI wafers through wafer bonding techniques [120, 123]. Figure 3.18a shows a thin-film LN MZM that consists of a LNOI substrate bonded onto a SOI wafer [120]. Here, the optical mode is coupled from the Si WGs into the LN WGs via vertical adiabatic couplers, figure 3.18b and c, where Δn_{eff} can be induced by an applied V. Thin-film LN MZMs were reported with BW $>$ 100 GHz [122, 123] and $V_\pi L \sim$ 1.8 V·cm [121], resulting in an $\text{FOM}_{\text{ER}} \sim$ 5.4. Thin-film LN offers a high-bandwidth and low-loss modulation platform, however, the $V_\pi L$ means that cm long devices are needed to reduce V_π to CMOS compatible levels $<$ 1 V [97].

3.3.4 Modulation Schemes

Digital Modulation Schemes

Digital data, otherwise known as binary, consists of information being represented by two symbols, '0' and '1'. Digital data is encoded into the electrical domain by using line coding to generate a waveform with varying voltage or current [8]. These waveforms have two levels representing '0' and '1' bits of information. Figure 3.19a shows different line coding formats for representing binary data. Unipolar line code is shown in red, where '0' is represented by no signal, and '1' is represented by a pulse of amplitude A. Polar line code is shown in blue, where '0' is represented by a pulse of amplitude $-A$, and '1' is represented by a pulse of amplitude A. Bipolar line code is shown in yellow, where '0' is represented by no signal, and '1' is represented by a pulse of amplitude A or $-A$. In this case, the polarity of the amplitude changes for each consecutive '1' bit. Line codes can then be processed by a pulse shaper to adjust the waveform to comply to bandwidth requirements for the modulation scheme being used. Figure 3.19b shows the common pulse shapes used. For return-to-zero (RZ), shown in blue, the data signal will return to 0 after each '1' is transmitted. Whereas this will not be the case for non-return-to-zero (NRZ), shown in red, where the signal remains at 1 for each consecutive '1' bit. The fewer transitions for NRZ result in lower power consumption and a lower bandwidth as compared to RZ.

These waveforms are used to drive EO modulators and therefore convert the data stream from the electrical into the optical domain. The unmodulated optical carrier signal, $c(t)$, is described in terms of its amplitude A, angular frequency ω, and phase ϕ.

$$c(t) = A\cos(\omega t + \phi) \tag{3.46}$$

Data can be encoded into $c(t)$ by modulating either the amplitude, frequency, or phase. Amplitude-shift keying (ASK), or on-off keying (OOK), refers to modulating the amplitude of the optical carrier signal whilst keeping ω and ϕ constant. The amplitude of the modulated signal, $s(t)$, is given by $A_i(t) = m(t)$, where $1 \leq i \leq 2$ and $m(t)$ is a binary data stream. Therefore, the modulated output signal $s(t)$ becomes,

$$s(t) = A_i(t)\cos(\omega t + \phi). \tag{3.47}$$

$s(t)$ and $m(t)$ for ASK are shown in figure 3.21 where $m(t)$ is a unipolar NRZ signal. PAM is a special case of ASK where the amplitude of a pulsed optical carrier is modulated rather than that of a continuous wave. This results in $s(t)$ modulating between 0 and A for bit '0' and '1' respectively. Phase-shift keying (PSK) refers to modulating the phase of

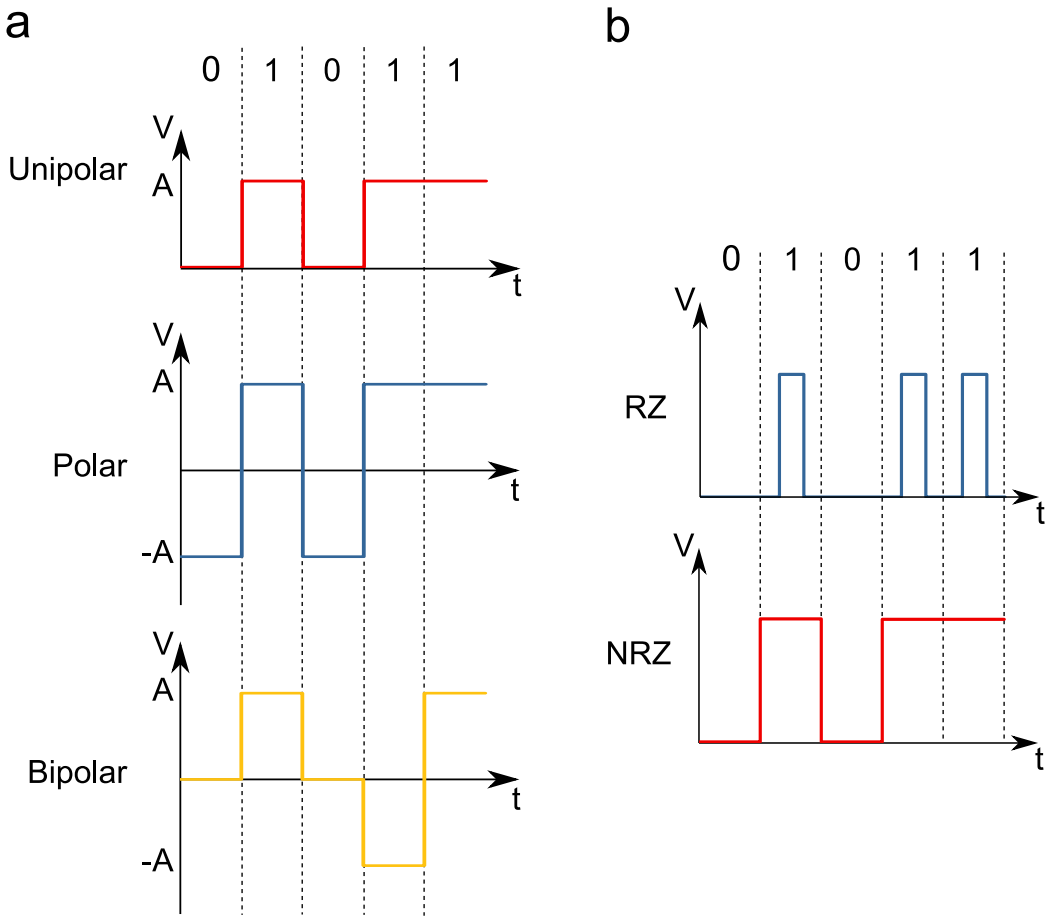

Fig. 3.19 (a) Line code formats for representing digital information in the electrical domain. (b) Return-to-zero (RZ) and non-return-to-zero (NRZ) pulse shapes

the optical carrier signal whilst keeping A and ω constant. In this case $\phi_i(t) = m(t)$, where $1 \leq i \leq 2$ and $m(t)$ is a binary data stream.

$$s(t) = A\cos(\omega t + \phi_i(t)) \tag{3.48}$$

Figure 3.21 shows $s(t)$ and $m(t)$ for PSK modulation, where $m(t)$ is a polar NRZ signal resulting in a π-phase difference between state '0' and '1'. One method to detect the phase of the PSK signal at the receiver is by comparing the phase of the current bit to the previous bit [8]. This is called differential phase-shift keying (DPSK), and involves modifying the data stream such that the resulting phase shift is relative to the previous bit and not the absolute phase of the optical carrier. Figure 3.20 shows how DPSK can be implemented with a delay circuit to delay $m(t)$ by the bit interval, T_b, and an XOR gate. $m(t)$ is generated by comparing the current bit of the NRZ data stream, $d(t)$, with the previous bit of $m(t)$ such that $s(t)$ only undergoes a phase shift when $m(t) \neq m(t - T_b)$. Therefore by inspecting $d(t)$ and $s(t)$, we

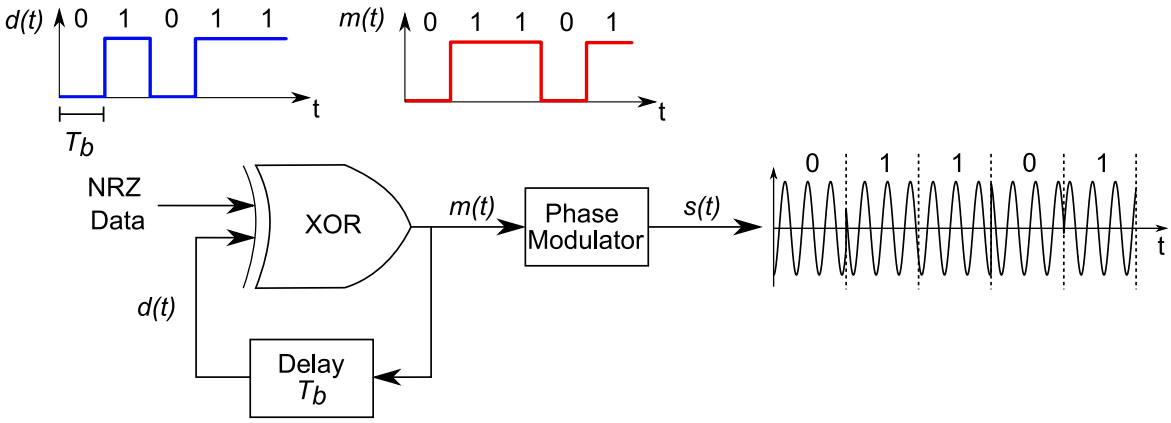

Fig. 3.20 Differential phase-shift keying (DPSK) using a differential precoder to generate the data stream $m(t)$ to drive the phase modulator.

see that a '0' has been transmitted when there is no change of phase, and a '1' has been transmitted when there is a change in phase.

Finally, frequency-shift keying (FSK) refers to modulating the frequency of the optical carrier signal whilst keeping A and ϕ constant. The frequency of the modulated signal is given by $\omega_i(t) = \omega_c + m(t)$, where ω_c is the carrier frequency, $1 \leq i \leq 2$ and $m(t)$ is a binary data stream.

$$s(t) = A\cos(\omega_i(t)t + \phi) \tag{3.49}$$

Figure 3.21 shows $s(t)$ and $m(t)$ for FSK, where $m(t)$ is a polar NRZ signal resulting in a difference in ω between state '0' and '1'.

Multi-Level Modulation Schemes

When moving from binary to multi-level modulation schemes information can now be represented by more that 2 symbols. The number of bits, B, that each symbol represents is given by [8]:

$$B = \log_2 M \tag{3.50}$$

where M is the total number of symbols. For digital modulation with only two levels available ($M = 2$), each state could only represent one bit of information, '0' and '1'. Now, if we had 4 levels ($M = 4$), each state can be made up of 2 bits, '00', '01', '10', and '11'. Hence, increasing the number of symbols will significantly increase the number of bits of information that can be transmitted per symbol. Each symbol is transmitted during a time interval, T_s, where the symbol rate, B_s, is given by [8]:

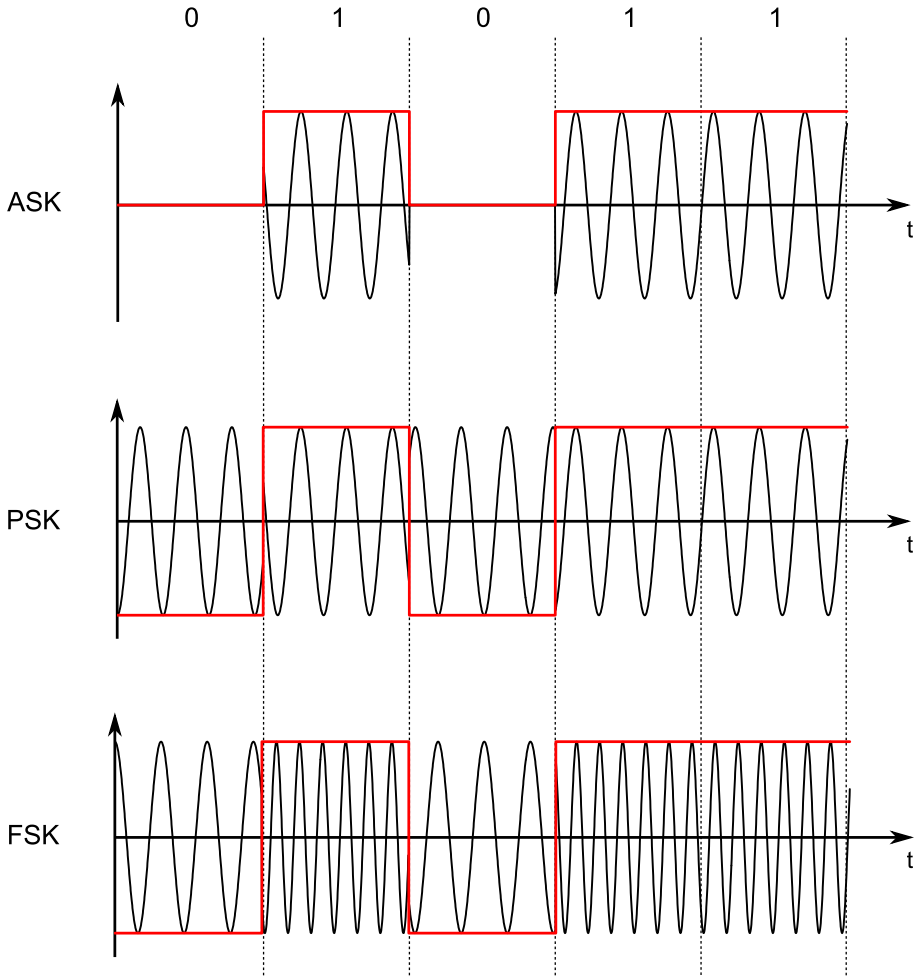

Fig. 3.21 Amplitude, phase, and frequency-shift keying of an optical carrier signal. Black curve shows modulated signal and red curve shows data signal.

$$B_s = \frac{1}{T_s} \tag{3.51}$$

Typically B_s is expressed in units of baud, which is equivalent to symbols/s. Therefore, the total number of bits that is transmitted per second is given by [8]:

$$B = B_s \log_2 M \tag{3.52}$$

4-level ASK and PSK is shown in figure 3.22 where 4 states are represented by a unique amplitude or phase. As before, 4-ASK requires that the phase and frequency remain constant for each symbol, and 4-PSK requires that the amplitude and frequency remain constant. ASK and PSK can be combined such that each symbol represents a unique combination of

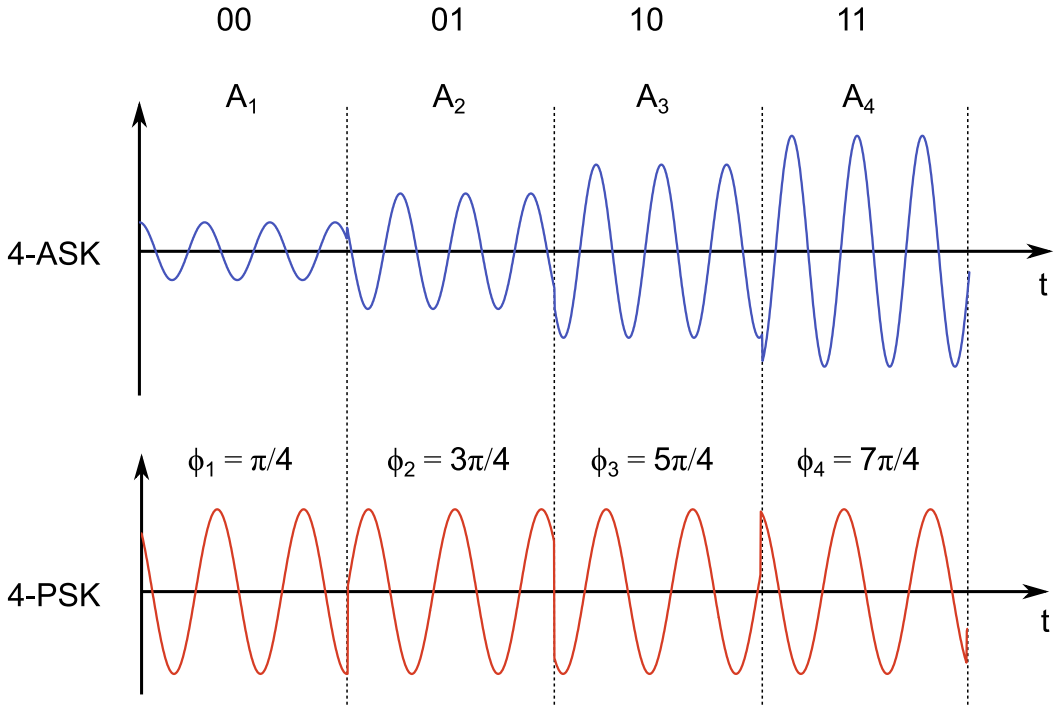

Fig. 3.22 (a) 4-level amplitude shift keying, (b) 4-level phase shift keying.

amplitude and phase. This is called quadrature amplitude modulation (QAM) or amplitude and phase-shift keying (APSK). In this case the transmitted signal is expressed as,

$$s(t) = A_i(t)\cos[\omega t + \phi_i(t)], \quad i = 1,2,...,M \tag{3.53}$$

Using $\cos(A+B) = \cos A \cos B - \sin A \sin B$, $s(t)$ becomes,

$$s(t) = m_I(t)\cos(\omega t) + m_Q(t)\sin(\omega t) \tag{3.54}$$

Where,

$$\begin{aligned} m_I(t) &= A_i(t)\cos[\phi_i(t)] \\ m_Q(t) &= -A_i(t)\sin[\phi_i(t)] \end{aligned} \tag{3.55}$$

$s(t)$ has now been expressed as the sum of an in-phase, I, and quadrature, Q, component which are modulated independently according to $m_I(t)$ and $m_Q(t)$. Symbols can be illustrated on the complex plane, which is called a constellation diagram. Typically the in-phase component is associated with the real axis and Q is associated with the imaginary axis. Figure 3.23 shows the constellation diagrams for different multi-level modulation schemes.

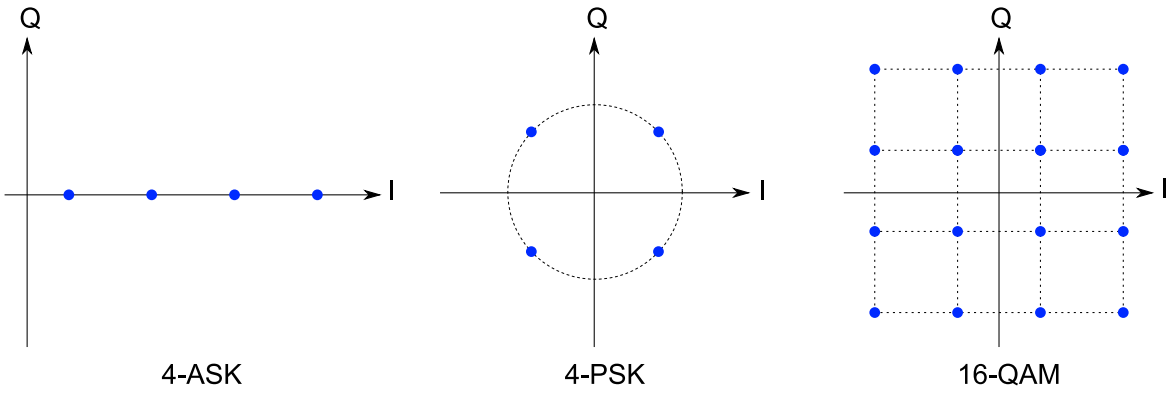

Fig. 3.23 Constellation diagrams for (a) 4 level amplitude-shift keying, (b) 4 level phase-shift keying, (c) 16-level quadrature-amplitude modulation schemes.

It can be seen that the Q component is not accessed for 4-ASK and the 4 amplitude levels are represented in the positive region of I. Each symbol for 4-PSK on the other hand has an I and Q component. As the amplitude remains constant, all symbols reside on a circle. The rectangular constellation diagram for 16-QAM shows the simultaneous amplitude and phase modulation for each symbol, which are no longer constrained to have a constant phase or amplitude as in ASK and PSK. The separation of symbols in the $I-Q$ plane will influence the error rate at the receiver. If the symbols are too close together, then symbols could be incorrectly detected. Figure 3.24 shows the implementation of an IQ modulator that is used to generate a 16-QAM signal [8]. The optical carrier signal is split by a 3 dB coupler into an I and Q branch which are $\pi/2$ out of phase. In this case a 4-ASK signal is used to drive two nested MZM such that they generate a 16-QAM signal.

3.3.5 Challenges

The ideal operating point for phase modulation is when there is no change in optical losses, otherwise known as pure phase modulation [8]. This is especially the case for complex modulation formats where intersymbol interference will cause errors at the receiver [8]. To reduce intersymbol interference, the symbol noise should be minimised and the symbols should be evenly spaced in the in-plane and quadrature axes [8]. Thus, any unwanted amplitude modulation from changing optical losses will increase symbol noise, and any non-linear phase modulation will result in irregular symbol spacing [8]. Pure phase modulation is difficult to achieve with Si modulators based on the plasma dispersion effect because, due to the Kramers-Kronig relations [23], any change in carrier concentration results in changes in both absorption and phase. Even if this were to be achieved, these devices would rely on doped Si WGs, requiring an increased optical power to overcome the additional optical

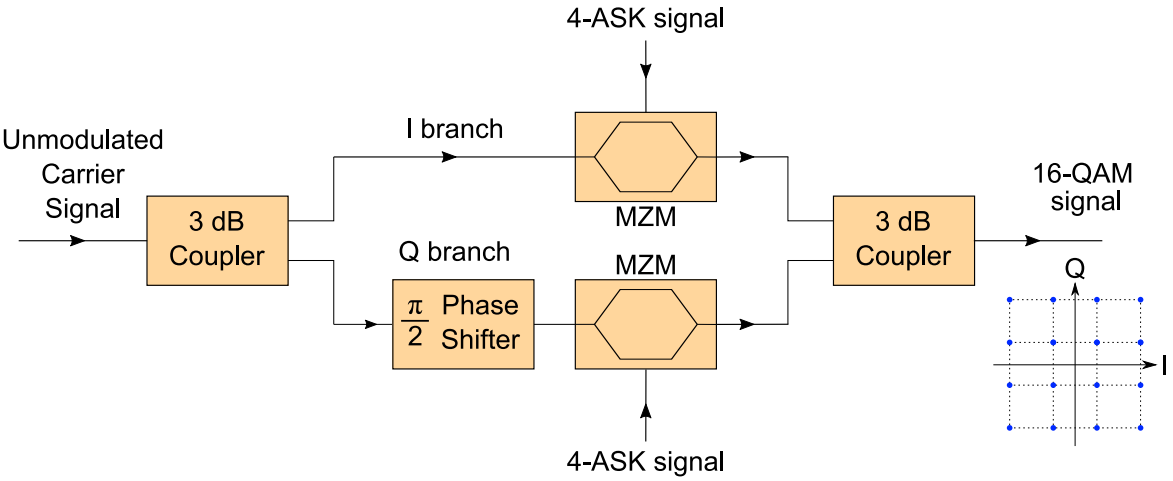

Fig. 3.24 Generation of a 16-QAM signal with an IQ modulator

losses introduced by dopants [90], when compared to undoped WGs. Thus, other materials, which do not rely on the plasma dispersion effect are required.

3.4 Receivers

3.4.1 Photodetection Mechanisms

PDs convert an optical signal into an electrical signal by absorbing photons and generating electron-hole pairs by exciting electrons from the valence band into the conduction band of a semiconductor [23]. These charge carrier pairs, or excitons, can then be separated by applying an electric field to produce a photocurrent, I_{ph} or photovoltage V_{ph} [23], figure 3.25. The energy of the photon depends on the frequency, f, and is given by $E = hf$ [23], and the energy required for the photon to be absorbed depends on the electronic structure of the material. For a semiconductor this energy needs to be greater than the band gap, E_{g}, which is defined as the energy difference between the bottom of the conduction band and the top of the valence band [23]. Two types of transition can occur that are dependent on the position in k-space of the initial and the excited states. When the initial and excited states are at the same points in k-space, a direct transition can occur if the $E \leq E_{\text{g}}$ [23]. However, if these points in k-space are not the same, then it is called an indirect transition that must be facilitated by a phonon in order to conserve energy and momenta [23]. Indirect transitions thus require the incoming photon to have a larger energy than that required for direct transitions [23]. Direct band gap semiconductors are defined as having the lowest point of the conduction band at the same point in k-space as the top of the valence band, and indirect band gap semiconductors are defined as having the lowest point of the conduction band at a different

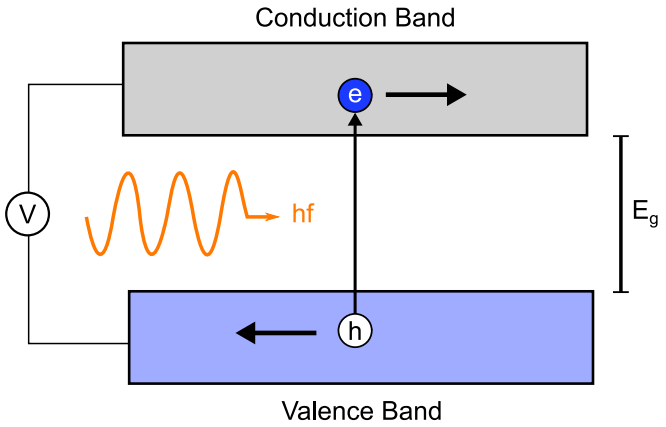

Fig. 3.25 Schematic showing a photon with energy $E = hf$ being absorbed in a semiconductor with a band gap, E_g, where $E > E_g$. The resulting electron-hole pair is then separated by an applied voltage.

point in k-space [23]. Si and Ge are examples of indirect band gap semiconductors with E_g = 1.11 eV and E_g = 0.66 eV at 300 K respectively [23]. Therefore, the E_g of the semiconductor used defines the spectral response of the PD by defining the cut-off frequency for a photon to be absorbed [8]. As well as transitions directly from the valence band to the conduction band it is also possible for photons with $E < E_g$ to be absorbed. In this case, impurities have been introduced to the semiconductor which create new energy levels within E_g allowing for sub band gap absorption [23].

3.4.2 Performance Metrics

Quantum efficiency

Quantum efficiency, η, describes the probability that an incident photon generates an exciton that contributes to the generated photocurrent, I_{ph} [65]. η can be between 0 and 1, where 1 is the most efficient PD [65]. The external quantum efficiency, η_{ext}, is defined as the ratio between the number of excitons contributing to I_{ph} and the number of incident photons [124]:

$$\eta_{ext} = \frac{I_{ph}/e}{P_{in}/hf} \tag{3.56}$$

The number of incident photons is given by the ratio of the input power, P_{in}, to the photon energy. Whereas the internal quantum efficiency η_{int} considers the number of excitons contributing to I_{ph} in comparison with the number of absorbed photons [124]:

$$\eta_{int} = \frac{I_{ph}/e}{P_{abs}/hf} \tag{3.57}$$

The number of absorbed photons is given by the ratio of the absorbed power, P_{abs}, and the photon energy. η_{ext} will be limited by the size of the photoactive area, surface reflections, and transmission through the semiconductor without abosrption [65]. However, η_{int} will be limited by internal processes that reduce the amount of photogenerated carriers from being collected, such as recombination or reflections from interfaces [65]. Therefore η can be increased by using a photodetection mechanism that increases the amount of absorbed photons and reduces recombination and internal loss.

Responsivity

The responsivity is the proportionality factor between P_{in} and the extracted photogenerated output which can either be in terms of I_{ph} or V_{ph} [124]. For a generated I_{ph} the responsivity, R_{I}, is given in A/W by [124]:

$$R_{\text{I}} = \frac{I_{\text{ph}}}{P_{\text{in}}}[\text{A/W}] \tag{3.58}$$

Current state-of-the-art Ge PDs can reach 1.19 A/W [125]. The photoinduced voltage responsivity, R_V, is given in units of V/W by [124]:

$$R_{\text{V}} = \frac{V_{\text{ph}}}{P_{\text{in}}}[\text{V/W}] \tag{3.59}$$

A high responsivity is desirable because it reduces the power consumption of the PD and results in a stronger photosignal that will be more tolerant to noise.

Noise equivalent power

Noise from the PD is defined as the the time varying fluctuations of the generated photocurrent around its average value [65]. The dominant sources of noise in PDs are shot or quantum noise from the statistical nature of generation and collection of photogenerated carriers, and dark and leakage current noise that arises from charge carrier generation when the device is not illuminated. Shot noise is associated with the uncertainty of the incident photon flux which is a quantum effect resulting from the discrete nature of photons and electrons [8]. This causes random fluctuations in the incident photon flux that obeys Poisson statistics, and leads to an uncertainty in the number of available photons to be detected [65]. Thermal or Johnson noise is due to the random motion of mobile carriers within an electrical resistive material that results in a random electrical current even with no incident power [65]. Johnson noise increases for increased temperatures and reduces for increased electrical resistance of the resistive material [65]. Therefore the noise determines the minimum-detectable optical power and the sensitivity of the detector [65]. In order to detect weak signals, amplifiers can

be used with PDs to maintain a given signal-to-noise (SNR) ratio.

Noise equivalent power (NEP) characterises the sensitivity of the device and is defined as the signal power that gives SNR = 1 and given in W $Hz^{-0.5}$[124]. This defines the smallest detectable signal and is used to define the detectivity D of the PD, $D = 1/\text{NEP}$ [124]. This can be normalised by the area of the photoactive region, A, and the frequency bandwidth, BW, to define the specific detectivity, D^*, that is the figure of merit used for comparing PDs [124]:

$$D^* = \frac{\sqrt{A \cdot BW}}{\text{NEP}} [\text{Jones}] \tag{3.60}$$

Highly sensitive detectors will have high values of D^* which are typically given in units of Jones which is equivalent to 1 cm $Hz^{0.5}W^{-1}$ [124].

Dark current

Dark current, I_d, is defined as the photocurrent generated by a PD when there is no illumination. In this case, I_d consists of electron-hole pairs that are generated without the absorption of incident photons. This encompasses all sources of leakage current that do not rely on incident illumination. For example, this can be facilitated by defects or result from thermal effects when there is not a sufficient band gap to limit the generation of electron-hole pairs. I_d is detrimental to PD performance as it contributes to the noise and should be minimised for increased signal-to-noise ratio.

Response time

The response time of the PD is limited by the transit time of the carriers, and the RC time constant of the PD and its circuitry [77]. Carrier transport within a semiconductor consists of a diffusion component due to the charge-density gradient, and a drift component that is due to an electric field [23]. Diffusion is a slower process than drift, which is limited by the recombination lifetime of the charge carriers, so should be minimised [23]. The drift current is determined by the drift velocity of the carriers, v_d, that is proportional to their mobility μ [23]:

$$v_\text{d} = \mu E \tag{3.61}$$

In Si and Ge, v_d is in the order of $\sim 10^7$ cm/s, which results in picosecond transit times for a depletion region 1 μm wide [77].

3.4.3 Integrated Device Configurations

Si defect photodetectors

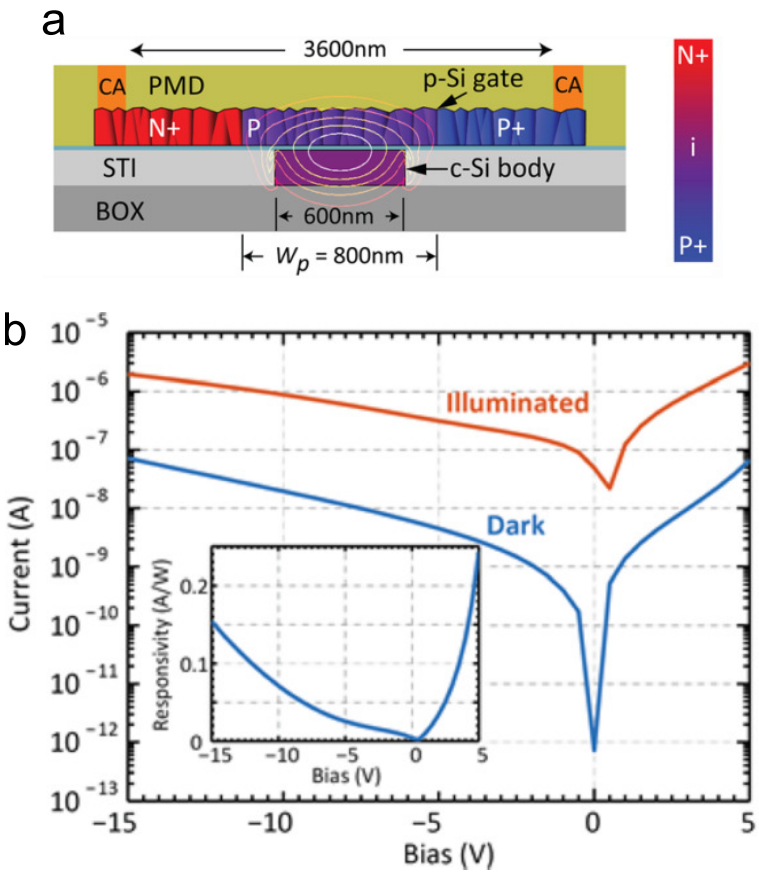

Fig. 3.26 (a) Schematic of Si defect PD based on a lateral p-n junction in poly-Si where infrared absorption is facilitated by dangling bonds in poly-Si, (b) I-V curve and responsivity as a function of applied V, adapted from Ref. [126]

Whilst the E_g = 1.1 eV of Si makes it ideal for low-loss WGs at the wavelengths commonly used for telecommunication (λ = 1.3 - 1.55 μm), it makes Si-based PDs a challenge. Sub band gap absorption can be facilitated in Si WGs by introducing lattice defects that create mid band gap energy states [127]. Defects can be produced with CMOS compatible ion implantation into the Si WG [127, 128] where responsivities reached 23 mA/W [128]. As well as creating defects, mid band gap states can be naturally created by the dangling bonds in polysilicon (poly-Si) that are occupied by dopant atom carriers [129]. Figure 3.26 shows the schematic and I-V curve for a Si defect PD where they use defects in poly-Si to facilitate sub band gap absorption [126]. They presented an integrated lateral p-n junction PD across a poly-Si ridge WG that had induced losses of 6 dB/cm leading to a responsivity of 0.15 A/W.

Si Schottky photodetectors

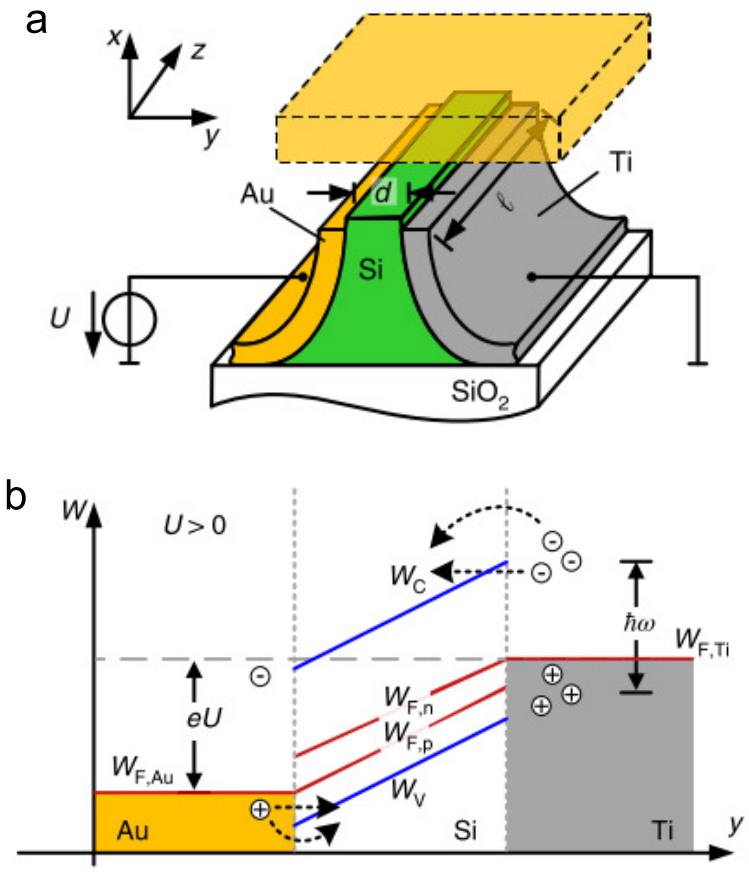

Fig. 3.27 (a) Device schematic of Au-Si-Ti plasmonic PD with an applied voltage, U, across the Au and Ti electrodes. (b) Energy band diagram for $U > 0$ of the Au-Si-Ti junction. Fermi levels are depicted by W_F and the edge of conduction band and valence band in Si are shown by W_C and W_V, adapted from Ref. [130].

Another way to enable sub band gap absorption in Si is to use the internal photoemission effect [131] that occurs at the metal-semiconductor junction. A Schottky potential barrier [23] is formed at the metal-Si interface that is less than E_g of Si, resulting in photoexcited carriers being transferred from the metal to Si for photons with $E < E_g$. The performance of these devices is limited by their low quantum efficiency ($\sim 1\%$) and low carrier injection into Si due to reflections caused by momentum mismatch between the carriers in the metal and the semiconductor [132]. However, the efficiency can be improved by concentrating light at the metal-Si interface to excite surface plasmon polaritons (SPP) that cause increased photoemission when they decay [133]. Figure 3.27 shows a device schematic and band diagram of a plasmonic Si detector where the thin Si WG ($\sim$ 100 nm) acts as a potential barrier between the Au and Ti electrodes [130]. The metal-semiconductor-metal structure

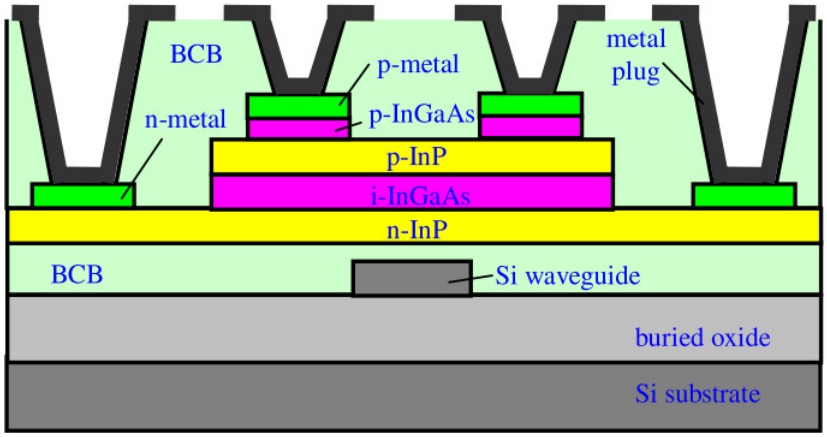

Fig. 3.28 Schematic of InGaAs PD integrated on a Si WG, adapted from Ref. [138].

guides SPPs which are absorbed at the metal-Si interface where they generate hot carriers [134]. As Ti has a larger imaginary component of the complex permittivity in comparison Au, the majority of SPP absorption occurs at the Ti-Si interface [134]. The authors note that the device does not rely on Au as the plasmonic material and so can be replaced with a more CMOS friendly material [135]. An applied voltage, U, across the Au and Ti electrodes reduces the potential barrier and thus increases the emission probability across the barrier by thermionic emission or tunnelling [134]. For low applied bias, I_d can be suppressed by using asymmetric metals with different Schottky barriers because it forms a built-in potential across Si [136, 137]. The device demonstrated $R_I = 0.12$ A/W at 1.55 μm and data reception of a 40 Gb/s data stream [134]. R_I can be increased by increasing the metal-Si interface by completely embedding a plasmonic WG within Si, with simulated values reaching 0.5 A/W at 1.55 μm [137]

Hybrid integration of III-V compound semiconductors

InGaAs is a direct band gap III-V compound semiconductor that is used as the active absorption material [138–140] because it has a larger absorption coefficient in the near-infrared than Si (E_g = 0.75 eV at room temperature) [141]. Due to the 8-10% lattice mismatch between Si and InGaAs [140], high-quality epitaxial growth is difficult to achieve which causes a degradation of the optical properties of InGaAs [14, 140]. Instead, separate III-V dies can be bonded to the SOI wafer [142], after which devices can be fabricated [138]. Figure 3.28 shows the schematic of an InP-InGaAs-InP p-i-n junction PD that has been die-to-wafer bonded to an SOI wafer with a benzocyclobutene (BCB) bonding layer [138]. Evanescent coupling is used to couple light from the Si WG to the InGaAs PD, where photogenerated excitons can be split by the built-in electric field in the depletion region of

the p-i-n junction [23]. This device achieved R_I = 1.1 A/W at 1.55 μm with a dark current of 10 pA [138].

Ge-on-Si photodetectors

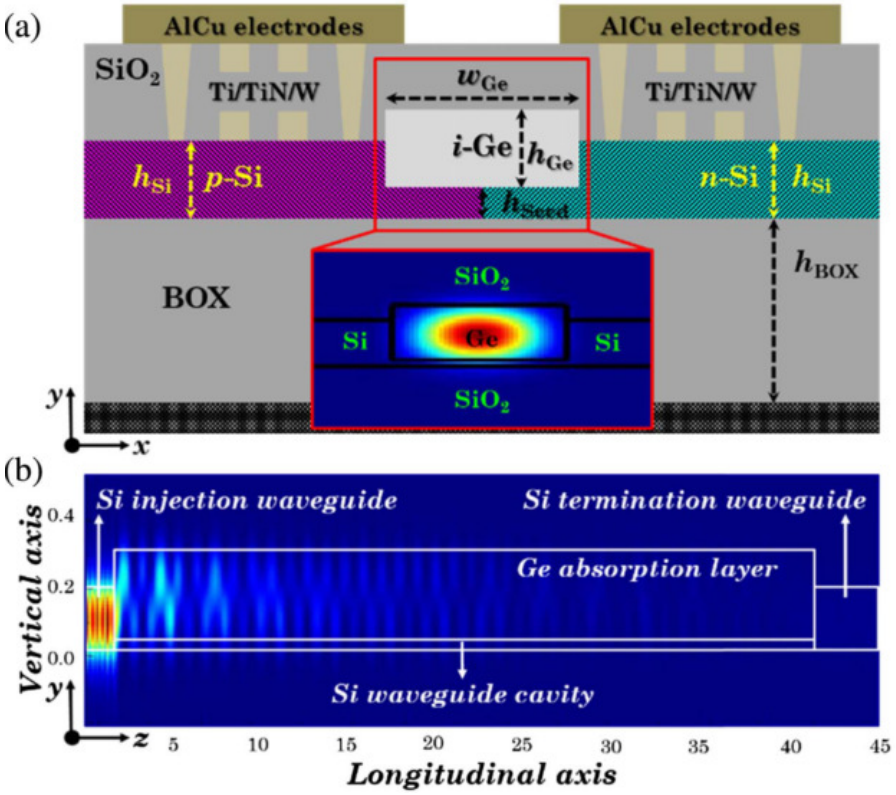

Fig. 3.29 (a) Schematic of butt-coupled Si-Ge-Si p-i-n PD, and (b) simulated optical intensity distribution in the 1 μm wide and 40 μm long Ge absorption layer, adapted from Ref. [125].

Ge is an indirect band gap semiconductor with E_g = 0.66 at 300 K [23] that is already used in the front-end-of-line CMOS processing [143]. The combination of a smaller E_g than Si, and therefore greater absorption at telecom wavelengths, and its CMOS compatibility make it desirable to use for integrated PDs. In spite of the 4% lattice mismatch between Ge and Si [144], high-quality and selective epitaxial growth of Ge-on-Si has enabled the monolithic integration of Ge PDs and Si WGs [143]. The schematic and electric field profiles of a 40 μm Ge PD are shown in figure 3.29 where a lateral p-i-n junction is formed between the p-Si and n-Si regions [125]. The Ge absorption layer was made by first etching the doped Si regions to leave a $\sim$ 60 nm Si seed layer and then selectively growing Ge by reduced pressure CVD [125]. The electric field profile, Figure 3.29b shows how the light is injected into the Ge absorption layer by butt coupling from the Si WG, which is then fully absorbed

after 40 μm propagation. They showed that I_d increases with increasing active area, where I_d reaches 100 nA for a 40 μm^2 device. However, I_d was also shown to increase with increasing reverse bias, where I_d rose to 150 nA for a -4 V bias. R_I has also been shown to increase with increasing device length, with a maximum value of 1.19 A/W. The bandwidth was shown to increase for higher reverse biases because the increased electric field that minimised diffusion carrier transport. A bandwidth of 30 GHz was shown for -4 V reverse bias, and data transmission up to 40 Gb/s was successfully detected. With R_I matching, and even exceeding, that of InGaAs based PDs the challenge for Ge PDs will be minimising I_d whilst maintaining the bandwidth required for high-speed applications.

3.4.4 Coherent Detection

The photocurrent generated from PDs is proportional to the intensity of the received signal and are therefore naturally suited to direct detection schemes where information is carried in the intensity of the optical carrier [145]. However, this means that the phase information will be lost for complex modulation formats that carry information in the combined intensity and phase of the optical carrier [145]. Instead, coherent detection systems can be used which are able to detect the complex optical field of the received signal [145]. Coherent systems combine the received optical signal with an optical local oscillator (LO). The combined signal enables $I_{ph}(t)$ to be linearly propotional to the received optical field, and thus enabling the phase information to be recovered. Coherent detection has the added bonus of downshifing the received optical signal at an optical carrier frequency so that electrical signal processing can be used to compensate for dispersion experienced during propagation [145]. Coherent systems are also more sensitive than direct detection systems because the LO acts as amplifier for the weaker received optical signal.

The received optical signal, $E_r(t)$, and the LO optical signal, $E_{LO}(t)$, are given by,

$$\begin{aligned} E_r(t) &= A_r s(t) \exp[-j(\omega_c t + \phi_c(t))] \\ E_{LO}(t) &= A_{LO} \exp[-j(\omega_{LO} t + \phi_{LO}(t))] \end{aligned} \tag{3.62}$$

where $s(t) = |s(t)| \exp(-j\phi_s(t))$ is the complex field envelope containing the transmitted signal information, A is the field amplitude, ω is the angular frequency of the carrier and LO, and ϕ is the phase of the carrier and the LO. $E_r(t)$ is combined with $E_{LO}(t)$ in a 2×2 coupler with the transfer matrix,

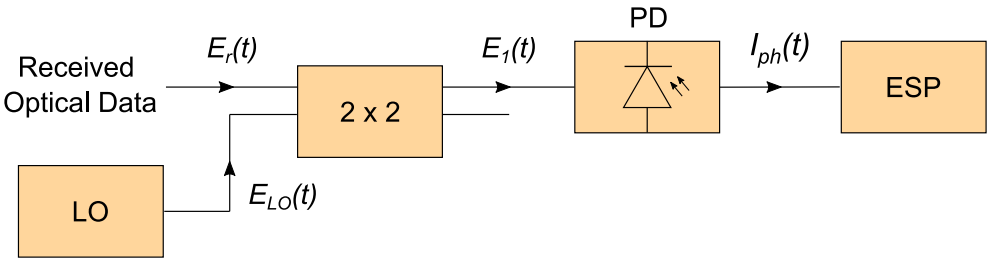

Fig. 3.30 Schematic of a coherent receiver.

$$\begin{pmatrix} E_1^{\text{out}} \\ 0 \end{pmatrix} = \begin{pmatrix} t & -j\kappa \\ -j\kappa & t \end{pmatrix} \begin{pmatrix} E_{\text{r}}(t) \\ E_{\text{LO}}(t) \end{pmatrix} \tag{3.63}$$

The combined electric field that is incident on the PD is given by,

$$E_1^{\text{out}} = tE_{\text{r}}(t) - j\kappa E_{\text{LO}}(t) \tag{3.64}$$

The photocurrent from the PD, $I_{\text{ph}}(t)$ is proportional to the absolute square of the incident optical field, E_1^{out}, and the responsivity R_{I}. Using $|x|^2 = xx^*$ and $\text{Re}[x] = \frac{x+x^*}{2}$ it can be shown that $I_{\text{ph}}(t)$ is given by,

$$I_{\text{ph}}(t) = R_{\text{I}}\left(t^2|A_{\text{r}}s(t)|^2 + \kappa^2|A_{\text{LO}}|^2 + 2t\kappa A_{\text{r}}A_{\text{LO}}\text{Re}\left[s(t)\exp(-j(\omega_{\text{IF}}(t) + \Delta\phi))\right]\right) \tag{3.65}$$

where ω_{IF} is the intermediate frequency defined as $\omega_{\text{IF}} = \omega_{\text{c}} - \omega_{\text{LO}}$. The first two terms are the direct detection terms of the received signal and the LO, and the last term is the coherent term which is the combination of the received signal and the LO [145]. Importantly, the coherent term is linearly proportional to the received signal and therefore preserves the phase information.

Balanced Coherent Detection

The direct detection terms are undesirable because they can interfere with the coherent term and introduce cross-talk which degrades $I_{\text{ph}}(t)$. These terms can be removed by using a balanced coherent system, pictured in figure 3.31. Here, two PDs are connected in series such that their photocurrents cancel each other out [65]. Here, the combined received optical signal and LO is passed to another PD that is connected such that the photocurrent from each PD is of opposite polarity [145].

The output electric fields for the directional couplers are given by,

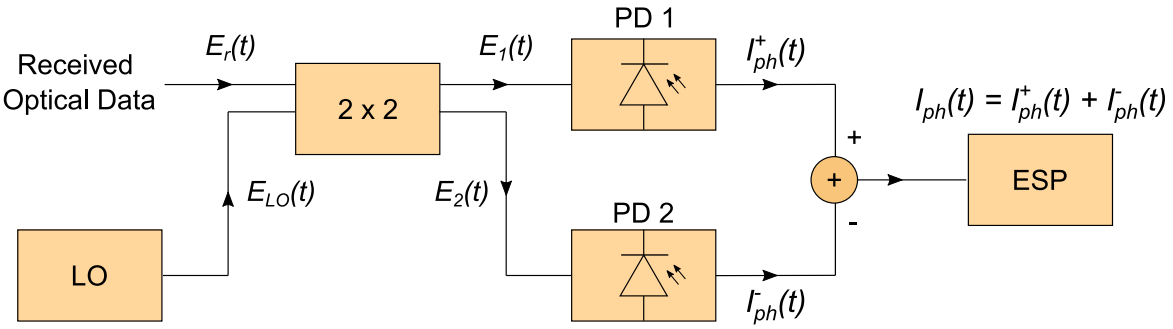

Fig. 3.31 Schematic of a balanced coherent receiver

$$\begin{pmatrix} E_1(t) \\ E_2(t) \end{pmatrix} = \begin{pmatrix} t & -j\kappa \\ -j\kappa & t \end{pmatrix} \begin{pmatrix} E_{\mathrm{r}}(t) \\ E_{\mathrm{LO}}(t) \end{pmatrix} \tag{3.66}$$

Using $\mathrm{Im}[x] = \frac{x-x^*}{2j}$ it can be shown that $I_{\mathrm{ph}}(t)$ is given by,

$$\begin{aligned} I^+_{\mathrm{ph}}(t) &= R_{\mathrm{I}}\left(t^2|A_{\mathrm{r}}s(t)|^2 + \kappa^2|A_{\mathrm{LO}}|^2 - 2t\kappa A_{\mathrm{r}}A_{\mathrm{LO}}\mathrm{Im}\left[s(t)\exp(-j(\omega_{\mathrm{IF}}(t)+\Delta\phi))\right]\right) \\ I^-_{\mathrm{ph}}(t) &= R_{\mathrm{I}}\left(\kappa^2|A_{\mathrm{r}}s(t)|^2 + t^2|A_{\mathrm{LO}}|^2 + 2t\kappa A_{\mathrm{r}}A_{\mathrm{LO}}\mathrm{Im}\left[s(t)\exp(-j(\omega_{\mathrm{IF}}(t)+\Delta\phi))\right]\right) \end{aligned} \tag{3.67}$$

Assuming 50:50 field splitting at the 2×2 coupler ($t = \frac{1}{\sqrt{2}}$, $t = \kappa$) the addition of $I^+_{\mathrm{ph}}(t)$ and $I^-_{\mathrm{ph}}(t)$ results in,

$$I_{\mathrm{ph}}(t) = -2R_{\mathrm{I}}A_{\mathrm{r}}A_{\mathrm{LO}}\mathrm{Im}\left[s(t)\exp(-j(\omega_{\mathrm{IF}}(t)+\Delta\phi))\right] \tag{3.68}$$

IQ Coherent Detection

For complex modulation formats, where $s(t)$ is complex, an IQ coherent receiver is required to reconstruct the imaginary component of $s(t)$ [145]. A balanced IQ coherent receiver is shown in figure 3.32 with one branch for the I component and another branch for the Q component. The received optical signal and LO are split by 3 dB power splitters and the LO signal goes through a $\pi/2$ phase shift for the Q branch. The output electric fields for the two directional couplers are given by,

$$\begin{pmatrix} E_1(t) \\ E_2(t) \\ E_3(t) \\ E_4(t) \end{pmatrix} = \frac{1}{\sqrt{2}} \begin{pmatrix} t & -j\kappa \\ -j\kappa & t \\ t & \kappa \\ -j\kappa & jt \end{pmatrix} \begin{pmatrix} E_{\mathrm{r}}(t) \\ E_{\mathrm{LO}}(t) \end{pmatrix} \tag{3.69}$$

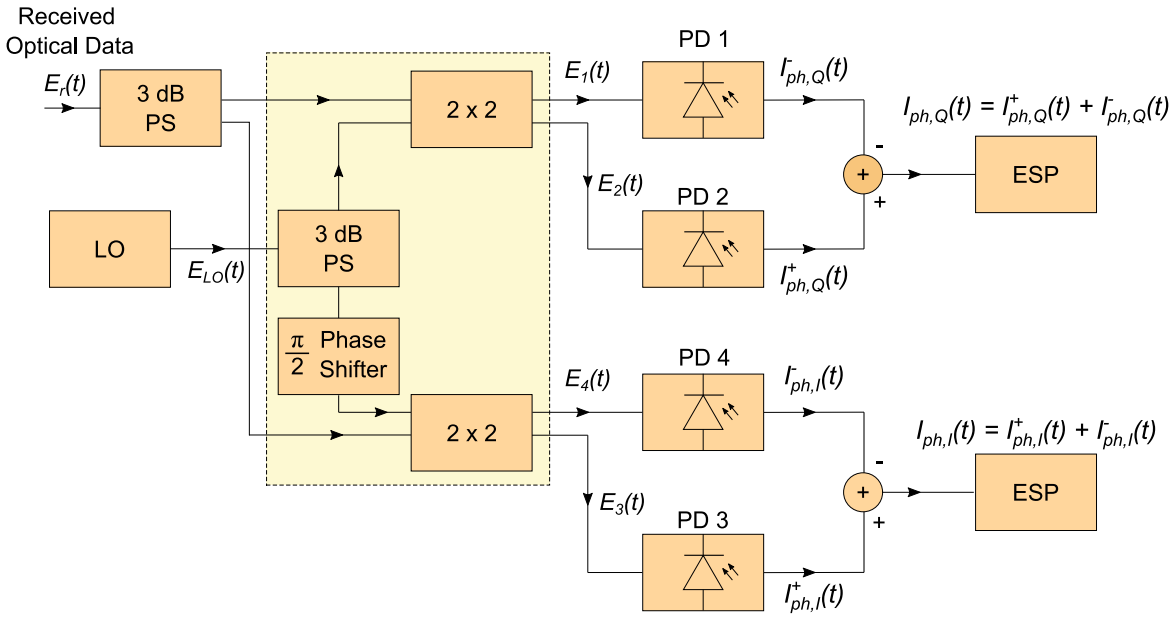

Fig. 3.32 Schematic of balanced IQ coherent receiver

where the factor of $\frac{1}{\sqrt{2}}$ represents the 3 dB power splitters and the $\pi/2$-phase shift is included in the coupler transfer matrix. $I^+_{\mathrm{ph,I}}(t)$ and $I^-_{\mathrm{ph,I}}(t)$ are the same as equation 3.67. $I_{\mathrm{ph,I}}(t)$ and $I_{\mathrm{ph,Q}}(t)$ are then given by,

$$\begin{aligned} I_{\mathrm{ph,I}}(t) &= R_{\mathrm{I}} A_r A_{\mathrm{LO}} \mathrm{Re}\left[s(t)\exp[-j(\omega_{\mathrm{IF}}t+\Delta\phi)]\right] \\ I_{\mathrm{ph,Q}}(t) &= -R_{\mathrm{I}} A_r A_{\mathrm{LO}} \mathrm{Im}\left[s(t)\exp[-j(\omega_{\mathrm{IF}}t+\Delta\phi)]\right] \end{aligned} \tag{3.70}$$

The complex current can then be reconstructed by the ESP such that $I_{\mathrm{ph}}(t) = I_{\mathrm{ph,I}}(t) - jI_{\mathrm{ph,Q}}(t)$.

3.4.5 Challenges

Enabling sub-band gap detection in Si has been a major issue for Si-based PDs. This has been demonstrated by introducing mid-band gap energy states by using poly-Si or defects, using a metal-Si interfaces to facilitate charge transfer across the Schottky barrier, or incorporating epitaxially grown Ge-on-Si. Currently Ge-on-Si PDs have shown the highest responsivities, but at the cost of extra fabrication complexity. The challenge will be to find a mechanism that enables sub-band gap detection with a large active area that leads to high quantum efficiency and increased responsivities, but with simpler fabrication steps.

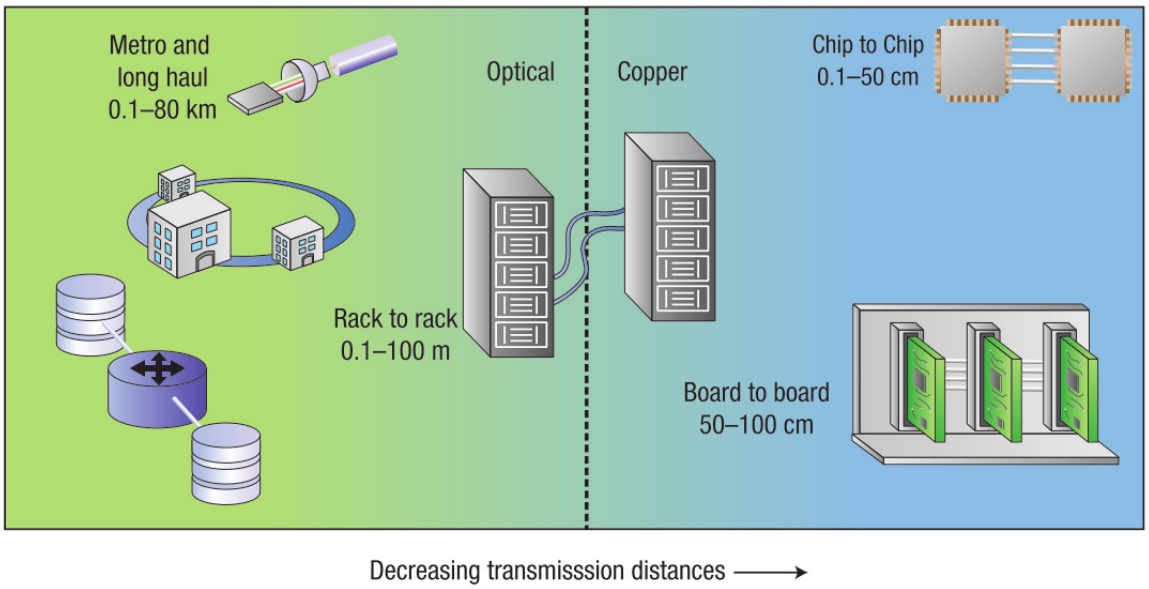

Fig. 3.33 Interconnect technology as a function of transmission distance, adapted from Ref. [146]

3.5 Optical Links

Optical fibres have been in use for commercial telecommunication networks since 1980 [147] and have continued to dominate long-haul communications. Research has focused on increasing data transmission rates and pushing optical networks to shorter length scales [146]. Figure 3.33 shows different examples of data communication networks over a range of length scales [146]. The market adoption of optical technologies is shown in green and the market adoption of electrical technologies is shown in blue. As the transmission distances decrease it shows the transition from optical to electrical technologies. For these short-reach applications, Cu based interconnect is favourable because the penalty of electro-optical conversion makes optical interconnect prohibitively expensive and complex [146, 148].

3.5.1 Performance Metrics

Operating Range

An optical link has a defined operating range within the electromagnetic spectrum. The choice of operating region will be determined by the properties of the communication channel, optical transmitter, and optical receiver. Table 3.1 lists approximate wavelength ranges for the different transmission bands within a optical link that uses a single-mode fibre as the channel medium [64]. A channel occupies a region of the electromagnetic spectrum, which is

Band	Description	Wavelength Range (nm)
O	Original	1260 - 1360
E	Extended	1630 - 1460
S	Short	1460 - 1530
C	Conventional	1530 - 1565
L	Long	1565 - 1625
U	Ultra-long	1625 - 1675

Table 3.1 Approximate wavelength ranges for different wavelength bands for transmission with a single-mode optical fibre [64].

given by its bandwidth [63]. Transmission systems with multiple channels are characterised by the spacing between each channel [63]. Typically the channel spacing is chosen to limit cross-talk between channels by ensuring that the channel spacing is larger than the bandwidth. For multiple channels in the frequency domain, the possible channel spacing is defined by the recommendation of the International Telecommunication Union [149, 150].

Capacity

The channel capacity is given by the bit-rate that the channel can support [63]. Channel capacities are standardised according to IEEE Ethernet standards which specify data rates for different technologies and implementations [151]. Current standards reach 400 Gb/s over 0.1 - 10 km, with different implementations depending on the required distance [151]. For shorter distances up to 100 m and above, 400 Gb/s can be transmitted by 16 lanes of multimode fibre [151]. Whereas, for longer distances up to 10 km and above, this is implemented with 8 channels in one single-mode fibre [151].

Spectral Efficiency

SE is defined as the capacity of a single channel per unit bandwidth [63]. For example, a channel with a bandwidth of 50 GHz that transmits data at 40 Gb/s has an SE = 0.8 b/s/Hz. Increased SE means that more data is transmitted within the same channel bandwidth. This is a key driver in the development of next-generation optical networks in order to increase channel capacities.

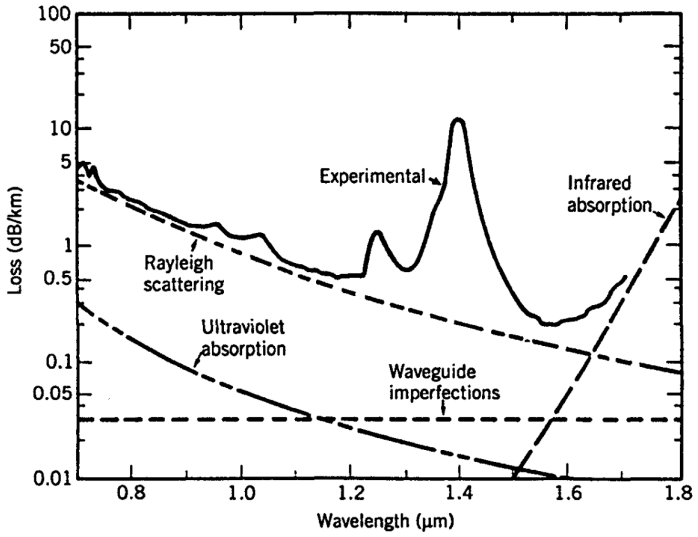

Fig. 3.34 Measured optical losses of a single-mode optical fibre as a function of wavelength. Data from [154], figure from [63]

Bit Error Rate

The bit error rate (BER) is defined as the average probability of incorrect bit detection [63]. For example, a BER = 10^{-9} is a typical operating requirement [63], which corresponds to an error occurring once in every 10^9 bits. This will depend on many factors in the complete optical link, such as the modulation format used, sources of noise, and the properties of the optical fibre. The smaller the BER the less errors there will be when receiving the data.

3.5.2 Long-haul Fibre-optic Networks

Optical fibres were proposed as a new communication medium in 1966 due to their increased information capacity compared to existing networks based on coaxial cables and microwaves [152]. High data rates were a problem for coaxial networks where losses greatly increased at high frequencies [63]. This lead to the need for electrical repeaters every 1 km to amplify the signal and compensate for the losses [63]. Microwave systems enabled larger repeater spacings, but struggled to reach high capacities because they were limited to the frequency of radio waves [63]. Until 1970, optical fibres had been limited by the quality of dielectric material available [152], but this changed in 1970 when Corning achieved propagation losses of 20 dB/km at 632 nm [153].

The first generation of commercial fibre-optic networks used GaAs lasers operating at 850 nm and graded-index multimode fibres [147]. These were capable of carrying 45 Mbit/s but needed to be regenerated after 7 km to over come losses and dispersion from the multimode

fibre [147]. The signal would be regenerated using an optoelectronic repeater that converted the optical signal back into the electrical domain where it could be amplified and then re transmitted by another transmitter [63]. Compared to the required 1 km repeater spacing for coaxial cables, fibre-optic networks became preferable for long-haul communications where the increased repeater spacing lowered installation and maintenance costs [63].

Second generation systems focused on increasing repeater spacings by moving to single-mode fibres that eliminated modal dispersion for high data rates [155]. Repeater spacings were extended by shifting the operating wavelength to 1.3 μm where single-mode fibres had propagation losses of 0.5 dB/km [156] and zero dispersion [157]. Figure 3.34 shows the measured optical loss of a single-mode fibre. This required lasers and detectors based on InGaAs/InP to be developed for operation at 1.3 um [158]. By 1987, second generation systems were commercially available and able to reach 1.7 Gb/s with repeater spacings of 50 km [63].

Third generation systems managed to increase repeater spacings further by further minimising propagation losses by moving to 1.55 μm where losses of 0.2 dB/km had been measured [154]. The increased fibre dispersion at 1.55 μm as opposed to 1.3 μm was managed by using a dispersion-shifted optical fibre [159], and using single longitudinal mode lasers [160], or a combination of the two. The first commercial systems in 1990 reached 2.5 Gb/s, which later increased to 10 Gb/s with repeater spacings of 60 - 70 km [63].

Fourth generation systems pushed the repeater spacings again by the development of optical amplifiers [161]. These used erbium doped fibres to amplify the optical signal without the need to convert the signal back into the electrical domain [161]. These were commercialised in 1990 and enabled amplifiers to be spaced 60 - 80 km apart [63]. Capacity was increased by implementing WDM to send different channels down the same fibre that are separated in the wavelength domain [63]. Repeaters were problematic for many channels of WDM, but the optical amplifier allows all to be amplified at the same time [63]. With the introduction of WDM, data rates of 10 Tbit/s were demonstrated with 273 channels [162].

The first four generations of fibre-optic networks are illustrated in figure 3.35. Next-generation networks focus on increasing capacity by increasing the spectral efficiency [63]. This can be achieved with complex modulation formats and coherent detection, or by using techniques such as polarisation-division multiplexing (PDM) and orthonogal-frequency division multiplexing (OFDM), to add more degrees of freedom or reduce the channel spacing [63]. For example, a single 50 GHz WDM channel that uses digital modulation formats to carry a 40 Gb/s signal has a spectral efficiency of 0.8 b/s/Hz. However, if PDM and 4-QAM modulation is used instead of a digital modulation format, then the channel now has a spectral efficiency of 3.2 b/s/Hz. This is equivalent to a 160 Gb/s signal for

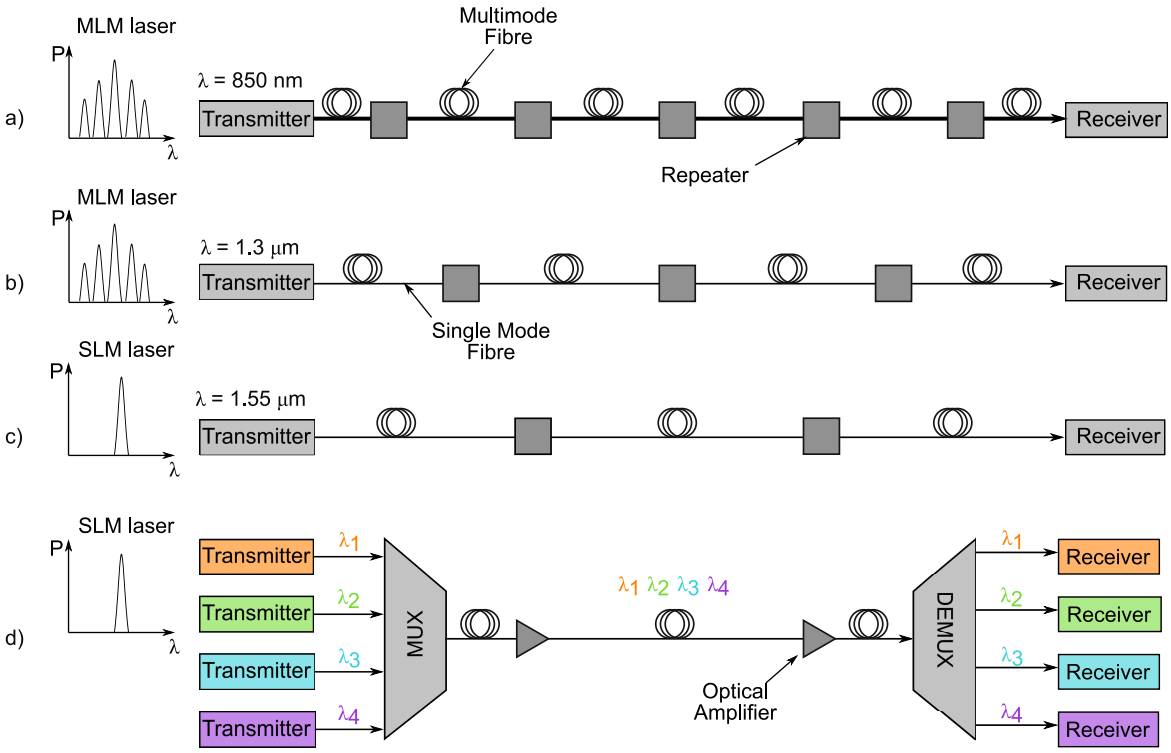

Fig. 3.35 First four generations of long-haul fibre-optic networks for telecommunications.

the same 50 GHz bandwidth. A spectral efficiency of 17.3 b/s/Hz has been demonstrated over 50 km of fibre for a 10 subcarrier superchannel that uses PDM and 4096-QAM [163]. These are considered fifth generation fibre-optic networks, and speeds up to 115 Tb/s have been demonstrated over 100 km of single-mode fibre with 64-QAM modulation and 250 WDM channels [164]. OFDM is similar to WDM, but that the channel spacing is less than the bandwidth of the channel, and the peak of one carrier coincides with the null of the neighbouring carriers [8]. This increases the capacity by increasing channel density, but with no cross-talk or inter carrier dispersion because the carriers are orthogonal to each other [8]. OFDM can be implemented with frequency combs [165–167] which removes the practical constraint on the number of channels by eliminating the need of individual transmitters and receivers for each channel.

However, the problem is that this is fast approaching the maximum capacity for single-mode fibres, as shown by the dashed line in figure 1.1 [5]. The theoretical capacity of a single communication channel with a fixed bandwidth is defined by the SNR at the receiver, which should increase with increasing SNR [168, 169]. It has been shown that this is not true for single-mode fibres which are limited by fibre non-linearities at the high powers required for high SNR [170]. This is shown on figure 3.36 which shows the spectral efficiency as a function of SNR for varying distances. It shows that spectral efficiency decreases

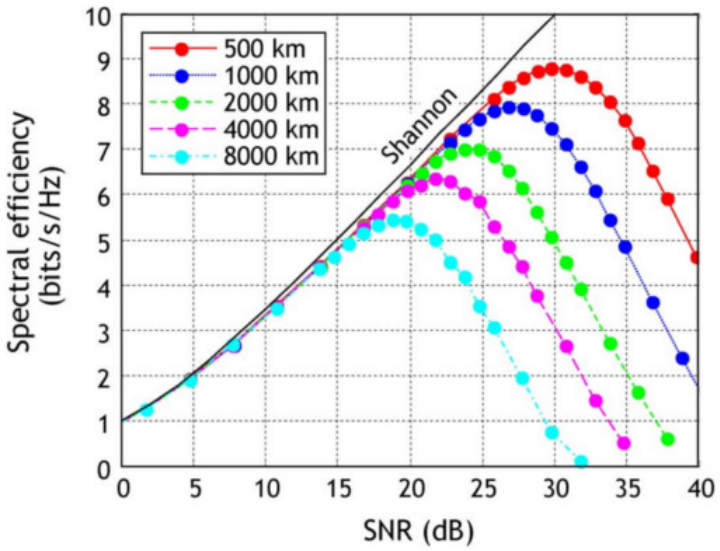

Fig. 3.36 Spectral efficiency as a function of SNR for different transmission distances in an optical fibre, adapted from Ref. [170]

after a certain SNR as a result of nonlinear signal distortion which has a bigger impact for longer transmission distances [170]. Considering the operating region of erbium-doped fibre amplifiers (EDFA), the usable bandwidth of single-mode fibres is approximately 10 THz [63]. Therefore, by assuming a spectral efficiency of 10 b/s/Hz, this equates to a maximum capacity of approximately hundreds of Tb/s.

New techniques such as space-division multiplexing (SDM) are required to surpass the maximum capacity of a single mode fibre [5, 171]. SDM uses different spatial modes within the same fibre to carry independent channels of information. It relies on different fibre technologies that support multiple spatial modes, a selection of which are shown in figure 3.37. One approach is to increase the number of single-mode cores within a fibre, as shown in figure 3.37 2 - 4. This is known as a multicore fibre (MCF) and is further categorised by the level of coupling between individual modes [171]. Another approach is to use multimode fibres (MMF) that support multiple modes that overlap each other for mode-division multiplexing (MDM) [5]. For an ideal MMF the different spatial modes do not couple to each other, but in reality digital signal processing techniques are required to overcome intermodal cross-talk [5]. Few-mode fibres (FMF) are therefore a suitable compromise where the limited number of modes reduces the intermodal dispersion [5]. Another option to increase the capacity is to use new fibre architectures, such as hollow-core fibres (HCF), that reduce fibre non-linearities [172]. In the case of HCFs, they have an ultra-low nonlinear coefficient because the central core is composed of air and so are not limited in the same way as single-mode fibres [172]. The current record of data transmission

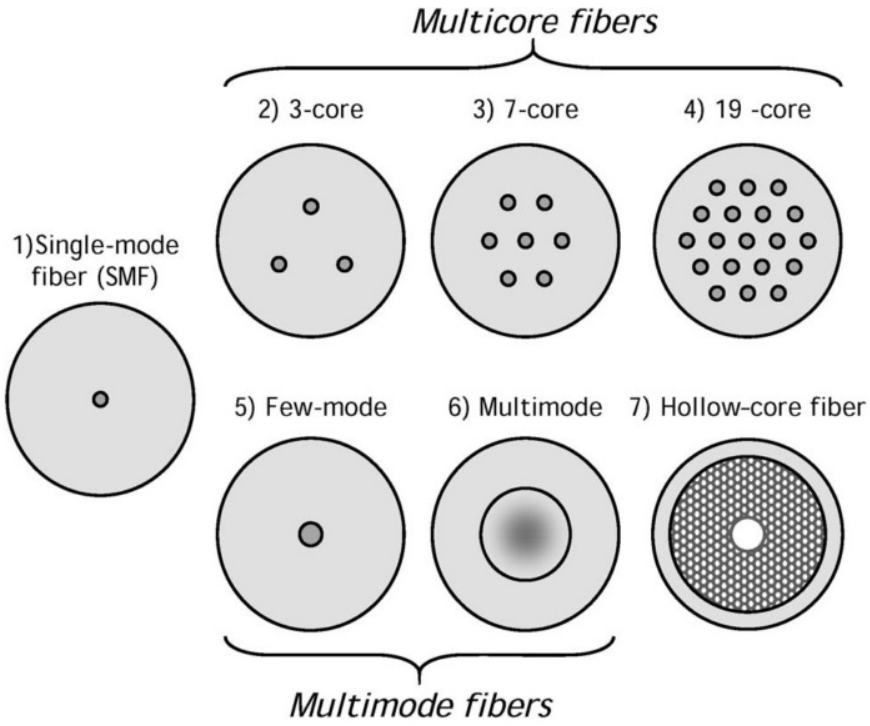

Fig. 3.37 Schematics of multicore or multimode optical fibre architectures used for space-division multiplexing, adapted from Ref. [171]

using a 6-mode 19-core fibre was 10 Pb/s in 2017 [173]. This enables capacities to continue increasing, as shown on figure 1.1, beyond the limit imposed by single-mode fibres. However, these methods require overhaul of the entire optical fibre network and maturity of new fibre architectures that are much more complex than existing technologies.

3.5.3 Short-Haul Optical Interconnect

Typically, short-reach applications, like board-to-board or chip-to-chip, have stuck with electrical interconnect because the cost and complexity of optical systems is too high to warrant replacing the existing electrical networks. However, as data rates move to Tb/s the adoption of optical networks is moving to shorter length scales because of the high resistance, and therefore, losses of electrical networks at high frequencies [146]. Pluggable optics has been made possible by Si Photonics and are widely used for data centre interconnect [175]. Figure 3.38a shows different Ethernet form factors that are used for different data transmission rates for rack-to-rack interconnect within a data centre [4]. It shows that above 200 Gb/s pluggable optical transceivers have replaced the form factors that use Cu cables. The optical module is plugged into the face plate of switches with optical fibres plugged into them and are responsible for the electro-optic conversion. These are becoming very popular

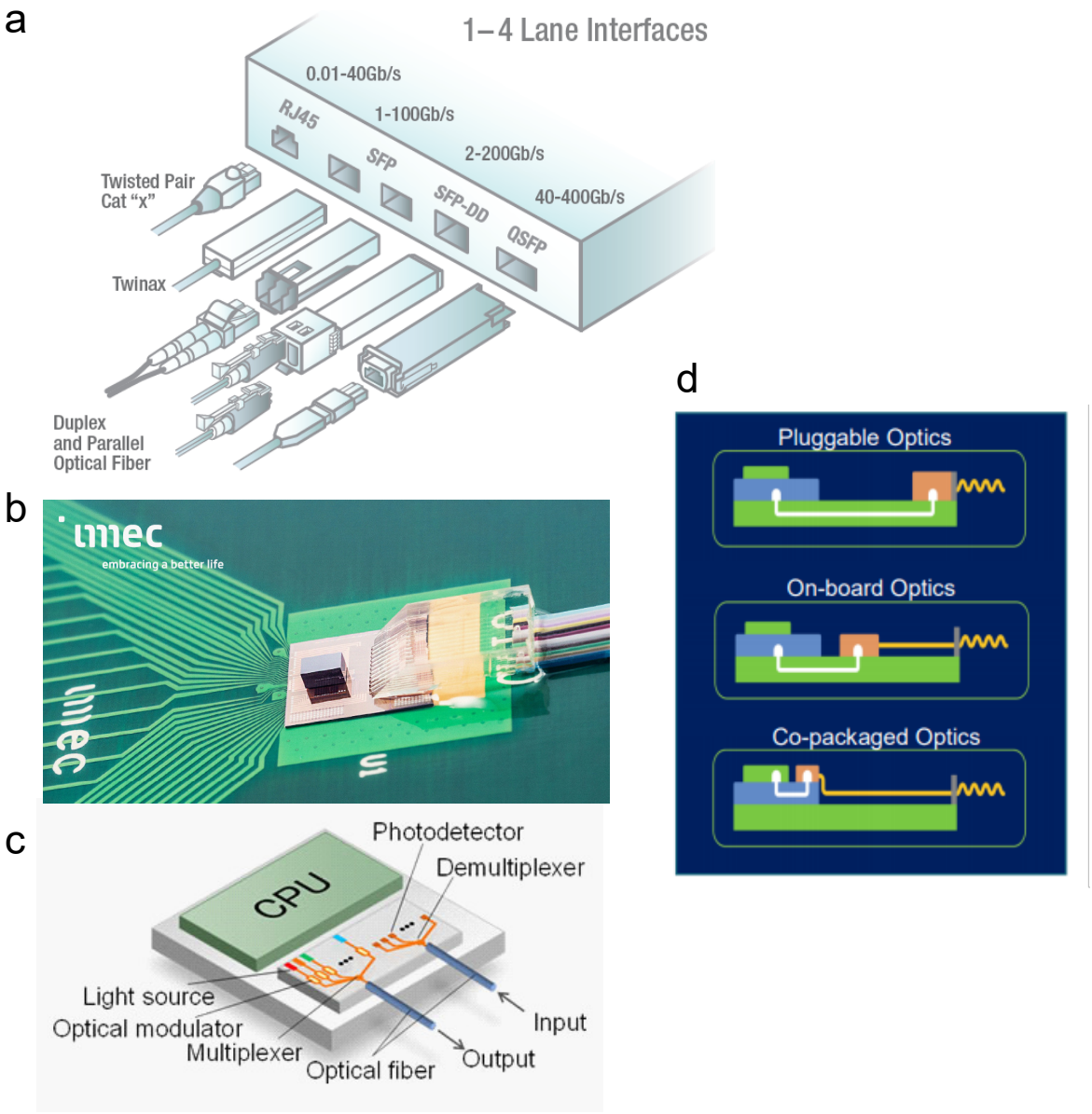

Fig. 3.38 (a) Common Ethernet port form factors for 1-4 lane interfaces using Cu cables (up to 100 Gb/s) and optical fibres (up to 400 Gb/s), adapted from Ref. [4], (b) image of photonic substrate bonded to a printed circuit board from IMEC, (c) schematic of a co-packaged optics integration scheme, adapted from Ref. [174], (d) schematic showing the evolution of pluggable optics to co-packaged optics. ASIC at the top (green), electro-optical transceiver (orange), ASIC packaging (blue), printed circuit board at the bottom (green), optical fibre (yellow), and electrical interconnect (white).

in data centres and in 2019 Intel announced their latest pluggable transceiver that supported 400 Gb/s transmission.

The modular nature of optical modules leads to limitations in bandwidth due to the power consumption of electrical interconnect as data rates go above 400 Gb/s. Ideally to reduce power, the optics should be as close to the application-specific integrated circuit (ASIC) as possible to reduce the parasitics associated with the electrical interconnect. One approach is to bring the optics onto the printed circuit board (PCB), known as on-board optics. Figure 3.38b shows an example of on-board optics where a Si photonic integrated circuit die is bonded onto a PCB. The Si photonic die has a bonded III-V laser and an optical fibre array that couples light in and out of the photonic circuits. This can be taken even further with co-packaged optics, figure 3.38c, where the Si photonic chip is in the same packaging as the central processing unit (CPU) [174]. Owing to the potential energy savings from intra data centre connectivity, there is a lot of interest from technology companies like Facebook and Microsoft to accelerate the development of co-packaged optics [176]. In 2020, Intel announced the first co-packaged switch that is capable of 12.8 Tb/s data transmission based on their Si photonic engines running at 1.6 Tb/s [177]. Figure 3.38d shows the different configurations of ASIC (top green) and EO transceiver (orange) for pluggable, on-board, and co-packaged optics. It shows that as the EO transceiver is brought closer to the ASIC, the length of electrical interconnect (white) decreases.

The adoption of optical interconnect for short-reach applications requires compact and low-power optical transceivers. High-density data transmission based on complex modulation formats is not practical due to the large size of the nested MZI structure used for IQ modulation. Typically, short-reach applications utilise coarse WDM with RRMs to increase the BW of transmitted information because of the compact size of RRs. Capacity can be increased with dense WDM using on-chip frequency combs as a single source to generate all channels for WDM [166, 167].

3.5.4 Challenges

The strain on existing optical networks is pushing the industry to consider completely new fibre architectures and transmission systems to keep up with the growing capacity demand of today's society. As usual with the adoption of new technology in industry, the main challenge is an economical one. Whilst lab based demonstrations have shown data transmission rates far exceeding commercial optical networks, the additional complexity associated with complex modulation formats or the investment required to replace the existing optical fibres is undesirable for industry. Ethernet standards currently for $>$ 100 Gb/s transmission already use PAM-4 modulation formats, but these are likely to move to complex QAM formats in

the future. This is not only motivated by the increase in spectral efficiency from moving to coherent systems, but it is also motivated by the added bonus of increased noise tolerance which is crucial for reducing errors at the receiver.

3.6 Conclusions

This chapter has focused on introducing the different components of a Si photonic optical link. The band gap of Si and refractive index contrast with SiO_2 has shown to be very good for submicron WGs because it enables low-loss propagation and strong confinement. The working mechanisms of passive photonic components were discussed, including WGs and coupling mechanisms, with particular interest in RR and MZI structures that can be used to manipulate light on-chip.

Moving onto transmitters, I reviewed different modulation mechanisms in Si and performance parameters used to describe modulators. I showed that the band gap of Si makes it difficult to build an Si EAM without the introduction of epitaxially grown Ge-on-Si. Si phase modulators have been demonstrated, based on the plasma dispersion effect, but these struggle with maintaining a high modulation efficiency without inducing high optical losses associated with the doped Si WGs. Instead, other materials, such as III-V semiconductors or LN have been integrated with Si WGs, which have successfully demonstrated increased modulation efficiency and low-losses. However, these materials are undesirable because they require expensive processing and wafer bonding techniques to be integrated onto SOI wafers. I have reviewed different modulation schemes for encoding information into an optical carrier. The choice of modulation scheme will depend on the desired spectral efficiency, noise tolerance, and system complexity for the required application. Multi-level or complex modulation formats are typically used for high-density data transmission, such as the case of long-haul optical fibre networks. Digital modulation formats are typically used for lower capacity data transmission, or for short-reach optical networks which require simpler, more compact transceivers.

Next I discussed PDs that are used in the receiver, describing the photodetection mechanism in semiconductors and the relevant PD performance parameters. I reviewed methods of facilitating sub-band gap absorption in Si, and then hybrid PDs based on the integration of III-V semiconductors and Ge. Si based PDs suffer from low responsivity due to the band gap of Si, and therefore other materials with a larger absorption coefficient are needed. Like with modulators, the integration of III-V semiconductors or Ge has been shown to improve the performance of hybrid PDs on the Si photonic platform, but at the cost of additional processing. I have then described coherent detection which is required for optical networks

based on complex modulation formats. In this case, unlike direct detection systems, the phase of the received signal is recovered. I have included system-level implementations for balanced coherent detection, which is useful to reduce noise in the generated photocurrent, and for an IQ coherent receiver which can determine the phase of the received signal.

Finally, I have reviewed the development of existing long-haul and short-reach optical fibre networks. I have shown that different technologies have been introduced to boost the data capacity in optical fibre networks, but that we are now reaching the limit of how much data can be transmitted in the existing network of single-mode fibres. As next-generation high-density long-haul data networks are expected to move to Tb/s data rates the challenge is to introduce complex modulation formats that increase the spectral efficiency. Increasing data rates also puts a lot of strain on the existing electrical interconnect networks that are used to process the vast amounts of data, driving the adoption of optical networks to shorter and shorter length scales. Industry is moving towards solutions that bring the optical transceivers closer and closer to the ASIC, with the demonstration of co-packaged optics. In both long-haul and short-reach cases, solutions to increasing data rates require low-power optical transceivers and investment to upgrade the existing networks.

Chapter 4

Graphene Integrated Silicon Photonics

4.1 Motivation

Graphene has many properties that make it ideal for the active material of integrated PDs and modulators [17, 96, 124, 178]. Firstly, graphene has shown to have $\mu > 50{,}000$ cm^2/Vs at room temperature [26–28] enabling high-speed operation and efficient performance. Secondly, due to the gapless band structure of massless Dirac fermions in SLG, the optical conductivity can be electrostatically controlled [32, 179]. Thirdly, unlike other materials, the band structure of SLG results in wavelength independent absorption in the visible to the mid-infrared range [30, 32]. Along with its electrical and optical properties, SLG is an attractive material for Si photonic optical links because it can be produced at the wafer scale [37, 178, 180] where it can be transferred without the need of wafer bonding [37]. SLG can be produced by CVD, which allows the flexibility to grow large-area polycrystalline films up to 30 inch [41] or single crystals with higher μ at predefined locations [44]. SLG films can be integrated in the CMOS back-end-of-line (BEOL), after fabrication of the integrated circuits, for waferscale processing, reducing cost and complexity of fabrication.

In this chapter I will discuss the state-of-the-art for WG-integrated graphene-based PDs (GPD) and modulators. Starting with GPDs, I will describe some of the different photodetection mechanisms available in graphene, and then review different configurations of WG-integrated GPDs that are designed for different photodetection mechanisms. I will then compare the performance of GPDs to other technologies and comment on the outstanding challenges. Next, I will move onto graphene-based modulators, describing the operating principle and the different operating regimes for electro-absorption and electro-refractive modulation. I will review existing implementations of WG-integrated graphene-based modulators and compare their performance to other technologies.

4.2 Graphene Integrated Photodetectors

4.2.1 Photodetection Mechanisms

There are four mechanisms for detecting light in graphene which are very different from traditional semiconductors due to its unique band structure and lack of band gap [124]. These are presented in figure 4.1. The dominant photodetection mechanism will largely depend on the device design and operating conditions [124].

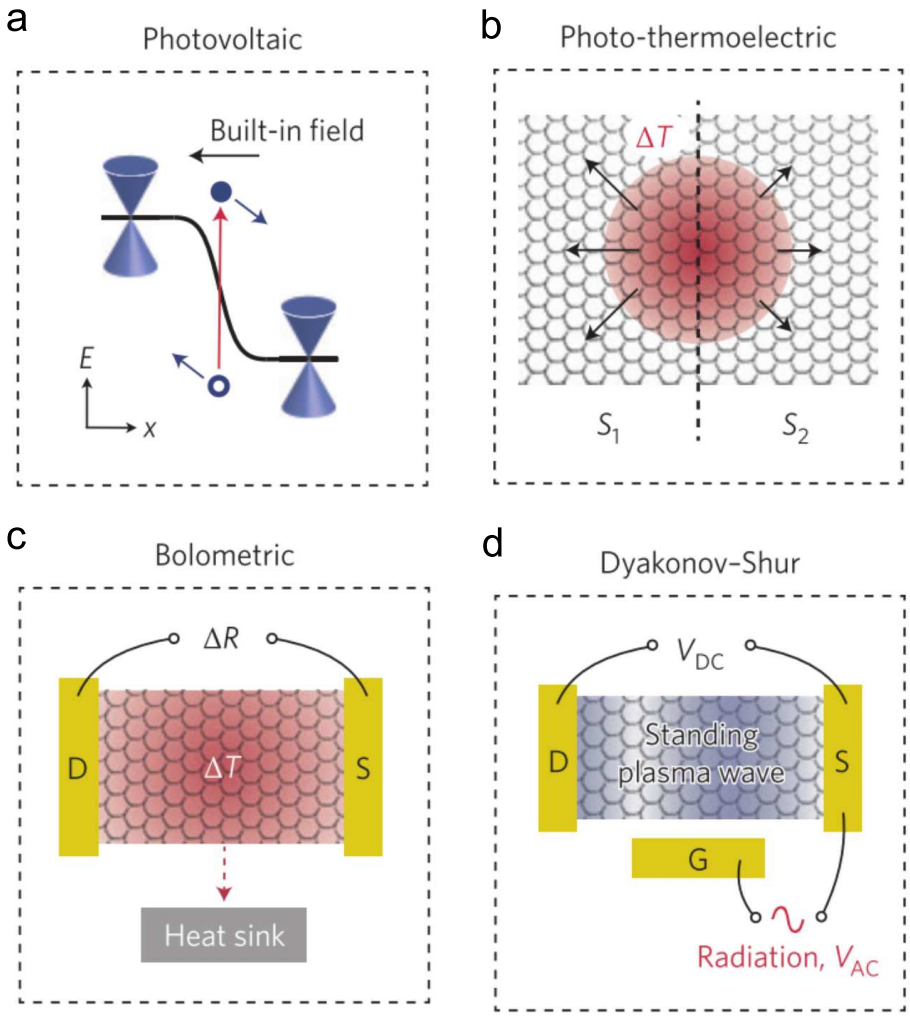

Fig. 4.1 Illustrations of the four photodetection methods in graphene, (a) photovoltaic, (b) photothermoelectric, (c) bolometric, and (d) dyakonov-Shur, adapted from Ref. [124].

Photovoltaic effect

The photovoltaic effect (PV), shown in figure 4.1a, generates a photocurrent, I_{ph}, by separating a photogenerated electron-hole pair within an electric field [124]. The sign of the resulting I_{ph} will depend on the direction of the electric field [124]. In the case of graphene this electric field can be created either by applying a bias, or at the interface between regions of different doping [124]. However, as graphene does not have a band gap it suffers from a high dark current, I_{d}, and therefore an in-built electric field at a p-n junction is preferable to an applied bias [124].

Photothermoelectric effect

The photothermoelectric effect (PTE), figure 4.1b, occurs when an induced temperature gradient, ∇T_e, causes a flow of charge carriers leading to a photothermoelectric voltage, V_{PTE} [181]:

$$V_{\text{PTE}} = (S_1 - S_2)\nabla T_e \tag{4.1}$$

Where S are the Seebeck coefficients in the two regions, which relates the induced V_{PTE} to the chemical potential, μ_C, and the electrical conductivity, $\sigma_{d.c}$, according to Mott's formula [124, 181, 182]:

$$S = -\frac{\pi^2 k_B^2 T_e}{3e}\frac{1}{\sigma_{d.c}}\frac{\partial \sigma_{\text{d.c.}}}{\partial \mu_C} \tag{4.2}$$

In graphene, ultra-fast (sub picosecond) electron-electron scattering is capable of carrier multiplication by generating a 'hot' carrier distribution from one photogenerated electron-hole pair [182]. This distribution can remain for nanoseconds because it relies on inefficient cooling by scattering with acoustic phonons as the energies of optical phonons ($\sim$ 200 meV) are too high [182]. The non-monotonic behaviour of the Seebeck coefficient in graphene enables the PTE to be identified experimentally by multiple sign changes of the induced I_{ph} [182].

Bolometric effect

The bolometric effect produces a change in conductivity of graphene due to an induced heating from the absorption of incident light [124]. A bolometer can detect the resulting thermal resistance R_{TH} that is related to the temperature increase dT from the absorbed power dP [124]:

$$R_{\mathrm{th}} = \frac{\mathrm{dT}}{\mathrm{dP}} \tag{4.3}$$

The sensitivity of bolometric photodetectors depends on R_{TH}, which in graphene is relatively high due to inefficient electron-phonon scattering limiting heat dissipation [124]. The response time of the device is given as the product of R_{TH} and the heat capacity C_{th}, and can therefore have a fast response due to the limited density of states and volume of graphene [124]. The bolometric effect does not directly generate I_{ph}, and instead an applied bias is required to monitor the conductance of the channel [124].

4.2.2 Integrated Device Configurations

Metal-graphene-metal (MGM) photodetectors are simple structures where graphene is gated by metal contacts and I_{ph} is generated at the metal-graphene interfaces due to the PV effect and the PTE [183–187]. In this configuration, charge transfer from the metal contact to graphene causes the Fermi level in the graphene beneath the contact to be shifted, figure 4.2b. This forms a built-in electric field along the edge of the contact between the contacted and uncontacted graphene which splits the photogenerated electron-hole pairs in graphene and generates a I_{ph} [184]. WG-integration offers the added benefit of increasing the interaction length of the graphene channel, thus increasing I_{ph} whilst still maintaining broadband operation. The device depicted in figure 4.2 uses a mechanically exfoliated graphene flake deposited on top of a Si WG showing responsivities up to 50 mA/W for a 24 μm device length, as well as $\sim$ 18 GHz bandwidth from 1310 - 1650 nm [183]. As the PV effect relies on the built-in electric field, no applied bias is required and therefore $I_{\mathrm{d}} = 0$ [183]. The responsivty of MGM photodetectors is limited by the weak built-in electric field at the metal-graphene interface, but even with a demonstrated $R_{\mathrm{I}} \sim 7$ mA/W without an applied bias, MGM PDs have shown a BW $\sim$ 41 GHz that demonstrated data transmission of 50 Gb/s [186]. The responsivity can be increased up to 0.1 A/W [185] by applying a bias across the graphene channel, or to $\sim$ 0.36 A/W by increasing the PTE contribution to I_{ph} by gating the graphene channel [187].

By applying a bias across the graphene channel there is an additional component to I_{ph} from the bolometric effect [189]. The bolometric effect does not directly generate I_{ph}, and requires an applied bias in order to detect the change in conductivity that is associated with the absorption induced temperature change [124]. The contribution to I_{ph} can be distinguished by a negative polarity in comparison to the DC current from the applied V [189]. As the bolometric effect does not rely on a built-in electric field, the interaction

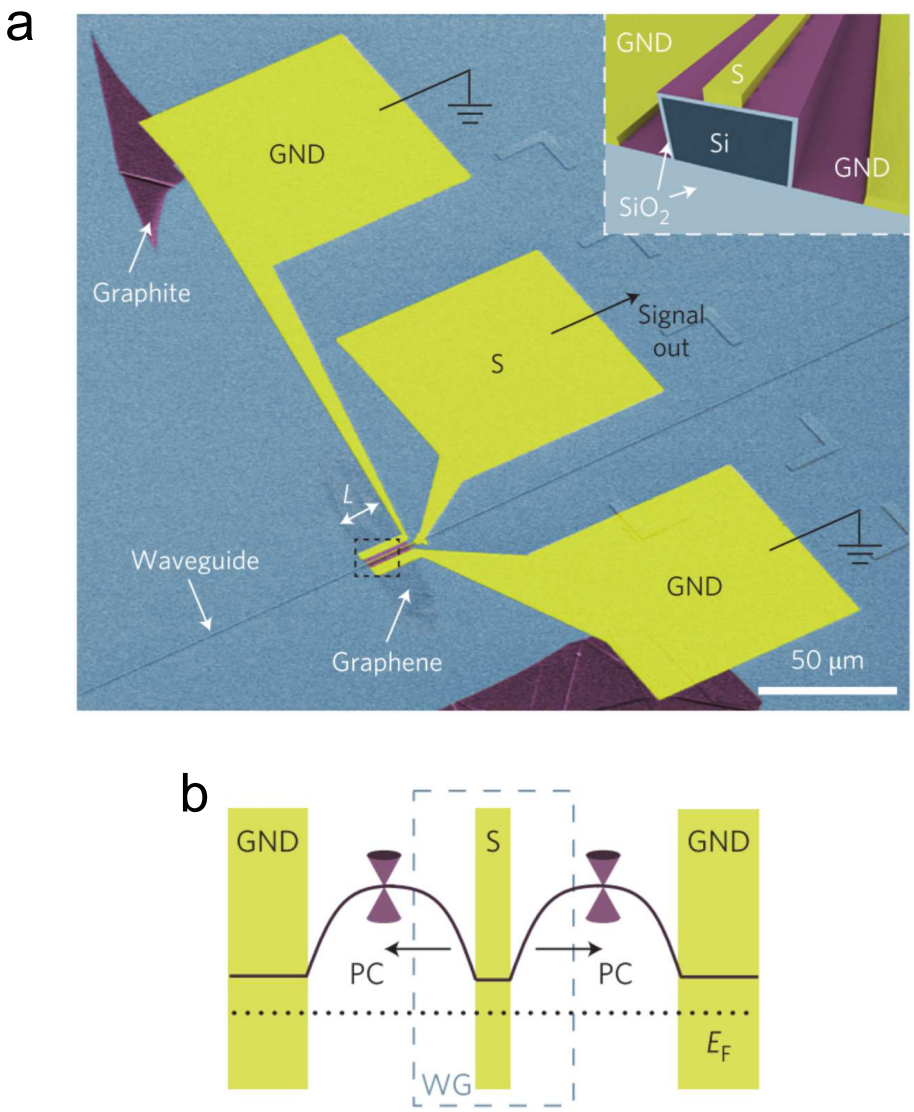

Fig. 4.2 (a) Scanning electron microscope image of the WG-integrated GPD, inset shows an enlarged view of device showing the central source contact, ground contacts, and the active area of graphene shown in pink, (b) band profile profile of the graphene channel resulting from charge-transfer from the metal contacts, adapted from Ref. [183]

area between the graphene and the propagating light can be increased [186]. Figure 4.3a shows the schematic of a graphene photodetector that is operated such that the dominant photodetection mechanism is the bolometric effect [188]. The increased interaction area, with additional plasmonic enhancement, has pushed $R_I \sim 0.5$ A/W [190]. Owing to the small C_{th} of graphene, GPDs based on the bolometric effect have fast response times [124]) with BWs up to 110 GHz, capable of data reception at 100 Gb/s PAM-4 [190].

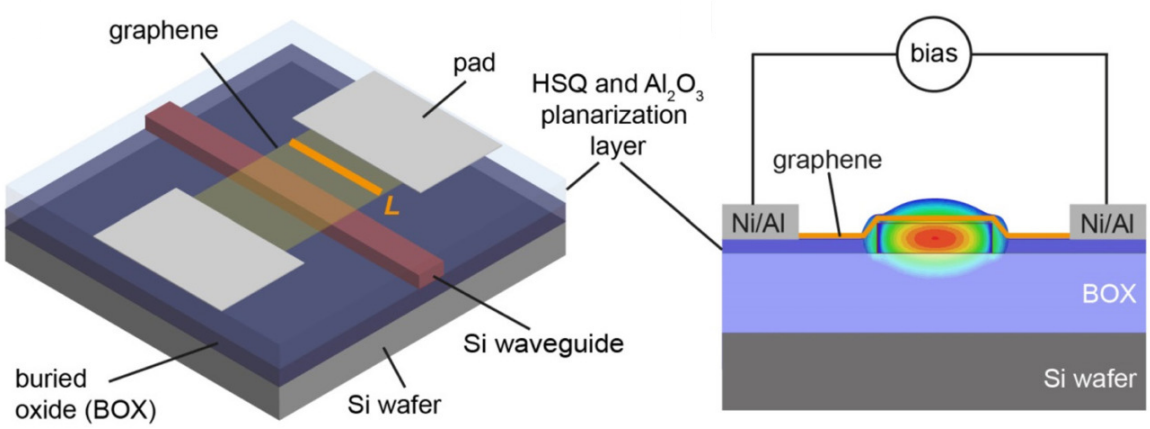

Fig. 4.3 (a) Device structure of a GPD based on the bolometric effect, (b) cross-section showing modal field profile and applied bias, adapted from Ref. [188]

The required bias for GPDs based on the bolometric effect is not desirable because of the unavoidable I_d [124]. Instead, other photodetection mechanisms, such as the PTE, can be used to boost the responsivity of GPDs without an applied bias [124]. Typically the PTE GPDs use a split-gate device geometry which can be used to tune the doping profile in a graphene channel and create a p-n junction above a WG [191–193]. Operating without an applied voltage, the PTE generates V_{ph} and an associated voltage responsivity R_V [124]. It is advantageous to directly generate V_{ph} instead of I_{ph} as a transimpedance amplifier is no longer needed to convert I_{ph} into a voltage to drive the receiver electronics [145]. The PTE can be identified by the 6-fold pattern in the polarity of V_{ph}, figure 4.4c, due to the nonmonotonic behaviour of the Seebeck coefficient as a function of E_F of graphene [182]. R_V has increased from $\sim$ 3.5 V/W [192] by using different methods to enhance the interaction between graphene and the propagating light. Examples include using plasmonic split-gates to excite a surface plasmon polariton which increased R_V to $\sim$ 12.2 V/W [193], or by using a resonant structure, figure 4.4a, which boosted R_V to $\sim$ 90 V/W [191]. PTE GPDs have been demonstrated with $f_{3dB} > 67$ GHz [194].

4.2.3 Performance comparison

In comparison to PDs based on semiconductors, GPDs have a number of benefits that make them an attractive technology. Firstly, broadband operation due to the linear band structure and lack of bandgap are ideal for communications over a wide range of frequencies. This is simply not possible with another material. Secondly, the different photodetection mechanisms offer flexibility in device design and operation. Even with an applied bias, R_I of GPDs (0.5 A/W [190]) is not as high as that of existing Ge-on-Si PDs (1.19 A/W [125]).

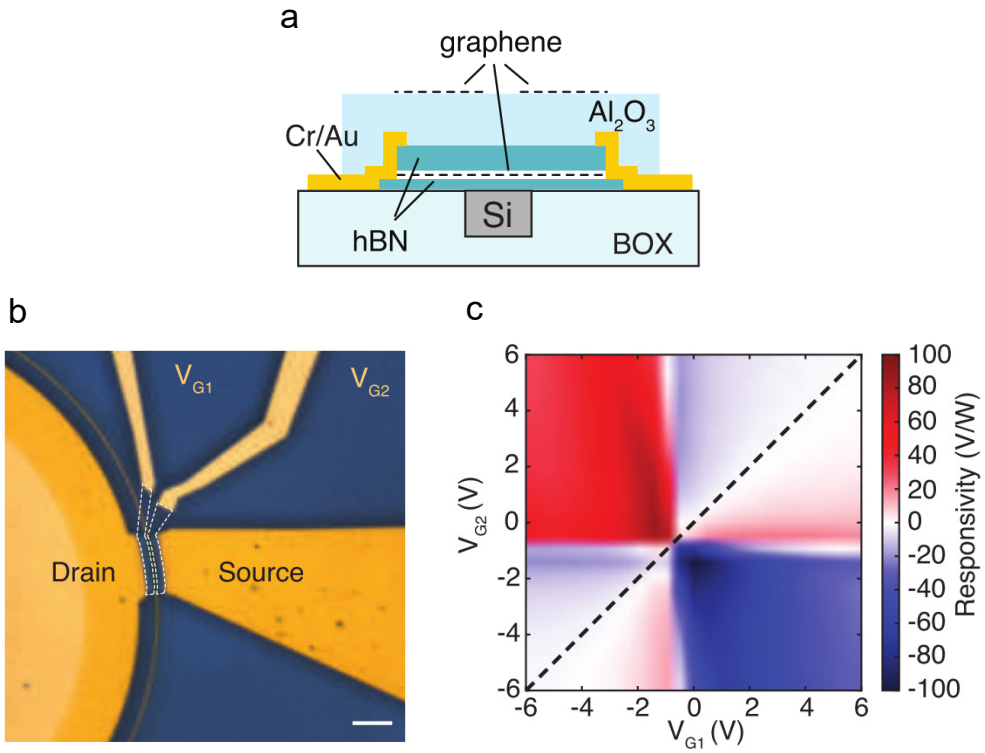

Fig. 4.4 (a) Device schematic of a RR GPD based on the PTE, (b) optical image of the fabricated device, scale bar 5 μm, (c) measured V_{ph} as a function of gate V, adapted from Ref. [191]

The unavoidable I_{d} associated with an applied bias on a GPD has pushed advancements in bias-free operation based on different photodetection mechanisms available in graphene. Eliminating I_{d} by operating with a zero applied bias not only reduces the power consumption of GPDs, but also reduces the noise and hence errors in data reception. Thirdly, the high μ of carriers in graphene also enables fast device operation with intrinisic bandwidths $>$ 200 GHz [195, 196].

4.3 Graphene Integrated Modulators

4.3.1 Modulation Mechanism

Graphene's surface conductivity $\sigma(\omega)$, derived from Kubo's formula [197], depends on the angular frequency of the light (ω), intraband scattering time of graphene (τ), Fermi level (E_{F}), and temperature (T) [198]:

$$\sigma(\omega) = \frac{\sigma_0}{2}\left[\tanh\left(\frac{\hbar\omega + 2E_\mathrm{F}}{4k_BT}\right) + \tanh\left(\frac{\hbar\omega - 2E_\mathrm{F}}{4k_BT}\right)\right] - i\frac{\sigma_0}{2\pi}\log\left[\frac{(\hbar\omega + 2E_\mathrm{F})^2}{(\hbar\omega - 2E_\mathrm{F})^2 + (2k_BT)^2}\right] + i\frac{4\sigma_0}{\pi}\frac{E_\mathrm{F}}{\hbar\omega + i\hbar/\tau} \tag{4.4}$$

Where $\sigma_0 = e^2/4\hbar$ is the frequency-independent, or universal, conductivity of SLG [30, 199] due to interband transitions, $\hbar$ is the reduced Planck's constant, and k_B is the Boltzmann constant. The first two terms represent interband transitions which are heavily dependent on the energy of the incident light ($E = \hbar\omega$) and E_F. Due to Pauli blocking, interband transitions become suppressed when $2E_\mathrm{F} > \hbar\omega$ [31]. For λ=1.55μm, or E = 0.8 eV, Pauli blocking occurs for $E_\mathrm{F} > 0.4$ eV. The third term represents intraband transitions that only depend on τ. Intraband transitions dominate for low energy photons ($\omega < 2000$ cm^{-1} [32]) and for $2E_\mathrm{F} > \hbar\omega$. Intraband transitions are dependent on τ because they rely on scattering for conservation of momentum [200]. Therefore, absorption by intraband transitions increases for shorter τ [96]. τ can be related to μ by [201],

$$\mu = \frac{e\tau v_\mathrm{F}^2}{E_\mathrm{F}} \tag{4.5}$$

We can therefore use τ to model the quality of graphene [96], where high quality SLG is considered as having $\tau > 100$ fs [96].

4.3.2 Operating Regimes

By electrostatically controlling E_F it is possible to modulate $\sigma(\omega)$ of graphene, which in-turn, modulates the complex effective refractive index [20, 203] of the propagating light, leading to a change in phase and absorption along the propagation direction [12]. Figure 4.5 shows the simulated change in effective refractive index and absorption as a function of E_F for different scattering rates Γ. It shows that Γ, which is the inverse of τ, greatly impacts the absorption for $E_\mathrm{F} > 0.4$ eV, where smaller τ results in increased absorption. It shows that depending on the chosen E_F, or operating point, graphene can be used as a phase or amplitude modulator [204]. The optimum operating point for amplitude modulation is at the onset of Pauli blocking, where the change in absorption is greatest [205]. This is not the case for phase modulation, where the optimum point is beyond the Pauli blocking condition when

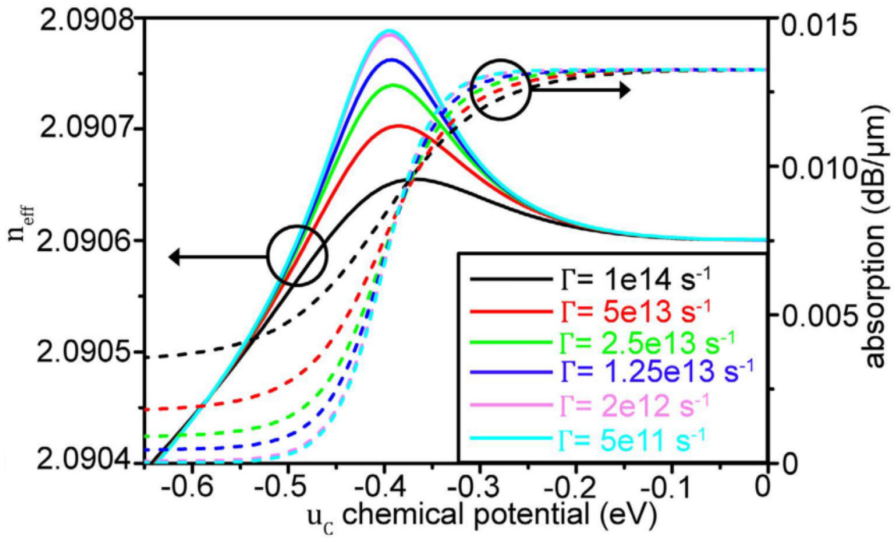

Fig. 4.5 Simulated n_{eff} and absorption as a function of E_{F} of SLG, adapted from Ref. [202]

there is a linear change in n_{eff}, but where absorption is minimised and remains constant with increasing E_{F} [206].

4.3.3 Integrated Device Configurations

Electro-absorption

The first experimentally demonstrated WG-integrated graphene-based EAM had ER = 0.1 dB/μm, operating speed $>$ 1 GHz, and a device area of 25 μm^2 [207]. The device, shown in figure 4.6a, consisted of a single-layer of CVD grown SLG deposited onto a Si WG with a 7 nm Al_2O_3 dielectric to form a capacitor structure. An applied bias across the doped Si WG and the contact to SLG would generate a perpendicular electric field that would accumulate charges at the graphene interface and shift E_{F} of graphene. Figure 4.6b shows the measured electro-optic response of the SLG EAM as a function of applied V. It shows that transmission is minimised between $\sim$ -1 and $\sim$ 3 V when $E_{\text{F}} < \hbar\omega/2$ and interband transitions are allowed. When V is increased, E_{F} increases and interband transitions start to become blocked and transmission increases. This design was later improved by adding a second SLG to increase the light-graphene interaction and remove the need for using doped Si WGs [208]. This increased ER to 0.16 dB/μm for a 40 μm device length [208]. In recent years, DSLG EAMs have been shown to support 50 Gb/s [209] data transmission, $\text{FOM}_{\text{EA}} \sim$ 2.2 [210], with BWs up to $\sim$ 35 GHz [210], while SLG EAMs have demonstrated 5$\times$25 Gb/s WDM tranmission [211].

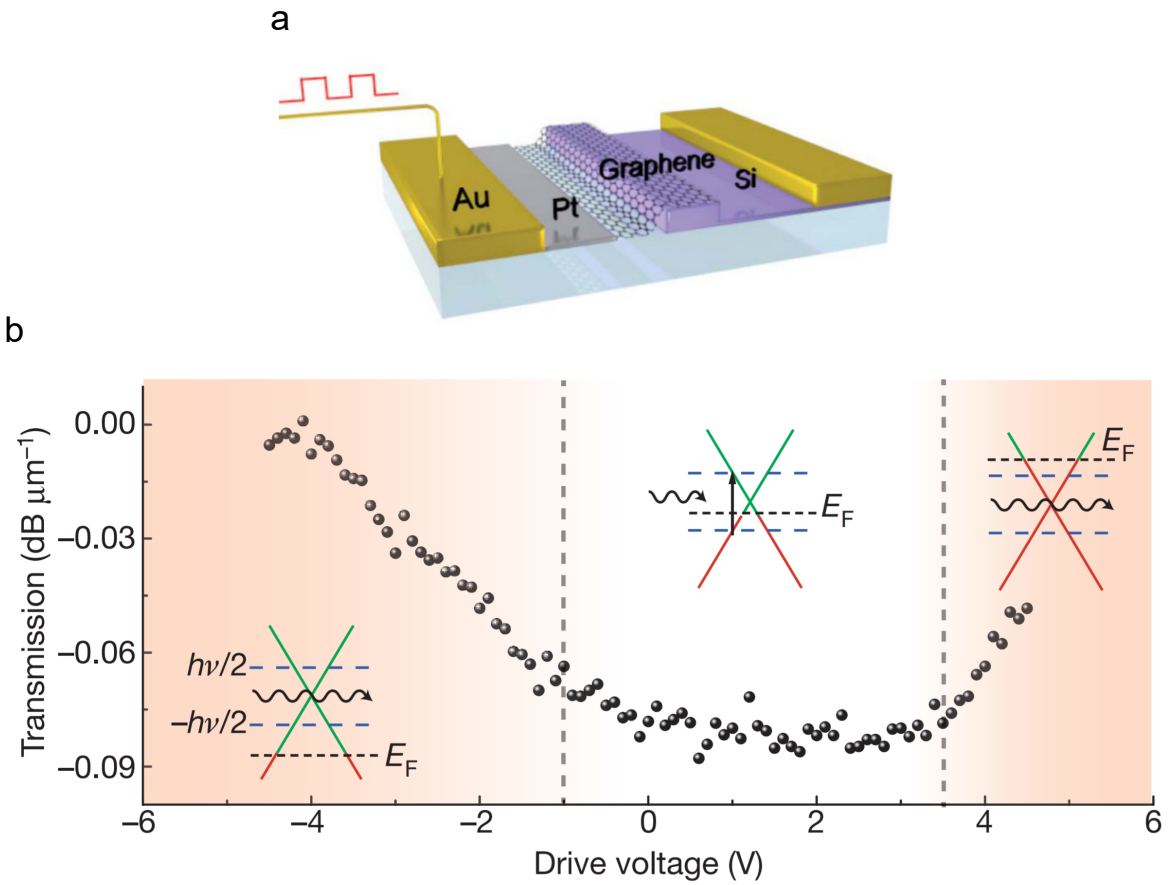

Fig. 4.6 (a) Device schematic of the first graphene-based WG-integrated EAM, (b) measured electro-optic response of SLG EAM as a function of V, adapted from Ref. [207].

Electro-refraction

As well as a change in optical losses, figure 4.5 shows that graphene modulators simultaneously induce a change in n_{eff} [202]. The resulting $\Delta\phi$ from the graphene modulator can be observed when it is is placed on a passive photonic component whose transmission depends on the phase. Typically these are interferometric devices such as a RR [213] or MZI [202, 212], where the induced change in optical loss and n_{eff} affects the observed output interference pattern. Figure 4.7a shows the device schematic and image of a fabricated single layer graphene MZM [212]. Here, an applied V across the Si-SiO_2-SLG capacitor modulates the MZM transmission as shown in figure 4.7b, where the ER depends on the change in optical losses of SLG and λ_{res} depends on Δn_{eff}. This SLG MZM had $V_\pi L \sim 0.28$ V·cm and a 5 GHz bandwidth [212].

DSLG RRMs have also been demonstrated, where an applied V across the DSLG stack modulates the resonant condition and Q-factor of the RR [213]. The DSLG RRM was fabricated on a 30 μm SiN RR and achieved and ER $\sim$ 15 dB per 10 V. Due to the compact

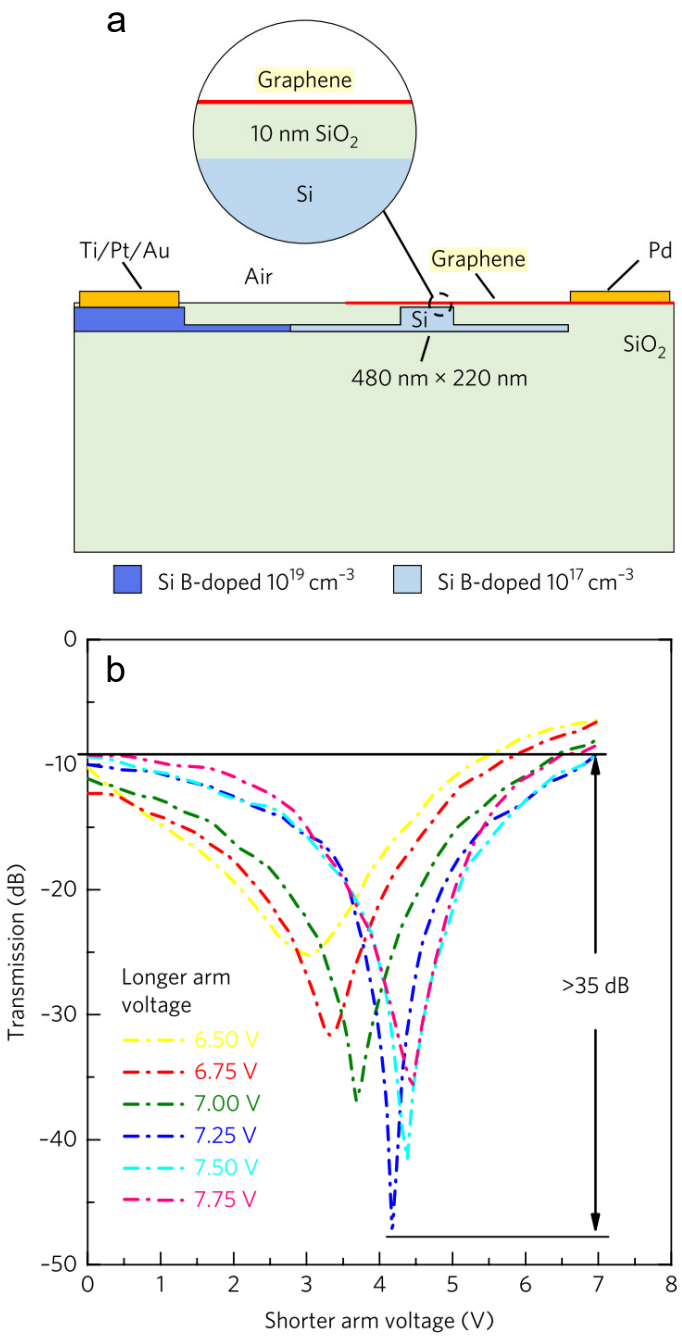

Fig. 4.7 (a) Cross-section of graphene-based MZI phase modulator, (b) optical micrograph of the modulator showing 300 μm and 400 μm SLG active device areas, (c) measured electro-optic response as a function of applied voltage on the longer and shorter arm, adapted from Ref. [212].

size of the DSLG RRM in comparison to the SLG MZM the bandwidth could be increased

to 30 GHz. Speeds exceeding 100 GHz have been predicted for submicron devices with an energy per bit of less than 1 fJ/bit [101].

4.3.4 Performance Comparison

Graphene-based modulators have demonstrated efficient amplitude and phase modulation with superior performance than other technologies. Graphene-based EAMs have demonstrated $\text{FOM}_{\text{EA}} \sim 2.2$ [210], better than that of Ge-on-Si EAMs ($\text{FOM}_{\text{EA}} \sim 1.6$ [91]). Graphene-based modulators have achieved a $V_\pi L \sim 6$ times better than the lowest reported LN [121], and ~ 2 times better than the lowest reported Si [110] phase modulators. However, this corresponds to $\text{FOM}_{\text{ER}} \sim 66$ VdB which is greater than the lowest reported Si (~ 30 VdB [113]), LN (~ 5.4 VdB [121]), and III-V (~ 0.8 VdB [115]) modulators. The high FOM_{ER} is caused by the high IL of graphene-based modulators which is far greater than simulated values. This is likely due to damage done to graphene during processing which increases τ. Whilst BW ~ 30 GHz [213] have been demonstrated with graphene-based modulators, it is far off the BW of Si and LN modulators which reach > 100 GHz [110, 120, 122]. However, both the IL and the BW should be improved with optimised processing techniques that preserve τ and reduce device parasitics which limit the BW.

4.4 Conclusions

Graphene has been shown to be a promising material for opto-electronic applications, and in this chapter I have reviewed the state-of-the-art graphene-based integrated PDs and modulators. GPDs can be designed to use different mechanisms for generating I_{ph} or V_{ph} depending on the operating conditions. I_{d} is a problem for GPDs, so configurations which do not require an applied bias are preferred. These GPDs use the PTE to boost the responsivity without the need of an applied bias, as is the case for GPDs based on the bolometric effect. Not only do GPDs based on the PTE exhibit no I_{d}, they also directly V_{ph} which removes the need for a transimpedance amplifier that is typically used in receivers that use PDs that generate I_{ph}. Bias-free PTE GPDs benefit from large BWs, broadband operation, and zero I_{d} which is not possible with another material. Graphene-based modulators have been demonstrated which take advantage of high μ and electrostatic gating to modulate the optical conductivity via Pauli blocking. Graphene enables the simultaneous modulation of n_{eff} and α, and depending on the operating conditions can be used for amplitude or phase modulation. Graphene-based EAMs, RRMs, and MZMs have previously been demonstrated using a single or double layer of SLG. Graphene is capable of offering a broadband and efficient platform

for photodetection and modulation, which, unlike III-V, Ge, or LN, can be integrated onto Si photonic wafers without the need for wafer bonding or epitaxy.

Chapter 5

Modelling and Design of Graphene Integrated Modulators

5.1 Introduction

I will now discuss the design of the DSLG modulator and discuss the modelling that I used to estimate the performance. The modulator performance will be maximised by increasing the overlap between graphene and the propagating modal field profile. This could be achieved by designing the photonic circuits such that more of the modal field profile propagates outside of the WG core. This can be achieved by using a photonic platform with a reduced Δn or by reducing the WG dimensions. Although, this will ultimately be a trade-off between maximising the modulation efficiency whilst also minimising the insertion loss due to increased levels of scattering of the delocalised mode. However, throughout this project I will be using passive photonic circuits that have already been designed and externally fabricated. Using already prepared photonic circuits meant that I did not have control over the dimensions of the photonic structures used. Therefore, the discussion of design optimisation will focus on the DSLG stack that I will fabricate on top of the planarised photonic substrates that I have available.

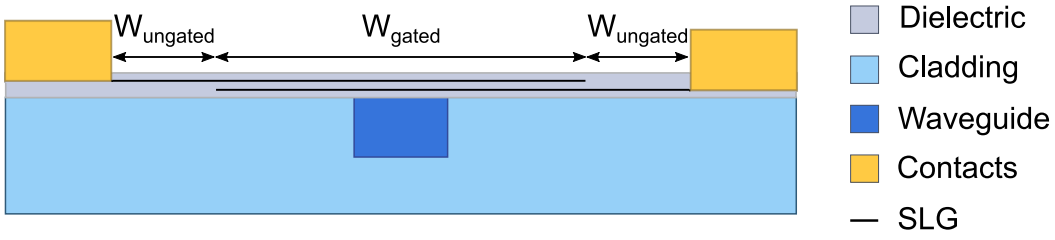

Fig. 5.1 Generic cross-section of double single-layer graphene modulator to be simulated.

A generalised schematic of the proposed structure for the DSLG modulator is shown in figure 5.1. It consists of a planarised passive photonic circuit substrate that contains dielectric WGs embedded within a cladding. I chose to proceed with a double layer design so that I could use one SLG to gate the other SLG, meaning that I did not need to use doped WGs. This is attractive for industry because it will reduce the fabrication cost and complexity associated with doped WGs. The DSLG modulator is fabricated directly on top of the passive substrate and consists of two layers of SLG separated by a dielectric material of thickness d. Each SLG is encapsulated within the dielectric and can be accessed by a metal contact. Encapsulating SLG is critical in order to protect SLG from the environment and preserve its electrical properties. I used Al_2O_3 as the gate dielectric because it can be deposited at low temperature ($<120^oC$ [214]), which helps to prevent SLG damage. The thickness of the encapsulation layer is not critical for device performance, so I have chosen to encapsulate the DSLG stack, above and below, by 10 nm of Al_2O_3. I have chosen to encapsulate the entire DSLG stack to maintain symmetry between the two SLG films so that both SLG will be in the same material environment. When a V is applied across both contacts the SLGs will act as electrodes of a capacitor structure and a perpendicular electric field will be generated. This will shift E_F of the SLGs and thus modulate the optical properties of the SLGs, and in turn, modulate the optical properties of the propagating light. The length of the active region where the SLG overlap is W_{gated}, and the length of the region where the SLG do not overlap is $W_{ungated}$, as shown in figure 5.1.

I optimised the device design by simulating the device performance in the optical and electrical domain. In particular, I used optical simulations to enhance the modulation efficiency and electrical simulations to enhance the operational BW. I used the simulations to investigate the effect of the following parameters of the design, the choice of optical platform, the width of the overlapping region of the two SLG, and the minimum separation of the edge of the contact at the WG. I did not investigate the gate dielectric thickness because I wanted to ensure $V_{bias} < 15$ V. Even though this is not compatible with CMOS voltage requirements, V_{bias} can be supplied from a separate power supply.

5.2 Optical Performance

5.2.1 Simulator Models

The behaviour of the modulator in the optical domain was simulated using software that models the electromagnetic fields within the structure. Electromagnetic fields within a device are modelled by numerically approximating Maxwell's equations with computational

electromagnetic methods [215]. Finite-difference methods achieve this by discretising, or meshing, the electric and magnetic fields by dividing the cross-section of the device into smaller elements. The differential operators in Maxwell's curl equations below can then be approximated by differences in the evaluated fields at each point in the mesh [65]:

$$\begin{aligned} \nabla \times \mathbf{E} &= -\frac{\partial \mathbf{B}}{\partial t} \\ \nabla \times \mathbf{H} &= \mathbf{J} + \frac{\partial \mathbf{D}}{\partial t} \end{aligned} \tag{5.1}$$

The accuracy of the results depends on the relative mesh size compared to the device geometry. Maxwell's equations can be solved in the time-domain to study propagation in time, or in the frequency-domain to study the frequency distribution. Optical performance of the proposed design was simulated using the Finite-Difference Eigenmode (FDE) solver in Lumerical MODE Solutions software. This uses the eigenmode expansion method to calculate the eigenmodes and eigenvalues of Maxwell's equations in the frequency domain [216]. Each solution, or mode, will have its own electromagnetic field profile and complex effective refractive index [12]. The field profile will illustrate the spatial distribution of the field amplitude. From this, I can identify the optimum placement of the modulator so that it interacts with the most intense region of the field as possible. From the simulation I can extract the power contained in the WG by integrating the spatial distribution of the modal power density across the dimensions of the WG.

The optical properties of SLG have been modelled by the surface conductivity approach which treats SLG as a 2d material [20], and is given by equation 4.4. The effect of the SLG modulator is quantified by monitoring the complex refractive index of the mode. The real component of the complex refractive index is used to calculate the resulting ϕ with equation 3.4. The imaginary component of the complex refractive index is used to calculate the resulting α with equation 3.7. The quality of SLG is modelled by the intraband scattering time τ. It is converted into the intraband scattering rate γ used in the simulations by $\tau = \frac{\hbar}{\gamma}[\mathrm{eV}]$. τ can be converted to a mobility, μ, by equation 4.5. An applied V across the modulator will generate a perpendicular electric field that will shift E_F of SLG and therefore modulate $\sigma(\omega)$. E_F is related to V, by considering the sum of the potential applied across the oxide and the surface V due to the accumulated charges at each SLG [97, 206],

$$|V - V_\mathrm{Dirac}| = \frac{e}{C_\mathrm{ox}} \frac{1}{\pi} \left(\frac{E_\mathrm{F}}{\hbar v_F} \right)^2 + 2\frac{|E_\mathrm{F}|}{e} \tag{5.2}$$

The first term of 5.2 represents the potential across the oxide, given by the ratio of the total accumulated charge at each SLG and the oxide capacitance per unit area, C_{ox}. The total accumulated charge is calculated from the accumulated surface carrier density of SLG, which is related to E_F by equation 2.18. The second term of 5.2 represents the total surface V resulting from the charge accumulation layer at both layers of SLG [97].

5.2.2 Optical Performance Metrics

The simulated EO response of the modulator shows the change in complex effective refractive index as a function of E_F. From this I can extract the expected performance of the SLG modulator for both amplitude and phase modulation. For phase modulation I can use the simulated Δn_{eff} over a specific V range and equation 3.4 to calculate the minimum device length, L_{min}, required to achieve $\Delta\phi = \pi/2$. Reaching $\Delta\phi = \pi/2$ will enable two DSLG modulators to be used in a push-pull configuration within a MZM to achieve the required π-phase shift for IQ modulation. This can then be used to calculate the expected phase modulation efficiency, $V_\pi L$. For amplitude modulation I can use the simulated optical losses per unit length over a specific V range to calculate L_{min} required to achieve an ER of at least 6 dB for PAM-4 modulation [8]. The IL for phase or amplitude modulation can be estimated by using the calculated L_{min} and the associated optical losses at V_{bias}. The IL can then be used to calculate FOM_{EA} and FOM_{ER}.

5.2.3 Design Parameters

In order to maximise the modulation efficiency of the device, the interaction between the optical mode and the active region of the modulator needs to be maximised. The active region of the modulator is the section of overlapping SLG which will be doped by the electric field generated from the applied V. Improved modulation efficiency can be achieved by either increasing the size of the active region of the modulator, or by enhancing the electric field at the active region. The active region can be enlarged by increasing W_{gated}. Whereas the intensity of the electric field at the active region can be enhanced by changing the structure of the optical platform such that more of the field profile overlaps with the active region of the modulator. For optical platforms with a smaller Δn, the optical mode will be less confined and overlap more with the active region of the modulator. The device cross-section could be further modified by adding WG material on top of the DSLG modulator in order to pull the optical mode up from the substrate. This would fully embed the active region of the DSLG modulator within the WG and so overlap more with the more intense regions of the field.

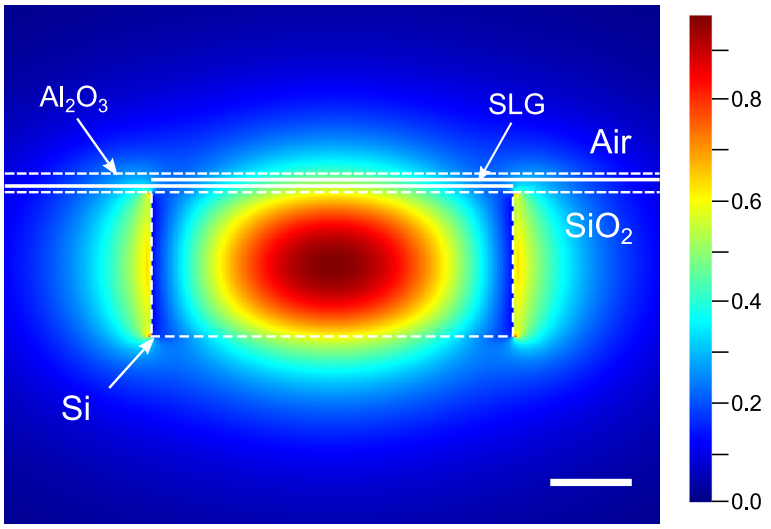

Fig. 5.2 Simulated electric field profile (E_x) of the fundamental transverse electric (TE) mode confined within a 450 nm $\times$ 220 nm Si WG at $\lambda = 1.55\mu$m, scale bar is 100 nm.

The minimum separation between the metal contacts and the WG can be determined by simulation. It is important to ensure the metal contacts are placed far enough away from the edge of the WG to avoid unnecessary optical losses due to the field being absorbed by the contacts. This will depend on the optical platform being used, as modes which are more confined can have contacts placed closer to the WG.

5.2.4 Results

All simulations were performed at λ = 1.55μm and 300 K. Figure 5.2 shows the x-component of the simulated electric field profile of the fundamental TE mode. The simulated structure uses a 450 nm $\times$ 220 nm Si WG embedded in SiO_2 cladding with the DSLG modulator on top. I modelled Si and SiO_2 with the Palik material model with n_{Si} = 3.48 [69] and n_{SiO2} = 1.44 [70] at λ = 1.55 μm respectively. W_{gated} = 450 nm, $W_{ungated}$ = 1 μm, each SLG is encapsulated by 10 nm of Al_2O_3 and separated from the other SLG by 20 nm of Al_2O_3. Al_2O_3 has been modelled with the Palik material model with n_{Al2O3} = 1.75 at λ = 1.55 μm [217]. Red areas represent high intensity regions of the electric field and blue regions represent low intensity regions. The simulation shows that 78% of the optical power is confined within the WG. The remaining optical power is concentrated at the edges of the WG, where the active device region of the modulator is placed.

I simulated the EO response of the modulator by monitoring the complex refractive index of the fundamental TE mode whilst increasing E_F of the SLG. Both SLG have been modelled as intrinsic, where $V = 0$ corresponds to $E_F = 0$ eV. This means that the ungated regions of

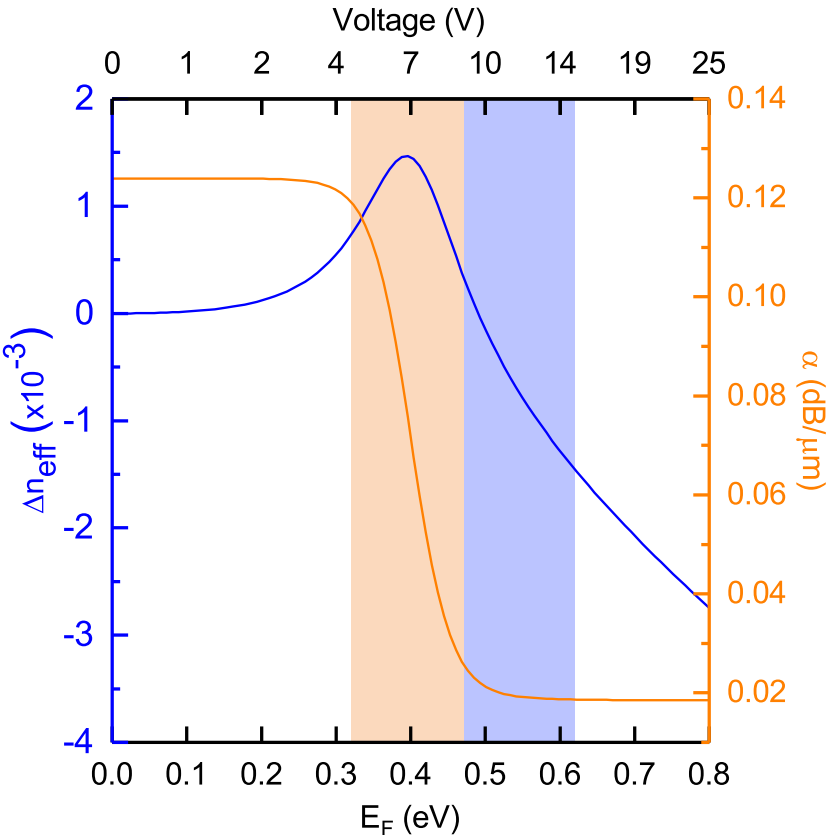

Fig. 5.3 Simulated Δn_{eff} (blue) and α (orange) of the DSLG modulator as a function of E_{F}. The orange region represents the amplitude modulation operating regime, and the blue region represents the phase modulation operating regime. The simulated structure uses 450 nm $\times$ 220 nm Si WGs with $d_{\text{Al2O3}} = 20$ nm ($\varepsilon_r = 8$). Simulation was performed at $\lambda = 1.55\mu$m at 300 K, $\tau = 440$ fs for both SLG, $W_{\text{gated}} = 450$ nm, $W_{\text{ungated}} = 1\ \mu$m ($E_{\text{F}} = 0$ eV).

SLG, that are outside of the active region, will have $E_{\text{F}} = 0$ eV. The simulation uses $\tau = 440$ fs for both SLG, which corresponds to $\mu = 10{,}000$ cm^2/Vs at $E_{\text{F}} = 0.4$ eV. Figure 5.3 shows the simulated EO response of the DSLG modulator in terms of Δn_{eff} and α, as a function of E_{F}. I calculated the V required to gate the device using equation 5.2 and considering $d_{\text{Al2O3}} = 20$ nm ($\varepsilon_r = 8$). Δn_{eff} changes sign as E_{F} increases and will result in an observed positive $\Delta\phi$ for $E_{\text{F}} < 0.5$ eV and a negative $\Delta\phi$ for $E_{\text{F}} > 0.5$ eV. α begin to decrease > 0.2 eV corresponding to the onset of Pauli blocking when interband transitions start to become suppressed. Beyond 0.5 eV, α is minimised and does not significantly change. In this region SLG is considered transparent. The choice of V_{bias}, or operating point, defines the position on the EO response curve. Whereas the amplitude of the driving signal, or peak-to-peak V, V_{pp}, defines the operating range around the operating point. SLG can be used for both amplitude or phase modulation, but in each case the operating region will be different. For

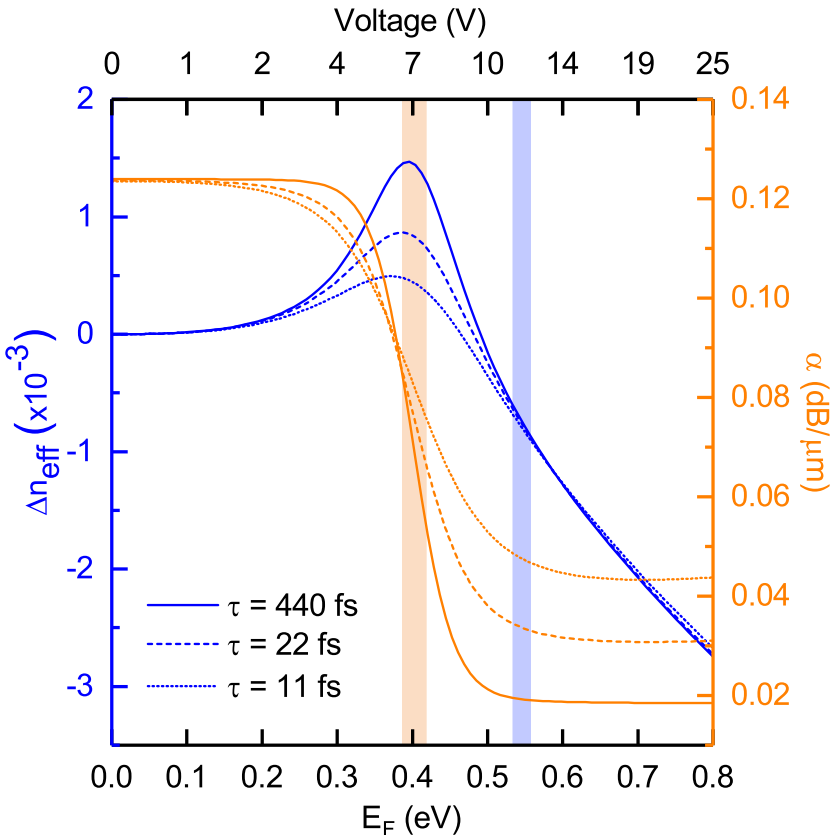

Fig. 5.4 Simulated Δn_{eff} (blue) and α (orange) of the DSLG modulator as a function of E_{F} for different quality of SLG. Solid line corresponds to τ = 440 fs, dashed line to τ = 22 fs, and dotted line for τ = 11 fs. Simulation was performed at λ = 1.55μm at 300 K, with a 450 nm $\times$ 220 nm Si WG, d_{Al2O3} = 20 nm ($\varepsilon_r = 8$), W_{gated} = 450 nm, W_{ungated} = 1 μm (E_{F} = 0 eV).

an amplitude modulator configuration the operating region will be at the transition from high to low absorption. This is shown by the orange region in figure 5.3. The operating point will be at the steepest gradient of $\frac{d\alpha}{dV}$, where the largest change in transmission will occur for the smallest applied V. However, for phase modulation the ideal operating region will be in the transparent region where the optical losses remain constant, but where $\frac{d\Delta n_{\text{eff}}}{dV}$ changes quasi-linearly. This region is shown in blue in figure 5.3, which requires a higher V_{bias} than the amplitude modulation regime.

I repeated the same simulation for τ = 22 and 11 fs to simulate the effect of varying SLG quality on optical performance. This corresponds μ = 500, and 250 cm^2/Vs at E_{F} = 0.4 eV. τ = 440 fs represents higher quality SLG, however more moderate values of 22 and 11 fs were chosen to replicate the predicted decrease in μ after SLG processing. The simulated EO

curves for each quality of SLG are shown in figure 5.4. The operating regimes for amplitude modulation (orange) and phase modulation (blue) have been limited to V_{pp} = 1 V so that the DSLG modulator can comply with CMOS voltage requirements [97]. Firstly I will calculate the simulated performance metrics for the case of amplitude modulation considering V_{bias} corresponding to E_F = 0.4 eV. I extracted the expected $\Delta\alpha$ per volt for each τ and calculated L_{min} in order to reach an ER of 6 dB. I calculated the IL based on the minimum optical losses during operation, which occurs at $V_{bias} + V_{pp}/2$. The extracted performance metrics are summarised in table 5.1. L_{min} is in the order of hundreds of μm's, however, even for τ = 440 fs, L_{min} still results in a significant IL that limits FOM_{EA} to < 1. This is due to V_{bias} and a small V_{pp} that makes it difficult to access the low-loss regime. A larger ER is needed between the high-loss regime ($\hbar\omega \geq 2E_F$) and the low-loss regime ($\hbar\omega \leq 2E_F$) to improve the modulation efficiency whilst keeping the same V_{pp}. If the full ER could be accessed with V_{pp} = 1 V then L_{min} could be reduced to 57 μm for τ = 440 fs and the IL would be reduced to $\sim$ 1 dB. The ER can be increased and the α_{min} reduced by using SLG with the highest τ possible. This is shown in figure 5.4 where the ER increases by $\sim$ 32% and the α_{min} decreases by $\sim$ 42% by using SLG with τ = 440 fs instead of τ = 11 fs.

τ (fs)	$\Delta\alpha$ (dB/cm)	L_{min} (μm)	α (dB/cm)	FOM_{EA}
440	-305	197	525	0.58
22	-187	321	655	0.29
11	-126	477	752	0.17

Table 5.1 Simulated performance metrics of DSLG amplitude modulator, assuming ER = 6 dB, V_{bias} = 6 V, and V_{pp} = 1 V.

Now I will move to phase modulation where V_{bias} will be at > 0.5 eV where there is still a linear change in Δn_{eff}, but interband transitions are blocked and α remains constant. Considering V_{pp} = 1 V, I extracted the expected Δn_{eff} and then calculated L_{min} to achieve $\Delta\phi = \pi/2$. I calculated the IL from the minimum optical losses during operation, which occurs at $V_{bias} + V_{pp}/2$. This is summarised in table 5.2. We see that L_{min} is longer for phase modulation than for amplitude modulation. This is because we have chosen to operate in the low-loss regime where $\frac{\Delta n_{eff}}{dV}$ is not at its maximum. Even though this is not the optimum working point for phase modulation, it will ensure that amplitude modulation is minimised, which is required for modulation schemes that require pure phase modulation. This makes it possible to reduce α by $\sim$ 50% as compared to amplitude modulation. $V_\pi L$ is better than the lowest reported LN and Si phase modulators [110, 121]. The low $V_\pi L$ means that only mm long devices are needed to reach a π phase shift instead of the cm long LN or Si devices. Miniaturising device lengths will enable increased circuit densities and therefore reduced

power consumption from electrical interconnect.

τ (fs)	Δn_{eff} ($\times 10^{-3}$)	L_{min} (μm)	α (dB/cm)	$V_\pi L$ (V·cm)	FOM_{ER} (VdB)
440	-0.268	1446	190	0.29	55
22	-0.249	1558	330	0.31	103
11	-0.221	1752	467	0.35	168

Table 5.2 Simulated performance metrics of DSLG phase modulator, assuming $\Delta\phi = \pi/2$, V_{bias} = 11 V, and $V_{\text{pp}} = 1V$.

The previous simulations have all considered an active region limited to the size of the WG. In order to increase the modulation efficiency, the interaction between the field profile and the active region needs to be increased. By sweeping W_{gated} I can see the effect it has on the optical performance in terms of modulation efficiency and optical losses. Increasing W_{gated} should improve the optical performance of the DSLG modulator, because of the increased active area, but it will also impact other parameters such as the cut-off frequency. The structure with the minimum device active area is defined when the SLG only overlaps above the WG. The structure with the maximum device active area is defined when the SLG overlaps over the majority of the area between the contacts, with only a small region left ungated ($\sim$ 10 nm) on either side. The simulated structure, shown in figure 5.5c, considers a 450 nm $\times$ 220 nm Si WG with d_{Al2O3} = 20 nm ($\varepsilon_r = 8$). Both SLG were modelled with τ = 440 fs, W_{ungated} = 1 μm and ungated sections had E_{F} = 0 eV. Figure 5.5a shows the simulated $\Delta\alpha$ of a DSLG EAM operated at V_{bias} = 6 V with V_{pp} = 1 V, where α is extracted at V_{bias} + V_{pp}/2. Figure 5.5b shows the simulated Δn_{eff} of a DSLG phase modulator operated at V_{bias} = 11 V with V_{pp} = 1 V, where α is extracted at V_{bias} + V_{pp}/2. The blue region on figures 5.5a, b, and d represent the width of the WG which is 450 nm. It is apparent that if W_{gated} is smaller than the width of the WG that the optical performance will be reduced, shown by the decrease in $\Delta\alpha$ and Δn_{eff}. Figure 5.5a and b show that as W_{gated} increases from 450 nm to 1.05 μm that $\Delta\alpha$ and Δn_{eff} increase by $\sim$ 34%, and that α decreases by $\sim$ 93 %. Importantly, figure 5.5a and b show that increasing W_{gated} above $\sim$ 1 μm does not further increase the modulation efficiency or decrease optical losses. The associated performance metrics are summarised in table 5.3 and 5.4. For clarity I have considered the case of minimum active area and maximum active area. The increased modulation efficiency leads to L_{min} reducing from $\sim$ 197 to $\sim$ 147 μm for an EAM configuration, and from $\sim$ 1.4 mm to $\sim$ 1 mm for phase modulation. Increasing W_{gated} reduces optical loss because there is a smaller proportion of ungated SLG that is at a lower doping, and therefore absorbs more light. When W_{gated} is greater than 1 μm this results in optical losses of $>$ 400 dB/cm for amplitude modulation,

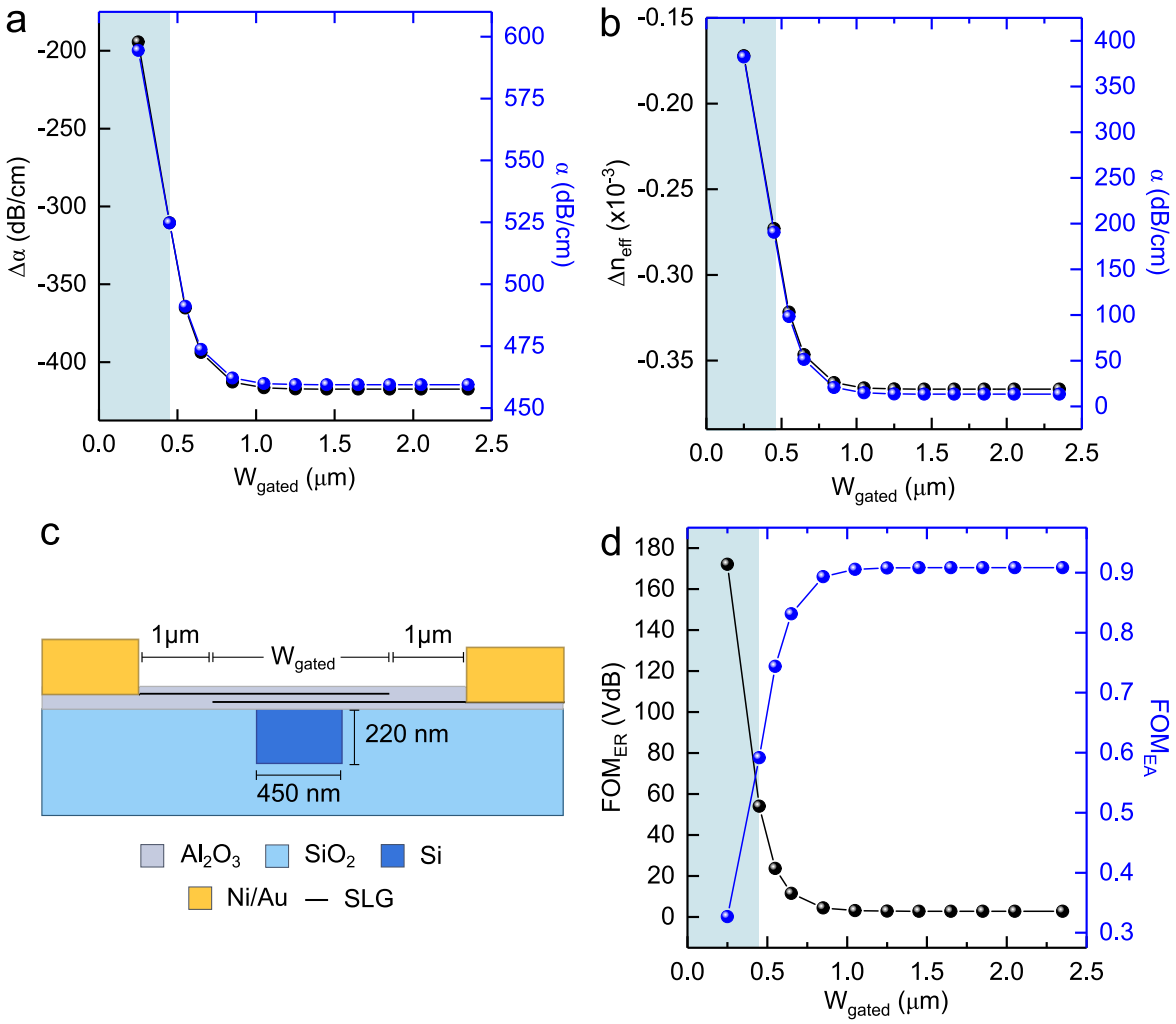

Fig. 5.5 a) Simulated $\Delta\alpha$ and α as a function of W_{gated} for a DSLG EAM with V_{bias} = 6 V and V_{pp} = 1 V, b) simulated Δn_{eff} and α as a function of W_{gated} for a DSLG phase modulator with V_{bias} = 11 V and V_{pp} = 1V, c) simulated device structure illustrating W_{gated}, d) simulated FOM_{ER} and FOM_{EA} as a function of W_{gated}. All simulations consider τ = 440 fs, d_{Al2O3} = 20 nm ($\varepsilon_r = 8$), and E_{F} = 0 eV for the ungated SLG regions. Blue regions on a, b, and d represent the width of the WG.

but < 20 dB/cm for phase modulation. Whilst the optical losses for amplitude modulation are impractical for real-world applications, the optical losses for phase modulation are more manageable. Figure 5.5d shows the resulting FOM_{EA} and FOM_{ER} as a function of W_{gated}. Benefiting from increased modulation efficiency and decreased optical losses, figure 5.5c shows that as W_{gated} is increased from 450 nm to 1.05 μm that FOM_{ER} decreases by $\sim$ 95%, and FOM_{EA} increases by $\sim$ 53%. Therefore, it is clear that a small increase in W_{gated} can increase the overall optical performance of DSLG EAMs and phase modulators. The final choice of W_{gated} will be a trade-off between maximising optical performance whilst maintaining a reasonable $f_{3\text{dB}}$. Here, a larger W_{gated} will lead to a reduction in $f_{3\text{dB}}$ owing to the increased device capacitance. The relationship between W_{gated} and $f_{3\text{dB}}$ will be discussed in the next section.

Active Area	$\Delta\alpha$ (dB/cm)	L_{min} (μm)	α (dB/cm)	FOM_{EA}
Minimum	-305	197	525	0.58
Maximum	-410	147	459	0.89

Table 5.3 Simulated performance metrics of DSLG EAM for minimum and maximum active region size, assuming ER = 6 dB, V_{bias} = 6 V, and V_{pp} = 1 V.

Active Area	Δn_{eff} ($\times 10^{-3}$)	L_{min} (μm)	α (dB/cm)	$\text{V}_\pi L$ (V·cm)	FOM_{ER} (VdB)
Minimum	-0.268	1446	190	0.29	55
Maximum	-0.360	1076	13	0.22	3

Table 5.4 Simulated performance metrics of DSLG phase modulator for minimum and maximum active region size, assuming $\Delta\phi = \pi/2$, V_{bias} = 11 V, and $V_{\text{pp}} = 1V$.

Another approach to increase the interaction between the field profile and the modulator is to use the SiN optical platform that has a lower Δn. The simulated structure now consists of SiN WGs embedded in SiO_2 cladding, where the Kischkat material model was used for SiN with n_{SiN} = 2.46 [74] at λ = 1.55 μm. Δn for the SiN platform is $\sim$ 20% lower than Si (n_{Si} = 3.42), resulting in a more delocalised mode. This is beneficial because a larger area of the mode field profile will overlap with the active region of the modulator, resulting in an increased modulation efficiency. Whilst the reduced Δn for the SiN platform improves the modulation efficiency it will also decrease the overall circuit density because the dimensions of single-mode SiN WGs are bigger than for Si WGs. Wider single-mode WGs would lead to wider modulators, so would need to be taken into account when considering the BW of the modulator which is dependent on the device capacitance and resistance. Figure 5.6b shows

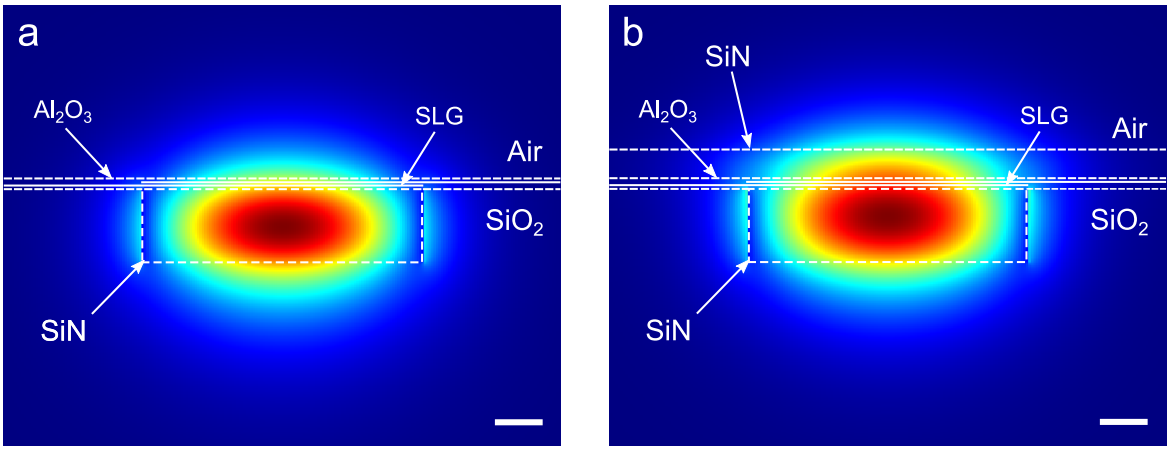

Fig. 5.6 Simulated electric field profile (E_x) of the fundamental transverse electric (TE) mode confined within a 1.2 μm $\times$ 260 nm SiN WG. (a) strip WG structure, (b) inverted ridge WG structure with 100 nm SiN on top of modulator. Scale bars are 200 nm.

the field profile of the x-component of the electric field for the fundamental transverse electric (TE) mode of a single-mode SiN strip WG with dimensions 1.2 μm $\times$ 260 nm. Now $\sim$ 70% of the optical power is contained within the WG core for the SiN strip WG. This is lower than the Si strip WG in figure 5.2 which has $\sim$ 78% of the power contained within the core. The overlap between the mode profile and the active region can be further increased by using an inverted ridge WG structure by depositing SiN on top of the SLG modulator. The top layer draws the mode up so that the active region intersects with a higher intensity region of the electric field. This is shown in figure 5.6b where $\sim$ 62% of the power is confined within the WG core, resulting in even more of the modal profile overlapping with the active region of the SLG modulator. Further depositions of Si or SiN after fabrication of the modulator could damage the SLG and degrade τ due to the high deposition temperatures (up to 400^{o}C for PECVD). Therefore, the benefits of improved modulation efficiency and the negative impact of further processing would need to be fully considered.

The simulated EO response of the DSLG modulator on a SiN strip WG and embedded within a SiN inverted ridge WG is shown in figure 5.7. I consider the device structure with the minimum active region so that we can compare the expected performance on the SiN platform with the previous simulations. Both SLG had τ = 440 fs and ungated sections had E_F = 0 eV. The increased interaction between the more delocalised mode, in comparison to Si, and the active area can be seen from the larger ER between the high and low-loss regimes. In the high-loss regime ($E_F < 0.2$ eV) more of the modal profile is absorbed by the active region, and then as E_F is increased a larger proportion of the active region can be used to control the transition to the low-loss regime. This is why we see the ER between the high and low-loss

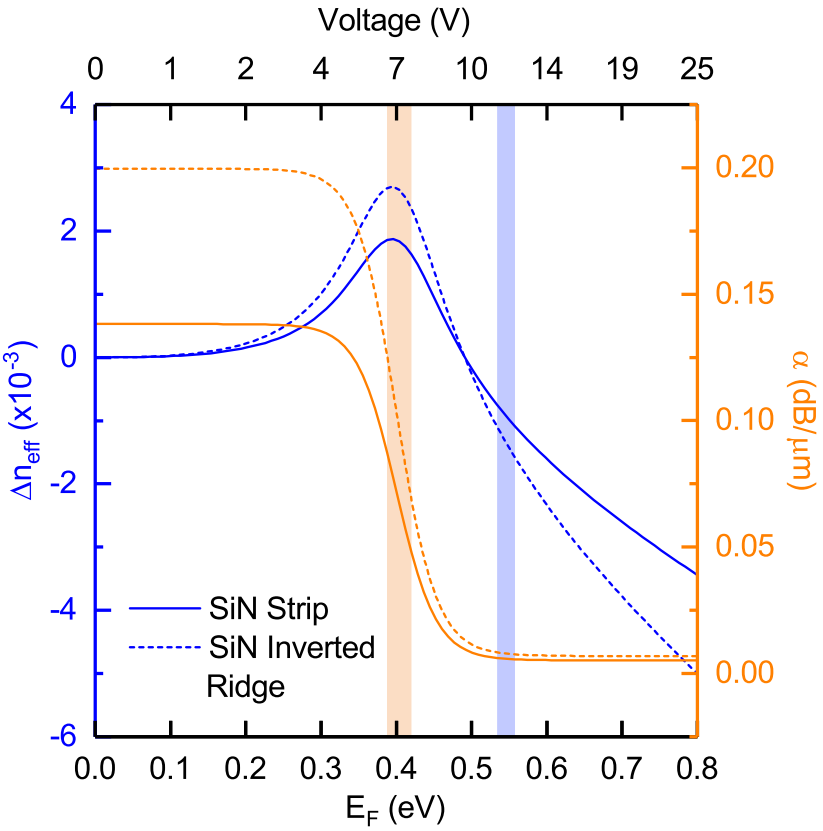

Fig. 5.7 Comparing the simulated Δn_{eff} (blue) and α (orange) of the DSLG modulator on a 1.2 μm $\times$ 260 nm SiN strip WG (solid), and 1.2 μm $\times$ 260 nm inverted SiN ridge WG (dashed) with 100 nm SiN slab on top of the modulator. Operating regions are highlighted for amplitude modulation (orange) and phase modulation (blue) considering V_{pp} = 1 V. τ = 440 fs for both SLG, W_{gated} = 1.2 μm, W_{ungated} = 1.6 μm (E_{F} = 0 eV), and d_{Al2O3} = 20 nm (ε_r = 8).

regimes increase by $\sim$ 44% from -0.13 dB/μm for the SiN strip WG to -0.19 dB/μm for the inverted ridge WG. If the whole ER could be accessed by V_{pp} this would lead to minimum EAM device lengths $<$ 45 μm. Considering V_{pp} = 1 V, the extracted device parameters for the EAM configuration are shown in table 5.5. The device parameters are compared to the Si strip WG shown in figure 5.3, however it is important to note that the Si and SiN platforms are not like-for-like because the WG dimensions for single-mode operation are different for Si and SiN platforms. The increased modulation efficiency reduces L_{min} for amplitude modulation as compared to the Si platform. For operation within the orange region of figure 5.7, $L_{\text{min}} \sim$ 155 μm and $\sim$ 107 μm for the SiN strip and inverted ridge WG respectively. Unfortunately, the increased interaction between the more delocalised mode and the active area also results in a $\sim$ 43% increase in α for the SiN inverted ridge structure compared to the SiN strip WG. For both SiN WG structures FOM_{EA} is higher than that for Si strip

WGs due to the increased modulation efficiency. There is not a great difference between the FOM_{EA} for the SiN strip and inverted ridge WG because the increased modulation efficiency is balanced by the increased IL.

Optical Platform	Confinement Factor	$\Delta\alpha$ (dB/cm)	L_{min} (μm)	α (dB/cm)	FOM_{EA}
Si strip	78%	-305	197	525	0.58
SiN strip	70%	-388	155	478	0.81
SiN inverted ridge	62%	-561	107	686	0.82

Table 5.5 Comparison of simulated performance metrics of DSLG amplitude modulator on different optical platforms, assuming ER = 6 dB, V_{bias} = 6 V, and V_{pp} = 1 V. IL has been extracted at $V_{bias} + V_{pp}/2$

For the phase modulator configuration we see an increased modulation efficiency for the SiN platform compared to Si, leading to reduced L_{min}. Like the EAM configuration, the SiN inverted ridge structure is $\sim$ 44% more efficient than the SiN strip WG for phase modulation. This enables $V_\pi L$ to reduce by $\sim$ 70% from 0.23 to 0.16 V·cm. α is $\sim$ 38% higher for the SiN inverted ridge WG compared to the SiN strip WG. The increase in α is attributed to greater absorption by SLG resulting from the more delocalised mode of the SiN inverted ridge structure.

Optical platform	Confinement Factor	Δn_{eff} ($\times 10^{-3}$)	L_{min} (μm)	α (dB/cm)	$V_\pi L$ (V·cm)	FOM_{ER} VdB
Si strip	78%	-0.268	1446	190	0.29	55
SiN strip	70%	-0.338	1146	56	0.22	13
SiN inverted ridge	62%	-0.490	791	76	0.16	12

Table 5.6 Comparison of simulated performance metrics of SLG phase modulator on different optical platforms, assuming $\phi = \pi/2$, V_{bias} = 11 V, and V_{pp} = 1 V. IL has been extracted at $V_{bias} + V_{pp}/2$

As well as the difference in modulation efficiency due to the different modal confinement of the Si and SiN platforms, we also see that it affects the minimum required distance between the contacts and the WG. Si and SiN WGs were simulated with varying distances separating the contacts and the edge of the WG. The extracted optical losses were then analysed to determine the minimum safe distance where the contacts do not interact with the optical mode. Figure 5.8 shows the comparison of the different platforms. For the Si platform, there is an increase in optical loss when the contacts are placed < 0.8 μm from the WG. To account for fabrication tolerances I have chosen to use a distance of 1 μm to ensure that there are no additional losses. For the SiN platform however, it can be seen that a larger distance

is required due to the more delocalised optical mode. The optical losses start to increase below 1.5 μm, so I have chosen to use a minimum distance of 1.6 μm which also allows for fabrication errors.

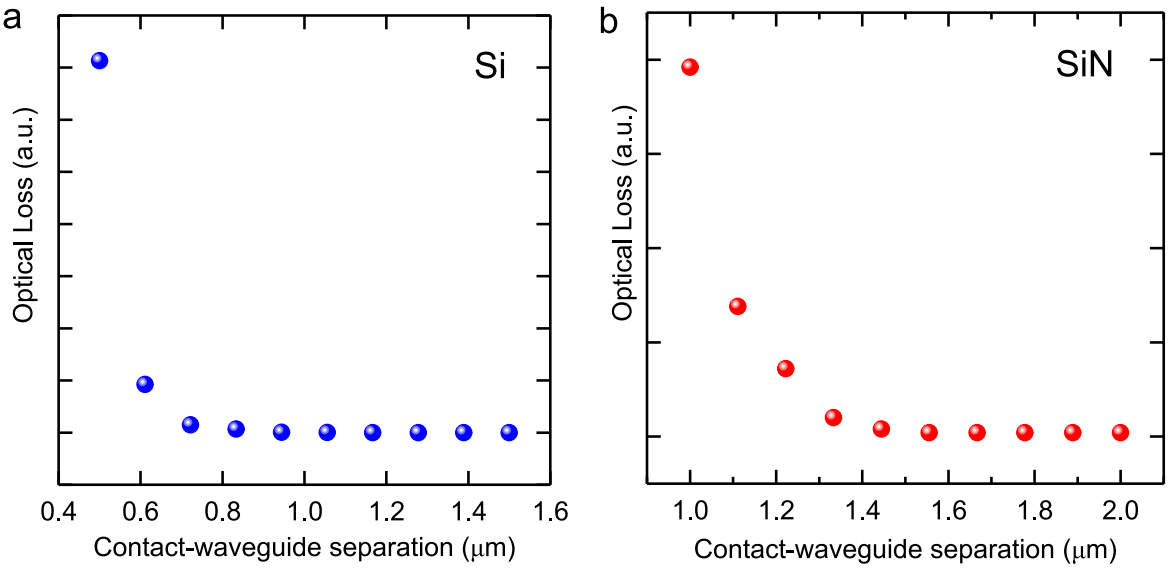

Fig. 5.8 Simulated optical losses for Si and SiN single-mode WGs with different distances separating the contacts and the WG at λ = 1.55 μm. (a) Si strip WG 450 nm $\times$ 220 nm , (b) SiN strip WG 1.2 μm $\times$ 260 nm.

5.3 Electrical Performance

5.3.1 Circuit Models

The operational speed of the device is defined by the cut-off frequency, f_{3dB}, at which the power of the modulated signal has decreased by half [94]. The dominant factor that limits the cut-off of the DSLG modulator is the RC response which is given by the product of the device resistance, R, and capacitance C, [10]. This was estimated by electrical modelling where I considered the different contributions to the total circuit impedance $Z_T(\omega)$. SLG has been modelled by equivalent resistors and capacitors connected in series. As in the previous section, the quality of graphene, and its effect on its electrical properties, is modelled by τ.

I calculated R by considering R_S as a function of E_F. The gated sections and ungated sections of SLG are modelled with different E_F. $\sigma_{d.c}$ is related to N and μ by equation 2.15. $\sigma_{d.c}$ can be rewritten in terms of E_F using equation 2.18. Equation 4.5 can then be used to relate μ and τ such that,

$$\sigma_{\text{d.c.}} = \frac{e^2 \tau E_{\text{F}}}{\hbar^2 \pi} + \frac{4e^2}{h} \tag{5.3}$$

where the second term is σ_{min} [21]. From $\sigma_{\text{d.c.}}$ we can calculate the sheet resistance R_{S} by equation 2.12. R_{S} is then normalised by the channel geometry to yield the resistive component for each SLG.

$$R = \frac{L}{W} R_{\text{S}} \tag{5.4}$$

Therefore, by using different values of τ and E_{F} I can model the effect of different qualities of SLG and doping on the R. The contact resistance, R_{C}, for each SLG is calculated by normalising a reference value, $R_{\text{C,ref}}$, given in $\Omega \cdot \mu$m, to a contact length L_{C} in μm.

$$R_{\text{C}} = \frac{R_{\text{C,ref}}}{L_{\text{C}}} \tag{5.5}$$

C is given as a series contribution of the quantum capacitance, C_{Q}, for each SLG, and the oxide capacitance, C_{ox}. C_{Q} is modelled for different E_{F} by calculating the carrier concentration N. C_{Q} is related to N by [218],

$$C_{\text{Q}} = \frac{2e^2 \sqrt{N}}{\hbar v_F \sqrt{\pi}} \tag{5.6}$$

To account for charged impurities at the SLG-Al_2O_3 interface and defects introduced during growth or device fabrication I modelled N as the sum of the doping-dependent carrier concentration and the additional carrier concentration resulting from impurities [218] and defects [219]. The doping-dependent carrier concentration is given by 2.18. I assumed a typical impurity density of $\sim 10^{12}\text{cm}^{-2}$ which leads to an effective increase in carrier concentration of $\sim 10^{11}\text{cm}^{-2}$ [218]. I estimate the effective increase in carrier concentration due to point-defects to be $\sim 10^{10}\text{cm}^{-2}$ [219].

The frequency response of the modulator was modelled by its equivalent RC circuit with impedance $Z_{\text{T}}(\omega)$. $Z_{\text{T}}(\omega)$ is defined in terms of the RC contributions from the contacts and each SLG connected in series such that,

$$Z_{\text{T}}(\omega) = R_{\text{C,1}} + R_{\text{C,2}} + R_{\text{ungated,1}} + R_{\text{ungated,2}} + Z_{\text{C}}(\omega) \tag{5.7}$$

where R_{C} is the resistance from the contact of each SLG, R_{ungated} is the resistance contribution from the ungated SLG sections, and $Z_{\text{C}}(\omega)$ is the impedance of the overlapping SLG sections. Each SLG was split into gated and ungated sections depending on whether the

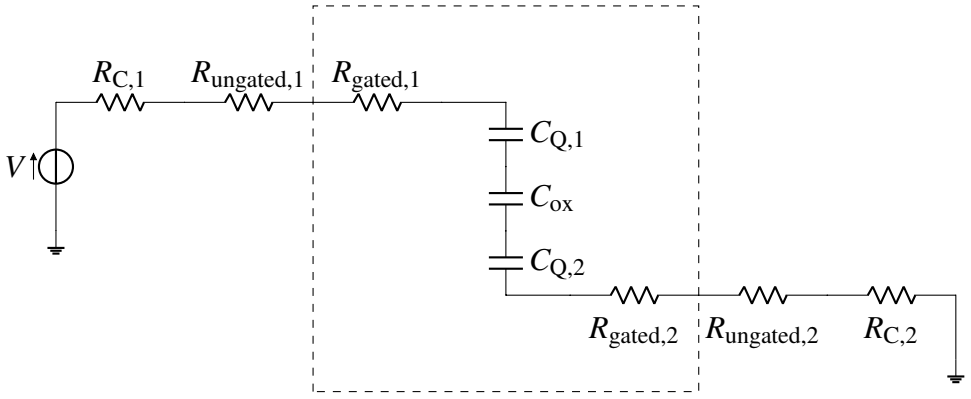

Fig. 5.9 Equivalent electrical circuit for SLG modulator used to calculate the total circuit impedance $Z_T(\omega)$. Components contained within the dashed line represent the components that contribute to the impedance of the overlapping SLG section $Z_C(\omega)$.

SLG was part of the overlapping region. Ungated sections are expected to be at a lower E_F than gated sections, and therefore have an increased resistance contribution. These ungated sections are expressed as a purely resistive component that does not depend on frequency. The overlapping region forms a capacitor structure that has an impedance of $Z_C(\omega)$. Each SLG acts as an electrode that will have additional capacitive and resistive contributions to the circuit due to the finite conductivity of SLG. Therefore, $Z_C(\omega)$ represents the geometrical capacitance, C_{ox}, of the overlapping region as well as the RC contribution from each electrode. This is given as the resistance of the gated sections, R_{gated}, and the equivalent capacitance C_{eq},

$$Z_C(\omega) = R_{gated,1} + R_{gated,2} + \frac{1}{j\omega C_{eq}} \tag{5.8}$$

Where C_{eq} is modelled as a series combination of C_Q of each SLG and C_{ox}, such that,

$$C_{eq} = \frac{1}{\frac{1}{C_{ox}} + \frac{1}{C_{Q,1}} + \frac{1}{C_{Q,2}}} \tag{5.9}$$

The equivalent circuit is shown in figure 5.9 where the components contained within the dashed line represent the components that contribute to $Z_C(\omega)$.

5.3.2 Electrical Performance Metrics

I extract the frequency response of the DSLG modulator by modelling the frequency dependent current, $I(\omega)$, that flows through the circuit at a nominal drive V, V_D. Using Ohm's law and the simulated $Z_T(\omega)$, $I(\omega)$ is given by,

$$I(\omega) = \frac{V_{\mathrm{D}}}{Z_{\mathrm{T}}(\omega)} \tag{5.10}$$

The frequency response of the DSLG modulator itself depends on the V drop across the modulator, $V_{\mathrm{M}}(\omega)$. When $I(\omega)$ starts to flow and $V_{\mathrm{M}}(\omega)$ goes to 0 the modulator is no longer considered to be operational. Considering that C_{ox} is the dominant capacitance contribution, the impedance of the modulator, $Z_{\mathrm{M}}(\omega)$, is given by $Z_{\mathrm{M}}(\omega) = 1/j\omega C_{\mathrm{ox}}$ [10], such that,

$$V_{\mathrm{M}}(\omega) = \frac{I(\omega)}{j\omega C_{\mathrm{ox}}} \tag{5.11}$$

By substituting $I(\omega)$ from equation 5.10 into equation 5.11, $V_{\mathrm{M}}(\omega)$ is normalised by V_{D} and defined in terms of the R and C.

$$\frac{V_{\mathrm{M}}(\omega)}{V_{\mathrm{D}}} = \frac{1}{\frac{C_{\mathrm{ox}}}{C} + j\omega R C_{\mathrm{ox}}} \tag{5.12}$$

The DSLG modulator BW is given by $f_{3\mathrm{dB}}$ that is defined as the frequency where the transmitted power, $P_{\mathrm{out}}/P_{\mathrm{in}}$ drops by 3 dB. By converting V_{M} in terms of P ($P \propto V^2$ [10]), this is given by,

$$\frac{P_{\mathrm{out}}}{P_{\mathrm{in}}} = 20\log_{10}\frac{V_{\mathrm{M}}(\omega = f_{3\mathrm{dB}})}{V_{\mathrm{M}}(\omega = 0)} = -3\mathrm{dB} \tag{5.13}$$

In terms of V this corresponds to $V_{\mathrm{M}}(\omega)$ dropping to $\frac{1}{\sqrt{2}}$ of its original value. Figure 5.10a shows the simulated $Z_{\mathrm{T}}(\omega)$ and $V_{\mathrm{M}}(\omega)/V_{\mathrm{D}}$ as a function of frequency, with $f_{3\mathrm{dB}}$ marked with a dashed line. For frequencies $< f_{3\mathrm{dB}}$ the circuit shows capacitive behaviour where the $Z_{\mathrm{T}}(\omega)$ drops linearly on a logarithmic scale. For frequencies $> f_{3\mathrm{dB}}$ current begins to flow through the DSLG modulator and the circuit tends to resistive behaviour with constant Z_{T}. Figure 5.10b shows the resulting transmitted power associated with the simulated $Z_{\mathrm{T}}(\omega)$ as a function of frequency. $f_{3\mathrm{dB}}$ is shown by the dashed line.

5.3.3 Design Parameters

Equation 5.12 shows that $f_{3\mathrm{dB}}$ can be increased by decreasing R and C. For the DSLG structure R can be reduced by optimising R_{C} and increasing τ. R_{C} is reduced by choosing fabrication methods that increase the ratio of edges to surface contact to the SLG [60]. The other contributions to R come from R_{S} of SLG. Using the highest quality of SLG, with the highest τ, is crucial for reducing R_{S} of each SLG. This is particularly important for the ungated SLG sections which will have a higher resistance because E_{F} is lower than the gated SLG sections.

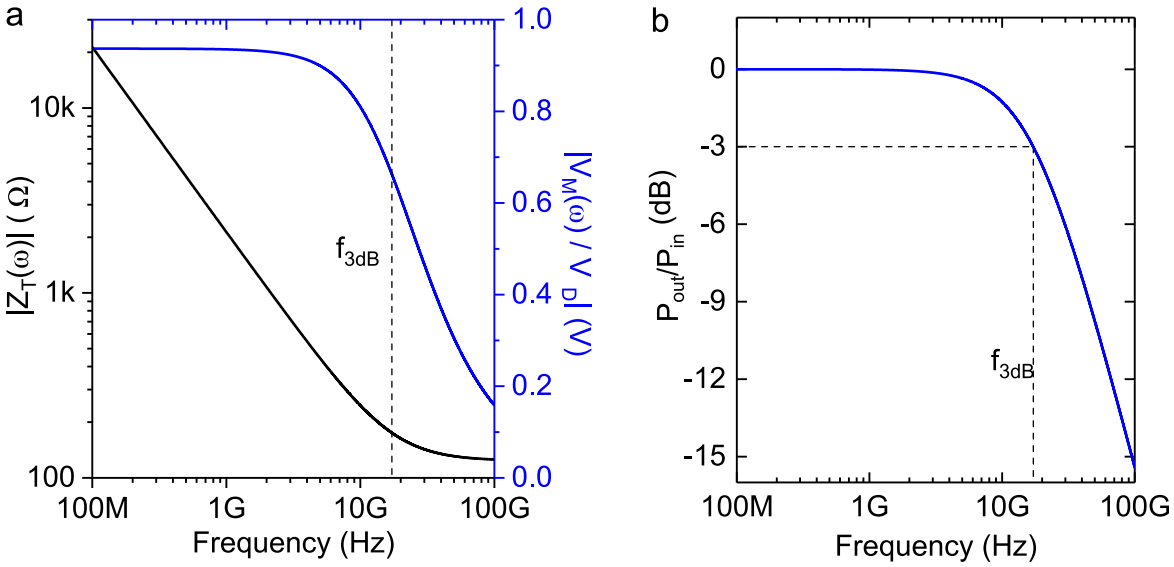

Fig. 5.10 Simulated (a) $Z_T(\omega)$ and $V_M(\omega)/V_D$ as a function of frequency, and (b) transmitted power as a function of frequency, in both plots f_{3dB} is illustrated with a dashed line.

On the other hand, C can be reduced by optimising the geometry of the overlapping region of the SLG. C could also be reduced by using a gate dielectric material with a lower ε_r, however this will increase the required V_{bias}. In theory, C will be minimised by minimising W_{gated}. However, this will increase the proportion of SLG that is ungated and hence increase R. The optimum size of W_{gated} will be a trade-off between reducing R by minimising $W_{ungated}$, but also reducing C by minimising W_{gated}.

5.3.4 Results

The frequency response was simulated considering a 50 μm DSLG modulator with a contact-contact separation of 2.45 μm, consisting of a 450 nm wide Si WG and a contact-WG separation of 1 μm. The simulations uses d_{Al2O3} = 20 nm and ε_r = 8. The gated sections were modelled with E_F = 0.4 eV to coincide with the onset of Pauli Blocking for λ = 1.55 μm. C_Q for each SLG was calculated with an estimated additional carrier concentration of $\approx 10^{10}$ cm^{-2} from defects and $\approx 10^{11}$ cm^{-2} from impurities. Figure 5.11a shows the simulated f_{3dB} as a function of E_F of the ungated SLG sections for τ = 440 fs (green), 110 fs (yellow), 22 fs (blue), and 11 fs (red). Assuming intrinsic SLG, as in the previous section, 5.11a shows that for all τ, f_{3dB} is limited to $<$ 10 GHz when E_F = 0 eV for the ungated SLG sections. This is due to the high R_S when E_F of the ungated sections is 0 eV. As E_F of the ungated sections increases to 0.1 eV, f_{3dB} dramatically increases as R_S rapidly decreases. The increase in f_{3dB} is most pronounced for SLG with the highest τ, where f_{3dB} increases from 7 GHz at E_F = 0

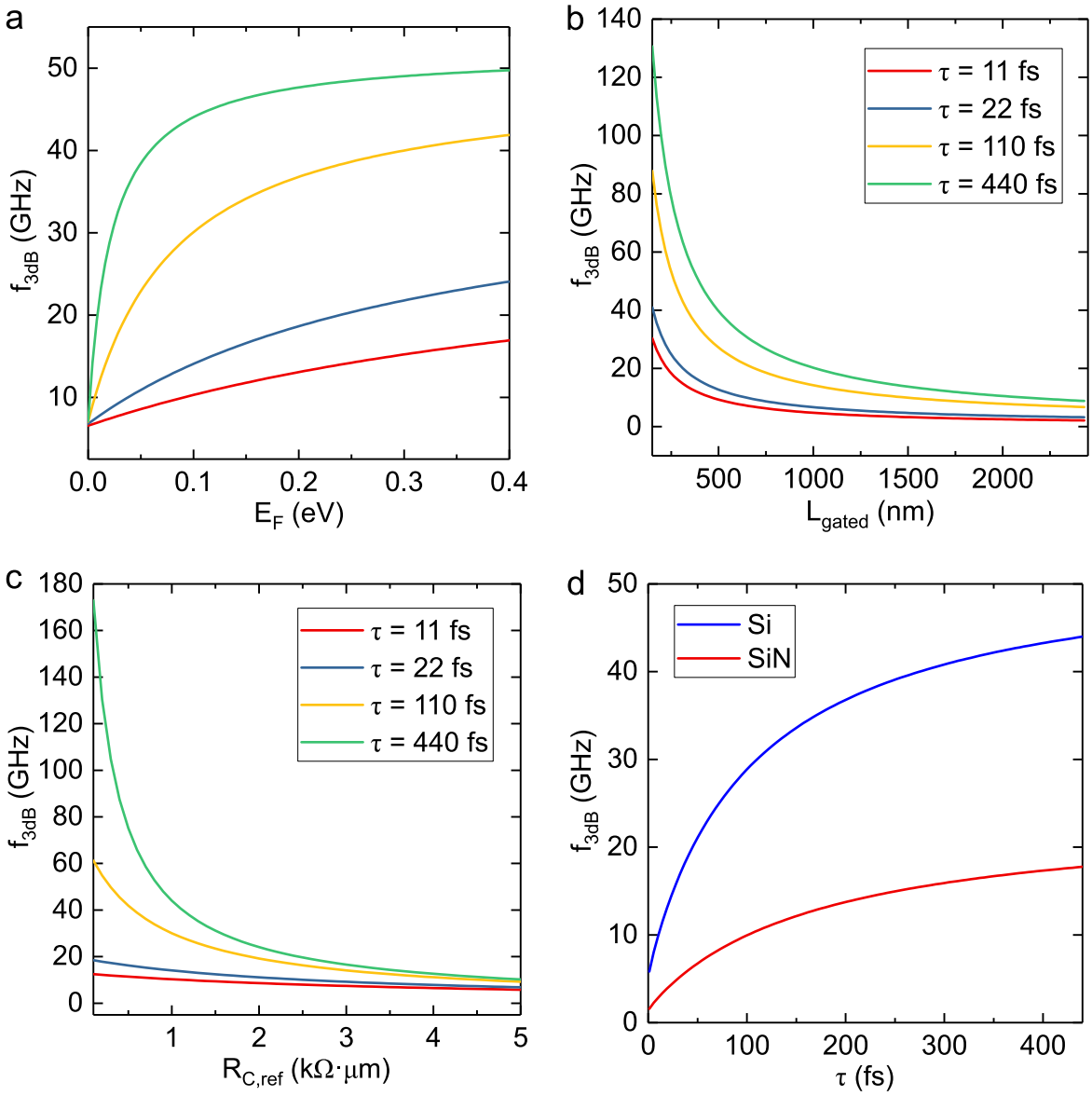

Fig. 5.11 Simulated f_{3dB} as a function of (a) E_F of the ungated SLG sections for various τ, assuming W_{gated} = 450 nm and $R_{C,ref}$ = 1,000 $\Omega \cdot \mu$m, (b) W_{gated} for various τ assuming E_F = 0.1 eV for the ungated SLG sections and $R_{C,ref}$ = 1,000 $\Omega \cdot \mu$m, (c) $R_{C,ref}$ for various τ assuming W_{gated} = 450 nm and E_F = 0.1 eV for the ungated SLG sections, and (d) τ assuming $R_{C,ref}$ = 1,000 $\Omega \cdot \mu$m and E_F = 0.1 eV for the ungated SLG sections. The blue curve represents a DSLG modulator on Si with W_{gated} = 450 nm and a 1 μm separation between the contact and the edge of the WG. The red curve represents a DSLG modulator on SiN with W_{gated} = 1.2 μm and a 1.6 μm separation between the contact and the edge of the WG. Simulations consider a 50 μm DSLG modulator, d_{Al2O3} = 20 nm (ε_{Al2O3} = 8), E_F = 0.4 eV for gated SLG sections, C_Q was calculated with an estimated additional carrier concentration of $\approx 10^{10}$cm^{-2} from defects and $\approx 10^{11}$cm^{-2} from impurities.

eV to 44 GHz at $E_F = 0.1$ eV for $\tau = 440$ fs. Therefore, any residual doping that is introduced during fabrication will naturally reduce R_S of the ungated sections which is beneficial for increasing f_{3dB}. Thus, for the rest of the simulations I have assumed $E_F = 0.1$ eV which is a typical residual doping after device processing [212].

Figure 5.11b shows f_{3dB} as W_{gated} was varied from 150 nm to 2.45 μm for $\tau = 440$ fs (green), 110 fs (yellow), 22 fs (blue), and 11 fs (red). The maximum W_{gated} was defined as the contact-to-contact distance considering a 1 μm separation between the WG and the contact and a 450 nm wide WG. The change in f_{3dB} is due to the competing contributions of C and R as W_{gated} is varied. For large W_{gated}, C increases as the overlapping area increases, and $R_{ungated}$ decreases as the proportion of ungated graphene decreases. For small W_{gated}, C decreases as the overlapping area is reduced, and $R_{ungated}$ increases as the proportion of ungated graphene increases. Even though $R_{ungated} > R_{gated}$ I found that the R_{gated} was still in the same order of magnitude as R_C and that the highest f_{3dB} resulted from the minimum sized W_{gated}. For each τ there appears to be a turning point as W_{gated} decreases where f_{3dB} starts to increase as the effect of decreasing C becomes more dominant than increasing R. For lower quality graphene a much smaller overlapping region is needed in order to compensate for the much higher R_S. However, for higher quality graphene the effect of reducing the overlapping region is visible for much larger overlapping regions due to naturally lower R_S. Reducing W_{gated} to less than the width of the WG will adversely affect the optical performance of the modulator as the active area that overlaps with the optical mode decreases.

Figure 5.11c shows the simulated f_{3dB} as $R_{C,ref}$ is varied from 100 to 5,000 $\Omega \cdot \mu$m, considering $W_{gated} = 450$ nm. It shows that f_{3dB} increases for lower $R_{C,ref}$, and that the effect is greatest for higher quality SLG. This means that for lower quality SLG, focusing on reducing $R_{C,ref}$ may not result in the desired increase in f_{3dB}, and optimising other parameters would be more beneficial. Taking the example of $R_{C,ref} = 3{,}000\ \Omega \cdot \mu$m, this leads to $R_C \sim 60$ Ω for the 50 μm long device. R_S drops from $\sim 3{,}504\ \Omega/\square$ for $\tau = 11$ fs, to $\sim 186\ \Omega/\square$ for $\tau = 440$ fs. This leads to $R_{ungated} \sim 70\ \Omega$ for $\tau = 11$ fs, and $R_{ungated} \sim 4\ \Omega$ for $\tau = 440$ fs. For higher quality SLG, we see that R_C is the dominant contribution to R and therefore results in a dramatic increase in f_{3dB} as $R_{C,ref}$ is reduced. Figure 5.11c shows that it is essential to achieve a combination of high τ and low R_C in order to reach $f_{3\,dB} > 20$ GHz. However, the yield of the contacts needs to be prioritised for system implementations that involve many devices.

For a specific τ, I have shown that f_{3dB} can be increased by reducing R_C, reducing $W_{ungated}$, or increasing the residual doping of the ungated SLG sections. However, as shown in 5.11a, b, and c the resulting f_{3dB} is highly dependent on τ. Figure 5.11d shows the simulated f_{3dB} as a function of τ varying from 1 to 440 fs considering $R_{C,ref} = 1{,}000\ \Omega \cdot \mu$m

and E_F = 0.1 eV for the ungated SLG sections, and the overlapping SLG sections limited to the width of the WG. The blue curve represents a DSLG modulator on Si where W_{gated} = 450 nm and the contacts are placed 1 μm from the edge of the WG, and the red curve represents a DSLG modulator on SiN with W_{gated} = 1.2 μm and the contacts placed 1.6 μm from the edge of the WG. f_{3dB} increases from $\sim$ 6 GHz to $\sim$ 44 GHz on Si, and from $\sim$ 2 GHz to $\sim$ 18 GHz on SiN as τ increases from 1 to 440 fs. In comparison to Si, f_{3dB} is limited to $<$ 20 GHz on SiN because of the larger device dimensions of single-mode SiN WGs and increased contact separation. Figure 5.11d shows that using SLG with the highest τ possible is essential for high-speed operation. Increasing τ leads to higher f_{3dB} because of the reduction of R_S and therefore lower R_{gated} and $R_{ungated}$.

5.4 Conclusions

In this chapter I have discussed the design of a DSLG modulator that can be used for amplitude of phase modulation depending on V_{bias}. I have presented the results of optical simulations to determine L_{min} required to achieve ER = 6 dB, in the case of amplitude modulation, and a $\Delta\phi = \pi/2$ for phase modulation. I have compared the modulation efficiency for different qualities of SLG, where the highest quality SLG has the largest τ. I have discussed how the modulation efficiency can be improved by increasing the overlap between the optical mode profile and the active area of the DSLG modulator. This can either be achieved by increasing W_{gated}, using an inverted ridge WG structure instead of a strip WG, or by using the SiN platform that has a lower Δn in comparison to Si. I have presented the results of electrical simulations to determine f_{3dB} as a function of residual doping, W_{gated}, R_C, and τ. I have shown that f_{3dB} can be increased for higher E_F of the ungated sections, minimised W_{gated} and R_C, and the highest τ possible. I have also shown that the SiN is not suitable for applications that require BW $>$ 20 GHz. This is due to the larger WG dimensions and contact separation required due to the more delocalised mode. This will result in a larger device dimensions which will increase C, R_{gated}, and $R_{ungated}$, and therefore reduce f_{3dB}.

It will be difficult for DSLG EAMs to be commercially viable owing to their small FOM_{EA}. The FOM_{EA} of SLG based EAMs is limited by the high optical losses that are unavoidable when operating at the steepest slope of $\frac{d\alpha}{dV}$. Instead, amplitude modulation could be achieved by using the simultaneous $\Delta\phi$ and a resonant photonic structure. This would benefit from the lower optical losses associated with the higher V_{bias} used for phase modulation. With a low $V_\pi L$, DSLG phase modulators have the potential for being efficient modulators, however their FOM_{ER} needs to be reduced in order for them to be attractive for commercial applications. Even with lower optical losses at the V_{bias} used for phase

modulation, FOM_{ER} is still limited by optical losses. The optical losses can be reduced by using SLG with the highest τ possible, or by optimising the width of the overlapping SLG region. Indeed, increasing the width of the overlapping region will reduce the optical losses, but this will also reduce the theoretical cut-off frequency of the DSLG modulator. The choice of W_{gated}, as a trade-off between reduced optical losses and increased f_{3dB}, also depends on τ. For $\tau > 110$ fs, W_{gated} could be increased by a few hundred nms from the edge of the WG whilst still maintaining a cut-off frequency > 20 GHz. However, for worse quality graphene with $\tau < 110$ fs, the high R_S means that even slightly increasing W_{gated} might result in f_{3dB} not being able to reach 20 GHz. Thus, I will use W_{gated} that matches the width of the WG, because I would like to maximise f_{3dB} of the DSLG modulators, but also account for any degradation of τ that might occur during device fabrication.

The simulations have assumed that both SLG have the same τ and residual doping. This is the best case scenario, but in reality there might be differences because each layer undergoes different amounts of processing. The DSLG modulator will be limited by the SLG with the lowest τ, leading to a reduced modulation efficiency and f_{3dB} and higher IL. Whereas differences in residual doping will lead to different positions on the EO response curve for each layer at a given V_{bias}. This will cause the measured EO response of the DSLG modulator to deviate from the simulated curves, with the possibility of reduced modulation efficiency due to the competing influence from each layer. Consistency in SLG growth and processing will be key to preserving the properties of SLG and symmetry between the layers. This involves growing high-quality material with low defects and high μ, but also preserving these qualities throughout device fabrication. I have chosen to limit the overlapping section to the WG width, to reduce C and maximise f_{3dB}, and use $d_{Al2O3} = 20$ nm to limit $V_{bias} < 15$ V. To operate in the transparent regime, the dielectric should support the required V to reach $E_F > 0.4$ eV without breakdown. By minimising the size of W_{gated}, I also reduce the probability of breakdown due to pinholes in the dielectric. Edge contacts should be used to contact SLG to minimise the R_C, but if the yield of this type of contacts is an issue then the traditional top contact can be used.

Chapter 6

Graphene-Silicon Photonic Integration

6.1 Introduction

An advantage of graphene-based Si photonic links is that graphene processing techniques can be used in the back-end-of-line (BEOL) in CMOS fabrication. BEOL processing refers to the fabrication of interconnect layers, contacts, and dielectrics that are used to connect the active components in integrated electronic circuits [220]. An important parameter for BEOL processes is the thermal budget which determines the duration and temperature of the thermal processes used. The thermal budget is specific to the CMOS process being used because it depends on the processes and materials that have been used to fabricate the integrated electronic circuits. Reducing the thermal budget is desirable for CMOS foundries because it limits the diffusion of dopants used in the doped Si regions, as well as and maintaining the resistivity and structural properties of the contacts and dielectrics [220]. The techniques used for transfer, patterning, and contacting graphene do not rely on high temperatures ($>150^{o}$C) so are favourable for BEOL processing. This is a considerable benefit when considering that other materials, such as III-V, require higher processing temperatures. Minimising the temperature is also driven by the desire to reduce damage done to graphene during processing which will degrade the performance of the graphene-based active components.

In this chapter I will describe the experimental techniques that I used to fabricate the GPDs and DSLG modulators. Starting with fabrication techniques, I will describe the transfer method that I used to transfer the SLG films grown by CVD onto the photonic substrates. I will then explain the process that I used to shape the transferred SLG films with electron-beam lithography (EBL) and reactive-ion etching (RIE). I will describe the process that I used to deposit the Al_2O_3 by atomic layer deposition (ALD) that I used for SLG encapsulation and gate dielectric. This will include characterisation of the deposited films to determine the ε_r of Al_2O_3. I will then discuss the procedure I used to fabricate edge contacts to SLG, and present

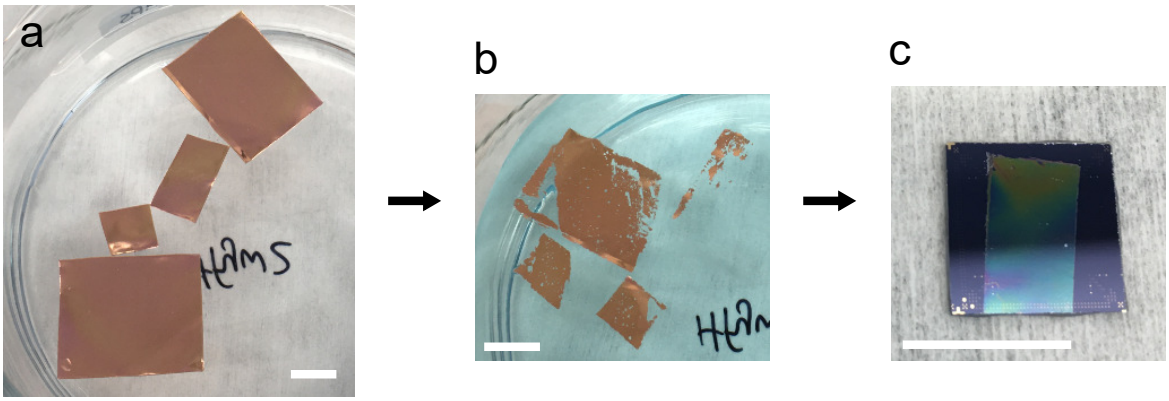

Fig. 6.1 (a) SLG on Cu initially placed in APS solution, (b) after several hours in APS solution the Cu has started to etch, (c) SLG transferred onto Si/SiO_2 substrate with PMMA support layer used during the transfer process, all scale bars 1 cm.

the characterisation of R_C by TLM measurements. Next I will move onto the techniques that I used characterise the integrated DSLG modulators. This will include the experimental setup to measure the static electro-optic response, and dynamic electro-optic bandwidth.

6.2 Scalable Fabrication of Graphene-based Photodetectors and Modulators

6.2.1 Graphene Transfer

I used the wet transfer process to transfer the CVD grown SLG films on Cu foils [37]. I prepared the SLG on Cu by cutting to size and flattening before being taped onto a piece of polyethylene terephthalate (PET) as a support during spin coating. It was important that a continuous frame was created around the edge to stop the polymethyl methacrylate (PMMA) coating the back-side of the foil, and that enough of the edge of the foil was covered to have a clean edge. The back-side SLG is removed so that the chemical etchant can access the Cu foil. The top-side SLG is protected during the Cu etching process by a supporting polymer layer that is spin-coated on the top-side SLG. I deposited PMMA (A4 950) that was spin-coated at 4000 rpm for 40 s before removing the PET from the sample by cutting along the inside of the tape frame. The sample was placed with the back-side up in the reactive-ion-etcher, and an O_2 plasma was used to remove the SLG that was on the backside of the foil. A solution of 2 g of ammonium persulfate (APS) in 150 ml of de-ionised (DI) water was prepared to chemically etch the Cu foil. The samples are placed top-side up in the etchant solution and left for approximately 6 - 7 hours before the Cu has etched. Figure 6.1a

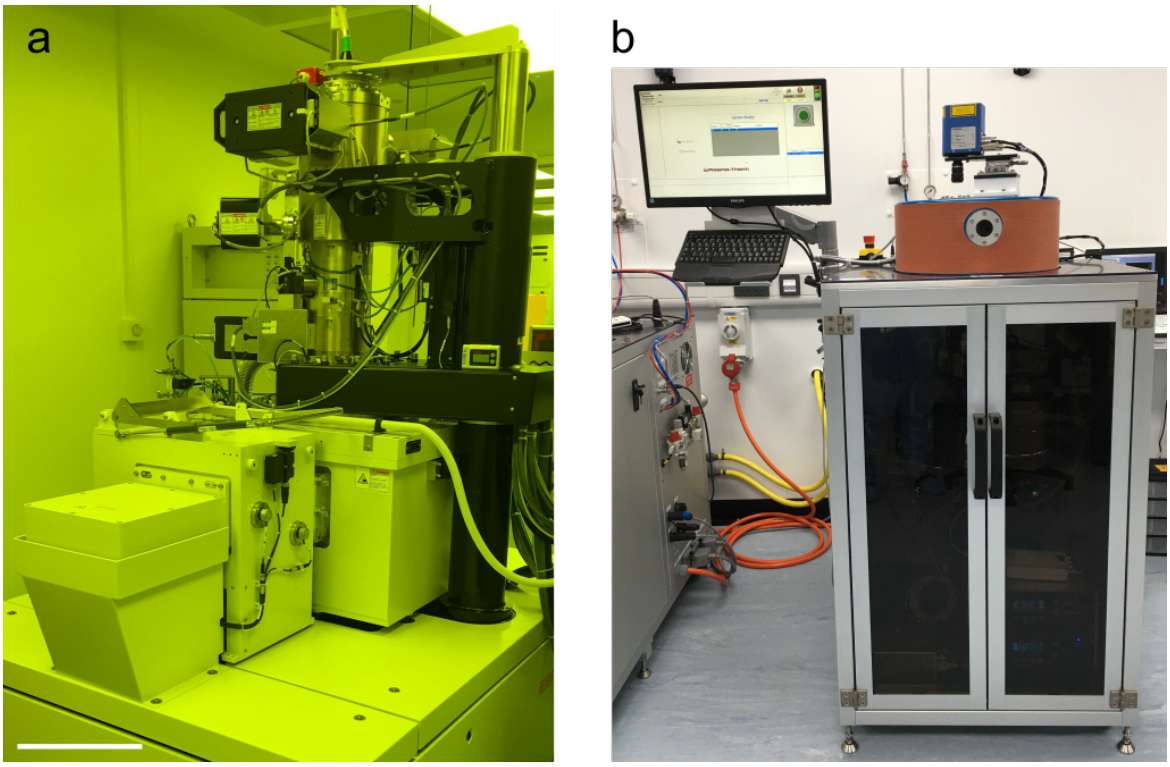

Fig. 6.2 (a) Raith EBPG5200 EBL system, (b) Vision 320 RIE system. Scale bar 30 cm.

shows the SLG on Cu foils once they have been placed in the beaker of APS and figure 6.1b shows the same SLG on Cu foils after the Cu has begun to be etched. Once the Cu has been etched the samples can be fished with a small piece of PET into a beaker of DI water where it is left for 10 minutes. After this, the samples are fished into another beaker of DI water for another 10 minutes to remove any APS residues. In the meantime the transfer substrates can be prepared by cleaning with acetone and isopropyl alcohol (IPA) and then using an O_2 plasma to activate the surface to improve adhesion with SLG. The samples can now be fished out onto the target substrates and left to dry overnight. The substrates are left to dry at an angle to reduce the water at the substrate-SLG interface. The next day the PMMA support can be removed by leaving the sample in a covered beaker of acetone for 1 hour, before finally removing the acetone with IPA and drying with N_2. Figure 6.1c shows a transferred SLG film on a Si/SiO_2 substrate before the support PMMA has been removed.

6.2.2 Electron-Beam Lithography

I used electron beam lithography (EBL) to shape the SLG channel and define the contacts. EBL, instead of optical lithography, was required due to the precise alignment requirements of the SLG channels with the WG and the other SLG layer. The device geometry was designed

in KLayout software using different layers for different features. A positive polymer resist was used that became soluble after exposure and was removed by dissolving in a prepared 3:1 solution of isopropyl alcohol (IPA) and methyl isobutyl ketone (MIBK). The sample was submerged in developer solution for 30 seconds and then inspected with a microscope to check that the pattern was clearly developed. When shaping SLG I used a single layer of PMMA (A4 495) which was spin coated for 40 s at 4000 rpm and then baked for 5 minutes at 120^{o}C. When defining contacts I used a double layer of resist so that I could achieve an undercut resulting from a faster development rate of the first layer of resist in comparison to the second. An undercut is important for removing resist with metal deposited on top of it, known as lift-off, because there is limited areas for acetone to access the resist. Therefore, by introducing an undercut at the edge of the patterned areas it increases the access points for acetone and facilitates lift-off. The first layer of the double-layer resist was MMA (EL9) copolymer that was spin-coated for 40 s at 3000 rpm and then baked for 3 minutes at 120^{o}C. The second layer of PMMA (A2 950) was spin-coated for 40 s at 3000 rpm and baked for 5 minutes at 120^{o}C. The second layer was deposited through the lid of the spin-coater when the substrate was already spinning in order to minimise the mixing between the two layers of resist. I used the Raith EBPG5200 EBL system with a dose of 1000 μC/cm^2, a 100 kV accelerating voltage, and a beam current of 5 nA for the pattern edges and 150 nA for the large pattern areas. After exposure and development, the SLG in the exposed area was removed by a low power O_2 plasma using an RIE, figure 6.2b, before removing the remaining resist in acetone and IPA.

6.2.3 Dielectric

I have used Al_2O_3 as a gate dielectric because it can be deposited at low temperature ($<$120^{o}C [214]). This is contrast to using other dielectrics, such as SiO_2 or SiN, which need to be deposited at higher temperatures (up to 400^{o}C for PECVD [220]). Using a low-temperature deposition process not only prevents damage to SLG, but it also is favourable for BEOL CMOS processing. I deposited Al_2O_3 by ALD at 120^{o}C using the Cambridge Nanotech Savannah S100 G1 system. After an initial purge of N_2, I apply consecutive cycles of 22 ms pulses of deionized water (DI) and 17 ms pulses of trimethylaluminum precursors at 6 s intervals. I calibrated the recipe using a Si test substrate and measuring the thickness after 200 cycles. I measured the thickness using the Woollam Spectroscopic Ellipsometer M-2000XI shown in figure 6.3a. From the calibration I determined a deposition rate of 0.84 Angstrom/cycle which I used to calculate how many cycles are needed for the desired thickness. When depositing Al_2O_3 onto SLG I first deposited a 1 nm Al seed layer to increase wetting of SLG and increase a high Al_2O_3 nucleation density [214]. For each deposition I

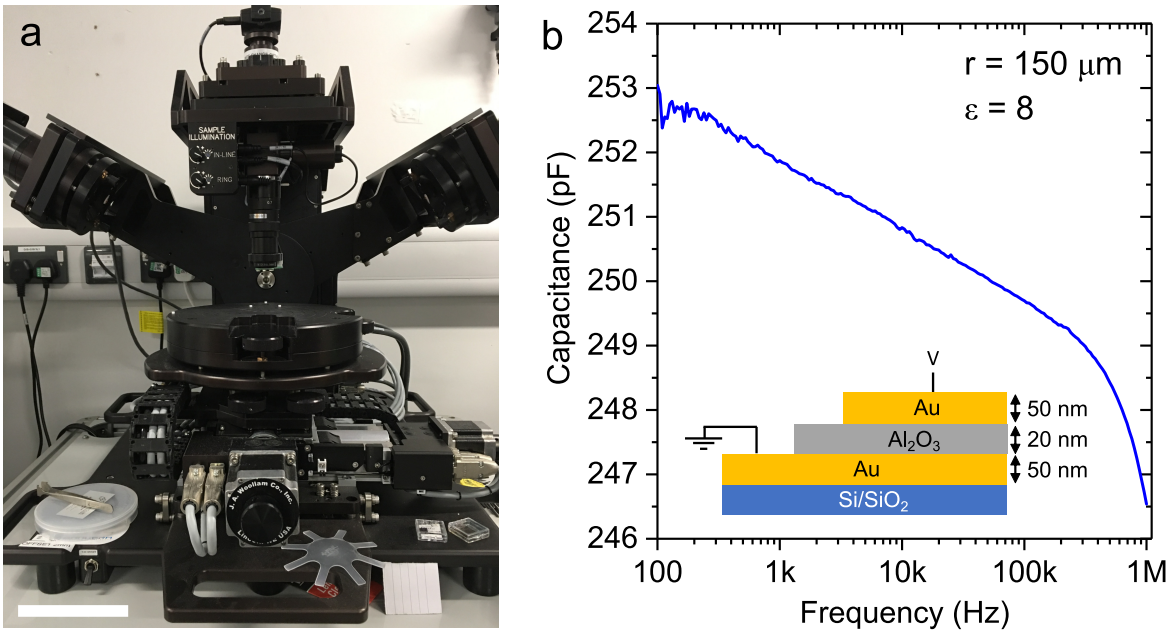

Fig. 6.3 (a) Woollam Spectroscopic Ellipsometer M-2000XI system, scale bar 10 cm. (b) Measured capacitance of Au-Al_2O_3-Au capacitors (inset) with an Agilent 4294A Precision Impedance Analyser. Calculated $\varepsilon_r \sim 8$ for circular capacitors with a radius of 150 μm.

included a dummy Si substrate so that I could check the deposited thickness at each step of fabrication with the ellipsometer.

I characterised the dielectric constant, ε_r, of the deposited Al_2O_3 by fabricating Au-Al_2O_3-Au circular capacitors and using an impedance analyser to measure the frequency-dependent impedance. From the measured capacitance, shown in figure 6.3b, I calculated ε_r with equation 2.17. This resulted in $\varepsilon \sim 8$. At the end of device fabrication, when the SLG stack is fully encapsulated by Al_2O_3, Al_2O_3 needs to be removed from the contacts so that they are accessible. I use optical lithograpy to define the areas that need to be etched, and then etch the Al_2O_3 in buffered hydrofluoric acid.

6.2.4 Metallisation

SLG can be contacted by depositing metal directly on top, known as top contacts, or by depositing metal at the edge, known as edge contacts [58, 61, 62]. Edge contacts are made by removing the SLG from beneath the contacts by using with an O_2 plasma etch directly after lithography so that only the edge of the SLG is in contact with the metal. Edge contacts to CVD grown SLG have been shown to have R_C as low as 130 $\Omega \cdot \mu$m [62] because of the increased amount of edges, where the majority of charge injection into SLG occurs [60], as well as reducing contaminants at the SLG-metal interface [62]. Before metallisation, I

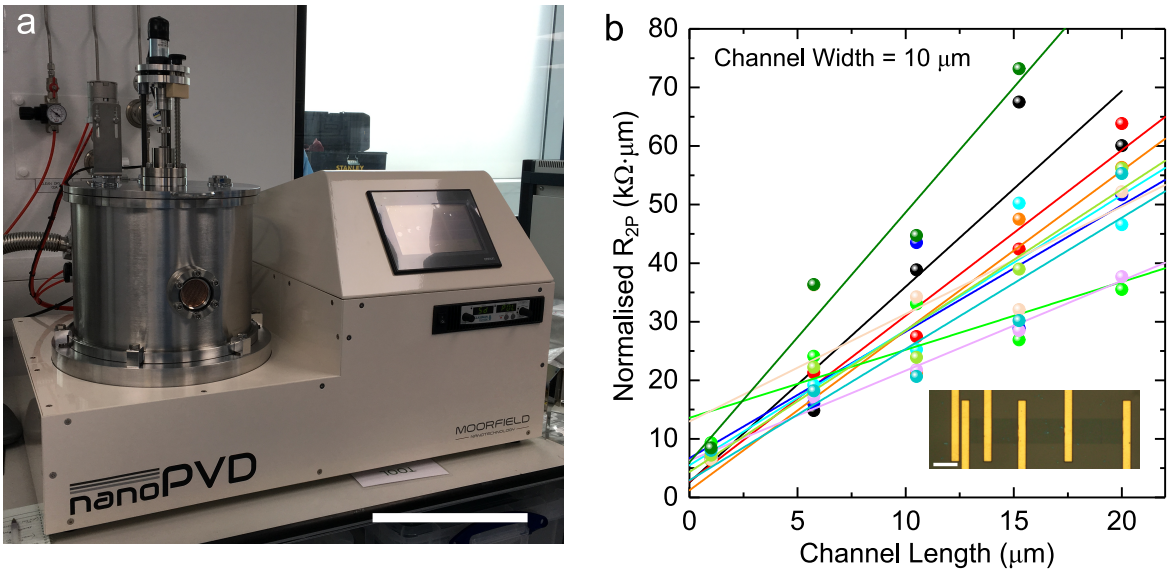

Fig. 6.4 (a) Moorfield NanoPVD sputter coating system, scale bar 30 cm. (b) Measured 2-point resistance (normalised by channel width) of TLMs (inset, scale bar 10 μm)

defined the edge contacts with EBL using the double-layer resist and performed an O_2 plasma etch. I used a variety of metal deposition techniques for different stages of fabrication. I used thermal evaporation, where the metal source is heated by an applied voltage, when depositing the Al seed layer prior to ALD of Al_2O_3 on SLG because it is a low energy process and thus will not damage the SLG. When making edge contacts I use sputter coating because I want to maximise the side-wall coverage to ensure that the SLG is uniformly contacted. I fabricated the edge contacts in the Moorfield NanoPVD sputter coating system, figure 6.4a, which uses an Ar plasma to sputter coat the desired metals. The edge contacts consisted of an adhesion layer of 15 nm of Ni, followed by 50 nm of Au. I calibrated the deposition rates of Ni and Au by depositing each target for 600 s under 20 sccm Ar and measuring the thickness with AFM. From the calibration I measured a deposition rate of 0.18 nm/s for Ni at 15% power and 0.102 nm/s for Au at 30% power. Therefore, for 15 nm of Ni and 50 nm of Au I deposited the Ni target for 83 s and the Au target for 490 s. I prepared the samples by applying Kapton tape over unused areas of the sample to make it easier to remove the unwanted metal on PMMA. After deposition the samples are left in acetone to dissolve the resist underneath the metal. Bubbles can be seen underneath the regions of metal to be removed once the acetone has started to intercalate underneath the metal. By a process of moving the sample back and forth inside a petri dish of acetone the unwanted metal can be removed. During this process the sample can be viewed under the microscope, whilst still in acetone, to monitor the progress and appearance of the metal.

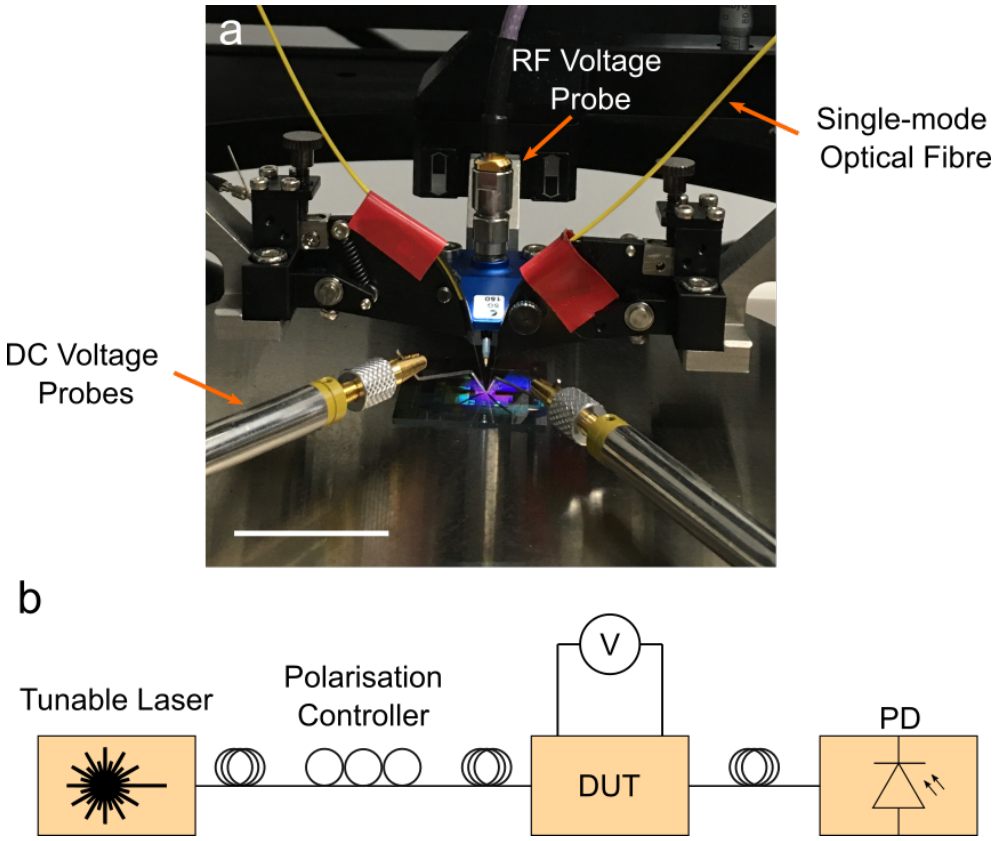

Fig. 6.5 (a) Image of Si photonic substrate, optical fibres, DC voltage probes, and radio frequency (RF) voltage probe, Scale bar 3 cm, (b) block diagram of the experimental setup for measuring the electro-optic response of integrated graphene modulators.

R_C can be extracted using the TLM method [56]. The inset of figure 6.4b is an image of the TLM that I fabricated with a 10 μm SLG channel with different channel lengths. Figure 6.4b shows the measured 2-point resistance plots for the different channel lengths that have been normalised by the channel width. The intercept of the linear fit of the normalised resistance gives $2R_C$. The 14 TLMs had a 98% contact yield, minimum $R_C \sim 610\ \Omega \cdot \mu$m, maximum $R_C \sim 6.7\ \text{k}\Omega \cdot \mu$m, and an average $R_C \sim 2.9\ \text{k}\Omega \cdot \mu$m. The spread of the data points in figure 6.4b shows that even with a high yield, the contacts are not uniform. This is likely due to non-uniformities in the SLG and can be improved with process optimisations.

6.3 Charactersiation of Integrated Graphene Modulators

6.3.1 Electro-Optic Response

The EO response of the DSLG modulators are measured using the optical setup shown in figure 6.5. A tunable laser (Agilent 8164B Lightwave Measurement System) is used as the unmodulated optical carrier which is coupled into the photonic circuits using angled single-mode optical fibres and grating couplers. The position of the fibres and the polarisation of the source laser are adjusted to minimise coupling losses and maximise the power coupled into the confined optical mode. The steady-state response is measured by applying a DC voltage (Keysight Technologies B2900 Series Precision Source/Measure Unit) across both contacts and measuring the optical power at the output, P_{out}, with the power meter in the tunable laser. The transmitted power, P_t, is expressed in dB and represents the ratio of P_{out} and the input power, P_{in},

$$P_{\text{t}} = 10\log\left(\frac{P_{\text{out}}}{P_{\text{in}}}\right) \tag{6.1}$$

For a DSLG EAM, who's transmission does not depend on wavelength, I will measure P_{out} at a single wavelength, but for a DSLG RRM or MZM I will measure P_{out} across a range of wavelengths.

6.3.2 Electro-Optical Bandwidth

The EO BW is measured by applying a sinusoidal voltage to the DSLG modulator. The voltage signal is a combination of a sinusoidal voltage generated using an Agilent E8257D PSG signal generator combined with a DC voltage, V_{bias}, via a bias tee. The amplitude of the sinusoidal signal from the signal generator was 10 dBm, corresponding to V_{pp} = 2 V using the following formula,

$$P[\text{dBm}] = 10\log_{10}\frac{V_{\text{rms}}^2}{RP_{\text{in}}} \tag{6.2}$$

where $V_{\text{rms}} = \frac{V_{\text{pp}}}{2\sqrt{2}}$, P_{in} = 1 mW and R = 50 Ω. The optical output from the DSLG modulator is then amplified with a Keyopsys CEFA-C-HG EDFA followed by a 1 nm narrow-band optical filter, before going into a InGaAs photodetector with a BW $>$ 40GHz (Newport 1014). The narrow-band filter is used to remove the noise resulting from the spontaneous emission from the EDFA [161], and to ensure that the PD input power is below the safe input power given by the photodetector specifications. The modulated output signal is recorded on an Agilent PSX N9030A electrical spectrum analyser (ESA). By monitoring the amplitude of the modulated signal with increasing frequency, I can measure the frequency response of

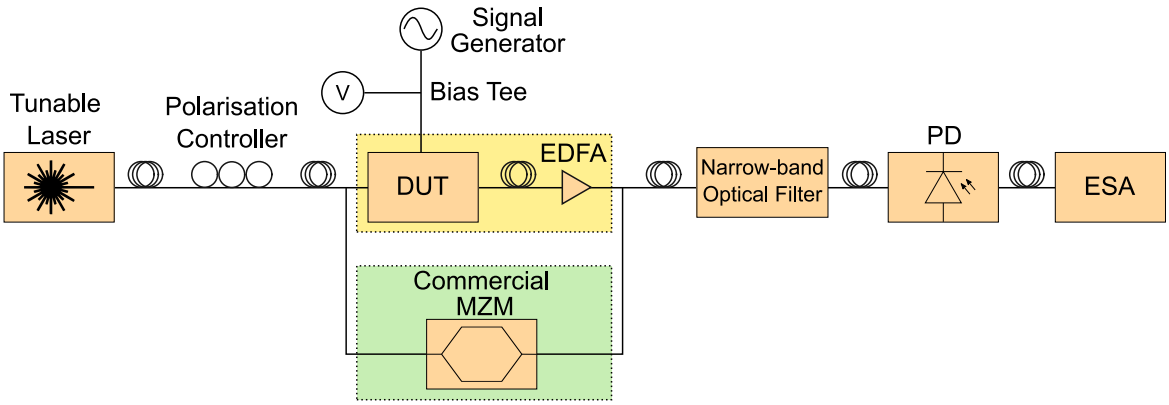

Fig. 6.6 Block diagram of the experimental setup to measure the electro-optic bandwidth of the device under test (DUT), which in this case is an integrated graphene modulator. The yellow box represents the components used to measure the response of the graphene modulator and the green box represents the components used to calibrate the setup.

the DSLG modulator. The setup is calibrated by repeating the measurement with the same configuration, but with a Thorlabs LN05S-FC amplitude modulator with $f_{3\text{dB}} \sim 40$ GHz. During the calibration, the DSLG modulator and EDFA are replaced with the commercial modulator, shown by the green box in figure 6.6. A final normalisation is then done for the frequency response of the Thorlabs LN05S-FC modulator, taken from the supplied data sheet. Figure 6.6 shows a block diagram of the measurement setup. The yellow box represents the components used to measure the EO BW of the DSLG modulator and the green box represents the components used to calibrate the measurement setup.

6.4 Summary

This chapter has summarised the different experimental techniques and measurement setups that I have used to fabricate integrated DSLG modulators. I have used methods that are scalable and that can be used across the wafer scale in the back-end-of-line of the CMOS production line. I have described the wet transfer method that I have used to transfer polycrystalline CVD grown SLG onto the photonic substrates, and then how I have patterned the transferred films with EBL and O_2 plasma etching. I explained the deposition process of the Al_2O_3 dielectric and the method of characterisation using the ellipsometer and impedance measurements. I have discussed how I will fabricate Ni/Au edge contacts by O_2 plasma etch and sputter coating and presented characterisation results using TLM measurements. Finally I have described the experimental setup that I used to measure the electro-optic response and bandwidth of integrated graphene modulators.

Chapter 7

Electro-Absorption Graphene Modulators

7.1 Introduction

EAMs use an electrically induced change in absorption to modulate the intensity, or amplitude, of an optical signal [8]. EAMs are simple and compact devices that are used in direct detection systems for modulation formats that only use amplitude modulation to encode information [8]. An EAM consists of an active component placed on a WG such that the active component modulates the power attenuation coefficient, α, of the propagating light. The operation of an EAM is shown in figure 7.1. The V-dependent P_t, shown in blue, of the EAM corresponds to the EO response of the device. In the case of graphene, P_t goes from low to high with increased V as E_F is increased and interband transitions become blocked. The operating point, V_{bias}, is chosen at the transition from low to high transmission on the EO curve. The optimum operating point on the EO curve is at the steepest gradient, where the largest change in P_t can be achieved with the smallest V. The data stream in the electrical domain, shown in green, is applied via a time-dependent V signal to the EAM. This is characterised by the peak-to-peak voltage, V_{pp}, which determines the voltage representing a '0' or '1' data bit. This causes the position on the EO curve to change, and therefore P_t. The data stream has now been converted into the optical domain, shown in orange, where P_{min} represents a '0' bit and P_{max} represents a '1' bit.

In this chapter I will present the results of DSLG EAMs that I fabricated based on the design discussed in chapter 5. In particular, as discussed in chapter 5, I will fabricate the DSLG EAMs on the Si and SiN photonic platforms to investigate the difference in

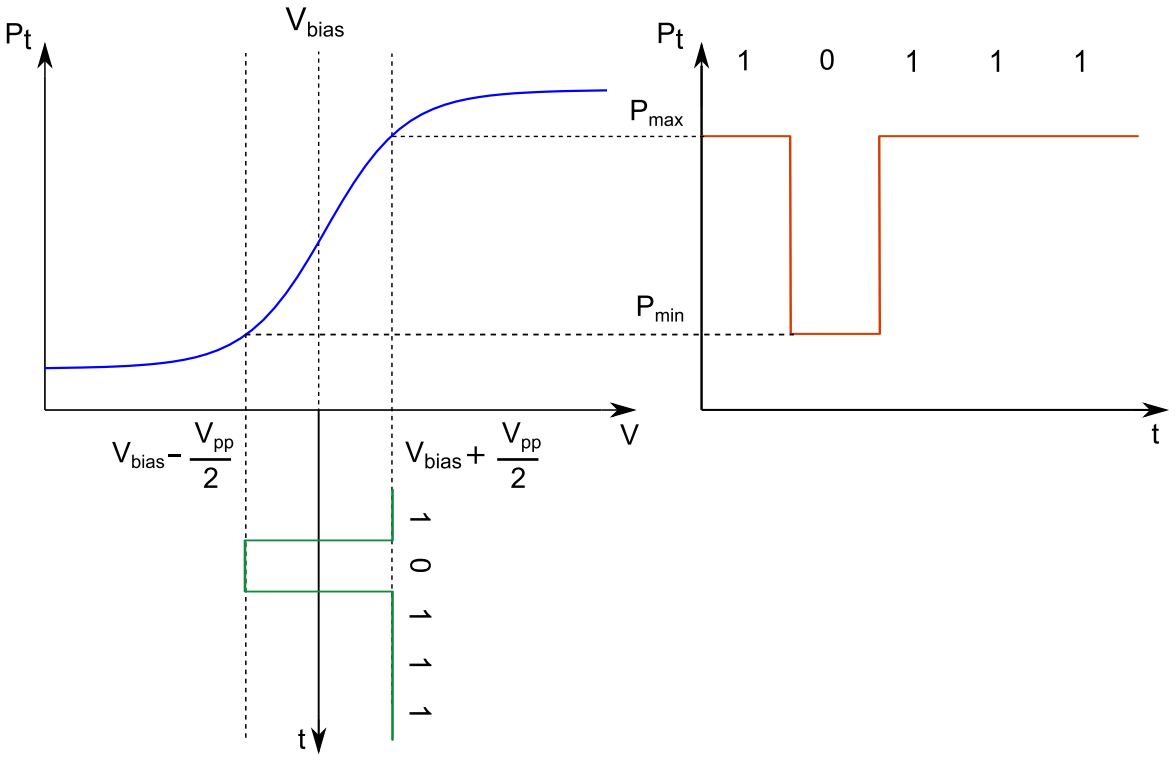

Fig. 7.1 EAM operation as an amplitude modulator showing the V-dependent P_t of the EAM (blue), the time-dependent V signal for the data stream (green), and the time-dependent P_t of the EAM (orange). By modulating the driving voltage $V_{pp}/2$ around the operating point, V_{bias}, the transmission of the EAM modulates between P_{min} and P_{max}.

performance of the DSLG EAMs resulting from the different refractive index contrast of the two platforms. I will describe the fabrication of the devices, and then present the EO response and BW of the DSLG EAMs on the two platforms. I will then conclude the chapter by discussing the differences and implications associated with the two platforms.

7.2 Fabrication

For DSLG EAMs to be usable in short reach optical communications systems that use PAM-4 modulation they must achieve an ER = 6 dB [8], however a reduced ER would be suitable for binary modulation formats. As direct detection systems are preferred for short-reach applications, it is preferable that the EAMs are compact. In chapter 5, I found that on Si, considering τ = 11 fs, that the DSLG EAM would need $L_{mod} \sim 500$ μm to reach ER = 6 dB with V_{pp} = 1 V. This is the ideal case, where V_{pp} = 1 V, however, to make the DSLG EAMs more compact I will aim to meet the target specification by reducing L_{mod} and considering a larger V_{pp}. To that end, I designed the DSLG EAMs on Si with L_{mod} = 50 μm, 75 μm, 100

μm, and 150 μm. Considering a 1 μm separation between the edge of the metal contact and the WG, I designed the DSLG stacks on Si with overlapping SLG regions of the WG width, the WG width plus 300 nm either side, WG width plus 600 nm either side, and WG width plus 900 nm either side. All devices with different W_{gated} had L_{mod} = 150 μm because it would make it easier to see the effect of the changing overlapping region width on the EO response. I designed the DSLG EAMs on SiN with active lengths of 50 μm to 100 μm in increments of 10 μm. Considering a 1.6 μm separation between the edge of the metal contact and the WG, I designed the DSLG EAMs on SiN with overlapping regions ranging from 0 μm to the width of the WG plus 1.5 μm either side.

I fabricated the DSLG EAMs on the Si platform using planarised passive photonic circuits that were designed and fabricated by IMEC. The Si substrates included TE mode straight strip WGs that were 220 nm thick and 450 nm and 550 nm wide. The planarised passive photonic circuits on SiN were designed by CNIT and fabricated by Infotec. The SiN subtrates included TE mode straight strip WGs that were 260 nm thick with widths of 0.8 μm, 1 μm, 1.2 μm, and 1.5 μm. I fabricated the DSLG stack on top of the passive substrates following the procedure described in section 6.2. On the Si substrates I transferred and patterned polycrystalline CVD SLG that was grown by Dr Osman Balci and Dr Sachin Shinde at the University of Cambridge. On the SiN substrates I transferred and patterned polycrystalline CVD SLG that was supplied by Graphenea. The thickness of each ALD deposition of Al_2O_3 was measured using ellipsometry. Due to a fabrication error, d_{Al2O3} = 27 nm for the SiN EAM and d_{Al2O3} = 20 nm for the Si EAM. After the final encapsulation of the DSLG stack, 100 nm of SiN was deposited by plasma-enhanced CVD (PECVD) at 300$^{\text{o}}$C onto the SiN EAM sample. As discussed in chapter 5, the efficiency of the DSLG modulator embedded within an inverted ridge WG should be greater than a strip WG because the interaction of the DSLG stack and the optical mode is increased. In order to access the contacts the SiN needed to be etched above the contacts. I used optical lithography to define the areas to be etched, and then used 30 s inductively coupled plasma (ICP) RIE at 12 mTorr using 10 sccm sulfur hexafluoride (SF_6) and 50 sccm fluoroform (CHF_3) with a 40 W RF bias and 400 W ICP bias. This was followed by a 120 s O2 plasma etch at 10 W to remove the photoresist residues that remained after etching the SiN. The contacts could then be accessed on both samples as described in section 6.2.

After fabrication I measured unexpectedly high losses for the DSLG EAMs on SiN with $P_{\text{t}} \sim$ -30 dB for a straight 800 μm WG and $\sim$ -60 dB through the EAM. The same losses were not observed on the Si sample, indicating that the additional losses originated from the SiN deposition onto the DSLG stack. Increased propagation losses or bending losses could have been introduced by increased scattering from the non-optimised PECVD SiN

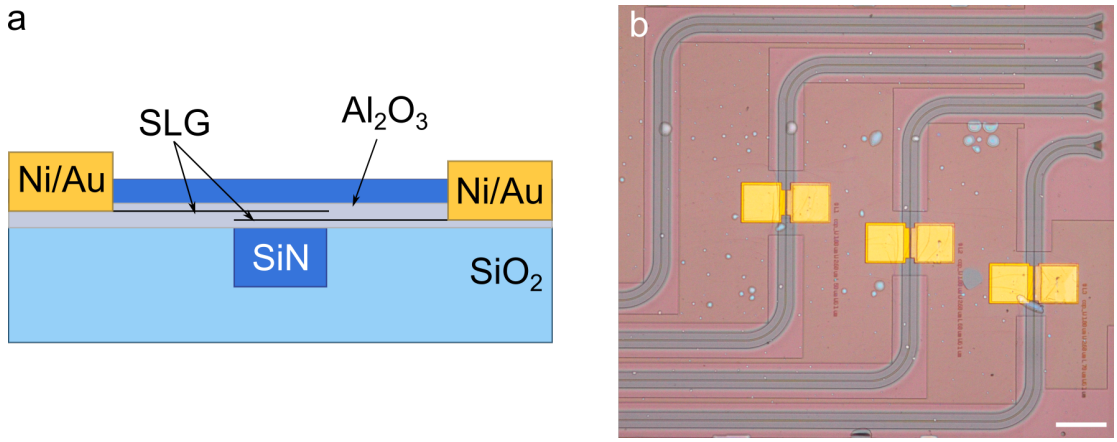

Fig. 7.2 (a) Schematic of DSLG EAM embedded within an inverted ridge SiN WG, (b) optical image of fabricated DSLG EAMs on SiN with SiN removed above the grating couplers and WGs to reduce losses. Scale bar 100 μm.

deposition, or from improper design of the photonic circuits for operation as an inverted ridge WG. To reduce the losses I etched the SiN on top of the WGs and the grating couplers, only leaving the area above the DSLG modulator with the inverted ridge WG structure. Figure 7.2b shows the fabricated DSLG EAMs on SiN WGs. The light pink areas around the WGs show the areas that have had SiN removed.

7.3 Results

7.3.1 Electro-Optic Response

I measured the EO response of the DSLG EAMs following the procedure described in section 6.3 at 1.55 μm with P_{in} = 1 mW. I measured devices with a variety of WG dimensions, L_{mod}, and W_{gated}, however, due to a low device yield and a limited number of devices that share the same WG dimensions, I cannot extract complete trends. The DSLG EAMs shown in figure 7.3 have been selected for simplicity and because they encompassed the largest voltage range. Figure 7.3a shows the EO response of a DSLG EAM with L_{mod} = 75 μm and W_{gated} = 450 nm on a 450 nm $\times$ 220 nm Si straight strip WG. Figure 7.3b shows the EO response of a DSLG EAM with L_{mod} = 60 μm and W_{gated} = 1.2 μm on a 1.2 μm $\times$ 260 nm SiN inverted ridge WG. The DSLG EAM on Si is biased between -10 and 17 V and the DSLG EAM on SiN was biased between -15 and 15 V. To extract the IL, P_t needs to be normalised to account for the additional propagation and coupling losses introduced from processing. Losses increase due to the additional Al_2O_3 on the grating couplers, roughness of the deposited Al_2O_3, and residues from SLG transfer and processing. The additional losses

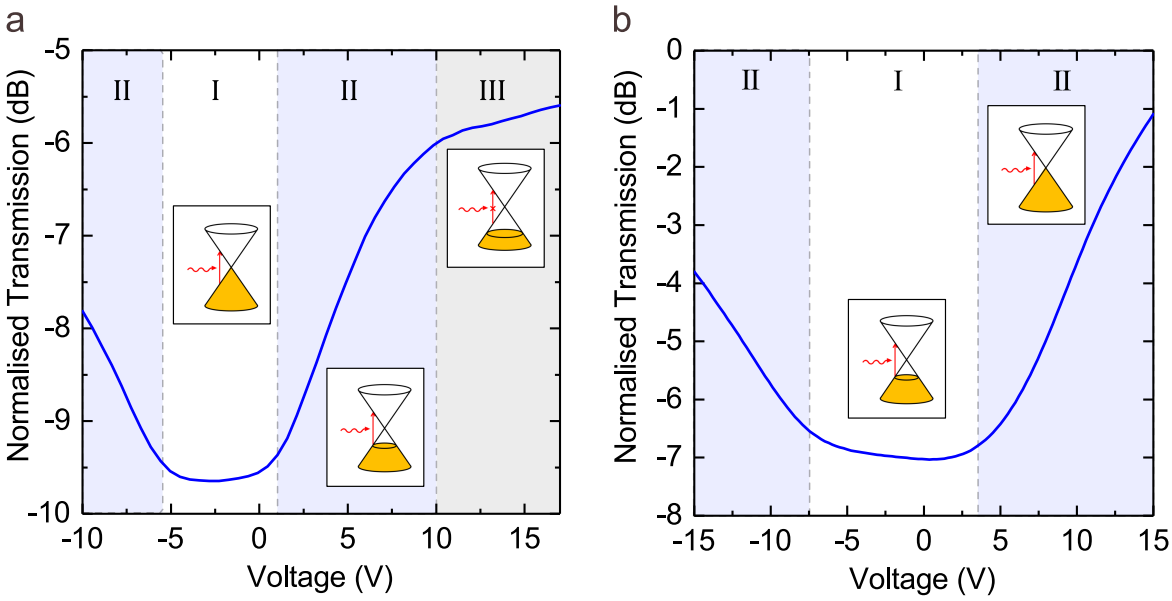

Fig. 7.3 Measured EO response at λ = 1.55 μm of a DSLG EAM with (a) L_{mod} = 75 μm and W_{gated} = 450 nm on a 450 nm $\times$ 220 nm Si straight strip WG, (b) L_{mod} = 60 μm and W_{gated} = 1.2 μm on a 1.2 μm $\times$ 260 nm SiN inverted ridge WG.

can be subtracted by measuring the transmission through a similar WG with same dimensions and grating couplers, that has undergone the same processing steps as the DSLG modulator. Figure 7.2b shows a WG without an EAM on it that is used to normalise the measured transmission. The lowest transmission in figure 7.3 occurs in region I when $E_{\text{F}} < 0.4$ eV and interband transitions of SLG are allowed. As V increases in region II, transmission increases as E_{F} approaches $\pm$ 0.4 eV, and interband transitions become blocked. In region III, the transmission plateaus when $E_{\text{F}} > 0.4$ eV and SLG enters the transparent regime where P_{t} varies $< 8\%$ as a function of V. This follows the expected behaviour of a region of minimum transmitted power around the Dirac point [32], where E_{F} = 0 eV, transitioning to maximum transmission, as $\mid E_{\text{F}} \mid$ increases. For intrinsic SLG, where the Dirac point coincides with V = 0, this curve would be centred at 0 V [24]. The Dirac point is $\sim$ -2.3 V on Si and $\sim$ -1.8 V on SiN. I calculated the residual doping at zero applied voltage by calculating the charge carrier concentration with equation 2.16. From this I can then calculate E_{F} from equation 2.18. This corresponds to $E_{\text{F}} \sim 250$ meV for the DSLG EAM on Si and $\sim$ 190 meV for the DSLG EAM on SiN. This is consistent with typical electrical measurements of Hall bars that I fabricated in the same way as the EAMs.

Even-though the DSLG EAM on SiN did not reach the transparency regime it still had a larger ER than Si due to the increased interaction of the DSLG stack and the optical mode. A larger applied V would be required to gate SLG > 0.4 eV and into transparency owing to

Optical Platform	L_{mod} (μm)	$\Delta\alpha$ (dB/cm)	α (dB/cm)	ER (dB)	IL (dB)	FOM_{EA}
Si	75	480	794	3.6	6	0.6
SiN	60	888	181	5.33	1	5.33

Table 7.1 Measured performance metrics of DSLG EAM on Si and SiN WGs assuming V_{bias} = 5 V for Si and V_{bias} = 10 V for SiN, and V_{pp} = 10 V.

its thicker gate dielectric. I did not push the applied V further to avoid the risk of dielectric breakdown. The ideal operating points for DSLG EAMs corresponds to the steepest point on the EO response curve. In this case, $V_{bias} \sim 5$ V for the DSLG EAM on Si and $V_{bias} \sim 10$ V for the DSLG EAM on SiN. The extracted performance metrics at V_{bias} for the DSLG EAMs considering V_{pp} = 10 V are shown in table 7.1. I determined $\Delta\alpha$ from the measured EO response curve by extracting ΔP_t at $V_{bias} \pm V_{pp}/2$ and then normalising ΔP_t by L_{mod}. This resulted in an ER $\sim$ 3.6 dB ($\Delta\alpha \sim 480$ dB/cm) for the DSLG EAM on Si, and an ER $\sim$ 5.33 dB ($\Delta\alpha \sim 888$ dB/cm) for the DSLG EAM on SiN. I extracted the IL at $V_{bias} + V_{pp}/2$ corresponding to $\sim$ 6 dB for Si and $\sim$ 1 dB for SiN. This corresponds to $\alpha \sim 794$ dB/cm for Si and $\sim$ 181 dB/cm for SiN when normalised by L_{mod}. This leads to $FOM_{EA} \sim 0.6$ for Si and $FOM_{EA} \sim 5.33$ for SiN. The FOM_{EA} of the DSLG EAM on Si is much lower than the DSLG EAM on SiN because it is limited by higher optical losses. This is shown in table 7.1 where the modulation efficiency of the DSLG EAM on Si is half that of the DSLG EAM on SiN, but the optical losses are $\sim$ 4 times higher. Whilst the FOM_{EA} of the DSLG EAM on SiN is better than other SLG and DSLG EAMs ($FOM_{EA} \sim 2$ [210, 211]), it requires a very large V_{pp}. Reducing V_{pp} will be important for reducing the dynamic power consumption of DSLG EAMs, which can be achieved by increasing L_{mod}. Ultimately, the choice of L_{mod} will be a trade-off between reaching the desired circuit capacity and limiting V_{pp}.

In this case, L_{mod} would need to be increased on both optical platforms in order to achieve a 6 dB ER for PAM-4 modulation. Figure 7.4 shows the EO response of 3 different DSLG EAMs with varying L_{mod} and W_{gated} on 550 nm $\times$ 220 nm Si strip WGs. Figure 7.4a shows the shortest DSLG EAM with L_{mod} = 50 μm and W_{gated} = 500 nm. Here, W_{gated} was supposed to match the width of the WG (550 nm), however due to an error in the device mask layout this was reduced to 500 nm. As this device is very short, this DSLG EAM only showed an ER $\sim$ 2.5 dB. As expected, figure 7.4b shows that the ER can be increased to $\sim$ 6 dB by using a longer DSLG EAM with the same W_{gated}. Figure 7.4c shows that by increasing W_{gated} the ER is $\sim$ 6.2 dB. Even though the ER has not increased as much as expected, by increasing W_{gated} it is clear that optical losses have reduced in comparison to figure 7.4b. Figure 7.4b and c show that it is possible to reach an ER that is appropriate

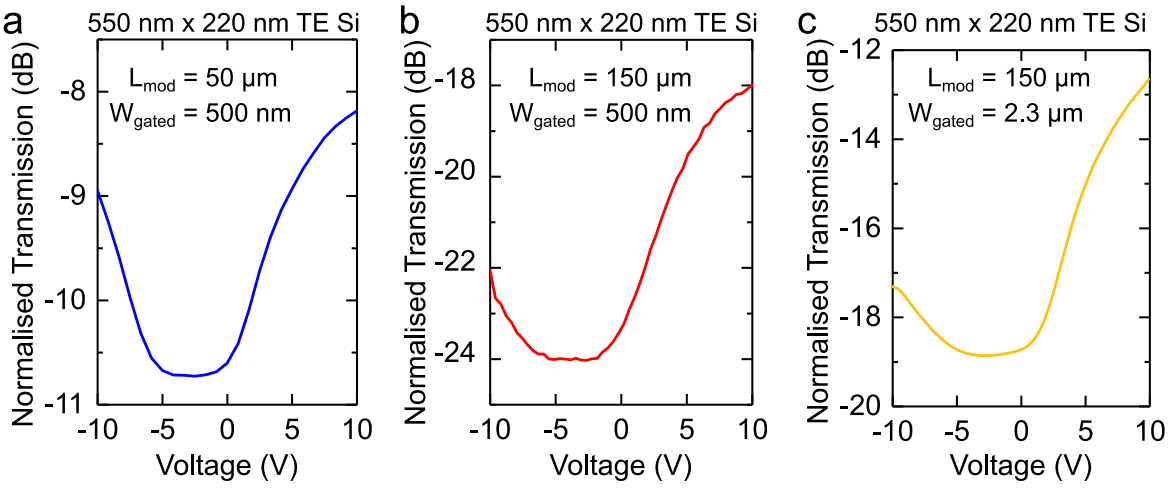

Fig. 7.4 Measured EO response of a DSLG EAM with varying L_{mod} and W_{gated}.

for PAM-4 modulation using DSLG EAMs on Si, but that this would require $V_{\text{pp}} \sim 12$ V for $L_{\text{mod}} = 150\ \mu$m and would result in optical losses that are too high for commercial devices.

By monitoring the change in transmission with V I can extract α induced by the DSLG EAM with,

$$P_{\text{t}} = \frac{P_{\text{out}}}{P_{\text{in}}} = e^{-\alpha L_{\text{mod}}} \tag{7.1}$$

Where L_{mod} is the active device length of the DSLG modulator. α is then given by,

$$\alpha = -\frac{1}{L_{\text{mod}}} \ln \frac{P_{\text{out}}}{P_{\text{in}}} \left[\frac{1}{\text{m}}\right] \tag{7.2}$$

α can then be normalised by L_{mod} and converted to dB/m by,

$$\alpha = \frac{1}{L_{\text{mod}}} 10 \log e^{-\alpha L_{\text{mod}}} \left[\frac{\text{dB}}{\text{m}}\right] \tag{7.3}$$

Figure 7.5 shows the comparison of the simulated (empty circles) and measured (solid circles) $\Delta\alpha$ for the DSLG EAMs on Si (blue) and SiN (red). The simulations have assumed $\tau = 13$ fs for both SLG and $E_{\text{F}} = 0.2$ eV for the ungated SLG sections on both photonic platforms. It is clear that by 16 V the DSLG EAM on Si has $E_{\text{F}} > 0.4$ eV and has entered the transparency regime where interband transitions are blocked. This is not the case, however, for the DSLG EAM on SiN, which has not reached transparency for the same V because it has a thicker gate dielectric (~ 27 nm) in comparison to Si (~ 20 nm). This means that

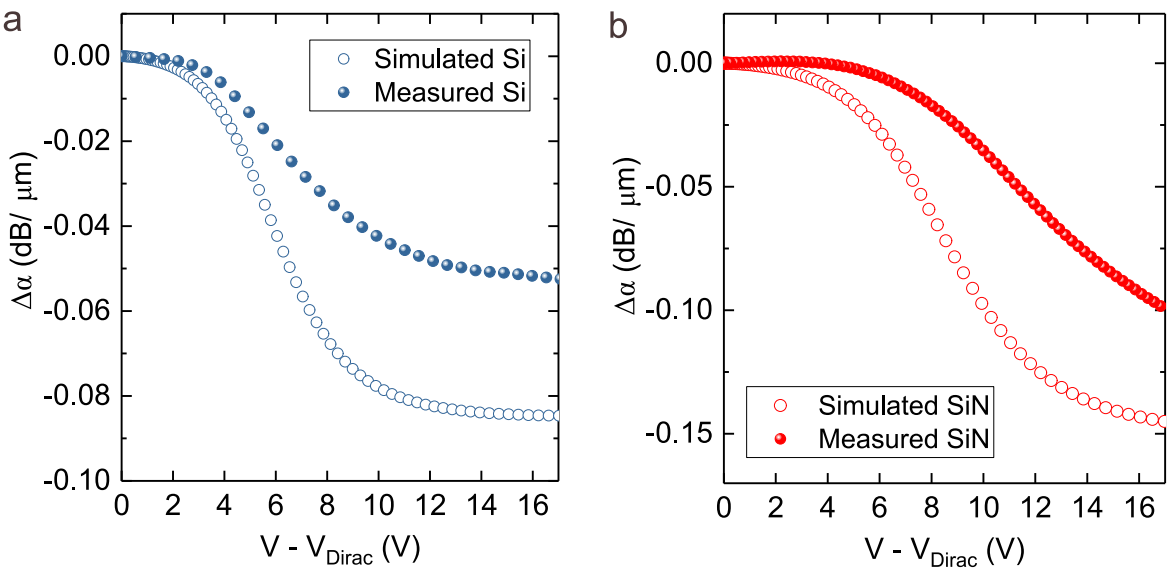

Fig. 7.5 Comparison of measured and simulated $\Delta\alpha$ for DSLG EAMs on (a) Si strip and (b) SiN inverted ridge WGs. Simulations are performed at 1.55μm at 300 K considering a 450 nm $\times$ 220 nm Si WG and SiN inverted ridge WG with 1.2 μm $\times$ 260 nm SiN strip WG and 100 nm SiN slab. d_{Al2O3} = 20 nm for Si, and d_{Al2O3} = 27 nm for SiN (ε_r=8). W_{gated} = 450 nm and 1.2 μm for the Si and SiN, and $W_{ungated}$ = 1 μm for Si and 1.6 μm for SiN. For both Si and SiN, SLG has been modelled with τ = 13 fs and with E_F = 0.2 eV for ungated SLG sections.

a higher V is required for the DSLG EAM on SiN to reach transparency. We see that $\frac{\Delta\alpha}{dV}$ for both the Si and SiN case is lower than the simulated values. This is attributed to the asymmetry between the two SLG that reduces the induced ΔE_F from V, thereby shifting the Pauli blocking condition to higher V. The measured $\Delta\alpha$ for both platforms is lower than the simulated values. The difference between measured and simulated $\Delta\alpha$ is assigned to increased propagation losses due to residues remaining on SLG from processing.

7.3.2 Electro-Optic Bandwidth

Next I have investigated the effect of a lower Δn on f_{3dB} of the DSLG EAMs. Figure 7.6 shows the EO frequency response of the DSLG EAMs on Si and SiN that I measured following the procedure described in section 6.3 with V_{pp} = 1 V. The device shown in figure 7.6a is a DSLG EAM with L_{mod} = 50 μm and W_{gated} = 500 nm on a 550 nm $\times$ 220 nm Si strip WG. The device shown in figure 7.6b is a DSLG EAM with L_{mod} = 60 μm and W_{gated} = 1.2 μm on a 1.2 μm $\times$ 260 nm SiN inverted ridge WG. In order to compare the two platforms I have selected DSLG EAMs that have similar L_{mod}. The same V_{bias} will be used for each platform as the previous section. From figure 7.6 I extracted $f_{3dB} \sim$ 13 GHz for SiN

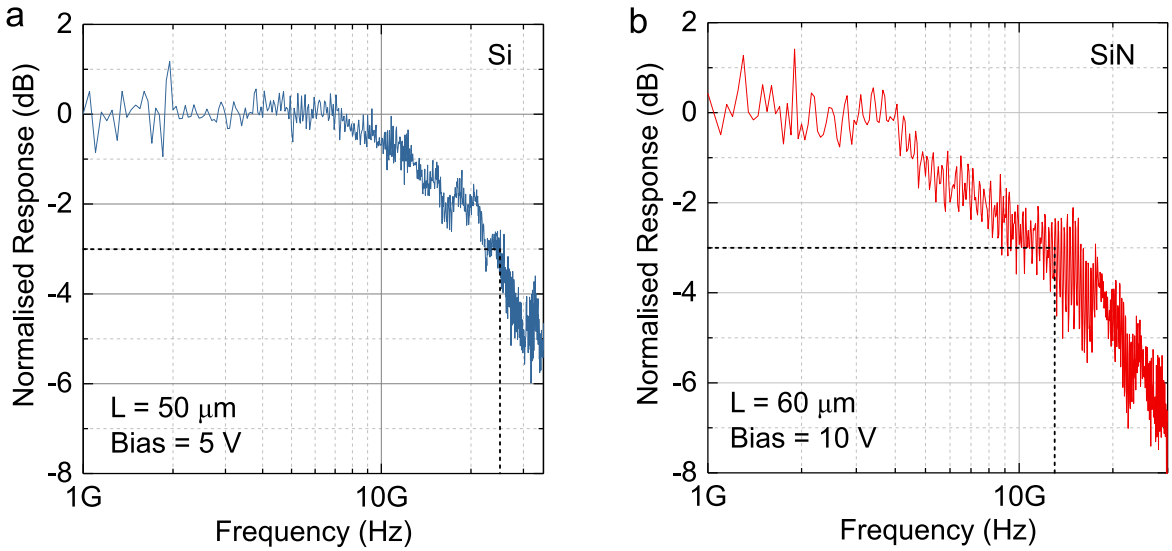

Fig. 7.6 Frequency response of a DSLG EAM with (a) with L_{mod} = 50 μm, W_{gated} = 500 nm, on a 550 nm $\times$ 220 nm Si strip WG, with V_{bias} = 5 V and V_{pp} = 1 V, (b) with L_{mod} = 60 μm, W_{gated} = 1.2 μm, on a 1.2 μm $\times$ 260 nm Si inverted ridge WG, with V_{bias} = 10 V and V_{pp} = 1 V.

and $\sim$ 25 GHz for Si. We see that $f_{3\text{dB}}$ of the DSLG EAM on Si is almost twice that of a similar DSLG EAM on SiN. This is due to the larger total size of the DSLG EAM on the SiN platform. The reduced Δn of the SiN platform, as compared to Si, means that single-mode SiN waveguides are wider than Si waveguides and that a larger contact-contact spacing is required. The DSLG EAM on SiN in figure 7.6b is over twice as wide as the Si waveguide, with a contact-contact spacing that is 60% larger that the case of Si. As discussed in chapter 5, this increases C, because the overlapping SLG region is larger, as well as increased R, because the ungated SLG regions are larger. Combined, this has a significant impact on $f_{3\text{dB}}$ which is $\propto$ 1/RC.

7.4 Conclusions

I have designed, fabricated, and measured DSLG EAMs on Si and SiN optical platforms. The lower refractive index of SiN in comparison to Si results in different performances of DSLG EAMs in terms of ER and $f_{3\text{dB}}$. The DSLG EAMs on SiN waveguides have been designed to maximise the interaction of the DSLG stack with the more delocalised mode. This was achieved by encapsulating the DSLG stack with SiN such that the DSLG stack is embedded at the centre of the resulting ridge waveguide structure. This means that more

of the optical mode is located outside the core of the waveguide, and can therefore interact more strongly with the DSLG stack.

I have shown that DSLG EAMs could achieve an ER $\sim$ 6 dB which would be suitable for PAM-4 modulation, but that this would require $V_{pp} > 10$ V. Such high V_{pp} is undesirable because it leads to high dynamic power consumption ($E \propto V_{pp}^2$). V_{pp} can be reduced by increasing L_{mod}, however the associated increase in IL and decrease in f_{3dB} would need to be investigated. The measured EO response show that it will be very difficult for DSLG EAMs to be directly driven by CMOS circuitry (V_{pp} = 1 V) because the available ER is limited to $<$ 1 dB.

DSLG EAMs on Si struggle with high IL, which will only get worse as L_{mod} increases in order to reduce V_{pp} to more practical levels. Due to the reduced modulation efficiency of the DSLG EAMs on Si, a large L_{mod} is needed to achieve a large enough ER for multi-level modulation formats. However, at the same time, L_{mod} should be minimised in order to reduce the IL of DSLG EAMs on Si. Therefore, DSLG EAMs on Si would not be suitable for systems that use multi-level modulation formats, and could instead be used for binary modulation formats that do not require a large ER.

I have demonstrated an $f_{3dB} \sim 25$ GHz for the DSLG EAMs on Si, which is close to the highest demonstrated for a DSLG EAM ($\sim$ 29 GHz [209]). I have shown that the SiN optical platform enables a larger ER in comparison to Si, but I have also shown that the increased device dimensions result in a lower f_{3dB}. f_{3dB} is reduced because a more delocalised mode means that wider waveguides are needed, increasing W_{gated}, and that the contacts need to be placed farther away from the waveguide, increasing $W_{ungated}$. The reduced operating bandwidth limits the utilisation of DSLG EAMs on SiN for high-speed applications that require greater than $\sim$ 20 GHz. This is also unlikely to be improved for longer devices, which have an increased capacitance, that are needed for more useful ERs. This means that DSLG EAMs on SiN would be more suitable for applications that require maximised modulation efficiency, but which do not require high-speed operation.

Chapter 8

Ring Resonator Graphene Modulators

8.1 Introduction

A RRM uses an active component incorporated on the ring or the directional coupler to modulate the transmission spectrum of the RR [12]. The active component can modulate the transmission by either controlling the transmission coefficients of the directional coupler or the ring, or by controlling the ϕ of the light within the ring [71]. Unlike the EAM, the transmission of a RRM depends on λ [12]. Therefore, the simultaneous Δn_{eff} and $\Delta\alpha$ from the DSLG modulator will modulate the transmission spectrum of the RRM [12]. RRM are very compact devices, using RRs with radii of ten's of micrometres [87, 213], thus are suitable for compact applications like short-reach interconnect applications. RRs can be designed to operate at specific λ [12], so can be used for wavelength-division multiplexing [211] to increase the density of transmitted information.

As RRs are sensitive to n_{eff} and α of the ring, they can be used for both amplitude and phase modulation [71]. Figure 8.1 show how amplitude modulation can be achieved with a RRM. 8.1a shows how the Q-factor of the resonance can be controlled by the directional coupler transmission coefficient, t, or the single-pass ring transmission coefficient, a, with the active component. This is the case for pure amplitude modulation where ϕ is unchanged. By operating at $\lambda_{\text{op}} = \lambda_{\text{res}}$ the transmission on the through port modulates from high to low transmission with an applied bias. Figure 8.1b shows how controlling ϕ in the ring results in amplitude modulation. Changing ϕ alters the resonant condition of the ring and therefore results in a shift of $\Delta\lambda_{\text{res}}$. By choosing λ_{op} on the shoulder of the resonance it is possible to achieve large amplitude modulation as the resonance peak shifts with an applied V. This is the case for pure phase modulation where the Q-factor remains unchanged. Depending on the modulation mechanism of the active component the amplitude modulation can be

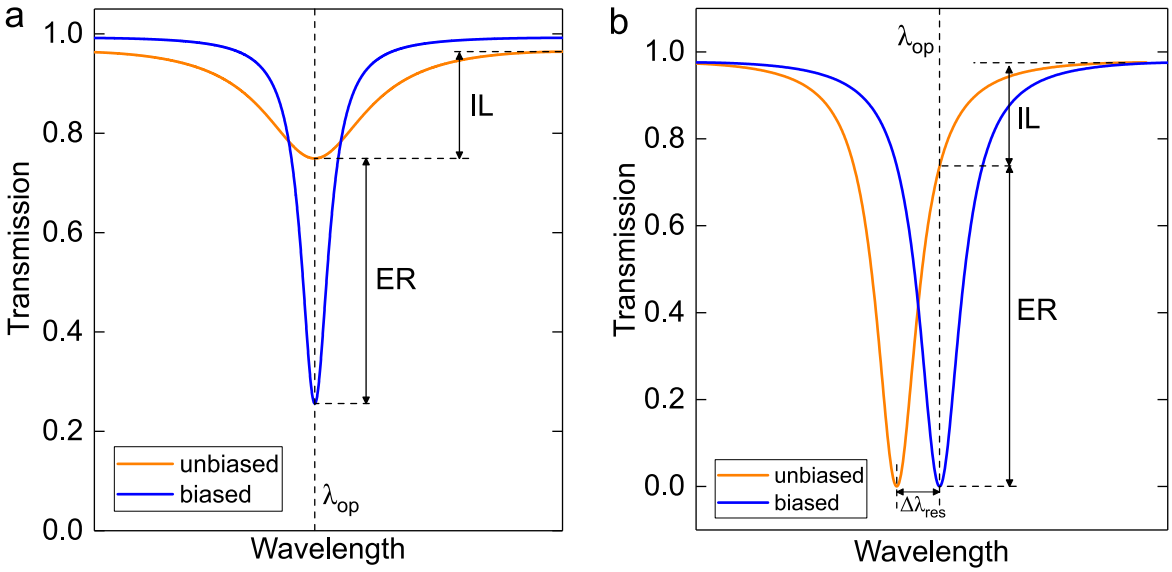

Fig. 8.1 Amplitude modulation with a RRM due to an applied bias. (a) Pure amplitude modulation by changing the Q-factor by controlling t or a. (b) Pure phase modulation by changing ϕ in the ring.

either of these methods, or a combination of both. Using pure phase modulation would be optimal solution as it does not result in extra losses. The resulting ER and IL of the RRM for each scenario has been shown on figure 8.1. This shows that even with a small Δn_{eff}, a RRM can achieve a large ER. However, this means that unlike the EAM, the RRM is wavelength sensitive so would require precise control over system parameters such as wavelength and temperature.

In this chapter I will present the results of the DSLG RRMs that I fabricated on the Si photonic platform. This will include a description of how I fabricated the devices and characterised their EO response. By analysing $\Delta\lambda_{\text{res}}$ and Q-factor of the RRM as a function of V I will extract the induced Δn_{eff} and $\Delta\alpha$ from the DSLG modulator. From this I will determine the FOM_{EA} and FOM_{ER} by considering the combined phase and amplitude modulation resulting from the DSLG modulator.

8.2 Fabrication

If the DSLG RRMs were to be used for amplitude modulation in direct detection systems, then like with the DSLG EAMs, the DSLG RRMs will need to reach an ER = 6 dB to be usable in systems that use PAM-4 modulation [8]. However, unlike the DSLG EAMs, the ER can be achieved with a combination of an induced Δn_{eff} and $\Delta\alpha$ from the DSLG RRM.

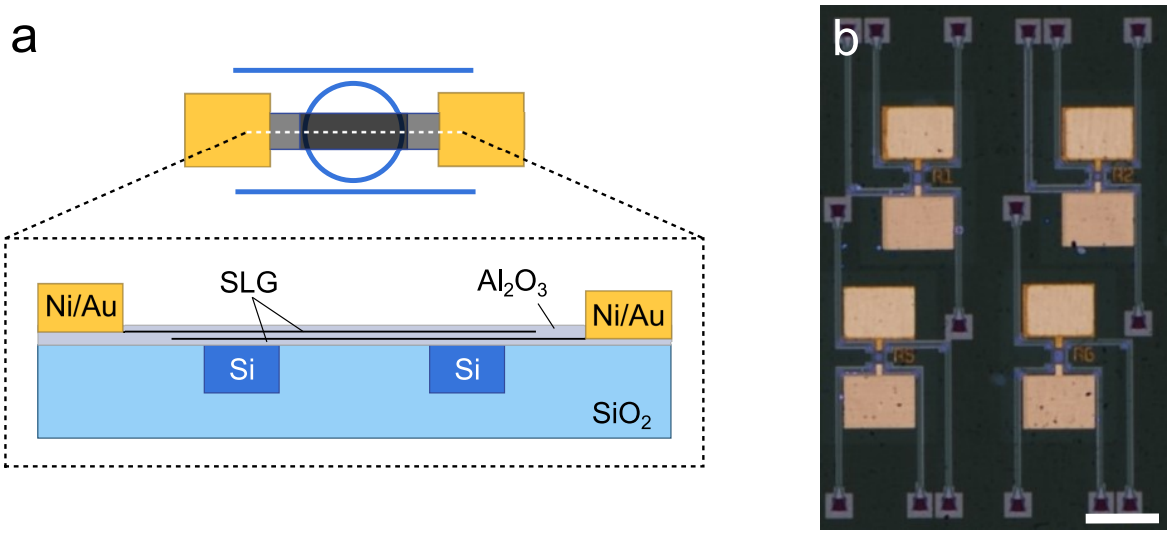

Fig. 8.2 (a) Schematic of DSLG RRM with the cross-section corresponding to white dashed line in top device schematic, (b) optical micrograph of fabricated DSLG RRMs. Scale bar is 100 μm

I fabricated the DSLG RRMs using passive photonic substrates that were designed by Dr Alfonso Ruocco at the University of Cambridge and fabricated by IMEC. I fabricated the DSLG RRMs using add-drop RRs made of 450 nm $\times$ 220 nm Si WGs, ring radii $<$ 15 μm, coupling distances ranging from 150 to 220 nm, and straight coupling lengths from 0 to 10 μm. The schematic of the DSLG modulators is shown in figure 8.2a. I designed the DSLG stack so that the active area covered as much of the ring as possible because I wanted to maximise the induced $\Delta\alpha$ and Δn_{eff} from the DSLG modulator. Unfortunately, due to the poor image contrast of the dielectric EBL markers that were provided on the photonic substrates, I needed to deposit metal EBL markers that I could use to fabricate the DSLG stack. Therefore, to compensate for systematic misalignment errors between the native markers and my own metal markers I extended the overlapping region $\sim$ 400 nm beyond the edge of WGs. However, this will reduce $f_{3\text{dB}}$ due to the increased overlapping region of the two SLG. Ideally one of the contacts would be placed inside the ring, but because the ring radii were $<$ 15 μm and I was unable to fabricate vias, I would not be able to characterise the DSLG RRMs with our measurement setup.

I fabricated the DSLG RRMs following the procedure described in section 6.2. I fabricated the DSLG stack by transferring and patterning polycrystalline CVD SLG that was grown by Dr Osman Balci and Dr Sachin Sinde at the University of Cambridge. The polycrystalline CVD SLG films were grown on Cu foils at 1000$^{\text{o}}$C, under 5 sccm of CH_4 and 20 sccm of H_2 as for Ref.[40]. I transferred the SLG films by wet transfer, patterned the SLG channels and defined the contacts with EBL, and sputter coated 15/50 nm Ni/Au edge contacts. I

encapsulated each SLG in 10 nm of Al_2O_3 where each SLG was separated by 20 nm of Al_2O_3. After each ALD deposition of Al_2O_3 I measured the thickness using ellipsometry. Finally I used optical lithography and etching in hydrofluoric acid to remove Al_2O_3 above the contacts. Figure 8.2b shows optical images of the fully fabricated DSLG RRMs.

8.3 Results

8.3.1 Electro-Optic Response

I measured the EO response following the procedure described in section 6.3 with $P_{\text{in}} = 1$ mW. By maximising the active area of the DSLG RRMs many of the RRMs could not be measured because the losses of the RRs was too high. This meant that that the ER of the RRs was minimised, and any induced $\Delta\alpha$ or Δn_{eff} from the DSLG modulator could not be observed. Therefore, I am not able to present any trends relating to the varying coupling distances and lengths. Instead, for simplicity, I will present the DSLG RRM that showed the largest response from the DSLG modulator. Figure 8.3 shows the EO response of an 18 μm DSLG RRM where V was swept from 0 to 14 V. The RRM was fabricated on an add-drop RR made of 450 nm $\times$ 220 nm Si WGs, $L_{\text{ring}} \sim 45$ μm, and directional couplers with a 150 nm separation. Unlike the EAM configuration described in chapter 7, using a RR allows the simultaneous change of phase and optical loss of the light propagating in the ring to be measured from the transmission spectrum [71]. Figure 8.3a and 8.3b shows that as V increases the ER of the resonances increases by ~ 8 dB and λ_{res} shifts to shorter λ. The changing λ_{res} (blue) and ER (orange) as a function of V are plotted in figure 8.3c. We see that λ_{res} initially shifts to longer λ, until > 7 V when it starts to shift to shorter λ. This follows the expected behaviour described in section 5 where λ_{res} red shifts when $E_{\text{F}} < 0.4$ eV and $\Delta n_{\text{eff}} > 0$, and blue shifts when $E_{\text{F}} > 0.4$ eV and $\Delta n_{\text{eff}} < 0$. The ER increases with increasing V as the losses of SLG are reduced. The DSLG RRM is more intrinsic than the DSLG EAMs in chapter 7, with the Dirac point at ~ 1 V, which corresponds to a residual doping of ~ 165 meV with equation 2.16 and 2.18.

From equation 3.25 and 3.26 we see that the FWHM and Q-factor of the resonance strongly depends on t and a [71]. Therefore, by assuming that t_1 and t_2 do not change with V, I can attribute the changing Q-factor to the changing absorption of the DSLG modulator. a is the ratio of the E after one round trip in the ring and the E that entered the ring [71]. a is related to the losses experienced in one round trip, α_{ring}, including the loss contributions from the couplers and propagation along the ring of length L_{ring} by,

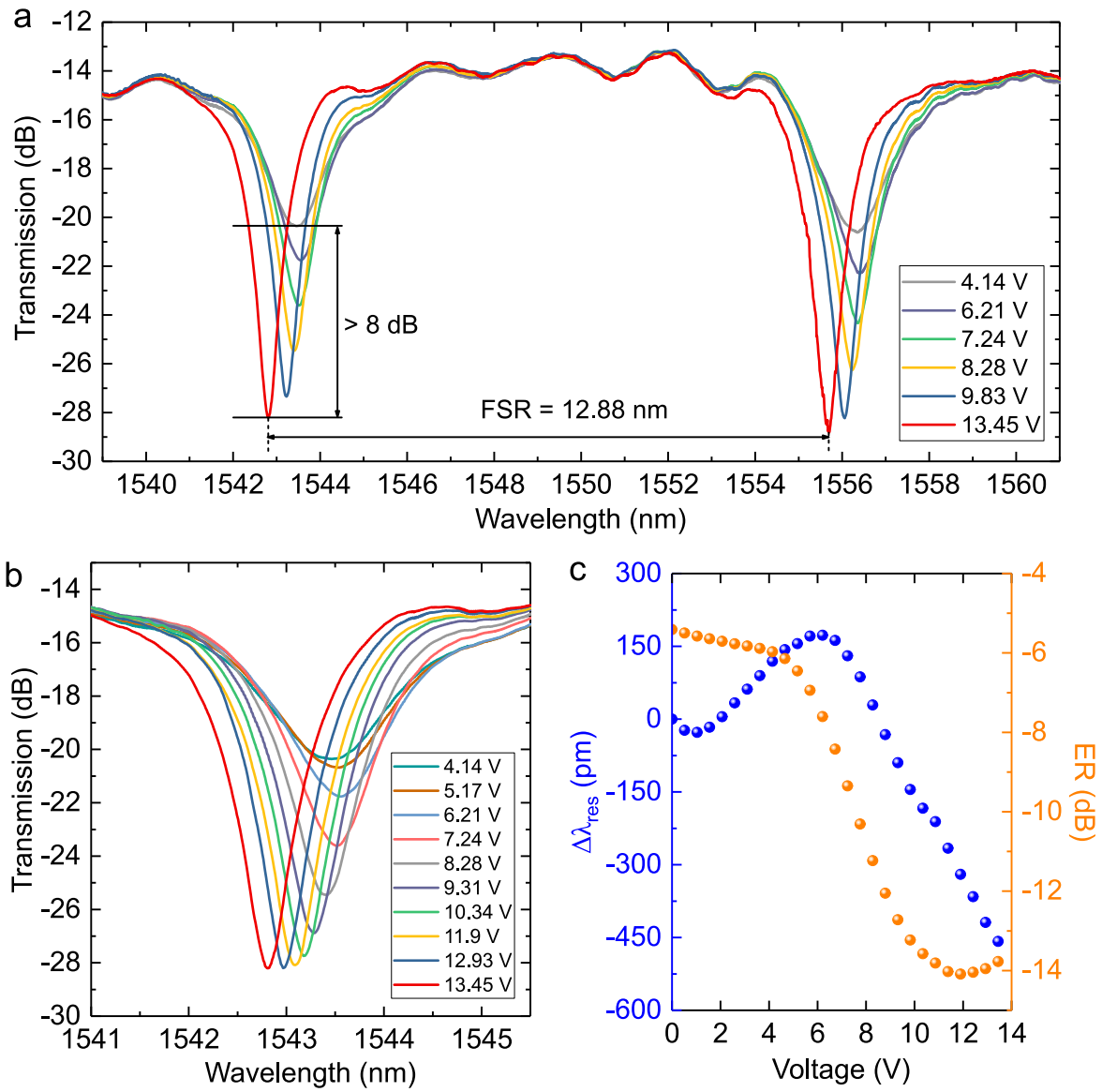

Fig. 8.3 (a) EO response of a DSLG RRM with $L_{\text{mod}} \sim 18\ \mu$m on a add-drop RR with $L_{\text{ring}} \sim 45\ \mu$m, 150 nm distance between the bus and ring WG, and 450 nm $\times$ 220 nm Si WG. (b) Close-up of one resonance peak, (c) extracted shift of interference fringe position, λ_{res}, (blue) and ER (orange) with increasing V.

$$\left(\frac{E_{\text{out}}}{E_{\text{in}}}\right)^2 = a^2 = e^{-\alpha_{\text{ring}} L_{\text{ring}}} \tag{8.1}$$

Using equation 3.25 and 3.26, Q can be related to a by [71],

$$\text{Q-factor} = \frac{\pi n_g L \sqrt{t_1 t_2 a}}{(1 - t_1 t_2 a)\lambda_{\text{res}}} \tag{8.2}$$

By rearranging equation 8.2 and using the quadratic formula I arrived at an expression for a,

$$a = \left(\frac{-\pi n_g L \sqrt{t_1 t_2} \pm \sqrt{\left(\pi^2 n_g^2 L^2 t_1 t_2 + 4Q^2 \lambda_{\text{res}}^2 t_1 t_2\right)}}{2Q\lambda_{\text{res}} t_1 t_2} \right)^2 . \tag{8.3}$$

I simulated $n_{\text{g}} = 4.18$ with an FDE simulation using the same device cross-section and measured λ_{res}. I assumed that $t_1 = t_2$ because the rings were designed with the same coupling distance and length for the through and drop port. Assuming that t does not change after fabrication of the RRM, I estimated t_1 and t_2 from the transmission of the RR before device fabrication, shown by the red curve in figure 8.5a. By sweeping different values of t for the empty ring, I can calculate the associated a and ER with equation 8.3 and 3.21. By comparing the measured ER to the calculated ER I can estimate t, which in this case was $\sim$ 0.9745. I can then calculate α_{ring} using equation 8.1 such that,

$$\alpha_{\text{ring}} = -\frac{2\ln a}{L_{\text{ring}}} \tag{8.4}$$

Considering that the V-dependent $\Delta\alpha_{\text{ring}}$ is only due to the DSLG modulator, the absorption of the DSLG modulator, α_{mod}, can be directly linked to α_{ring} by,

$$\left(\frac{I}{I_0}\right)_{\text{mod}} = e^{-\alpha_{\text{mod}} L_{\text{mod}}} = e^{-\alpha_{\text{ring}} L_{\text{ring}}} \tag{8.5}$$

where L_{mod} is the active length of the DSLG modulator. α_{mod} is then converted to dB and normalised by L_{mod} by,

$$\alpha_{\text{mod}} = \frac{1}{L_{\text{mod}}} 10\log_{10}(e^{-\alpha_{\text{ring}} L_{\text{ring}}}). \tag{8.6}$$

From equation 8.6, $\Delta\alpha_{\text{mod}}$ is defined as the change in α_{mod} compared to the Dirac point.

I can extract the phase modulation achieved by the DSLG modulator by monitoring λ_{res} as a function of V. The DSLG modulator changes the effective refractive index of the ring, $n_{\text{eff,ring}}$, such that the resonant condition of the ring changes [71]. This results in a shift of the resonances, $\Delta\lambda_{\text{res}}$, that is proportional to $\Delta\phi$ by,

$$\Delta\phi = k_0 \Delta n_{\text{eff,ring}} L_{\text{ring}} \tag{8.7}$$

The measured $\Delta\lambda_{\text{res}}$ can be related to $\Delta\phi$ by using the FSR as a known $\Delta\phi = 2\pi$. Using expression 3.23 $\Delta\phi$ is defined in units of π as,

$$\Delta\phi[\pi] = \frac{\Delta\lambda_{\text{res}}}{\text{FSR}/2} \tag{8.8}$$

Considering that the V-dependent $\Delta n_{\text{eff,ring}}$ is only due to the DSLG modulator, I can directly attribute $\Delta n_{\text{eff,ring}}$ to $\Delta n_{\text{eff,mod}}$. By rearranging equation 8.7 for $\Delta n_{\text{eff,ring}}$ and substituting equation 8.8 and 3.23, $\Delta n_{\text{eff,mod}}$ is related to λ_{res} by,

$$\Delta n_{\text{eff,mod}} = \frac{\Delta\lambda_{\text{res}} n_g}{\lambda_{\text{res}}} \tag{8.9}$$

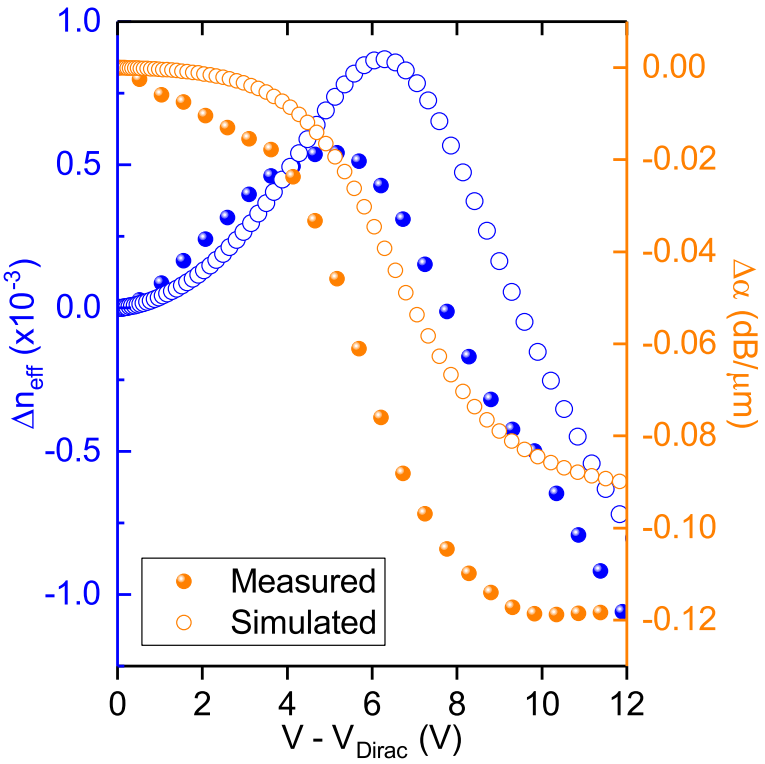

Fig. 8.4 Comparison of extracted Δn_{eff} and $\Delta\alpha$ with simulated values. Simulations performed at 1.55μm at 300 K, τ = 22 fs, Si WG (450 nm $\times$ 220 nm), d_{Al2O3} = 20 nm (ε_r = 8), W_{gated} = 450 nm, W_{ungated} = 1 μm (E_{F} = 0.2 eV).

Figure 8.4 shows the extracted Δn_{eff} and $\Delta\alpha$ of the DSLG RRM as compared to the simulated values. Δn_{eff} and $\Delta\alpha$ follow the same behaviour as the simulation, where α is at its highest around the Dirac point, before starting to significantly decrease $>$ 4 V as E_{F} approaches 0.4 eV. Above 8 V, $\Delta\alpha$ begins to flatten as $E_{\text{F}} > 0.4$ eV and interband transitions become blocked. Δn_{eff} follows the simulated behaviour where Δn_{eff} is positive and begins to increase until $>$ 5 V when it begins to decrease before becoming negative $>$ 8 V. Above 10 V Δn_{eff} decreases quasi-linearly whilst $\Delta\alpha$ remains constant. This is the ideal working point for

pure phase modulation. The simulations consider both SLG with $\tau = 22$ fs, which corresponds to $\mu = 500$ cm^2/Vs at $E_F = 0.4$ eV. The observed differences between the measured and simulated Δn_{eff} and $\Delta\alpha$ could be due to asymmetries between the two SLG. In the simulation I have assumed that both SLG have the same residual doping, however this is unlikely to be the case as each SLG has undergone different levels of processing during fabrication. In the case of $\Delta\alpha$, the initial decrease of < 4 V can be explained by a difference in doping between the two SLG, such that the absorption in one SLG has started decreasing before the other. This would also explain why > 10 V that $\Delta\alpha$ becomes flat as V is sufficiently high that both SLG have $E_F > 0.4$ eV. Discounting the initial $\Delta\alpha \sim 0.02$ dB/μm would bring the measured $\Delta\alpha$ at 12 V closer to the simulated value. Different residual doping between the two SLG would also reduce the induced ΔE_F from applied V, thereby shifting the Pauli blocking condition to higher V, and reducing $\frac{d\Delta n_{\text{eff}}}{dV}$ and $\frac{d\Delta\alpha}{dV}$.

From figure 8.3c we can extract the $V_\pi L$ of the DSLG RRM. By determining $\Delta\phi$ in units of π we can conveniently scale the V applied for the observed $\Delta\phi$ to the V required for a full π-phase shift, $\Delta\phi_\pi$. This is only possible in the linear regime of $\frac{d\lambda_{\text{res}}}{dV}$, figure 8.3c. Considering $V_{\text{pp}} = 1$ V, equation 8.8 becomes,

$$\Delta\phi_{1\text{V}}[\pi] = \frac{d\lambda_{\text{res}}}{dV}\frac{1}{\text{FSR}/2} \tag{8.10}$$

where $\frac{d\lambda_{\text{res}}}{dV} = k_0 L_{\text{ring}}\frac{d\Delta n_{\text{eff}}}{dV}$, and the V-scaling factor is defined by the conversion of $\Delta\phi_{1\text{V}}$ to $\Delta\phi_\pi$,

$$V\text{-scaling factor} = \frac{1}{\Delta\phi_{1\text{V}}[\pi]} \tag{8.11}$$

The V required for π-phase shift becomes,

$$V_\pi = \frac{1}{\Delta\phi_{1V}[\pi]} \cdot 1V \tag{8.12}$$

Therefore, for a DSLG modulator of length L_{mod} we can calculate the phase modulation efficiency as,

$$V_\pi L = \frac{1}{\Delta\phi_{1V}[\pi]} \cdot L_{\text{mod}} \tag{8.13}$$

By linearly fitting λ_{res} from figure 8.3c, and using equation 8.10 and 8.13 I extracted a $V_\pi L \sim 0.12$ V·cm. This 50% lower than the lowest reported DSLG phase modulator with $V_\pi L \sim 0.28$ V·cm [212]. Our $V_\pi L$ is ~ 15 times better than the lowest reported LN (~ 1.8 V·cm[121]), and ~ 4 times better than the lowest reported Si (~ 0.52 V·cm [110]) phase modulators. Whilst the extracted efficiency of the DSLG RRM is very low, it is important to

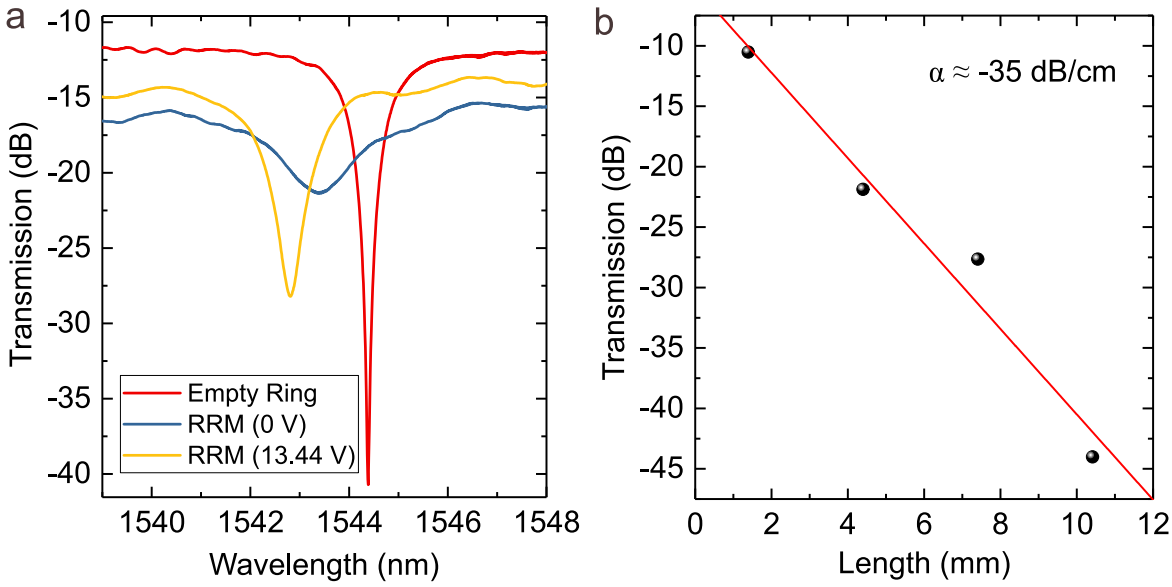

Fig. 8.5 (a) Measured transmission of the RR before fabrication (red), after fabrication of DSLG RRM with $V_{\text{bias}} = 0$ (blue), and after fabrication of DSLG RRM with $V_{\text{bias}} = 13.44$ V (yellow), (b) measured propagation losses after fabrication of DSLG RRM, as measured from reference WGs using the cut-back method.

note that this DSLG RRM is far from reaching a π-phase shift because the active region is only ~ 18 μm long. It is only with increased V_{pp} or L_{mod}, or a combination of the two, that the DSLG RRM can reach a π-phase shift and the real world efficiency can be measured. In this case, it will important to see how increasing V_{pp} or L_{mod} will affect the IL and BW of the DSLG RRM. However, if optical losses can be reduced from more mature SLG processing, then this extracted modulation efficiency (~ 0.12 V·cm) is a promising sign that future SLG based RRMs can deliver efficient phase modulation with a functional $\Delta\phi$.

In order to calculate FOM_{EA} and FOM_{ER} I need to extract the IL of the DSLG modulator. Typically this would be achieved by normalising the transmission with another RR that has undergone the same fabrication, but without a DSLG modulator. Unfortunately, I did not have this available so need to estimate IL. Figure 8.5a shows the transmission of the RR before fabrication (red), after fabrication with no applied bias (blue), and after fabrication with an applied bias (yellow). As I described earlier, I used the transmission of the RR before fabrication to estimate t, which I then used to calculate a and α_{ring} after fabrication. I accounted for the additional propagation losses due to fabrication in α_{ring} by using the measured propagation losses, shown in figure 8.5b, calculated from the cut-back method with reference WGs on the same sample. For $L_{\text{ring}} = 45$ μm this would add an additional IL $\sim$ 0.16 dB. I have estimated the IL of the DSLG RRM by considering α_{ring} at the operating V. This will depend on whether the RRM is being operated in the amplitude or phase modulation

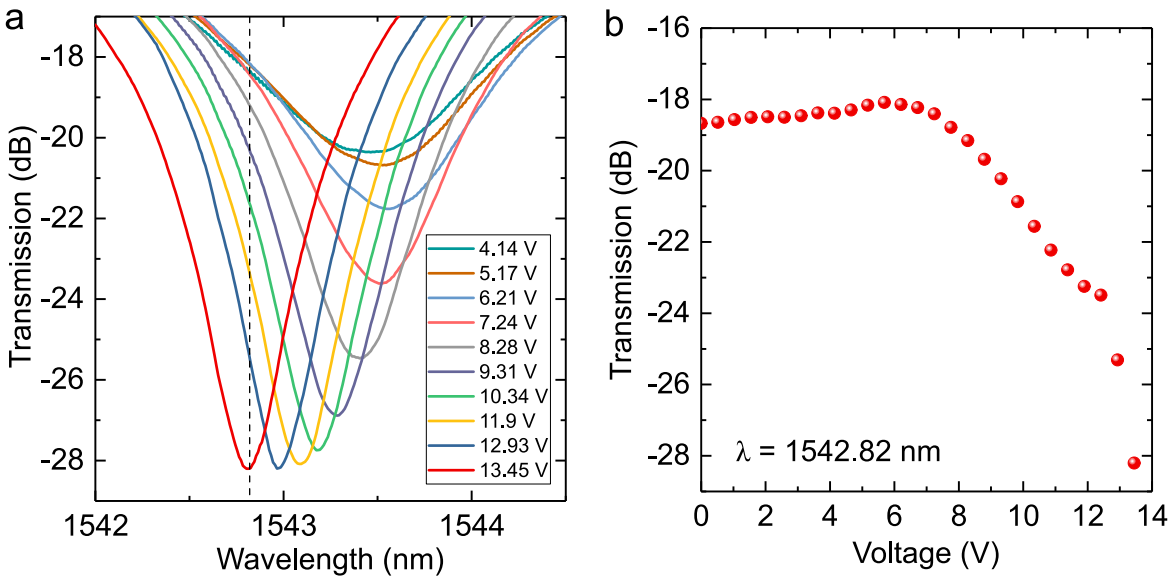

Fig. 8.6 Operation of a 18 μm DSLG RRM as an amplitude modulator. (a) Wavelength-dependent transmission of DSLG RRM with increasing V, operating wavelength (λ_{op} = 1542.82 nm) shown by dashed line. (b) EO response of DSLG RRM as an amplitude modulator showing the voltage-dependent transmission at λ_{op} = 1542.82 nm.

regime. At 10 V, a corresponds to $\sim$ 1.28 dB, accounting for an additional $\sim$ 0.16 dB from fabrication, resulting in an IL $\sim$ 1.12 dB and $\alpha \sim$ 621 dB/cm. This leads to an $FOM_{ER} \sim$ 74.5 VdB, which is similar to that of state-of-the-art SLG phase modulators ($\sim$ 66 VdB [212]). This shows that even with a record-low $V_\pi L$, the FOM_{ER} of the DSLG RRM is limited by high optical losses.

To calculate FOM_{EA} I need to extract the ER from the EO response of the DSLG RRM in operation. The EO response is obtained by extracting the transmitted power of the DSLG RRM at λ_{op} at different V. This is shown in figure 8.6a where λ_{op} is shown by the dashed line. Figure 8.6b shows the resulting EO response of the RRM when it is operated at λ_{op} = 1542.82 nm, which is a result of the simultaneous amplitude and phase modulation. It can be seen that $<$ 6 V there is no considerable change in transmission, but $>$ 6 V transmission drops by -1.2 dB/V as the resonance begins to shift to shorter λ and the ER increases. Transmission continues to decrease until 12 V when it starts to drop by -4.55 dB/V. This increase in the rate of change of transmission is because λ_{op} is approaching the minimum transmission of the resonance, so a larger change in transmission can be achieved. I calculated FOM_{EA} by considering the RRM operating at λ_{op} = 1542.82 nm with V_{bias} = 13 V and V_{pp} = 1 V. By considering P_t at $V \sim$ 12.4 V and $\sim$ 13.4 V the ER can be directly calculated as $\sim$ 4.71 dB for $\Delta V \sim$ 1 V. At these conditions, the ER $\sim$ 4.71 dB and IL $\sim$ 1.05 dB ($\alpha \sim$ 580 dB/cm), leading to $FOM_{EA} \sim$ 4.48. Our FOM_{EA} is the highest reported for SLG or DSLG EAMs,

doubling the current value of $\sim$ 2.03 [211], as demonstrated by a SLG EAM. As shown in figure 8.6b the modulation efficiency is maximised above 12 V because we benefit from the large ER enabled by pure phase modulation.

8.3.2 Electro-Optic Bandwidth

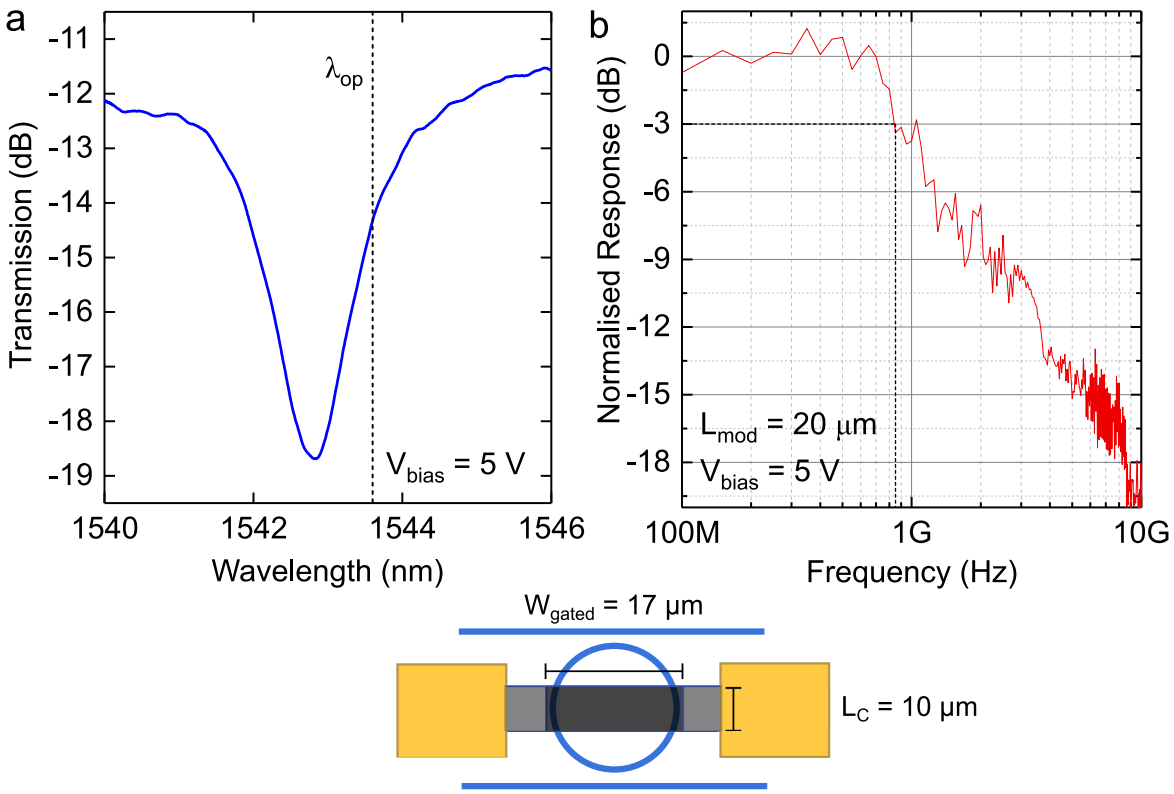

Fig. 8.7 (a) Transmission of a DSLG RRM ($L_{\text{mod}} \sim 20\ \mu$m) at $V_{\text{bias}} = 5$ V with dashed line showing $\lambda_{\text{op}} = 1543.6$ nm, (b) measured EO frequency response at λ_{op} with $V_{\text{pp}} = 1$ V. Device schematic shown below shows dimensions of overlapping SLG region.

I measured the EO BW following the procedure described in section 6.3 using $V_{\text{pp}} = 1$ V. Unfortunately, due to damage to the device caused by dielectric breakdown, I was not able to measure the device shown in figure 8.3. Instead I am presenting a similar device that had similar dimensions with $L_{\text{mod}} \sim 20\ \mu$m and $W_{\text{gated}} \sim 17\ \mu$m. The RR had $L_{\text{ring}} \sim 58\ \mu$m, coupling length of 6 μm, and a coupling separation of 180 nm. I selected V_{bias} and λ_{op} so that I could maximise the signal response in the ESA. Figure 8.7a shows λ_{op} by the dashed line for $V_{\text{bias}} = 5$ V. Figure 8.7b shows the measured EO response as a function of f, with $f_{3\text{dB}} \sim$850 MHz. The EO BW of the device is limited to the MHz range because of the aspect ratio of the device, shown in figure 8.7. The aspect ratio limits $f_{3\text{dB}}$ because of

the large overlapping region (170 μm^2), which increases R_{gated} and C_{ox}, but also because of the large resistances resulting from the short length of contacted SLG (L_{C} = 10 μm). Such short contacted regions significantly increase R_{C} through equation 5.5, and R_{ungated} and R_{gated} through equation 5.4. This is a constant trade-off for SLG based devices, where reduced L_{mod} leads to a lower capacitance, but at the cost of higher resistance. The increase in resistance is inevitable when using DSLG modulators with small L_{mod}, so reducing C_{ox} is essential. Here, C_{ox} can be reduced by placing the contact to one of the SLG inside the ring. This would reduce W_{gated} from $\sim$ 17 μm to $\sim$ 450 nm, leading to C_{ox} reducing from $\sim$ 600 fF to $\sim$ 15 fF. As well as a reduction in C_{ox}, this would also result in a reduction of R_{gated} from $\sim$ 1420 Ω to $\sim$ 40 Ω. In this case, the simulated f_{3dB} would increase from hundreds of MHz to $\sim$ 18 GHz for τ = 22 fs, R_{C} = 1,000 Ω$\cdot\mu$m, L_{C} = 10 μm, W_{gated} = 450 nm (E_{F} = 0.4 eV), and W_{ungated} = 1 μm (E_{F} = 0.2 eV). Further fabrication runs would be needed to confirm whether reducing W_{gated} will impact other parameters such as the modulation efficiency, which might be reduced due to a decreased active area. In this case, the expected f_{3dB} for a reduced overlapping SLG region does not exceed 20 GHz because it is limited by the low value of τ. Here, the reduction in τ could be attributed to increased short-range scattering from defects and residues on the SLG films as a result from SLG processing. Thus, for applications that require $f_{\text{3dB}} > 20$ GHz then new processing techniques are required to maintain high values of τ during device fabrication. For example, if τ could be improved to 44 fs then f_{3dB} would exceed 25 GHz. When using RRs, the achievable optical BW, $f_{\text{3dB}}^{\text{opt}}$, is limited by the cavity photon lifetime τ_{cav} [65]. τ_{cav} is related to the Q-factor through equation 3.27 and $f_{\text{3dB}}^{\text{opt}}$ by equation 3.28. Owing to the losses of our DSLG RRM, the Q-factor is $\sim$ 2000 which corresponds to $\tau_{\text{cav}} \sim$ 1.6 ps and $f_{\text{edB}}^{\text{opt}} \sim$ 48 GHz. Therefore, the RRM is not limited by τ_{cav}, and only on the geometry of the DSLG modulator.

8.4 Conclusions

In this chapter I have presented the results of DSLG RRMs that I have designed and fabricated on Si WGs. I have described how an RRM can be operated as an amplitude and phase modulator and presented the device design and fabrication process. I have shown the V-dependent transmission of the DSLG RRMs and extracted Δn_{eff} and α of the DSLG modulator by analysing $\Delta\lambda_{\text{res}}$ and ΔQ-factor with V. I compared the measured Δn_{eff} and α to simulated values (τ = 22 fs) which followed the same behaviour, where the observed differences were attributed to asymmetries between the two SLG. From $\Delta\lambda_{\text{res}}$ I calculated a $V_\pi L \sim$ 0.12 V·cm, which is a factor of two better than state-of-the-art SLG phase modulators [212]. I estimated the IL by extracting α_{ring} from a and accounting for additional propagation

losses from fabrication as measured from reference WGs. From this, considering V_{bias} = 10 V, I then calculated an $\text{FOM}_{\text{ER}} \sim 74.5$ VdB. Whilst the small size of the active region of the DSLG RRMs have minimised the IL from the high optical losses of SLG, it has also limited the achievable $\Delta\phi$. This means that it is likely that L_{mod} would have to be increased in order to keep V_{pp} within practical ranges. Therefore, even with a record-low $V_\pi L$, high optical losses mean that it will be challenging to further decrease FOM_{ER} as L_{mod} increases. Significant reductions in the optical losses of SLG will be needed to make DSLG modulators competitive compared to other technologies.

I calculated FOM_{EA} from the extracted EO response at λ_{op} = 1542.82 nm. By considering V_{bias} = 13 V, I calculated an $\text{FOM}_{\text{EA}} \sim 4.48$, which is a factor of two better than state-of-the-art SLG EAMs (~ 2 [211]). Even though the $\Delta\phi$ induced by the DSLG modulator was far from being large enough for complex modulation formats, the resonant nature of the RR meant that $\Delta\phi$ could be translated into a reasonable ER. The ER demonstrated (~ 5 dB) by the DSLG RRM would be suitable for binary modulation formats, but would need to be slightly increased to be used for multi-level modulation formats like PAM-4. Like for phase modulation, the ER could be improved by increasing V_{pp}, L_{mod}, or a combination of the two. A smaller increase would be needed in comparison to phase modulation, leading to more compact DSLG RRMs for amplitude modulation, but the impact on the IL and cut-off frequency would need to be investigated further.

I have discussed the limitations to $f_{3\text{dB}}$ as a result of the aspect ratio of the the DSLG modulator. This means that the DSLG RRMs that I have presented are unsuitable for high-speed optical links that need BWs in the GHz range. I have discussed the limitations to $f_{3\text{dB}}$ as a result of the aspect ratio of the the DSLG modulator. I have explained that the large overlapping SLG region has largely restricted $f_{3\text{dB}}$ because of the increased C_{ox}. I have shown that reducing W_{gated} by contacting one of the SLG with a via can lead to a simulated $f_{3\text{dB}} \sim 20$ GHz (τ = 22 fs). $f_{3\text{dB}}$ can then be pushed further by improved SLG processing techniques to preserve τ through-out fabrication. With these design and process optimisations then future DSLG RRMs could provide efficient amplitude modulation that can be used in optical links operating > 20 GHz.

Chapter 9

Mach-Zehnder Graphene Modulators

9.1 Introduction

MZMs consist of a MZI with a phase modulator on one or both arms [8]. MZMs are used to convert $\Delta\phi$ into a change of amplitude by using interference with an MZI [8]. The modulators control the phase difference between the two arms of the MZM, $\Delta\phi_{\mathrm{MZM}}$ [8]. In comparison to EAMs and RRMs, MZMs require a larger area for the MZI and are more suited for applications that do not have strict area requirements. They are typically used for IQ modulation which, combined with coherent detection, is attractive for long-haul optical interconnect because it increases the spectral efficiency and noise tolerance [8]. However, IQ modulation is less attractive for short-reach applications due to the penalty of an increased area of the MZI and complexity associated with coherent detection.

Depending on the driving V, an MZM can be operated as either an amplitude or a phase modulator [8]. Figure 9.1a shows an MZM being operated as an amplitude modulator. Here, a data stream of '10111' is being transmitted with a time-dependent V, shown in green, that is used to drive the MZM. The output of the MZM, P_{t}, as a function of V is shown in blue. For a given V_{pp}, the resulting time-dependent output of the MZM is shown in orange. For amplitude modulation the ideal operating point, V_{bias}, will be when $P_{\mathrm{t}} = P_{\mathrm{max}}/2$. Relative to this point, a '0' bit will be represented by $V = V_{\mathrm{bias}} - V_{\pi}/4$ and a '1' bit will be represented by $V = V_{\mathrm{bias}} + V_{\pi}/4$. This corresponds to a peak-to-peak voltage of $V_{\mathrm{pp}} = V_{\pi}/2$ which causes the phase of the MZM output to change by $\pi/2$. A $\pi/2$ phase shift results in a transition from maximum to minimum transmission of the MZM, as shown in orange. Therefore, the data stream will be converted from the electrical to the optical domain by the MZM where the amplitude of the transmitted power will modulate between P_{max} and 0.

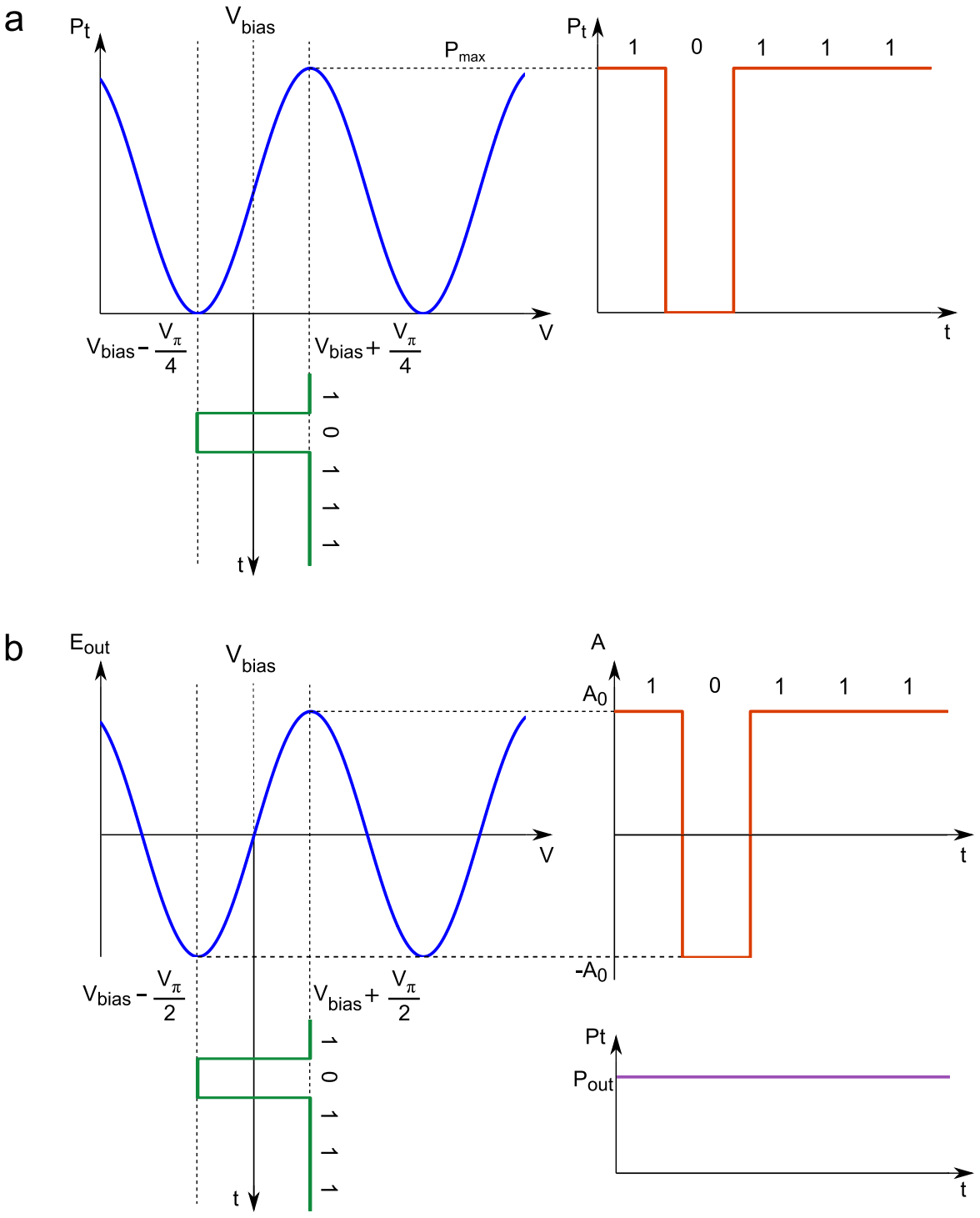

Fig. 9.1 MZM operation for (a) amplitude modulation showing the V-dependent P_t of the MZM (blue), the time-dependent V signal for the data stream (green), and the time-dependent P_t of the MZM (orange). By modulating the driving voltage $\pm V_\pi/4$ around V_{bias}, the transmission of the MZM modulates from P_{max} to 0. (b) Phase modulation showing the V-dependent output electric field of the MZM (blue) and the time-dependent V signal for the data stream (green). The time-dependent output of the MZM is given in terms of amplitude of electric field (orange) and transmitted power (purple). By modulating the driving voltage $\pm V_\pi/2$ around V_{bias} the phase of the output modulates by π.

On the other hand, if instead a larger V_{pp} was used then P_t would no longer depend on time, and the MZM will be a phase modulator. Figure 9.1b shows the operation of a MZM as a phase modulator. Again, a data stream of '10111' is being transmitted with a time-dependent V that is used to drive the MZM, shown in green. In this case it is more convenient to describe the output of the MZM in terms of the electric field, E_{out}, which is shown in blue. This time, for phase modulation, the ideal operating point is when E_{out} = 0. Now, instead of using $V_{pp} = V_\pi/2$ we choose to use $V_{pp} = V_\pi$. This means that a '0' bit is represented by $V = V_{bias} - V_\pi/2$ and a '1' bit is represented by $V = V_{bias} + V_\pi/2$. This means that the transmitted signal for bit '0' and '1' will differ in phase by a factor of π. The amplitude of the transmitted electric field of the MZM is shown in orange where it modulates between A_0 and $-A_0$. Unlike amplitude modulation, the P_t of the MZM remains constant as $P_t = |E_{out}|^2$. Therefore, the data stream will be converted from the electrical to the optical domain by the MZM where the phase of the transmitted power will be modulated by π.

In this chapter I will present the results of the DSLG MZMs that I designed for IQ modulation for high spectral efficiency data transmission in long-haul communication networks. I designed the DSLG MZMs on Si WGs following the discussion in chapter 5, specifically optimised for maximum BW which would be desirable for high-speed data transmission. Starting with a description of the fabrication of the DSLG modulators I will present the EO response and BW of the devices. In particular, I have investigated operating the DSLG MZM as a pure phase modulator which involves gating the DSLG MZM such that the E_F of SLG goes beyond 0.4 eV into the Pauli blocking regime where interband transitions are blocked and optical losses remain constant. This is of particular interest for IQ modulation which use pure phase modulation to generate the QAM constellation diagrams, and any unwanted amplitude modulation will result in increased intersymbol interference [8].

9.2 Fabrication

In order for the DSLG MZMs to be usable in coherent detection systems based on complex modulation formats they must demonstrate $\Delta\phi = \pi$. However, the DSLG MZMs could be operated in a push-pull configuration such that $\Delta\phi = \pi/2$ would also be acceptable. I fabricated the DSLG MZMs using passive Si photonic substrates that were designed and fabricated by IMEC using their SOI platform [221]. The MZIs were designed for operation at 1.55 μm (550 nm and 480 nm WG widths) and 1.65 μm (550 nm and 620 nm WG widths) and made of 220 nm thick single-mode TE Si WGs with 2 input and output ports and MMIs to split and recombine the light. I designed the DSLG modulators with L_{mod} = 100 μm, 200

μm, 300 μm, and 450 μm, where 450 μm was the longest DSLG modulator I could place within the arms of the MZI. To maximise f_{3dB} I designed the DSLG modulators with W_{gated} matching the width of the WG. I fabricated the DSLG stack by transferring and patterning polycrystalline CVD SLG grown by Dr Osman Balci and Dr Sachin Shinde at the University of Cambridge. The as-grown, as-transferred, and encapsulated SLG films are characterised by Raman spectroscopy at 514 nm and shown in figure 9.2.

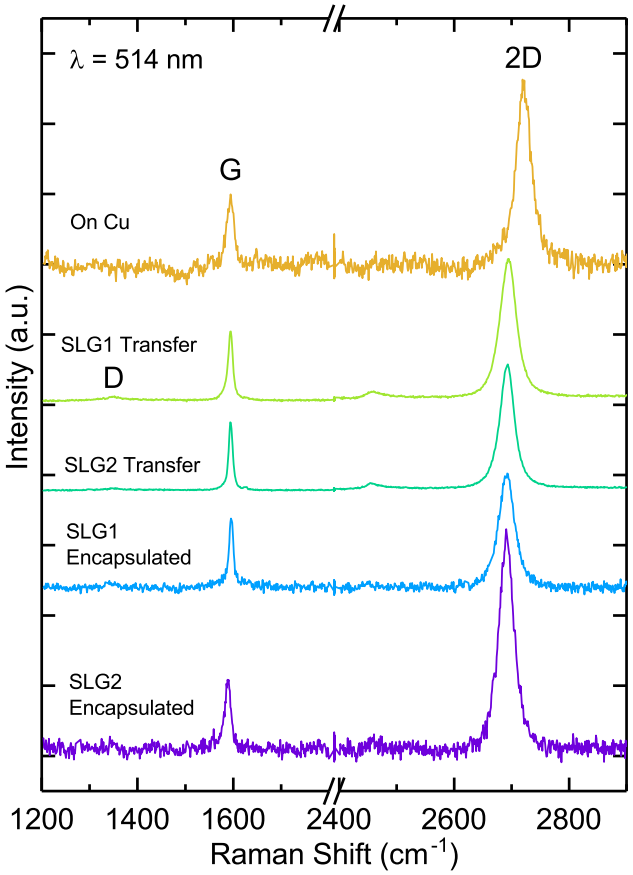

Fig. 9.2 Raman spectra at 514 nm for SLG1 and SLG2 for different processing steps, as-grown on Cu, after transfer, after device fabrication. The spectra are normalised to I(G) with Cu background PL removal [222].

The Raman spectra on Cu have had the photoluminescent background from the Cu foil removed [222]. The 2D peak is single-Lorentzian confirming the presence of SLG [49, 52], and the absence of a D peak indicates negligible defects [49, 50, 55]. The Raman spectra of the as-transferred SLG are in figure 9.2. I estimated E_F from I(2D)/I(G), A(2D)/A(G), FWHM(G) and Pos(G) [51, 54] as $E_F \sim 100$ meV ($N \sim 8\times10^{11}$ cm^{-2}) for the SLG closest to the WG (SLG1) and $E_F \sim 150$ meV ($N \sim 2\times10^{12}$ cm^{-2}) for the SLG farthest from the

SLG1	Pos(G) (cm^{-1})	FWHM(G) (cm^{-1})	Pos(2D) (cm^{-1})	FWHM(2D) (cm^{-1})	$\frac{I(2D)}{I(G)}$	$\frac{A(2D)}{A(G)}$	$\frac{I(D)}{I(G)}$
On Cu	1594	18	2721	31	2.6	4.6	-
As-transferred	1594	12	2694	33	2.1	5.8	0.04
Encapsulated	1596	11	2691	31	1.7	5	0.07

SLG2	Pos(G) (cm^{-1})	FWHM(G) (cm^{-1})	Pos(2D) (cm^{-1})	FWHM(2D) (cm^{-1})	$\frac{I(2D)}{I(G)}$	$\frac{A(2D)}{A(G)}$	$\frac{I(D)}{I(G)}$
On Cu	1594	18	2721	31	2.6	4.6	-
As-transferred	1595	10	2692	29	1.8	5.4	0.02
Encapsulated	1589	15	2691	30	3.2	6.4	0.1

Table 9.1 Raman fit parameters for SLG1 and SLG2 at different process steps of fabrication.

WG (SLG2). From the estimated E_F I calculated the average interdefect distance, L_D, and the defect density, N_D, using [55],

$$L_D^2[\text{nm}^2] = \frac{(1.2\pm0.3)\times10^3}{E_L^4[\text{eV}]^4}\left(\frac{I(D)}{I(G)}\right)^{-1}\{E_F[\text{eV}]\}^{-(0.54\pm0.04)} \tag{9.1}$$

$$N_D[\text{cm}^{-2}] = (2.7\pm0.8)\times10^{10}E_L^4[\text{eV}]\frac{I(D)}{I(G)}\{E_F[\text{eV}]\}^{0.54\pm0.04} \tag{9.2}$$

where E_L is the laser excitation energy, which is 2.41 eV for 514 nm excitation. By considering $E_F \sim 100$ meV and $E_F \sim 150$ meV, I calculated $N_D \sim 1\times10^{10}$ cm^{-2} for SLG1 and $N_D \sim 7\times10^9$ cm^{-2} and for SLG2 [50, 55]. Figure 9.2 plots the Raman spectra of the completed devices where SLG1 and SLG2 are encapsulated by Al_2O_3. From the Raman parameters I calculated $E_F \sim 200$ meV ($N \sim 3\times10^{12}$ cm^{-2}) for SLG1 and $E_F \sim 100$ meV ($N \sim 8\times10^{11}cm^{-2}$) for SLG2. Using I(D)/I(G) for SLG1 and SLG2, I calculated $N_D \sim 3\times10^{10}$ cm^{-2} for SLG1 and SLG2. N_D is higher for encapsulated SLGs due to additional defects introduced during processing. We see that SLG1 and SLG2 are not identical, as they have undergone different amounts of processing. Any differences in terms of E_F and N_D degrades the DSLG modulator performance, limited by SLG with the lowest τ. The final fabricated devices are shown in figure 9.3.

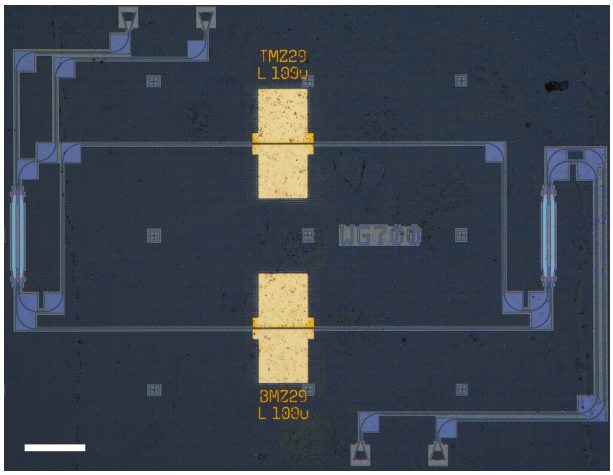

Fig. 9.3 Optical micrograph of DSLG MZM fabricated on a 2×2 Si MZI. PMMA residues and rolled-up SLG from SLG transfer are visible on contacts and around the DSLG modulators. Scale bar 100 μm.

9.3 Results

9.3.1 Electro-optic Response

I measured the voltage dependent transmission of the DSLG MZM following the procedure described in chapter 6.3 with P_{in} = 1 mW. Figure 9.4a shows the λ-dependent transmission of a DSLG MZM for different applied V, where the MZM consists of a 2×2 unbalanced MZI (550 nm × 220 nm Si TE WGs) with a 100 μm DSLG modulator on each arm. I have chosen to present this device for simplicity because it shows the widest range of the EO response of SLG. To maximise the transmitted power one device is biased at 10 V so that it is transparent, whilst the V applied to the other device is swept. Figure 9.4b shows the extracted $\Delta\lambda_{\text{res}}$ and ER with as a function of V. The ER is minimised near the Dirac point, because the absorption of the SLG on the active arm is highest, whilst the device on the other arm is transparent. ER then increases with increasing V, as absorption by the active arm is reduced, until flattening $>$ 10 V, when SLG on both arms are transparent and interband transitions are blocked. Above 10 V we see in figure 9.4c that the ER does not significantly change as the voltage increases. This shows that the transparency regime is ideal for pure phase modulation, because we still have a quasi-linear change in phase and constant losses. A similar V-dependent change in λ_{res} and ER is observed on either side of the Dirac point, where there is a weaker effect for $V < 0$. The similarity around the Dirac point is due to the ambipolarity of SLG [24], and the asymmetry is due to different scattering rates of electrons and holes, resulting from an uneven distribution of positively or negatively charged impurities [223–226]. $V_{\text{Dirac}} \sim$ -1.3 V which corresponds to $\sim$ 180 meV using equation 2.16 and 2.18.

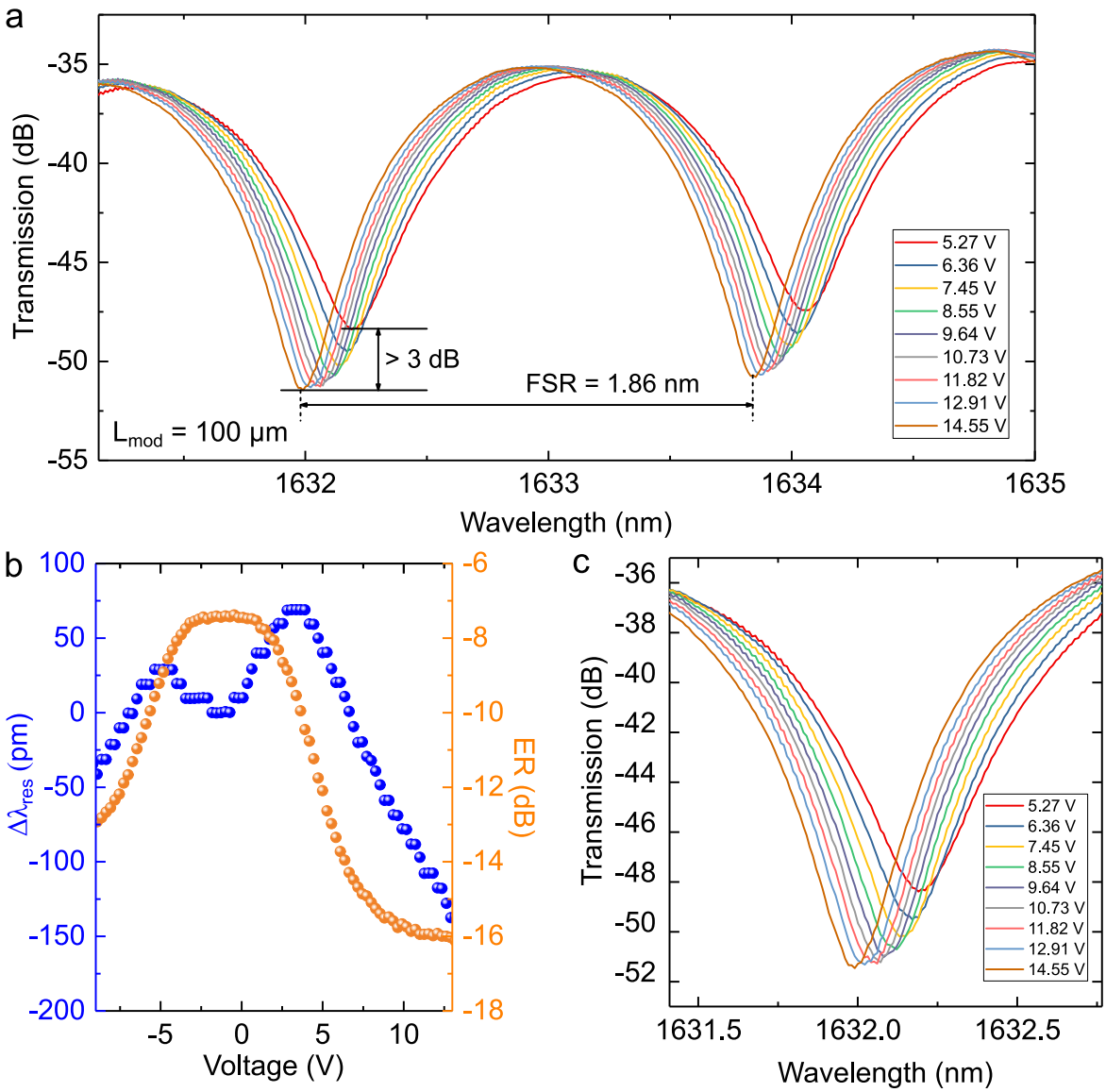

Fig. 9.4 (a) Voltage dependent transmission of a DSLG MZM containing a 100 μm DSLG modulator on each arm. One modulator is biased at 10 V whilst the voltage across the other is swept. MZM fabricated on a 550 nm $\times$ 220 nm Si 2$\times$2 unbalanced MZI. (b) Extracted $\Delta\lambda_{\text{res}}$ (blue) and ER (orange) as a function of V, (c) close-up of one resonance peak.

By linearly fitting the measured $\frac{d\lambda_{\text{res}}}{dV}$ in figure 9.4b, and using equation 8.10 and 8.13 I extracted $V_\pi L \sim 0.3$ V·cm, matching that of state-of-the-art SLG phase modulators [212]. However, unlike Ref.[212], our devices show pure phase modulation with negligible change in optical losses, a desirable property for IQ modulation. Considering $V_{\text{bias}} > 10$ V, in the transparency regime of figure 9.4b, I estimated the IL using the DSLG EAMs in chapter 7. In transparency, IL $\sim$ 5.6 dB for the 75 μm DSLG EAM, which corresponds to $\alpha \sim 746$ dB/cm

when normalised by L_{mod}. This is higher than state-of-the-art Si depletion ($\sim$ 22 dB/cm [113]), III-V ($\sim$ 19 dB/cm [115]), LN ($\sim$ 0.25 dB/cm [122]), and SLG ($\sim$ 236 dB/cm [212]) MZMs. I attribute the additional optical losses to scattering from resist residues and damage to SLG during device fabrication, degrading τ. The simulated optical loss of the same device structure is $\sim$ 93dB /cm for τ = 440 fs. So, IL can be further reduced with improved SLG processing. IL can also be further reduced by increasing the overlapping SLG region, as the ungated SLG sections are not in transparency, and contribute to optical losses. However, any increase in the overlapping SLG region to reduce IL, will increase C_{eq}, therefore reducing $f_{3\text{dB}}$. Due to the high optical loss, our DSLG phase modulator has $\text{FOM}_{\text{ER}} > 200$ VdB, which is far greater than the lowest reported Si ($\sim$ 30 VdB [113]), LN ($\sim$ 5.4 VdB [121]), and III-V ($\sim$ 0.8 VdB [115]) MZMs.

The observed $\Delta\lambda_{\text{res}}$ and ΔER with changing V is a direct result of the induced Δn_{eff} and $\Delta\alpha$ by the DSLG MZM. As described in chapter 8, the measured $\frac{d\lambda_{\text{res}}}{dV}$ and FSR can be used to calculate $\Delta\phi$ with equation 8.8. $\Delta\phi$ can then be used to extract Δn_{eff} with equation 3.4. The ER of the MZM is related to the difference in absorption between the two arms of the MZI, $\Delta\alpha_{\text{MZM}}$. Where $\Delta\alpha_{\text{MZM}}$ is defined in terms of the power attenuation coefficient and length of each arm $\Delta\alpha_{\text{MZM}} = \alpha_1 L_1 - \alpha_2 L_2$. If the propagating wave in one arm is completely absorbed there will be no interference at the output because there will only be one propagating wave remaining. This is the extreme case, however for more moderate losses the ER will increase when $\Delta\alpha_{\text{MZM}}$ is minimised and decrease when $\Delta\alpha_{\text{MZM}}$ is maximised. By monitoring the ER of the MZM with changing V we can directly extract $\Delta\alpha$ resulting from the DSLG modulator itself. The ER can be expressed as the ratio of maximum and minimum P_{t} of the DSLG MZM,

$$\text{ER} = \frac{P_{\text{t,max}}}{P_{\text{t,min}}} \tag{9.3}$$

For an MZM, P_{t} is given by equation 3.32, where $P_{\text{t,max}}$ occurs when $\Delta\phi_{\text{MZM}} = 0$, and $P_{\text{t,min}}$ occurs when $\Delta\phi_{\text{MZM}} = \pi$. Substituting $P_{\text{t,max}}$ and $P_{\text{t,min}}$ into equation 9.3 gives the ER of the MZM,

$$\text{ER} = \frac{1 + e^{\Delta\alpha_{\text{MZM}}} + 2e^{\frac{1}{2}\Delta\alpha_{\text{MZM}}}}{1 + e^{\Delta\alpha_{\text{MZM}}} - 2e^{\frac{1}{2}\Delta\alpha_{\text{MZM}}}} \tag{9.4}$$

Therefore 9.4 relates the measured ER and $\Delta\alpha_{\text{MZM}}$ between the two arms of the MZM. Using the quadratic formula I can solve equation 9.4 for $\Delta\alpha_{\text{MZM}}$ such that,

$$\Delta\alpha_{\text{MZM}} = 2\ln\left(\frac{-2(1+\text{ER}) + \sqrt{(2(1+\text{ER}))^2 - 4(1-\text{ER})(1-\text{ER})}}{2(1-\text{ER})}\right) \tag{9.5}$$

Considering that $\Delta\alpha_{MZM}$ is only due to the DSLG modulator, $\Delta\alpha$ can be directly linked to $\Delta\alpha_{MZM}$. $\Delta\alpha$ can then be converted to dB and normalised by L_{mod} given by,

$$\Delta\alpha = \frac{1}{L_{mod}} 10\log_{10}(e^{\Delta\alpha_{MZM}-\Delta\alpha_{MZM,Dirac}}) \tag{9.6}$$

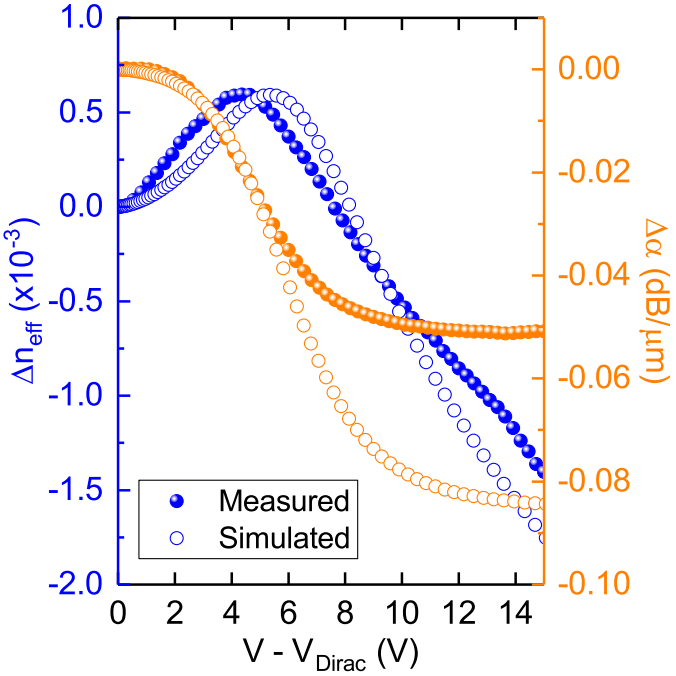

Fig. 9.5 Comparison of measured (solid circles) and simulated (open circles) Δn_{eff} (blue) and $\Delta\alpha$ (orange) for a 100 μm DSLG MZM. Simulation is performed at λ = 1.63 μm at 300 K with τ = 13 fs for both SLG. The simulation uses the same device structure as the measured device, 550 nm × 220 nm Si WG, $W_{gated} \sim$ 550 nm, $W_{ungated} \sim$ 1 μm (E_F = 0.2 eV), d_{Al2O3} = 20 nm (ε_r = 8).

where $\Delta\alpha_{MZM,Dirac}$ is defined as $\Delta\alpha_{MZM}$ at the Dirac point. The measured Δn_{eff} and $\Delta\alpha$ are shown in figure 9.5 along with the simulated values at λ = 1.63 μm. The corresponding V for the simulated values was calculated using equation 5.2 for $W_{gated} \sim$ 550 nm, $W_{ungated} \sim$ 1 μm (E_F = 0.2 eV), d_{Al2O3} = 20 nm (ε_r = 8), assuming that both SLGs have the same τ and residual doping. The measured values show a similar behaviour to the simulated values, with maximum absorption $<$ 3 V, which decreases as E_F approaches 0.4 eV, before reaching a minimum absorption $>$ 6 V when interband transitions become blocked. However, the measured values do not completely follow the simulated values because of asymmetries between the two SLG, as shown by Raman spectroscopy in Fig.9.2. Any asymmetry between the two SLG will reduce the induced ΔE_F from V, thereby shifting the Pauli blocking condition to a different V, and reducing the slope of Δn_{eff} and $\Delta\alpha$ with V. In figure 9.5

this is seen in the shift of the peak of Δn_{eff} from $\sim$ 5.3 to $\sim$ 4.3 V, and the reduced $\frac{d\Delta n_{\text{eff}}}{dV}$ above 5 V. The difference between the measured and simulated $\Delta\alpha > 6$ V is attributed to increased propagation losses due to residues remaining on the SLG from processing. As interband transitions in both SLG become blocked > 6 V, the minimum absorption is limited by the increased losses from the residues. Thus, a larger ER can be achieved with process optimisations to limit residues from SLG processing.

It is clear from figure 9.4 that the induced $\Delta\phi$ of the DSLG MZM with $L_{\text{mod}} = 100$ μm is not sufficient for coherent detection systems that use complex modulation formats. Therefore, a longer DSLG modulator will be needed to increase the induced $\Delta\phi$. Figure 9.6 shows the EO response of a DSLG MZM with a DSLG modulator with $L_{\text{mod}} = 450$ μm, and an unbalanced MZI made of 620 $\times$ 220 nm Si TE WGs. Due to the increased L_{mod} compared to the DSLG MZM shown in figure 9.4, the DSLG MZM reaches $\Delta\phi = \pi/2$ between $\sim$ 0 V and $\sim$ 9 V. Therefore, I will use the device with $L_{\text{mod}} = 450$ μm to calculate FOM_{EA} because it will be more representative of the devices that will be used in coherent detection systems based on complex modulation formats. I obtained the EO response of the DSLG MZM by monitoring the transmission as a function of V at a chosen λ_{op}. The voltage-dependent transmission of the device is shown in figure 9.6a, where figure 9.6b shows a zoomed in view of a resonance peak with λ_{op} shown by the dashed line. λ_{op} was chosen as 1631.56 nm as this coincided with λ_{res} at $V_{\text{bias}} = 9.59$ V. The corresponding transmission at λ_{op} is shown in figure 9.6c as a function of V. Figure 9.6c shows that the transmission remains relatively unchanged until $V_{\text{bias}} > 6$ V when the transmission begins to decrease. The rate of change of transmission increases sharply > 8 V as λ_{res} reaches λ_{op}. Here, the transmission changes by $\sim$ -22 dB/V, which is far greater than the DSLG RRM in chapter 8 owing to the greater Δn_{eff} and $\Delta\alpha$ that can be induced because L_{mod} for the DSLG MZM (450 μm) is much greater than the DSLG RRM (18 μm). I will first consider the DSLG MZM as an amplitude modulator. By considering P_{t} between $V \sim 8.4$ V and $V \sim 9.6$ V, this corresponded to an ER $\sim$ 21.7 dB for $\Delta V \sim 1.2$ V. I was unable to measure the IL of the DSLG MZM because I did not have a suitable reference MZI that had undergone the same fabrication. Instead, in order to calculate FOM_{EA} I estimated the IL from the DSLG EAMs in chapter 7 because they were fabricated at the same time. By considering $V_{\text{Dirac}} \sim$ -1.4 V, shown in the inset of figure 9.6b, I estimated the IL at $V_{\text{bias}} = 9$ V for the DSLG MZM from the IL of the DSLG EAM at $|V - V_{\text{Dirac}}| \sim 10$ V. The corresponding IL of the 75 μm DSLG EAM, shown in figure 7.3, at $|V - V_{\text{Dirac}}| \sim 10$ V is $\sim$ 6 dB, which leads to $\alpha \sim 800$ dB/cm when normalised by L_{mod}. Therefore, I estimate the IL of the 450 μm DSLG MZM as $\sim$ 36 dB, resulting in an $\text{FOM}_{\text{EA}} \sim 0.6$. The FOM_{EA} for the DSLG MZM is much lower than the DSLG RRM ($\sim$ 4.48) because it is limited by such a high IL (> 30 dB) resulting from increased L_{mod}.

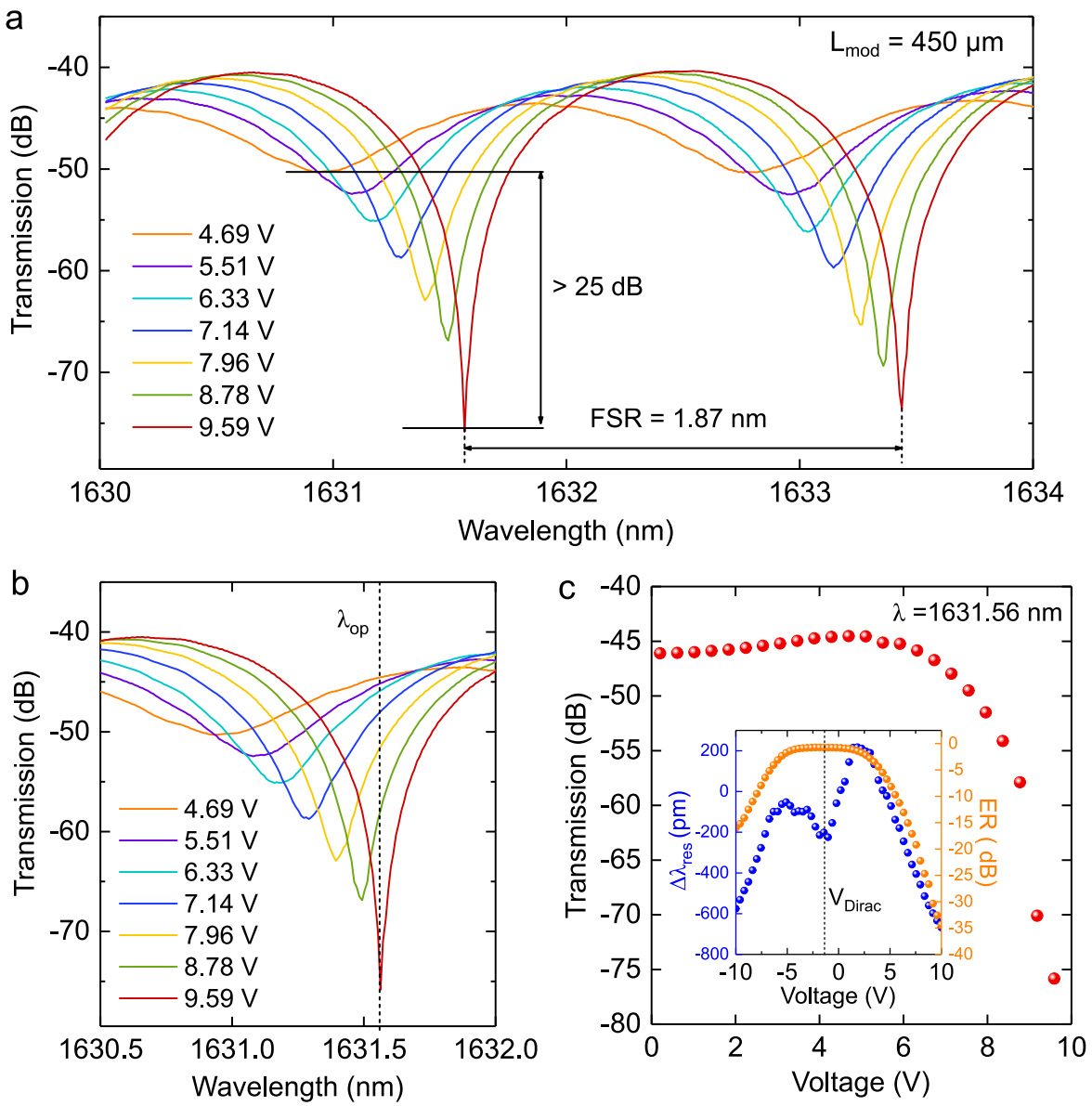

Fig. 9.6 (a) Voltage dependent transmission of a DSLG MZM containing a 450 μm DSLG modulator on each arm. One modulator is biased at 10 V whilst the voltage across the other is swept. The DSLG MZM was fabricated on a 2×2 unbalanced MZI made with 620 nm × 220 nm Si WGs. (b) Close-up of one resonance peak where dashed line indicates λ_{op} = 1631.56 nm, (c) extracted EO response as an amplitude modulator showing the V-dependent transmission at λ_{op} = 1631.56 nm, inset shows corresponding $\Delta\lambda_{res}$ (blue) and ER (orange) as a function of V.

9.3.2 Electro-optic Bandwidth

I measured the EO BW following the procedure described in section 6.3.2. Figure 9.7a shows the frequency response of a 50 μm DSLG modulator for different V_{bias}. f_{3dB} increases

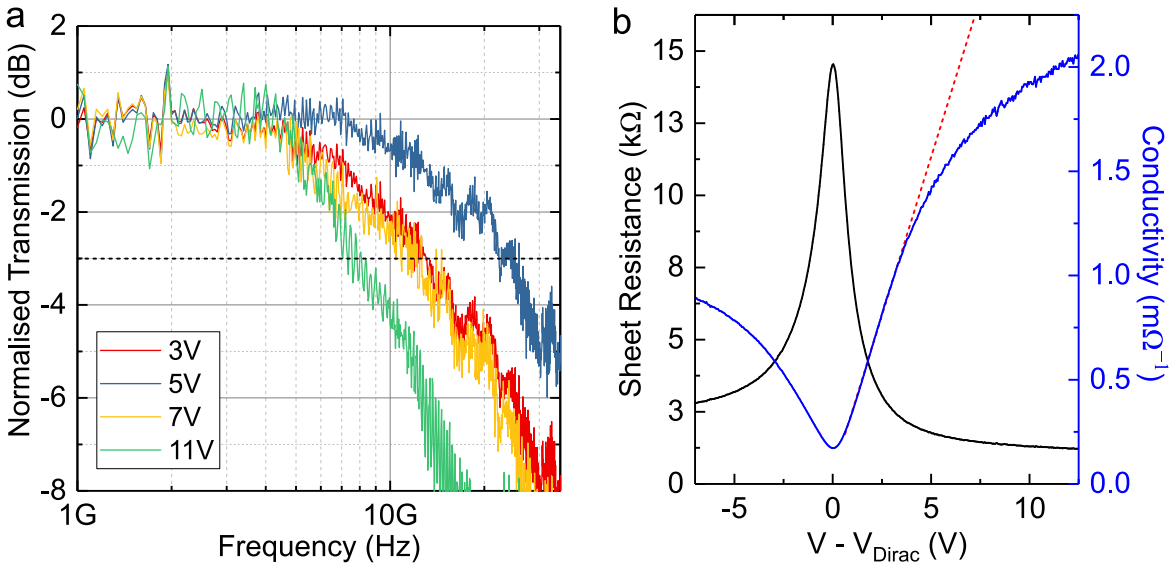

Fig. 9.7 (a) EO frequency response for a 50 μm DSLG EAM at λ_{op} = 1.55 μm as a function of V_{bias} with V_{pp} = 1 V, black dashed line shows -3 dB reduction in the transmission. The Si WG is 550 nm $\times$ 220 nm, (b) Measured R_S (black) and calculated $\sigma_{d.c.}$ (blue) for a Hall bar with channel dimensions 10 μm $\times$ 25 μm. Red dashed line is the $\sigma_{d.c.}$ linear fit for $|V - V_{Dirac}| > 0$, showing the transition from the linear to sublinear regime for $|V - V_{Dirac}| >$ 5 V.

from 13 to 25 GHz between 3 and 5 V, then decreases to 12 GHz for 7 V and 8 GHz for 11V. I attribute the decrease in $f_{3dB} > 5$ V to a reduction in μ due to increased short-range scattering of carriers as E_F increases. For these RC limited devices, I expect f_{3dB} to increase with V, because of the reduced R_S. I performed 4-point-probe measurements using top-gated Hall bar structures that were fabricated on the same sample and so underwent the same fabrication steps. Figure 9.7b shows the measured R_S as a function of V, normalised to the channel geometry, and the calculated $\sigma_{d.c.}$ using equation 2.12. I observe the expected [24] peak in R_S at the Dirac point, which decreases with increasing V. Even though R_S continues to decrease with V, I do not observe an increase of $f_{3dB} > 5$ V. The field-effect mobility, μ_{FE}, is derived from the measured $\sigma_{d.c.}$ using equation 2.19. Where the linear region of $\sigma_{d.c.}$ in figure 9.7b on either side of the Dirac point corresponds to a constant μ_{FE}. By doing a linear fit of $\sigma_{d.c}$ on either side of the Dirac point, and using equation 2.19 with a d_{Al2O3} = 20 nm (ε_r = 8), I extracted $\mu_{FE,h} \sim 450$ cm^2/Vs for holes and $\mu_{FE,e} \sim 870$ cm^2/Vs for electrons. As $V > 5$V, $\sigma_{d.c.}$ flattens and $\frac{d\sigma_{d.c.}}{dV}$ becomes sublinear. Sublinear behaviour at high carrier concentration ($> 10^{12}$cm^{-2}) was previously observed [223, 225], and attributed to short-range scattering from defects becoming the dominant scattering source over charged-impurities. In the sublinear region, equation 2.19, which assumes that $\frac{d\sigma_{d.c.}}{dV}$ is linear, is no longer valid, and μ_{FE} cannot be considered the same as in the linear region.

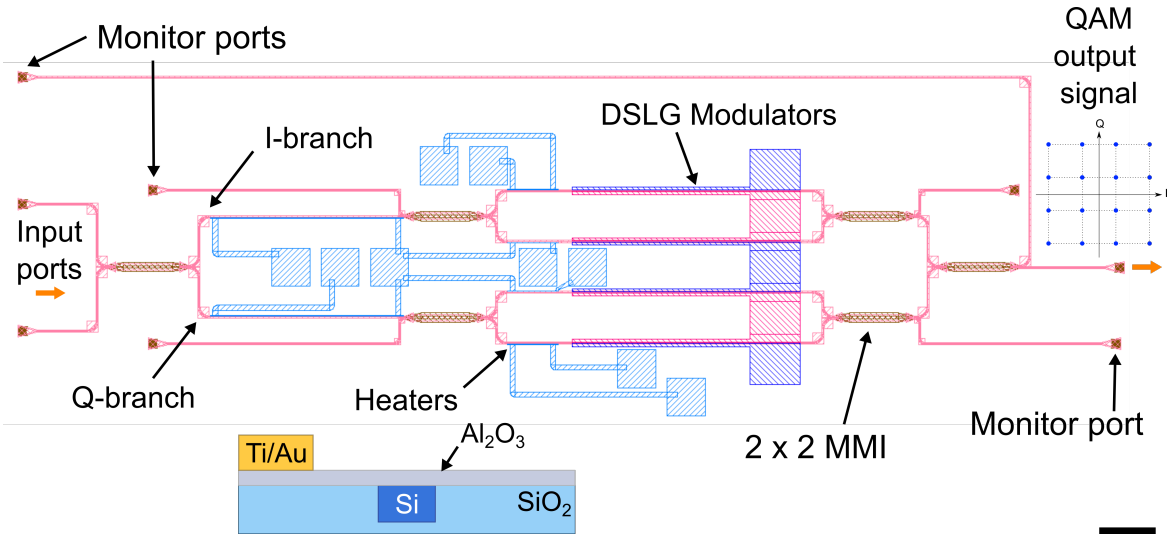

Fig. 9.8 Schematic of single-polarisation IQ modulator containing heaters (schematic shown in inset) and 8 DSLG modulators, scale bar 100 μm.

$\frac{d\sigma_{\text{d.c.}}}{dV}$ decreases by a factor ~ 3 between 5 and 10 V in figure 9.7b. I associate this with a comparable reduction in μ. As shown in chapter 5, figure 5.11d, $f_{3\text{dB}}$ strongly depends on μ. I thus assign the V-dependent slow-down in figure 9.7a to a decrease in μ above 5 V due to increased short-range scattering as carrier concentration increases. This would lead to a $f_{3\text{dB}}$ slow-down of the same order of magnitude as that measured between 5 and 11 V, where $f_{3\text{dB}}$ drops from 25 to 8 GHz. This contrasts the increase from 13 to 25 GHz between 3 and 5 V, where we are still in the linear region of $\sigma_{\text{d.c.}}$, and benefit from decreasing R_{S}. The transition to sublinear behaviour can be pushed to higher carrier concentrations by decreasing the sources of short-range scattering in SLG, from SLG processing improvements. Therefore, $f_{3\text{dB}}$ can be increased in the transparency regime by improving SLG growth and transfer, to limit any degradation of μ during fabrication.

9.3.3 IQ Modulator

Next, I moved onto integrating 8 DSLG MZMs together to build an IQ modulator. The passive Si photonic circuit for the IQ modulator was designed by Dr Alfonso Ruocco at the University of Cambridge and fabricated at IMEC. The passive circuit consisted of a nested MZI and 2×2 MMIs, as shown in figure 9.8. The input signal is split by the first MMI into the in-phase branch, I-branch, and the quadrature branch, Q-branch. The signal in each branch is then split again by another MMI into another MZI where an MZM will generate the in-phase and quadrature component of the QAM signal. These are then recombined by another MMI

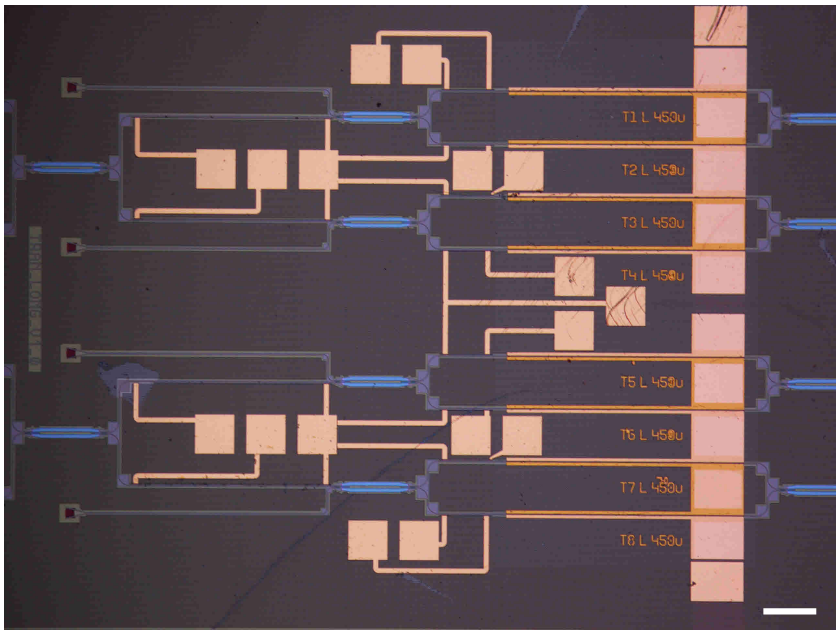

Fig. 9.9 Optical image of the fabricated IQ modulator, scale bar 100 μm

on the output port. Monitor ports are used for characterising individual components within the structure. The IQ modulator will consist of two nested MZIs, one for each polarisation.

Each branch consists of a MZM with two DSLG modulators that have been used for the I and Q branches so that they can be operated in push-pull configuration. In this case, to produce the QAM output signal, a π-phase difference is required between the two arms of the MZM. I maximised the DSLG modulator length in order to maximise $\Delta\phi$ induced by the DSLG modulators. A schematic of the heaters is shown in the inset of figure 9.8, which consists of a metal strip that is placed next to the WG. When a current is passed through the heater the induced temperature increase induces a change in the refractive index of Si, and therefore a phase shift [93]. In this case, I used 50 nm of Ti with a 5 nm Au layer to prevent oxidisation. The heaters also provide additional phase adjustments to account for any imbalance between the DSLG modulators. The heaters were placed 2 μm away from the Si WGs to ensure that they did not contribute to the optical losses. I chose the placement of the heater pads such that they would be suitable for wire bonding.

I fabricated the DSLG modulators in the IQ modulator following the procedure described in section 6.2. I used the wet transfer method to transfer the polycrstalline CVD SLG that was grown by Dr Osman Balci and Dr Sachin Shinde from the University of Cambridge. I patterned the 450 μm SLG channels using EBL and an O_2 plasma etch, and contacted each SLG with sputter coated Ni/Au (5/50 nm) edge contacts. I deposited a 20 nm Al_2O_3 gate dielectric by ALD and a thermally-evaporated 1 nm Al seed layer. Once I encapsulated the

top SLG layer with a further 10 nm Al_2O_3 I fabricated the heaters. I defined the heaters by EBL and then deposited 50 nm of Ti and 5 nm of Au by electron-beam evaporation. Finally, I deposited 200 nm Au by electron beam evaporation on top of the heater pads and interconnect so that they could be wire bonded. I defined the 200 nm Au layer by EBL with a double-layer resist consisting of MMA EL9 (40 s, 3000 rpm, 3 min @ 120 degrees) and PMMA A8 950 (40 s, 4000 rpm, 5 mins @ 120 degrees). I used a different double-layer resist for the 200 nm Au layer in comparison to the Ti/Au heaters to facilitate lift-off of a thicker metal layer. The fully fabricated dual-polarisation IQ modulator is shown in figure 9.9, showing the 8 DSLG modulators and heater pads.

I measured the EO response of the individual DSLG modulators using the monitor ports and following the procedure described in section 6.3. However, due to the low yield of the DSLG modulators I was not able to demonstrate IQ modulation. In this case, the yield was significantly impacted by a poor dielectric resulting in a high leakage current. This high leakage current meant that I could not sufficiently gate the SLG and therefore did not observe any modulation. This was a result of a fabrication error, so that the yield can be improved with further rounds of fabrication. Figure 9.10a shows the transmission of two DSLG modulators on the I-branch of the IQ modulator. The EO response shows the resulting change in amplitude as V increases and the flattening of the transmission > 8 V where the SLG become transparent. By considering the measured IL of the EAMs in chapter 7, we expected an IL of the DSLG modulator to be ~ 30 dB. However, as shown in figure 9.10a, the measured transmission losses were much higher than the expected IL. To extract the transmission losses on the sample I measured the transmission of 4 reference WGs of different lengths and then used the cut-back method [12]. Figure 9.10b shows the losses that I measured at 1.55 μm and the corresponding linear fits for WGs before fabrication and after fabrication. All SLG has been removed from the WGs after fabrication. I extracted $\alpha \sim 2.9$ dB/cm before fabrication and $\alpha \sim 35$ dB/cm after fabrication. To determine the source of loss that was introduced during fabrication I measured the transmission of the same 4 reference WGs at different stages of processing. Figure 9.10c shows the wavelength-dependent transmission of the ~ 1.4 mm WG before fabrication (black) and after various subsequent stages. Figure 9.10d shows the extracted transmission at 1.55 μm for the 4 different WG lengths. The red curve represents the first fabrication step and shows the change in transmission after the initial 10 nm deposition of Al_2O_3. We see that the losses increase from ~ 2.4 dB/cm to ~ 3.2 dB/cm because the transmission peak shifts to a longer wavelength due to the Al_2O_3 altering the coupling angle of the grating coupler. This can be mitigated by optimising the coupling angle such that the transmitted power coincides with the transmission peak. The green curve shows the transmission after the first SLG has been

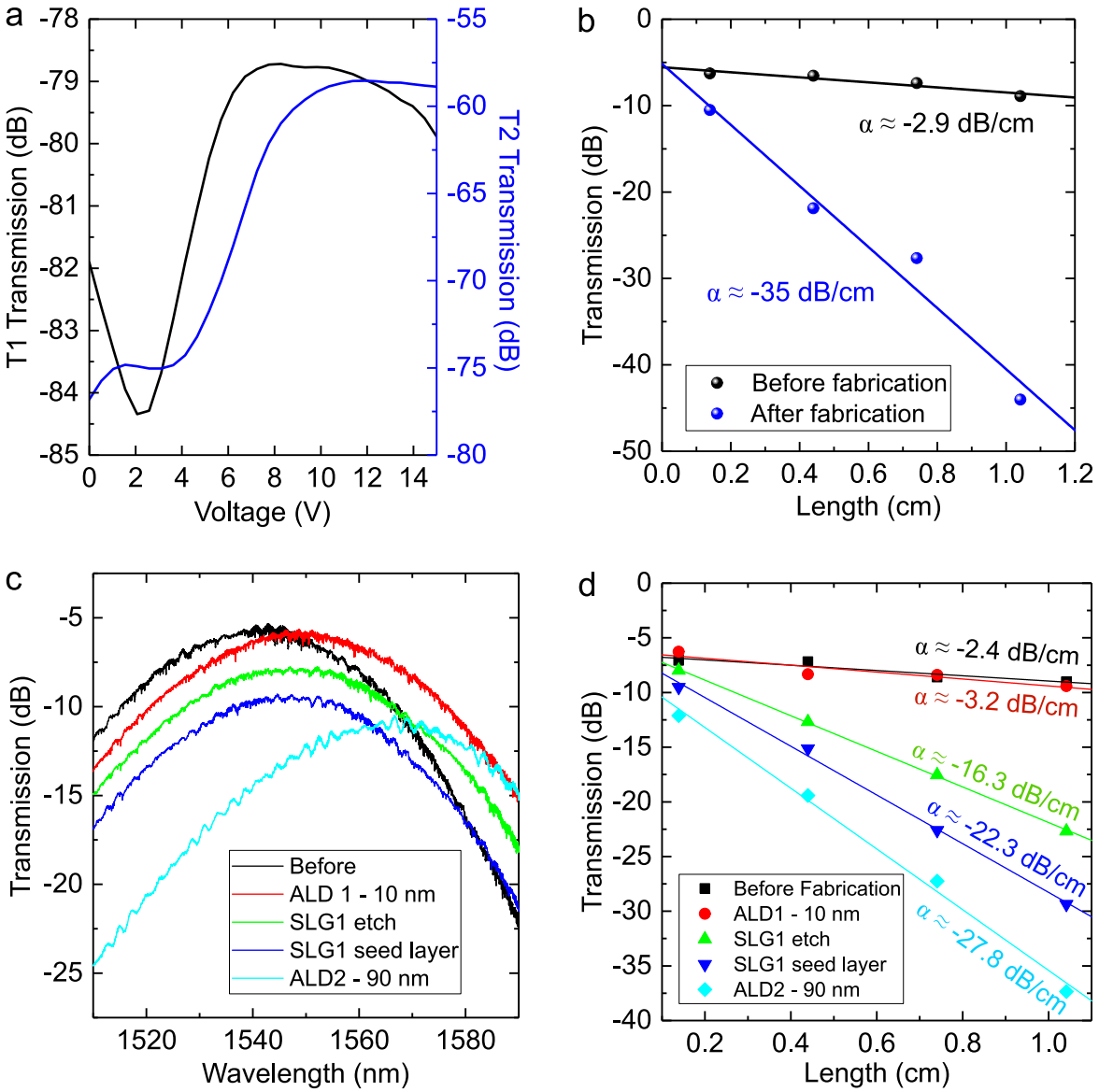

Fig. 9.10 (a) EO response of DSLG modulators on the I-branch of an IQ modulator. (b) Measured propagation loss at 1.55 μm as determined by the cut-back method. (c) Measured wavelength-dependent transmission of a $\sim$ 1.4 mm straight Si WG (450 nm $\times$ 220 nm) after different processing steps. (d) Extracted propagation loss at 1.55 μm of a $\sim$ 1.4 mm straight Si WG (450 nm $\times$ 220 nm) after different processing steps.

transferred and then removed by O_2 plasma. This time we see that even though the SLG has been removed, that the losses have increased from $\sim$ 3.2 to $\sim$ 16.3 dB/cm. The dark blue curve shows the transmission after a 1 nm seed layer of Al has been thermal evaporated onto the SLG, where losses increased from $\sim$ 16.3 to 22.3 dB/cm. The additional losses are attributed to incomplete oxidisation of the Al seed layer, such that remaining Al atoms will absorb light. The second ALD deposition again does not greatly increase the losses, but does shift the peak transmission to longer wavelengths. This leads to an increase from $\sim$ 22.3 to 27.8 dB/cm. Again, this can be taken into account by adjusting the coupling angle. Figure 9.10d shows that the largest increase in propagation losses comes from residues left on the WG after SLG transfer and processing. This could either be due resist or metal residues, or from rolled up SLG that cannot be removed by an O_2 plasma etch.

For these larger systems, the increased propagation losses from SLG processing have become a performance killer and techniques for limiting the additional sources are needed. I propose using a Au hard mask to protect the WG from contaminants during fabrication, which can then be removed once the devices have been completed. The process flow is shown in figure 9.11. Au was chosen because it is not etched by HF and because it can be dissolved in iodine. After depositing the initial 10 nm Al_2O_3 bottom encapsulation layer for SLG the area that will be covered by Au is patterned with EBL. This area will extend $\sim 2\ \mu$m either side of the WG. Owing to the adhesion with Al_2O_3, 50 nm of Au can be deposited without an initial adhesion layer of another metal such as Cr. It was important that only Au was deposited because metals such as Ni or Cr cannot be removed by dissolving in iodine. The SLG active devices will be fabricated as normal until the contacts are accessed by etching Al_2O_3 in HF, shown in step 4 of figure 9.11. Instead of only etching the area above the contacts to the DSLG devices, I will also access the WGs by etching the area covered by the Au hard mask. To prevent HF damaging the WG without the Au hard mask it was important to leave an region of the WG that is covered with the Au hard mask protected during the HF etch. Therefore it is necessary to use EBL instead of optical lithography because of the precise alignment required to define the overlapping region of the Au hard mask and the EBL resist. It is important to minimise the overlapping region, so that the iodine can still remove the Au, but also ensure that it is large enough to fully protect the WG that is not protected by the Au hard mask. I chose to use ZEP520A EBL resist instead of PMMA because it is more resistant to etching in HF. I applied ZEP520A at 2000 rpm for 60 s, followed by a 3 minute bake at 120^{o}C. During EBL I used a dose of 250 μC/cm^2 with a 5 nA beam current for 100 kV accelerating voltage. I developed the same in amyl acetate for 30 s and then a 30 s rinse in a 9:1 solution of MIBK:IPA. Before removing the Au hard mask, optical lithography is

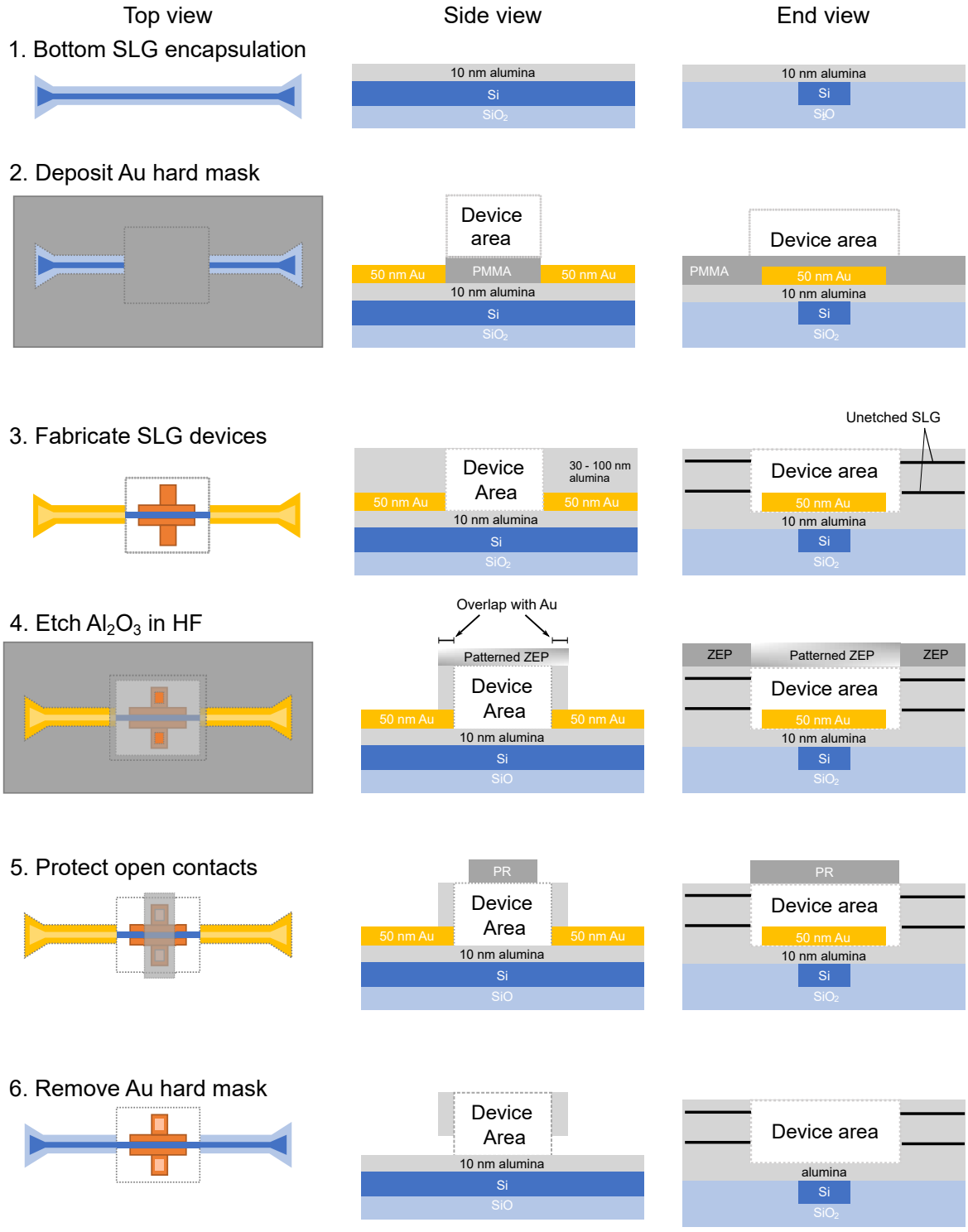

Fig. 9.11 Proposed process of Au-hard mask for WG protection during fabrication of DSLG modulators and GPDs.

used pattern the area surrounding the exposed contacts such that they are protected, step 5 in figure 9.11. Finally, the Au mask can be removed by dissolving in iodine.

9.4 Conclusions

In this chapter I have presented the results of the DSLG MZMs that I fabricated on Si MZIs. Whilst individually I have shown that DSLG MZMs can be efficient phase modulators ($V_\pi L \sim 0.3$ V·cm) that are capable of demonstrating $\Delta\phi = \pi/2$ and pure phase modulation, I have not been able to show all of these properties in the same device. All of these properties are desirable for IQ modulation, and if they can be combined this will lead to compact and low-power IQ modulators. Therefore, this is an encouraging step towards the development of graphene-based modulators that can be used for optical links based on complex modulation formats. However, it is clear from the extracted $\mathrm{FOM_{EA}}$ and $\mathrm{FOM_{ER}}$ that even though the DSLG MZMs show good modulation efficiency, that the overall performance is significantly limited by the high IL. The IL would need to be significantly reduced in order for DSLG MZMs to be commercially attractive. This will largely come from SLG processing improvements that will preserve τ throughout device fabrication. Improvements should focus on limiting sources of scattering that arise from the introduction of defects in SLG and residues remaining from SLG processing.

I measured the EO BW of the DSLG modulator as a function of V and observed that $f_{3\mathrm{dB}}$ decreased from ~ 25 GHz at $V_{\mathrm{bias}} = 5$ V to ~ 8 GHz at $V_{\mathrm{bias}} = 11$ V. Where $V_{\mathrm{bias}} = 5$ V is ideal for amplitude modulation and $V_{\mathrm{bias}} = 11$ V is ideal for pure phase modulation. The observed decrease of $f_{3\mathrm{dB}}$ at $V_{\mathrm{bias}} = 11$ V is problematic for using the DSLG modulator for high-speed IQ modulation. I suggest that the reduction in $f_{3\mathrm{dB}}$ could be caused by increased scattering at high carrier concentration, resulting in a effective decrease in μ above 5 V. However, the transition to sublinear $\sigma_{\mathrm{d.c}}$ can be pushed to higher V by optimising the fabrication process such that the sources of short-range scattering in SLG are reduced. This offers a potential solution to maintain $f_{3\mathrm{dB}}$ at the voltages required for pure phase modulation. As well as maintaining $f_{3\mathrm{dB}}$ at high voltages, reducing sources of short-range scattering should also increase τ, which would lead to further improvements of $f_{3\mathrm{dB}}$. Therefore, I believe that with suitable processing improvements that future DSLG modulators will be able to achieve high-speed IQ modulation.

Maintaining a high yield across all DSLG modulators in system-level implementations is critical because they rely on many individual devices working together. This requires the contact resistance, sheet resistance, and residual doping of SLG to be consistent across all devices. If these parameters are not uniform, then the performance of each device would differ and the device will not be usable without significant adjustments during operation. If the variation is too high then even adjustments will not be possible. Currently, the DSLG MZMs that I have presented do not have the yield necessary for IQ modulation, however, as the maturity of SLG processing continues to improve this will become more achievable.

Along with the yield, the high optical losses resulting from SLG processing are another important issue that needs to be addressed. Further process improvements, such as my proposed Au hard mask, are necessary for minimising additional optical losses introduced during fabrication, and therefore reducing the IL of the overall system.

Chapter 10

Conclusions and Outlook

10.1 Conclusions

In this thesis I have presented a study of graphene-based modulators to be used for integrated Si optical links. Rising data rates demand that future communication networks evolve beyond the limits imposed by existing technologies. Optical networks that currently use direct detection systems could increase capacity by moving to coherent systems which employ complex modulation formats to increase the spectral efficiency. Short-reach optical networks will move to shorter length scales as electrical interconnect consumes unmanageable amounts of power to process such quantities of data. In both cases, efficient and compact optical transceivers are required that can deliver low-power data transmission by increasing circuit densities. Next-generation optical transceivers utilise Si photonic technology to produce low-cost integrated photonics circuits that benefit from mature CMOS technology. I have reviewed different components of a Si photonic optical link, focusing on integrated PDs and modulators, and including the essential photonic components and system implementations. I have shown that Si-based PDs use new materials to increase performance and facilitate sub-band absorption, and that Si-based modulators also introduce new materials to increase performance and reduce the inherent losses associated with doped Si WGs. However, these hybrid platforms are undesirable because they involve expensive III-V materials, wafer bonding techniques, or epitaxial growth.

I have introduced graphene as a promising material for the active material of integrated PDs and modualators owing to its electrical and optical properties. I have presented the design and modelling of a DSLG modulator that uses a double layer of SLG with an applied bias to modulate the optical conductivity of graphene. This does not rely on an active photonic platform and can be used as an EAM or phase modulator. I have described the optical

and electrical modelling that I have used to estimate the device performance and optimise the design for high-speed operation. The modulation efficiency can be improved by increasing the interaction between SLG and the confined optical mode, and the modulation bandwidth can be improved by reducing the device resistance and capacitance. Of course there is always a trade-off, and optimising the design for either parameter will affect the other. To increase the SLG-light interaction I have investigated using different photonic platforms with different refractive index contrasts and the size of the overlapping SLG region. I have shown that the modulation efficiency will be increased for the largest overlapping region of SLG because this maximises the active area of the DSLG modulator where the non-overlapping regions of SLG do not contribute to $\Delta\sigma(\omega)$. I have also shown that using the SiN platform shows an improvement in modulation efficiency. In comparison to Si, SiN has a lower Δn which means that the optical mode is more delocalised and thus overlaps with a greater area of the overlapping SLG region. This could be further enhanced by embedding the DSLG stack inside an inverted ridge structure. I have estimated the proposed bandwidth of the DSLG modulator through electrical modelling considering the different contributions to the total circuit impedance $Z_{\mathrm{T}}(\omega)$, coming from each contact, R_{C}, ungated SLG sections, R_{ungated}, and gated SLG sections, R_{gated}. I have found that the modulation bandwidth is greatly reduced for a large overlapping SLG region. Previously, to avoid the increased resistance from R_{ungated}, it was considered beneficial to maximise the overlapping SLG region because the R_{gated} will be negligible. However, I found that the R_{gated} was in the same order of magnitude as R_C and consequently, the reduced resistance from a larger overlapping region was not enough to balanced the increase capacitance. Therefore, to optimise the design for high-speed operation I decided to minimise the overlapping SLG region and confine it to the same width as the WG. In order to maximise the BW it is important to reduce the length of the ungated sections, W_{ungated}, and hence R_{ungated}. W_{ungated} represents the distance between the contact and the edge of the WG and must be above a certain length otherwise it will result in optical losses into the contacts. Therefore, in comparison to the Si platform, I have shown that DSLG modulators on the SiN platform will be BW limited due to the increased WG width and contact separation that comes with a more delocalised mode. Critically, both modulation efficiency and bandwidth are inextricably linked to the SLG quality. Higher quality SLG with the largest intraband scattering time will maximise the modulation efficiency and bandwidth, as well as minimising the optical losses.

I fabricated DSLG modulators on different photonic components which are suited for different data transmission applications. Starting with straight WGs I fabricated DSLG EAMs on Si and SiN photonic platforms. In this configuration, the DSLG modulator controls

the optical losses of the optical mode which can be used in direct detection systems to encode information in the amplitude of the transmitted signal. The achievable ER of the DSLG EAMs is determined by L_{mod} and V_{pp}. This will be a trade-off between reducing the IL by minimising L_{mod}, and reducing the power consumption by minimising V_{pp}. Here, the overall performance of the DSLG EAMs on Si is limited by high optical losses which were introduced during device fabrication. This is shown by the measured $\text{FOM}_{\text{EA}} \sim 0.6$, which is much lower than other reported values ~ 2 [210, 211]. Such high optical losses meant that L_{mod} cannot be increased to reach an ER > 6 dB without resulting in an IL that is impractical for commercial applications. This means that DSLG EAMs on Si are unlikely to be attractive for direct detection systems that use multi-level modulation formats, but could instead be used for binary modulation formats if the optical losses are reduced. On the other hand, the DSLG EAMs on SiN did not suffer as much from high optical losses and achieved an $\text{FOM}_{\text{EA}} \sim 5.33$. Whilst the FOM_{EA} on SiN is higher than previously reported values, it still requires $V_{\text{pp}} = 10$ V. The reduced optical losses in comparison to the Si platform mean that L_{mod} could be increased in order to reduce V_{pp} to more practical levels whilst still maintaining a reasonable FOM_{EA}. However, the increased efficiency of the DSLG EAM on SiN comes at the cost of a reduced BW. The increased W_{gated} and W_{ungated} associated with DSLG EAMs on SiN result in $f_{3\text{dB}} \sim 13$ GHz for SiN and ~ 25 GHz for Si. Therefore, this means that whilst DSLG EAMs on SiN are more efficient that DSLG EAMs on Si, they are not suitable for high-speed data communications that require BW above 20 GHz. The large V_{pp} required to reach a useful ER and a practical IL is a major drawback for DSLG EAMs. V_{pp} can be reduced by increasing L_{mod}, but the associated increase in IL might not be acceptable for commercial systems. Therefore, unless optical losses can be greatly increased, then SLG based modulators would be more attractive in an electro-refractive configuration that can utilise the simultaneous $\Delta\phi$ from SLG. With a suitable reduction in optical losses and optimised device dimensions, SLG has the potential to enable high-speed, compact, and efficient EAMs for future short-reach interconnect.

Next, I fabricated DSLG modulators on Si add-drop RRs. RRMs are compact modulators which combine the induced Δn_{eff} and $\Delta\alpha$ from the DSLG modulator to modulate the resonant condition of the RR and the optical losses experienced in the ring. By monitoring $\Delta\lambda_{\text{res}}$ and ΔQ-factor with voltage I extracted Δn_{eff} and $\Delta\alpha$ from the DSLG modulator. Unlike the DSLG EAMs, I was able to apply a large enough voltage to the DSLG RRM to reach the Pauli blocking regime where $E_{\text{F}} > 0.4$ eV and interband transitions are forbidden. This is the first time that pure phase modulation has been demonstrated with SLG based modulators. This result represents a step forward in the development of SLG based modulators that

can be used in coherent communication networks which would benefit from pure phase modulation. The DSLG RRM that I have presented has demonstrated the lowest reported $V_\pi L$ for SLG based modulators with an extracted $V_\pi L \sim 0.12$ V·cm. This is a factor of ~ 2 lower than the state-of-the-art [212]. However, even with a record-low $V_\pi L$, the DSLG RRM is still limited by the high optical losses of SLG, which restrict the FOM_{ER} to ~ 74.5 V dB. The FOM_{ER} needs to be reduced in order for DSLG RRMs to be commercially attractive for phase modulation. This can be achieved with SLG processing improvements to limit additional optical losses that are introduced during device fabrication. Whilst the induced $\Delta\phi$ was too small to be useful for complex modulation formats, due to the resonant nature of the RR, the induced $\Delta\phi$ still resulted in an ER ~ 4.71 dB at $\lambda_{op} = 1542.82$ nm with $V_{pp} = 1$ V. This leads to an $FOM_{EA} \sim 4.48$, which is a factor of two better than the highest reported for SLG based modulators to date (~ 2 [211]). This ER would be suitable for direct detection systems that use binary modulation formats, but would need to be increased for multi-level modulation formats. For both phase modulation and amplitude modulation, the achievable $\Delta\phi$ or ER can be increased by increasing V_{pp} or L_{mod}. Although, any increase in V_{pp} or L_{mod} will also be accompanied by a rise in dynamic power consumption and IL. Therefore, it is crucial that the optical losses of SLG are reduced so that FOM_{ER} can be minimised and the FOM_{EA} is maintained whilst L_{mod} is increased. A large drawback of the DSLG RRMs that I have presented is that f_{3dB} was limited to < 1 GHz due to the aspect ratio of the device. However, this is not an inherent shortcoming of the device, and simulations show that f_{3dB} can be increased to ~ 20 GHz with the use of vias to contact one of the SLG inside the ring. Whilst the DSLG RRMs do not currently combine all the necessary properties for high-speed coherent communication networks, they have shown that they have the potential to be efficient and compact amplitude modulators that could be integrated into short-reach communications networks.

Finally, I have fabricated DSLG MZMs on 2×2 unbalanced Si MZIs that are intended for IQ modulation. In this configuration, the DSLG modulator controls $\Delta\phi$ and $\Delta\alpha$ between the two MZI arms, resulting in $\Delta\lambda_{res}$ and ΔER of the interference fringes in the transmission spectra of the MZM. I extracted Δn_{eff} and $\Delta\alpha$ from the DSLG modulator by monitoring $\Delta\lambda_{res}$ and ΔER as a function of V. Like with the RRMs, I was able to reach the Pauli blocking regime where SLG becomes transparent to absorption via interband transitions. This is a beneficial property for IQ modulation because the optical losses do not significantly change as a function of voltage. The DSLG MZMs were not as efficient as the DSLG RRMs, with an extracted $V_\pi L \sim 0.3$ V·cm, but managed to reach $\Delta\phi = \pi/2$ due to the increased L_{mod}. However, like with the DSLG RRMs, the DSLG MZMs suffered from excessive IL that

makes them impractical for commercial devices. As shown by an $\mathrm{FOM_{ER}} > 200$ V dB, this problem was greatly increased for the DSLG MZMs because of the increased device lengths. For DSLG MZMs to be commercially viable, it is essential that optical losses are drastically reduced through SLG processing improvements. These improvements must minimise the degradation of τ by protecting SLG from additional damage and reduce residues that result from device fabrication. I measured the EO BW as a function of V and observed that in $f_{3\mathrm{dB}}$ was limited to < 10 GHz in the transparency regime at $V_{\mathrm{bias}} = 11$ V. This was unexpected as $f_{3\mathrm{dB}}$ reached ~ 25 GHz when operated at $V_{\mathrm{bias}} = 5$ V for amplitude modulation. I attributed the $f_{3\mathrm{dB}}$ V-dependent slowdown to a reduction in μ of SLG as a result of scattering. However, I have proposed that this can be improved with process enhancements to limit the sources of short-range scattering in SLG. When combining DSLG modulators into systems it is critical that the yield and variability between devices is improved, and that the overall optical losses of the system are brought down. The additional optical losses on the passive photonic circuits largely occur when SLG cannot be fully etched from the WG surface. If these optical losses cannot be reduced then any improvement in reducing the IL of the DSLG MZMs themselves will not matter. However, appropriate processing improvements will be able to simultaneously reduce the insertion loss, increase the bandwidth, and increase the yield of SLG based MZMs. With these developments in place, the low $\mathrm{V_\pi L}$ of SLG based MZMs could be taken advantage of to build future low-power and compact IQ modulators for coherent communication networks.

10.2 Outlook

The development of graphene-based integrated photonics has shown significant progress in recent years, going beyond proof-of-concept devices and now looking to push the device performances towards real world applications for data communication. Future optical links demand low-power, high-speed, and efficient PDs and modulators to address the growing energy requirements of data transmission. The individual building blocks have already been demonstrated, but many outstanding challenges remain that limit the adoption into commercial systems. Graphene technology has reached a critical stage where the maturity of the platform needs to be accelerated. GPDs based on the PTE are capable of wavelength-independent operation with zero leakage current, unmatched by any other material. However, the challenge remains to increase the responsivity of GPDs with scalable materials without losing these vital properties. For a zero-band gap material, bias-free operation is critical to suppress I_{d}, but by directly generating V_{ph} instead of I_{ph}, GPDs could offer an alternative to traditional PDs that produce I_{ph}. This enables new receiver architectures that do not

require transimpedance amplifiers to convert I_{ph} into V_{ph}, reducing system complexity and power consumption. Whilst graphene modulators have demonstrated modulation efficiencies that match or surpass other technologies, they have been unable to meet all of the combined requirements that are needed for commercial devices. Largely the performance of graphene modulators is limited by the high IL resulting from residues and damage done to the SLG films during processing which increases τ. This not only increases IL, but also reduces f_{3dB} because of the increased device resistance. Thus, methods to preserve τ during processing are critical for graphene-based modulators to match theoretical predictions.

Even with superior performance, industry will only be convinced if the processing technology can be easily, and economically integrated in existing CMOS technology. I believe that this is the area where graphene struggles the most, and where the next gains will come from. Graphene benefits from processing techniques that are suitable for wafer scale processing but do not rely on complex dopant implantation, epitaxy, or high temperature ($> 250^{o}$C [142]) wafer bonding. However, graphene transfer methods are unlike traditional methods to integrate other materials into the Si photonic platform and come with their own unique challenges. Organisations and companies, such as IMEC and Aixtron, are ramping up on wafer scale processing technology, but the levels of metal contaminants from the Cu growth substrate, remain a challenge for integration in a CMOS production line. Residues from graphene processing lead to increased optical losses and thus high end-to-end IL. The majority of these additional losses originate from graphene wrinkles resulting from low-adhesion during the transfer process that cannot be removed with the usual O_2 plasma. This can be resolved by improving the transfer process, either by increasing the adhesion with the substrate or selective transfer, or methods, such as my proposed Au hard-mask, to protect the WGs. Highly-uniform SLG films over the wafer scale are critical to maximise the yield of GPDs and graphene-based modulators. In this thesis I have used polycrystalline CVD SLG films because it provides a simple method for transferring SLG onto highly-dense Si photonic substrates. For transmitters and receivers that are based on many GPDs or graphene-based modulators, non-uniformities will degrade the system performance. The uniformity of CVD SLG films can be improved by using ultra-smooth, single-crystal Cu growth substrates, or by optimising the growth for large graphene grain sizes. Eliminating SLG grain boundaries by moving to deterministic growth of single-crystal CVD graphene is a potential solution, but this will rely on alignment of the single-crystals during transfer which increases costs because it reduces through-put.

References

1. Cisco. *Cisco Visual Networking Index: Forecast and Trends, 2017-2022* tech. rep. (Cisco, 2019).
2. Ericcson. *Ericsson Mobility Report* tech. rep. June (2020).
3. IEEE Computer Society. *IEEE Standard for Ethernet* tech. rep. 31 August (IEEE Standards Association, 2018), 1–408.
4. Ethernet Alliance. *Ethernet Roadmap* tech. rep. (2020).
5. Richardson, D. J., Fini, J. M. & Nelson, L. E. Space-division multiplexing in optical fibres. *Nature Photonics* **7,** 354–362 (2013).
6. Wei, J., Cheng, Q., Penty, R. V., White, I. H. & Cunningham, D. G. 400 Gigabit Ethernet using advanced modulation formats: Performance, complexity, and power dissipation. *IEEE Communications Magazine* **53,** 182–189 (2015).
7. Sharif, M., Perin, J. K. & Kahn, J. M. Modulation Schemes for Single-Laser 100 Gb/s Links: Single-Carrier. *Journal of Lightwave Technology* **33,** 4268–4277 (2015).
8. Kumar, S. & Deen, M. J. *Fiber Optic Communications : Fundamentals and Applications.* eng (Wiley, Hoboken, 2014).
9. Miller, D. Rationale and challenges for optical interconnects to electronic chips. *Proceedings of the IEEE* **88,** 728–749 (2000).
10. Horowitz, P. & Hill, W. *The art of electronics.* eng (Cambridge University Press, Cambridge, 1980).
11. Meindl, J. D., Davis, J. A., Zarkesh-Ha, P., Patel, C. S., Martin, K. P. & Kohl, P. A. Interconnect opportunities for gigascale integration. *IBM Journal of Research and Development* **46,** 245–263 (2002).
12. Reed, G. T. & Knights, A. P. *Silicon photonics : an introduction* (Wiley, Chichester, 2004).
13. Thomson, D., Zilkie, A., Bowers, J. E., Komljenovic, T., Reed, G. T., Vivien, L., Marris-Morini, D., Cassan, E., Virot, L., Fédéli, J.-M., Hartmann, J.-M., Schmid, J. H., Xu, D.-X., Boeuf, F., O'Brien, P., Mashanovich, G. Z. & Nedeljkovic, M. Roadmap on silicon photonics. *Journal of Optics* **18,** 073003 (2016).
14. Roelkens, G., Van Campenhout, J., Brouckaert, J., Van Thourhout, D., Baets, R., Romeo, P. R., Regreny, P., Kazmierczak, A., Seassal, C., Letartre, X., Hollinger, G., Fedeli, J., Di Cioccio, L. & Lagahe-Blanchard, C. III-V/Si photonics by die-to-wafer bonding. *Materials Today* **10,** 36–43 (2007).
15. Poberaj, G., Hu, H., Sohler, W. & Günter, P. Lithium niobate on insulator (LNOI) for micro-photonic devices. *Laser and Photonics Reviews* **6,** 488–503 (2012).

16. Geim, A. K. & Novoselov, K. S. The rise of graphene. *Nature Materials* **6,** 183–191 (2007).

17. Bonaccorso, F., Sun, Z., Hasan, T. & Ferrari, A. C. Graphene photonics and optoelectronics. *Nature Photonics* **4,** 611–622 (2010).

18. Katsnelson, M. I. *Graphene : Carbon in Two Dimensions / Mikhail I. Katsnelson.* eng (2012).

19. Castro Neto, A. H., Guinea, F., Peres, N. M. R., Novoselov, K. S. & Geim, A. K. The electronic properties of graphene. *Reviews of Modern Physics* **81,** 109–162 (2009).

20. Hanson, G. W. Dyadic Green's functions and guided surface waves for a surface conductivity model of graphene. *Journal of Applied Physics* **103,** 064302 (2008).

21. Novoselov, K. S., Geim, A. K., Morozov, S. V., Jiang, D., Katsnelson, M. I., Grigorieva, I. V., Dubonos, S. V. & Firsov, A. A. Two-dimensional gas of massless Dirac fermions in graphene. *Nature* **438,** 197–200 (2005).

22. Martin, J., Akerman, N., Ulbricht, G., Lohmann, T., Smet, J. H., von Klitzing, K. & Yacoby, A. Observation of electron–hole puddles in graphene using a scanning single-electron transistor. *Nature Physics* **4,** 144–148 (2008).

23. Kittel, C. *Introduction to solid state physics.* 7th ed. eng (John Wiley & Sons, New York, 1996).

24. Novoselov, K. S., Geim, A. K., Morozov, S. V., Jiang, D., Zhang, Y., Dubonos, S. V., Grigorieva, I. V. & Firsov, A. A. Electric Field Effect in Atomically Thin Carbon Films. *Science* **306,** 666–669 (2004).

25. Dean, C. R., Young, a. F., Meric, I., Lee, C., Wang, L., Sorgenfrei, S., Watanabe, K., Taniguchi, T., Kim, P., Shepard, K. L. & Hone, J. Boron nitride substrates for high-quality graphene electronics. *Nature Nanotechnology* **5,** 722–726 (2010).

26. Banszerus, L., Schmitz, M., Engels, S., Dauber, J., Oellers, M., Haupt, F., Watanabe, K., Taniguchi, T., Beschoten, B. & Stampfer, C. Ultrahigh-mobility graphene devices from chemical vapor deposition on reusable copper. *Science Advances* **1,** e1500222 (2015).

27. Purdie, D. G., Pugno, N. M., Taniguchi, T., Watanabe, K., Ferrari, A. C. & Lombardo, A. Cleaning interfaces in layered materials heterostructures. *Nature Communications* **9,** 1–12 (2018).

28. De Fazio, D., Purdie, D. G., Ott, A. K., Braeuninger-Weimer, P., Khodkov, T., Goossens, S., Taniguchi, T., Watanabe, K., Livreri, P., Koppens, F. H., Hofmann, S., Goykhman, I., Ferrari, A. C. & Lombardo, A. High-Mobility, Wet-Transferred Graphene Grown by Chemical Vapor Deposition. *ACS Nano* **13,** 8926–8935 (2019).

29. Bolotin, K., Sikes, K., Jiang, Z., Klima, M., Fudenberg, G., Hone, J., Kim, P. & Stormer, H. Ultrahigh electron mobility in suspended graphene. *Solid State Communications* **146,** 351–355 (2008).

30. Nair, R. R., Blake, P., Grigorenko, A. N., Novoselov, K. S., Booth, T. J., Stauber, T., Peres, N. M. R. & Geim, A. K. Fine Structure Constant Defines Visual Transparency of Graphene. *Science* **320,** 1308–1308 (2008).

31. Pisana, S., Lazzeri, M., Casiraghi, C., Novoselov, K. S., Geim, A. K., Ferrari, A. C. & Mauri, F. Breakdown of the adiabatic Born–Oppenheimer approximation in graphene. *Nature Materials* **6,** 198–201 (2007).
32. Li, Z. Q., Henriksen, E. a., Jiang, Z., Hao, Z., Martin, M. C., Kim, P., Stormer, H. L. & Basov, D. N. Dirac charge dynamics in graphene by infrared spectroscopy. *Nature Physics* **4,** 532–535 (2008).
33. Novoselov, K. S., Fal'Ko, V. I., Colombo, L., Gellert, P. R., Schwab, M. G. & Kim, K. A roadmap for graphene. *Nature* **490,** 192–200 (2012).
34. Geim, A. K. Graphene: Status and Prospects. *Science* **324,** 1530–1534 (2009).
35. Novoselov, K. S. & Castro Neto, A. H. Two-dimensional crystals-based heterostructures: materials with tailored properties. *Physica Scripta* **T146,** 014006 (2012).
36. Hernandez, Y., Nicolosi, V., Lotya, M., Blighe, F. M., Sun, Z., De, S., McGovern, I. T., Holland, B., Byrne, M., Gun'Ko, Y. K., Boland, J. J., Niraj, P., Duesberg, G., Krishnamurthy, S., Goodhue, R., Hutchison, J., Scardaci, V., Ferrari, A. C. & Coleman, J. N. High-yield production of graphene by liquid-phase exfoliation of graphite. *Nature Nanotechnology* **3,** 563–568 (2008).
37. Bonaccorso, F., Lombardo, A., Hasan, T., Sun, Z., Colombo, L. & Ferrari, A. C. Production and processing of graphene and 2d crystals. *Materials Today* **15,** 564–589 (2012).
38. Torrisi, F., Hasan, T., Wu, W., Sun, Z., Lombardo, A., Kulmala, T. S., Hsieh, G.-W., Jung, S., Bonaccorso, F., Paul, P. J., Chu, D. & Ferrari, A. C. Inkjet-Printed Graphene Electronics. *ACS Nano* **6,** 2992–3006 (2012).
39. Li, X., Cai, W., Colombo, L. & Ruoff, R. S. Evolution of Graphene Growth on Ni and Cu by Carbon Isotope Labeling. *Nano Letters* **9,** 4268–4272 (2009).
40. Li, X., Cai, W., An, J., Kim, S., Nah, J., Yang, D., Piner, R., Velamakanni, A., Jung, I., Tutuc, E., Banerjee, S. K., Colombo, L. & Ruoff, R. S. Large-Area Synthesis of High-Quality and Uniform Graphene Films on Copper Foils. *Science* **324,** 1312–1314 (2009).
41. Bae, S., Kim, H., Lee, Y., Xu, X., Park, J.-S., Zheng, Y., Balakrishnan, J., Lei, T., Ri Kim, H., Song, Y. I., Kim, Y.-J., Kim, K. S., Özyilmaz, B., Ahn, J.-H., Hong, B. H. & Iijima, S. Roll-to-roll production of 30-inch graphene films for transparent electrodes. *Nature Nanotechnology* **5,** 574–578 (2010).
42. Li, X., Magnuson, C. W., Venugopal, A., An, J., Suk, J. W., Han, B., Borysiak, M., Cai, W., Velamakanni, A., Zhu, Y., Fu, L., Vogel, E. M., Voelkl, E., Colombo, L. & Ruoff, R. S. Graphene Films with Large Domain Size by a Two-Step Chemical Vapor Deposition Process. *Nano Letters* **10,** 4328–4334 (2010).
43. Wu, T., Zhang, X., Yuan, Q., Xue, J., Lu, G., Liu, Z., Wang, H., Wang, H., Ding, F., Yu, Q., Xie, X. & Jiang, M. Fast growth of inch-sized single-crystalline graphene from a controlled single nucleus on Cu-Ni alloys. *Nature Materials* **15,** 43–47 (2016).
44. Miseikis, V., Bianco, F., David, J., Gemmi, M., Pellegrini, V., Romagnoli, M. & Coletti, C. Deterministic patterned growth of high-mobility large-crystal graphene: a path towards wafer scale integration. *2D Materials* **4,** 021004 (2017).
45. Xu, X. *et al.* Ultrafast epitaxial growth of metre-sized single-crystal graphene on industrial Cu foil. *Science Bulletin* **62,** 1074–1080 (2017).

46. Casiraghi, C., Hartschuh, A., Lidorikis, E., Qian, H., Harutyunyan, H., Gokus, T., Novoselov, K. S. & Ferrari, A. C. Rayleigh imaging of graphene and graphene layers. *Nano Letters* **7,** 2711–2717 (2007).

47. Blake, P., Hill, E. W., Castro Neto, A. H., Novoselov, K. S., Jiang, D., Yang, R., Booth, T. J. & Geim, A. K. Making graphene visible. *Applied Physics Letters* **91,** 2007–2009 (2007).

48. Raman, C. V. & Krishnan, K. S. A new type of secondary radiation. *Nature* **121,** 501–502 (1928).

49. Ferrari, A. C. & Basko, D. M. Raman spectroscopy as a versatile tool for studying the properties of graphene. *Nature Nanotechnology* **8,** 235–246 (2013).

50. Cançado, L. G., Jorio, A., Ferreira, E. H., Stavale, F., Achete, C. A., Capaz, R. B., Moutinho, M. V., Lombardo, A., Kulmala, T. S. & Ferrari, A. C. Quantifying defects in graphene via Raman spectroscopy at different excitation energies. *Nano Letters* **11,** 3190–3196 (2011).

51. Basko, D. M., Piscanec, S. & Ferrari, A. C. Electron-electron interactions and doping dependence of the two-phonon Raman intensity in graphene. *Physical Review B* **80,** 1–10 (2009).

52. Ferrari, A. C., Meyer, J. C., Scardaci, V., Casiraghi, C., Lazzeri, M., Mauri, F., Piscanec, S., Jiang, D., Novoselov, K. S., Roth, S. & Geim, A. K. Raman Spectrum of Graphene and Graphene Layers. *Physical Review Letters* **97,** 187401 (2006).

53. Tuinstra, F. & Koenig, J. L. Raman Spectrum of Graphite. *The Journal of Chemical Physics* **53,** 1126–1130 (1970).

54. Das, A., Pisana, S., Chakraborty, B., Piscanec, S., Saha, S. K., Waghmare, U. V., Novoselov, K. S., Krishnamurthy, H. R., Geim, A. K., Ferrari, A. C. & Sood, A. K. Monitoring dopants by Raman scattering in an electrochemically top-gated graphene transistor. *Nature Nanotechnology* **3,** 210–215 (2008).

55. Bruna, M., Ott, A. K., Ijäs, M., Yoon, D., Sassi, U. & Ferrari, A. C. Doping dependence of the Raman spectrum of defected graphene. *ACS Nano* **8,** 7432–7441 (2014).

56. Schroder, D. K. *Semiconductor material and device characterization / Dieter K. Schroder.* 3rd ed. eng (IEEE Press ; Wiley-Interscience, Piscataway, N.J.] : Hoboken, N.J. ; [Chichester], 2006).

57. Anzi, L., Mansouri, A., Pedrinazzi, P., Guerriero, E., Fiocco, M., Pesquera, A., Centeno, A., Zurutuza, A., Behnam, A., Carrion, E. A., Pop, E. & Sordan, R. Ultra-low contact resistance in graphene devices at the Dirac point. *2D Materials* **5,** 025014 (2018).

58. Wang, L., Meric, I., Huang, P. Y., Gao, Q., Gao, Y., Tran, H., Taniguchi, T., Watanabe, K., Campos, L. M., Muller, D. A., Guo, J., Kim, P., Hone, J., Shepard, K. L. & Dean, C. R. One-Dimensional Electrical Contact to a Two-Dimensional Material. *Science* **342,** 614–617 (2013).

59. Xia, F., Perebeinos, V., Lin, Y.-m., Wu, Y. & Avouris, P. The origins and limits of metal–graphene junction resistance. *Nature Nanotechnology* **6,** 179–184 (2011).

60. Nagashio, K., Nishimura, T., Kita, K. & Toriumi, A. *Metal/graphene contact as a performance Killer of ultra-high mobility graphene analysis of intrinsic mobility and contact resistance* in *2009 IEEE International Electron Devices Meeting (IEDM)* (IEEE, 2009), 1–4.
61. Smith, J. T., Franklin, A. D., Farmer, D. B. & Dimitrakopoulos, C. D. Reducing Contact Resistance in Graphene Devices through Contact Area Patterning. *ACS Nano* **7,** 3661–3667 (2013).
62. Shaygan, M., Otto, M., Sagade, A. A., Chavarin, C. A., Bacher, G., Mertin, W. & Neumaier, D. Low Resistive Edge Contacts to CVD-Grown Graphene Using a CMOS Compatible Metal. *Annalen der Physik* **529,** 1–7 (2017).
63. Agrawal, G. P. (P. *Fiber-optic communication systems* 4th ed. (Wiley, Hoboken, N.J., 2010).
64. Ramaswami, R. & R, R. *Optical networks : a practical perspective.* 2nd ed. (Morgan Kaufmann, San Francisco, CA, 2002).
65. Saleh, B. E. A. *Fundamentals of photonics / Bahaa E.A. Saleh, Malvin Carl Teich.* Third edition. eng (2019).
66. Lipson, M. Guiding, modulating, and emitting light on Silicon-challenges and opportunities. *Journal of Lightwave Technology* **23,** 4222–4238 (2005).
67. Lee, K. K., Lim, D. R., Luan, H.-C., Agarwal, A., Foresi, J. & Kimerling, L. C. Effect of size and roughness on light transmission in a Si/SiO2 waveguide: Experiments and model. *Applied Physics Letters* **77,** 1617–1619 (2000).
68. Kurdi, B. N. & Hall, D. G. Optical waveguides in oxygen-implanted buried-oxide silicon-on-insulator structures. *Optics Letters* **13,** 175–177 (1988).
69. Edwards, D. F. in *Handbook of Optical Constants of Solids* 547–569 (Elsevier, 1985).
70. Philipp, H. R. in *Handbook of Optical Constants of Solids* 749–763 (Elsevier, 1985).
71. Bogaerts, W., de Heyn, P., van Vaerenbergh, T., de Vos, K., Kumar Selvaraja, S., Claes, T., Dumon, P., Bienstman, P., van Thourhout, D. & Baets, R. Silicon microring resonators. *Laser and Photonics Reviews* **6,** 47–73 (2012).
72. Vlasov, Y. A. & McNab, S. J. Losses in single-mode silicon-on-insulator strip waveguides and bends. *Optics Express* **12,** 1622 (2004).
73. Li, G., Yao, J., Thacker, H., Mekis, A., Zheng, X., Shubin, I., Luo, Y., Lee, J.-h., Raj, K., Cunningham, J. E. & Krishnamoorthy, A. V. Ultralow-loss, high-density SOI optical waveguide routing for macrochip interconnects. *Optics Express* **20,** 12035 (2012).
74. Kischkat, J., Peters, S., Gruska, B., Semtsiv, M., Chashnikova, M., Klinkmüller, M., Fedosenko, O., MacHulik, S., Aleksandrova, A., Monastyrskyi, G., Flores, Y. & Masselink, W. T. Mid-infrared optical properties of thin films of aluminum oxide, titanium dioxide, silicon dioxide, aluminum nitride, and silicon nitride. *Applied Optics* **51,** 6789–6798 (2012).
75. Bauters, J. F., Heck, M. J. R., John, D. D., Tien, M.-C., Li, W., Barton, J. S., Blumenthal, D. J., Bowers, J. E., Leinse, A. & Heideman, R. G. *Ultra-low-loss Single-mode Si3N4 Waveguides with 0.7 dB/m Propagation Loss* in *37th European Conference and Exposition on Optical Communications* **27** (OSA, Washington, D.C., 2011), Th.12.LeSaleve.3.

76. Bauters, J. F., Heck, M. J. R., John, D., Dai, D., Tien, M.-C., Barton, J. S., Leinse, A., Heideman, R. G., Blumenthal, D. J. & Bowers, J. E. Ultra-low-loss high-aspect-ratio Si3N4 waveguides. *Optics Express* **19,** 3163 (2011).
77. Reed, G. T. (*Silicon photonics : the state of the art* (Wiley, Chichester, 2008).
78. Agrawal, G. P. in *Optics in Our Time* 177–199 (Springer International Publishing, Cham, 2016).
79. Ang, M. T. W., Reed, G. T., Vonsovici, A. P., Evans, A. G. R., Routley, P. R., Blackburn, T. & Josey, M. R. *Grating couplers using silicon-on-insulator* in *Proc. SPIE 3620, Integrated Optics Devices III* (eds Righini, G. C. & Najafi, S. I.) **3620** (SPIE Proceedings, 1999), 79.
80. Almeida, V. R., Panepucci, R. R. & Lipson, M. Nanotaper for compact mode conversion. *Optics Letters* **28,** 1302 (2003).
81. Cardenas, J., Poitras, C. B., Luke, K., Luo, L.-W., Morton, P. A. & Lipson, M. High Coupling Efficiency Etched Facet Tapers in Silicon Waveguides. *IEEE Photonics Technology Letters* **26,** 2380–2382 (2014).
82. Mitomi, O., Kasaya, K. & Miyazawa, H. Design of a single-mode tapered waveguide for low-loss chip-to-fiber coupling. *IEEE Journal of Quantum Electronics* **30,** 1787–1793 (1994).
83. Taillaert, D., Van Laere, F., Ayre, M., Bogaerts, W., Van Thourhout, D., Bienstman, P. & Baets, R. Grating Couplers for Coupling between Optical Fibers and Nanophotonic Waveguides. *Japanese Journal of Applied Physics* **45,** 6071–6077 (2006).
84. Marchetti, R., Lacava, C., Khokhar, A., Chen, X., Cristiani, I., Richardson, D. J., Reed, G. T., Petropoulos, P. & Minzioni, P. High-efficiency grating-couplers: Demonstration of a new design strategy. *Scientific Reports* **7,** 1–8 (2017).
85. Taillaert, D., Bienstman, P. & Baets, R. Compact efficient broadband grating coupler for silicon-on-insulator waveguides. *Optics Letters* **29,** 2749 (2004).
86. Madsen, C. K. & Zhao, J. H. *Optical filter design and analysis : a signal processing approach* eng (John Wiley & Sons, New York, Chichester, 1999).
87. Xu, Q., Schmidt, B., Pradhan, S. & Lipson, M. Micrometre-scale silicon electro-optic modulator. *Nature* **435,** 325–327 (2005).
88. Gheorma, I. L. & Osgood, R. M. Fundamental limitations of optical resonator based high-speed EO modulators. *IEEE Photonics Technology Letters* **14,** 795–797 (2002).
89. Timurdogan, E., Sorace-Agaskar, C. M., Sun, J., Shah Hosseini, E., Biberman, A. & Watts, M. R. An ultralow power athermal silicon modulator. *Nature Communications* **5,** 1–11 (2014).
90. Soref, R. & Bennett, B. Electrooptical effects in silicon. *IEEE Journal of Quantum Electronics* **23,** 123–129 (1987).
91. Liu, J., Beals, M., Pomerene, A., Bernardis, S., Sun, R., Cheng, J., Kimerling, L. C. & Michel, J. Waveguide-integrated, ultralow-energy GeSi electro-absorption modulators. *Nature Photonics* **2,** 433–437 (2008).
92. Cocorullo, G. & Rendina, I. Thermo-optical modulation at 1.5μm in silicon etalon. *Electronics Letters* **28,** 83–85 (1992).

93. Harris, N. C., Ma, Y., Mower, J., Baehr-Jones, T., Englund, D., Hochberg, M. & Galland, C. Efficient, compact and low loss thermo-optic phase shifter in silicon. *Optics Express* **22,** 10487 (2014).

94. Reed, G. T., Mashanovich, G., Gardes, F. Y. & Thomson, D. J. Silicon optical modulators. *Nature Photonics* **4,** 518–526 (2010).

95. Ye, S.-W., Yuan, F., Zou, X.-H., Shah, M. K., Lu, R.-G. & Liu, Y. High-Speed Optical Phase Modulator Based on Graphene-Silicon Waveguide. *IEEE Journal of Selected Topics in Quantum Electronics* **23,** 76–80 (2017).

96. Romagnoli, M., Sorianello, V., Midrio, M., Koppens, F. H., Huyghebaert, C., Neumaier, D., Galli, P., Templ, W., D'Errico, A. & Ferrari, A. C. Graphene-based integrated photonics for next-generation datacom and telecom. *Nature Reviews Materials* **3,** 392–414 (2018).

97. Hu, C. *Modern semiconductor devices for integrated circuits / Chenming Calvin Hu.* eng (Pearson Education, Upper Saddle River, N.J. ; London, 2010).

98. Miller, D. Device Requirements for Optical Interconnects to Silicon Chips. *Proceedings of the IEEE* **97,** 1166–1185 (2009).

99. Tu, X., Liow, T.-Y., Song, J., Yu, M. & Lo, G. Q. Fabrication of low loss and high speed silicon optical modulator using doping compensation method. *Optics Express* **19,** 18029 (2011).

100. Feng, N.-N., Feng, D., Liao, S., Wang, X., Dong, P., Liang, H., Kung, C.-C., Qian, W., Fong, J., Shafiiha, R., Luo, Y., Cunningham, J., Krishnamoorthy, A. V. & Asghari, M. 30GHz Ge electro-absorption modulator integrated with 3μm silicon-on-insulator waveguide. *Optics Express* **19,** 7062 (2011).

101. Gosciniak, J. & Tan, D. T. H. Graphene-based waveguide integrated dielectric-loaded plasmonic electro-absorption modulators. *Nanotechnology* **24,** 185202 (2013).

102. Mastronardi, L., Banakar, M., Khokhar, A., Hattasan, N., Rutirawut, T., Bucio, T. D., Grabska, K. M., Littlejohns, C., Bazin, A., Mashanovich, G. & Gardes, F. High-speed Si/GeSi hetero-structure Electro Absorption Modulator. *Optics Express* **26,** 6663 (2018).

103. Frova, A. & Handler, P. Franz-Keldysh Effect in the Space-Charge Region of a Germanium p-n Junction. *Physical Review* **137,** A1857–A1861 (1965).

104. Lampin, J. F., Desplanque, L. & Mollot, F. Detection of picosecond electrical pulses using the intrinsic Franz–Keldysh effect. *Applied Physics Letters* **78,** 4103–4105 (2001).

105. Dainesi, P., Kung, A., Chabloz, M., Lagos, A., Fluckiger, P., Ionescu, A., Fazan, P., Declerq, M., Renaud, P. & Robert, P. CMOS compatible fully integrated Mach-Zehnder interferometer in SOI technology. *IEEE Photonics Technology Letters* **12,** 660–662 (2000).

106. Tang, C. & Reed, G. Highly efficient optical phase modulator in SOI waveguides. *Electronics Letters* **31,** 451–452 (1995).

107. Liu, A., Jones, R., Liao, L. & Samara-rubio, D. A high-speed silicon optical modulator based on a metal – oxide – semiconductor capacitor. *Nature* **427,** 615–619 (2004).

108. Irace, A., Breglio, G. & Cutolo, A. All-silicon optoelectronic modulator with 1 GHz switching capability. *Electronics Letters* **39,** 232 (2003).

109. Webster, M., Gothoskar, P., Patel, V., Piede, D., Anderson, S., Tummidi, R., Adams, D., Appel, C., Metz, P., Sunder, S., Dama, B. & Shastri, K. An efficient MOS-capacitor based silicon modulator and CMOS drivers for optical transmitters. *IEEE International Conference on Group IV Photonics GFP* **1,** 1–2 (2014).

110. Sun, J., Kumar, R., Sakib, M., Driscoll, J. B., Jayatilleka, H. & Rong, H. A 128 Gb/s PAM4 Silicon Microring Modulator With Integrated Thermo-Optic Resonance Tuning. *Journal of Lightwave Technology* **37,** 110–115 (2019).

111. Gardes, F. Y., Reed, G. T., Emerson, N. G. & Png, C. E. A sub-micron depletion-type photonic modulator in Silicon On Insulator. *Optics Express* **13,** 8845 (2005).

112. Liu, A., Liao, L., Rubin, D., Nguyen, H., Ciftcioglu, B., Chetrit, Y., Izhaky, N. & Paniccia, M. High-speed optical modulation based on carrier depletion in a silicon waveguide. *Optics Express* **15,** 660 (2007).

113. Li, M., Wang, L., Li, X., Xiao, X. & Yu, S. Silicon intensity Mach–Zehnder modulator for single lane 100Gb/s applications. *Photonics Research* **6,** 109 (2018).

114. Liu, S., Wu, K., Zhou, L., Lu, L., Zhang, B., Zhou, G. & Chen, J. Optical Frequency Comb and Nyquist Pulse Generation with Integrated Silicon Modulators. *IEEE Journal of Selected Topics in Quantum Electronics* **26** (2020).

115. Han, J. H., Boeuf, F., Fujikata, J., Takahashi, S., Takagi, S. & Takenaka, M. Efficient low-loss InGaAsP/Si hybrid MOS optical modulator. *Nature Photonics* **11,** 486–490 (2017).

116. Chen, H.-W., Peters, J. D. & Bowers, J. E. Forty Gb/s hybrid silicon Mach-Zehnder modulator with low chirp. *Optics Express* **19,** 1455 (2011).

117. Hiraki, T., Aihara, T., Hasebe, K., Takeda, K., Fujii, T., Kakitsuka, T., Tsuchizawa, T., Fukuda, H. & Matsuo, S. Heterogeneously integrated III-V/Si MOS capacitor Mach-Zehnder modulator. *Nature Photonics* **11,** 482–485 (2017).

118. Hiraki, T., Aihara, T., Fujii, T., Takeda, K., Tsuchizawa, T., Kakitsuka, T., Fukuda, H. & Matsuo, S. Heterogeneously Integrated Mach-Zehnder Modulator Using Membrane InGaAsP Phase Shifter and Hydrogen-Free SiN Waveguide on Si Platform. *European Conference on Optical Communication, ECOC* **2018,** 15–17 (2018).

119. Bennett, B. R., Soref, R. A. & Del Alamo, J. A. Carrier-Induced Change in Refractive Index of InP, GaAs, and InGaAsP. *IEEE Journal of Quantum Electronics* **26,** 113–122 (1990).

120. He, M., Xu, M., Ren, Y., Jian, J., Ruan, Z., Xu, Y., Gao, S., Sun, S., Wen, X., Zhou, L., Liu, L., Guo, C., Chen, H., Yu, S., Liu, L. & Cai, X. High-performance hybrid silicon and lithium niobate Mach–Zehnder modulators for 100 Gbit s -1 and beyond. *Nature Photonics* **13,** 359–364 (2019).

121. Wang, C., Zhang, M., Stern, B., Lipson, M. & Lončar, M. Nanophotonic lithium niobate electro-optic modulators. *Optics Express* **26,** 1547 (2018).

122. Wang, C., Zhang, M., Chen, X., Bertrand, M., Shams-Ansari, A., Chandrasekhar, S., Winzer, P. & Lončar, M. Integrated lithium niobate electro-optic modulators operating at CMOS-compatible voltages. *Nature* **562,** 101–104 (2018).

123. Weigel, P. O., Zhao, J., Fang, K., Al-Rubaye, H., Trotter, D., Hood, D., Mudrick, J., Dallo, C., Pomerene, A. T., Starbuck, A. L., DeRose, C. T., Lentine, A. L., Rebeiz, G. & Mookherjea, S. Bonded thin film lithium niobate modulator on a silicon photonics platform exceeding 100 GHz 3-dB electrical modulation bandwidth. *Optics Express* **26,** 23728 (2018).

124. Koppens, F. H. L., Mueller, T., Avouris, P., Ferrari, A. C., Vitiello, M. S. & Polini, M. Photodetectors based on graphene, other two-dimensional materials and hybrid systems. *Nature Nanotechnology* **9,** 780–793 (2014).

125. Benedikovic, D., Virot, L., Aubin, G., Amar, F., Szelag, B., Karakus, B., Hartmann, J.-M., Alonso-Ramos, C., Roux, X. L., Crozat, P., Cassan, E., Marris-Morini, D., Baudot, C., Boeuf, F., Fédéli, J.-M., Kopp, C. & Vivien, L. 25 Gbps low-voltage hetero-structured silicon-germanium waveguide pin photodetectors for monolithic on-chip nanophotonic architectures. *Photonics Research* **7,** 437 (2019).

126. Atabaki, A. H., Meng, H., Alloatti, L., Mehta, K. K. & Ram, R. J. High-speed polysilicon CMOS photodetector for telecom and datacom. *Applied Physics Letters* **109,** 111106 (2016).

127. Bradley, J. D. B., Jessop, P. E. & Knights, A. P. Silicon waveguide-integrated optical power monitor with enhanced sensitivity at 1550nm. *Applied Physics Letters* **86,** 241103 (2005).

128. Ackert, J. J. Silicon-on-insulator microring resonator defect-based photodetector with 3.5-GHz bandwidth. *Journal of Nanophotonics* **5,** 059507 (2011).

129. Preston, K., Lee, Y. H. D., Zhang, M. & Lipson, M. Waveguide-integrated telecom-wavelength photodiode in deposited silicon. *Optics Letters* **36,** 52 (2011).

130. Harter, T., Muehlbrandt, S., Ummethala, S., Schmid, A., Nellen, S., Hahn, L., Freude, W. & Koos, C. Silicon–plasmonic integrated circuits for terahertz signal generation and coherent detection. *Nature Photonics* **12,** 625–633 (2018).

131. Helman, J. S. & Sánchez-Sinencio, F. Theory of Internal Photoemission. *Physical Review B* **7,** 3702–3706 (1973).

132. Goykhman, I., Desiatov, B., Khurgin, J., Shappir, J. & Levy, U. Waveguide based compact silicon Schottky photodetector with enhanced responsivity in the telecom spectral band. *Optics Express* **20,** 28594 (2012).

133. Endriz, J. G. Surface waves and grating-tuned photocathodes. *Applied Physics Letters* **25,** 261–262 (1974).

134. Muehlbrandt, S., Melikyan, A., Harter, T., Köhnle, K., Muslija, A., Vincze, P., Wolf, S., Jakobs, P., Fedoryshyn, Y., Freude, W., Leuthold, J., Koos, C. & Kohl, M. Silicon-plasmonic internal-photoemission detector for 40 Gbit/s data reception. *Optica* **3,** 741 (2016).

135. Naik, G. V., Shalaev, V. M. & Boltasseva, A. Alternative plasmonic materials: Beyond gold and silver. *Advanced Materials* **25,** 3264–3294 (2013).

136. Casalino, M., Iodice, M., Sirleto, L., Rendina, I. & Coppola, G. Asymmetric MSM sub-bandgap all-silicon photodetector with low dark current. *Optics Express* **21,** 28072 (2013).

137. Gosciniak, J., Atar, F. B., Corbett, B. & Rasras, M. Plasmonic Schottky photodetector with metal stripe embedded into semiconductor and with a CMOS-compatible titanium nitride. *Scientific Reports* **9,** 1–12 (2019).

138. Sheng, Z., Liu, L., Brouckaert, J., He, S. & Van Thourhout, D. InGaAs PIN photodetectors integrated on silicon-on-insulator waveguides. *Optics Express* **18,** 1756 (2010).

139. Hawkins, A. R., Wu, W., Abraham, P., Streubel, K. & Bowers, J. E. High gain-bandwidth-product silicon heterointerface photodetector. *Applied Physics Letters* **70,** 303–305 (1997).

140. Joshi, A. M., Brown, R., Fitzgerald, E. A., Wang, X., Ting, S. M. & Bulsara, M. T. *Monolithic InGaAs-on-silicon shortwave infrared detector arrays* in *Photodetectors: Materials and Devices II* (eds Brown, G. J. & Razeghi, M.) **2999** (1997), 211–224.

141. Adachi, S. *Physical Properties of III-V Semiconductor Compounds* (Wiley, 1992).

142. Roelkens, G., Brouckaert, J., Van Thourhout, D., Baets, R., Nötzel, R. & Smit, M. Adhesive Bonding of InPInGaAsP Dies to Processed Silicon-On-Insulator Wafers using DVS-bis-Benzocyclobutene. *Journal of The Electrochemical Society* **153,** G1015 (2006).

143. Michel, J., Liu, J. & Kimerling, L. C. High-performance Ge-on-Si photodetectors. *Nature Photonics* **4,** 527–534 (2010).

144. Luan, H. C., Lim, D. R., Lee, K. K., Chen, K. M., Sandland, J. G., Wada, K. & Kimerling, L. C. High-quality Ge epilayers on Si with low threading-dislocation densities. *Applied Physics Letters* **75,** 2909–2911 (1999).

145. Hui, R. in *Introduction to Fiber-Optic Communications* 417–438 (Elsevier, 2020).

146. Alduino, A. & Paniccia, M. Interconnects: Wiring electronics with light. *Nature Photonics* **1,** 153–155 (2007).

147. Sanferrare, R. J. Terrestrial Lightwave Systems. *AT&T Technical Journal* **66,** 95–107 (1987).

148. DeCusatis, C. *Handbook of Fiber Optic Data Communication* (Elsevier Science, 2002).

149. ITU-T Recommendation G.694.1. *Spectral grids for WDM applications: DWDM frequency grid* (2003).

150. ITU-T Recommendation G.694.2. *Spectral grids for WDM applications: CWDM wavelength grid* (2003).

151. IEEE Standard for Ethernet. *IEEE Std 802.3-2018 (Revision of IEEE Std 802.3-2015),* 1–5600 (2018).

152. Kao, K. & Hockham, G. Dielectric-fibre surface waveguides for optical frequencies. *Proceedings of the Institution of Electrical Engineers* **113,** 1151–1158 (1966).

153. Kapron, F. P., Keck, D. B. & Maurer, R. D. Radiation Losses in Glass Optical Waveguides. *Applied Physics Letters* **17,** 423–425 (1970).

154. Miya, T., Terunuma, Y., Hosaka, T. & Miyashita, T. Ultimate low-loss single-mode fibre at 1.55 μm. *Electronics Letters* **15,** 106 (1979).

155. Kimura, T. Single-mode systems and components for longer wavelengths. *IEEE Transactions on Circuits and Systems* **26,** 987–1010 (1979).

156. Kawachi, M., Kawana, A. & Miyashita, T. Low-Loss single-mode fibre at the material-dispersion-free wavelength of 1.27 μm. *Electronics Letters* **13,** 442 (1977).

157. Payne, D. & Gambling, W. Zero material dispersion in optical fibres. *Electronics Letters* **11,** 176 (1975).

158. Hsieh, J. J. & Shen, C. C. Room-temperature cw operation of buried-stripe double-heterostructure GaInAsP/InP diode lasers. *Applied Physics Letters* **30,** 429–431 (1977).

159. Ainslie, B. & Day, C. A review of single-mode fibers with modified dispersion characteristics. *Journal of Lightwave Technology* **4,** 967–979 (1986).

160. Bell, T. E. Single-frequency semiconductor lasers. *IEEE Spectrum* **20,** 38–45 (1983).

161. Mears, R., Reekie, L., Jauncey, I. & Payne, D. Low-noise erbium-doped fibre amplifier operating at 1.54μm. *Electronics Letters* **23,** 1026 (1987).

162. Fukuchi, K., Kasamatsu, T., Morie, M., Ohhira, R., Ito, T., Sekiya, K., Ogasahara, D. & Ono, T. *10.92-Tb/s (273 × 40-Gb/s) triple-band/ultra-dense WDM optical-repeatered transmission experiment* in *Optical Fiber Communication Conference and International Conference on Quantum Information* (OSA, Washington, D.C., 2001), PD24.

163. Olsson, S. L., Cho, J., Chandrasekhar, S., Chen, X., Burrows, E. C. & Winzer, P. J. Record-high 17.3-bit/s/Hz spectral efficiency transmission over 50 km using probabilistically shaped PDM 4096-QAM. *2018 Optical Fiber Communications Conference and Exposition, OFC 2018 - Proceedings,* 1–3 (2018).

164. Renaudier, J., Meseguer, A. C., Ghazisaeidi, A., Tran, P., Muller, R. R., Brenot, R., Verdier, A., Blache, F., Mekhazni, K., Duval, B., Debregeas, H., Achouche, M., Boutin, A., Morin, F., Letteron, L., Fontaine, N., Frignac, Y. & Charlet, G. *First 100-nm Continuous-Band WDM Transmission System with 115Tb/s Transport over 100km Using Novel Ultra-Wideband Semiconductor Optical Amplifiers* in *2017 European Conference on Optical Communication (ECOC)* **2017** (IEEE, 2017), 1–3.

165. Hillerkuss, D. *et al.* 26 Tbit s-1 line-rate super-channel transmission utilizing all-optical fast Fourier transform processing. *Nature Photonics* **5,** 364–371 (2011).

166. Marin-Palomo, P., Kemal, J. N., Karpov, M., Kordts, A., Pfeifle, J., Pfeiffer, M. H., Trocha, P., Wolf, S., Brasch, V., Anderson, M. H., Rosenberger, R., Vijayan, K., Freude, W., Kippenberg, T. J. & Koos, C. Microresonator-based solitons for massively parallel coherent optical communications. *Nature* **546,** 274–279 (2017).

167. Hu, H., Da Ros, F., Pu, M., Ye, F., Ingerslev, K., Porto da Silva, E., Nooruzzaman, M., Amma, Y., Sasaki, Y., Mizuno, T., Miyamoto, Y., Ottaviano, L., Semenova, E., Guan, P., Zibar, D., Galili, M., Yvind, K., Morioka, T. & Oxenløwe, L. K. Single-source chip-based frequency comb enabling extreme parallel data transmission. *Nature Photonics* **12,** 469–473 (2018).

168. Shannon, C. E. A Mathematical Theory of Communication. *Bell System Technical Journal* **27,** 379–423 (1948).

169. Shannon, C. E. Communication in the Presence of Noise. *Proceedings of the IRE* **37,** 10–21 (1949).

170. Essiambre, R.-J., Kramer, G., Winzer, P. J., Foschini, G. J. & Goebel, B. Capacity Limits of Optical Fiber Networks. *Journal of Lightwave Technology* **28,** 662–701 (2010).

171. Essiambre, R. J. & Tkach, R. W. Capacity trends and limits of optical communication networks. *Proceedings of the IEEE* **100,** 1035–1055 (2012).

172. Cregan, R. F., Mangan, B. J., Knight, J. C., Birks, T. A., Russell, P. S. J., Roberts, P. J. & Allan, D. C. Single-mode photonic band gap guidance of light in air. *Science* **285,** 1537–1539 (1999).

173. Soma, D., Wakayama, Y., Beppu, S., Sumita, S., Tsuritani, T., Hayashi, T., Nagashima, T., Suzuki, M., Takahashi, H., Igarashi, K., Morita, I. & Suzuki, M. *10.16 Peta-bit/s Dense SDM/WDM transmission over Low-DMD 6-Mode 19-Core Fibre Across C+L Band* in *2017 European Conference on Optical Communication (ECOC)* (IEEE, 2017), 1–3.

174. Tanaka, S., Akiyama, T., Sekiguchi, S. & Morito, K. Silicon photonics optical transmitter technology for Tb/s-class I/O Co-packaged with CPU. *Fujitsu Scientific and Technical Journal* **50,** 123–131 (2014).

175. Blum, R. Silicon Photonics THE KEY TO DATA CENTRE CONNECTIVITY. *Optical Connections,* 33–34 (2017).

176. Facebook. *Co-Packaged Optics Collaboration* Accessed 10 September 2020. https://www.facebook.com/CoPackagedOpticsCollaboration.

177. Fathololoumi, S. *et al.* 1.6Tbps Silicon Photonics Integrated Circuit for Co-Packaged Optical-IO Switch Applications. *2020 Optical Fiber Communications Conference and Exhibition, OFC 2020 - Proceedings* **1,** 6–8 (2020).

178. Ferrari, A. C. *et al.* Science and technology roadmap for graphene, related two-dimensional crystals, and hybrid systems. *Nanoscale* **7,** 4598–4810 (2015).

179. Wang, F., Zhang, Y., Tian, C., Girit, C., Zettl, A., Crommie, M. & Shen, Y. R. Gate-variable optical transitions in graphene. *Science* **320,** 206–209 (2008).

180. Backes, C. *et al.* Production and processing of graphene and related materials. *2D Materials* **7,** 022001 (2020).

181. Echtermeyer, T. J., Nene, P. S., Trushin, M., Gorbachev, R. V., Eiden, A. L., Milana, S., Sun, Z., Schliemann, J., Lidorikis, E., Novoselov, K. S. & Ferrari, A. C. Photothermoelectric and Photoelectric Contributions to Light Detection in Metal–Graphene–Metal Photodetectors. *Nano Letters* **14,** 3733–3742 (2014).

182. Song, J. C. W., Rudner, M. S., Marcus, C. M. & Levitov, L. S. Hot Carrier Transport and Photocurrent Response in Graphene. *Nano Letters* **11,** 4688–4692 (2011).

183. Pospischil, A., Humer, M., Furchi, M. M., Bachmann, D., Guider, R., Fromherz, T. & Mueller, T. CMOS-compatible graphene photodetector covering all optical communication bands. *Nature Photonics* **7,** 892–896 (2013).

184. Mueller, T., Xia, F. & Avouris, P. Graphene photodetectors for high-speed optical communications. *Nature Photonics* **4,** 297–301 (2010).

185. Gan, X., Shiue, R.-J., Gao, Y., Meric, I., Heinz, T. F., Shepard, K., Hone, J., Assefa, S. & Englund, D. Chip-integrated ultrafast graphene photodetector with high responsivity. *Nature Photonics* **7,** 883–887 (2013).

186. Schall, D., Neumaier, D., Mohsin, M., Chmielak, B., Bolten, J., Porschatis, C., Prinzen, A., Matheisen, C., Kuebart, W., Junginger, B., Templ, W., Giesecke, A. L. & Kurz, H. 50 GBit/s Photodetectors Based on Wafer-Scale Graphene for Integrated Silicon Photonic Communication Systems. *ACS Photonics* **1,** 781–784 (2014).

187. Shiue, R.-J., Gao, Y., Wang, Y., Peng, C., Robertson, A. D., Efetov, D. K., Assefa, S., Koppens, F. H. L., Hone, J. & Englund, D. High-Responsivity Graphene–Boron Nitride Photodetector and Autocorrelator in a Silicon Photonic Integrated Circuit. *Nano Letters* **15,** 7288–7293 (2015).

188. Schall, D., Porschatis, C., Otto, M. & Neumaier, D. Graphene photodetectors with a bandwidth >76 GHz fabricated in a 6 wafer process line. *Journal of Physics D: Applied Physics* **50,** 124004 (2017).

189. Freitag, M., Low, T., Zhu, W., Yan, H., Xia, F. & Avouris, P. Photocurrent in graphene harnessed by tunable intrinsic plasmons. *Nature Communications* **4,** 1951–1958 (2013).

190. Ma, P., Salamin, Y., Baeuerle, B., Josten, A., Heni, W., Emboras, A. & Leuthold, J. Plasmonically Enhanced Graphene Photodetector Featuring 100 Gbit/s Data Reception, High Responsivity, and Compact Size. *ACS Photonics* **6,** 154–161 (2019).

191. Schuler, S., Muench, J. E., Ruocco, A., Balci, O., van Thourhout, D., Sorianello, V., Romagnoli, M., Watanabe, K., Taniguchi, T., Goykhman, I., Ferrari, A. C. & Mueller, T. High-responsivity graphene photodetectors integrated on silicon microring resonators, 1–11 (2020).

192. Schuler, S., Schall, D., Neumaier, D., Dobusch, L., Bethge, O., Schwarz, B., Krall, M. & Mueller, T. Controlled Generation of a p-n Junction in a Waveguide Integrated Graphene Photodetector. *Nano Letters* **16,** 7107–7112 (2016).

193. Muench, J. E., Ruocco, A., Giambra, M. A., Miseikis, V., Zhang, D., Wang, J., Watson, H. F., Park, G. C., Akhavan, S., Sorianello, V., Midrio, M., Tomadin, A., Coletti, C., Romagnoli, M., Ferrari, A. C. & Goykhman, I. Waveguide-Integrated, Plasmonic Enhanced Graphene Photodetectors. *Nano Letters* **19,** 7632–7644 (2019).

194. Mišeikis, V., Marconi, S., Giambra, M. A., Montanaro, A., Martini, L., Fabbri, F., Pezzini, S., Piccinini, G., Forti, S., Terrés, B., Goykhman, I., Hamidouche, L., Legagneux, P., Sorianello, V., Ferrari, A. C., Koppens, F. H., Romagnoli, M. & Coletti, C. Ultrafast, Zero-Bias, Graphene Photodetectors with Polymeric Gate Dielectric on Passive Photonic Waveguides. *ACS Nano* (2020).

195. Xia, F., Mueller, T., Lin, Y. M., Valdes-Garcia, A. & Avouris, P. Ultrafast graphene photodetector. *Nature Nanotechnology* **4,** 839–843 (2009).

196. Urich, A., Unterrainer, K. & Mueller, T. Intrinsic Response Time of Graphene Photodetectors. *Nano Letters* **11,** 2804–2808 (2011).

197. Kubo, R. Statistical-Mechanical Theory of Irreversible Processes. I. General Theory and Simple Applications to Magnetic and Conduction Problems. *Journal of the Physical Society of Japan* **12,** 570–586 (1957).

198. Chang, Y.-C., Liu, C.-H., Liu, C.-H., Zhong, Z. & Norris, T. B. Extracting the complex optical conductivity of mono- and bilayer graphene by ellipsometry. *Applied Physics Letters* **104,** 261909 (2014).

199. Kuzmenko, A. B., Van Heumen, E., Carbone, F. & Van Der Marel, D. Universal optical conductance of graphite. *Physical Review Letters* **100,** 2–5 (2008).

200. Mak, K. F., Sfeir, M. Y., Wu, Y., Lui, C. H., Misewich, J. A. & Heinz, T. F. Measurement of the opptical conductivity of graphene. *Physical Review Letters* **101,** 2–5 (2008).

201. Neugebauer, P., Orlita, M., Faugeras, C., Barra, A.-L. & Potemski, M. How Perfect Can Graphene Be? *Physical Review Letters* **103,** 136403 (2009).

202. Mohsin, M., Neumaier, D., Schall, D., Otto, M., Matheisen, C., Lena Giesecke, A., Sagade, A. A. & Kurz, H. Experimental verification of electro-refractive phase modulation in graphene. *Scientific Reports* **5,** 10967 (2015).

203. Falkovsky, L. A. & Pershoguba, S. S. Optical far-infrared properties of a graphene monolayer and multilayer. *Physical Review B - Condensed Matter and Materials Physics* **76,** 1–4 (2007).

204. Gosciniak, J. & Tan, D. T. H. Theoretical investigation of graphene-based photonic modulators. *Scientific Reports* **3,** 1897 (2013).

205. Liu, M., Yin, X., Ulin-Avila, E., Geng, B., Zentgraf, T., Ju, L., Wang, F. & Zhang, X. A graphene-based broadband optical modulator. *Nature* **474,** 64–67 (2011).

206. Sorianello, V., Midrio, M. & Romagnoli, M. Design optimization of single and double layer Graphene phase modulators in SOI. *Optics Express* **23,** 6478 (2015).

207. Liu, Y., Cheng, R., Liao, L., Zhou, H., Bai, J., Liu, G., Liu, L., Huang, Y. & Duan, X. Plasmon resonance enhanced multicolour photodetection by graphene. *Nature Communications* **2,** 579 (2011).

208. Liu, M., Yin, X. & Zhang, X. Double-Layer Graphene Optical Modulator. *Nano Letters* **12** (eds Pribat, D., Lee, Y.-H. & Razeghi, M.) 1482–1485 (2012).

209. Giambra, M. A., Sorianello, V., Miseikis, V., Marconi, S., Montanaro, A., Galli, P., Pezzini, S., Coletti, C. & Romagnoli, M. High-speed double layer graphene electroabsorption modulator on SOI waveguide. *Optics Express* **27,** 20145 (2019).

210. Dalir, H., Xia, Y., Wang, Y. & Zhang, X. Athermal Broadband Graphene Optical Modulator with 35 GHz Speed. *ACS Photonics* **3,** 1564–1568 (2016).

211. Alessandri, C., Asselberghs, I., Brems, S., Huyghebaert, C., Van Campenhout, J., Van Thourhout, D. & Pantouvaki, M. 5 × 25 Gbit/s WDM transmitters based on passivated graphene–silicon electro-absorption modulators. *Applied Optics* **59,** 1156 (2020).

212. Sorianello, V., Midrio, M., Contestabile, G., Asselberghs, I., Van Campenhout, J., Huyghebaert, C., Goykhman, I., Ott, A. K., Ferrari, A. C. & Romagnoli, M. Graphene–silicon phase modulators with gigahertz bandwidth. *Nature Photonics* **12,** 40–44 (2018).

213. Phare, C. T., Daniel Lee, Y.-H., Cardenas, J. & Lipson, M. Graphene electro-optic modulator with 30 GHz bandwidth. *Nature Photonics* **9,** 511–514 (2015).

214. Aria, A. I., Nakanishi, K., Xiao, L., Braeuninger-Weimer, P., Sagade, A. A., Alexander-Webber, J. A. & Hofmann, S. Parameter Space of Atomic Layer Deposition of Ultrathin Oxides on Graphene. *ACS Applied Materials and Interfaces* **8,** 30564–30575 (2016).

215. Davidson, D. B. *Computational Electromagnetics for RF and Microwave Engineering* 2nd ed. (Cambridge University Press, 2010).

216. Bienstman, P. & Baets, R. Optical modelling of photonic crystals and VCSELs using eigenmode expansion and perfectly matched layers. *Optical and Quantum Electronics* **33,** 327–341 (2001).

217. Tropf, W. J. & Thomas, M. E. in *Handbook of Optical Constants of Solids* 653–682 (Elsevier, 1997).

218. Xia, J., Chen, F., Li, J. & Tao, N. Measurement of the quantum capacitance of graphene. *Nature Nanotechnology* **4,** 505–509 (2009).

219. Arndt, A., Spoddig, D., Esquinazi, P., Barzola-Quiquia, J., Dusari, S. & Butz, T. Electric carrier concentration in graphite: Dependence of electrical resistivity and magnetoresistance on defect concentration. *Physical Review B - Condensed Matter and Materials Physics* **80,** 1–5 (2009).

220. Plummer, J. D. *Silicon VLSI technology : fundamentals, practice, and modeling / James D. Plummer, Michael Deal, Peter B. Griffin.* eng (Prentice Hall, Upper Saddle River, N.J. ; London, 2000).

221. Absil, P. P., Verheyen, P., De Heyn, P., Pantouvaki, M., Lepage, G., De Coster, J. & Van Campenhout, J. Silicon photonics integrated circuits: a manufacturing platform for high density, low power optical I/O's. *Optics Express* **23,** 9369 (2015).

222. Lagatsky, A. A., Sun, Z., Kulmala, T. S., Sundaram, R. S., Milana, S., Torrisi, F., Antipov, O. L., Lee, Y., Ahn, J. H., Brown, C. T., Sibbett, W. & Ferrari, A. C. 2 Mm Solid-State Laser Mode-Locked By Single-Layer Graphene. *Applied Physics Letters* **102,** 1–5 (2013).

223. Hwang, E. H., Adam, S. & Sarma, S. D. Carrier transport in two-dimensional graphene layers. *Physical Review Letters* **98,** 2–5 (2007).

224. Tan, Y. W., Zhang, Y., Bolotin, K., Zhao, Y., Adam, S., Hwang, E. H., Das Sarma, S., Stormer, H. L. & Kim, P. Measurement of scattering rate and minimum conductivity in graphene. *Physical Review Letters* **99,** 10–13 (2007).

225. Chen, J. H., Jang, C., Adam, S., Fuhrer, M. S., Williams, E. D. & Ishigami, M. Charged-impurity scattering in graphene. *Nature Physics* **4,** 377–381 (2008).

226. Aničić, R. & Mišković, Z. L. Effects of the structure of charged impurities and dielectric environment on conductivity of graphene. *Physical Review B* **88,** 205412 (2013).